7-30-2010

Gladwin Tensor Strainmeter Calibration using Seismic Data: Instrument Calibration Methods and Wave Gradiometry Applications

Elige Buckhanan Grant V

To the University Council:

The Dissertation Committee for Elige Buckhanan Grant V certifies that this is the approved version of the following electronic dissertation: "Gladwin Tensor Strainmeter Calibration using Seismic Data: Instrument Calibration Methods and Wave Gradiometry Applications."

_____

Charles Langston, Ph.D.
Major Professor

_____

Evelyn Roeloffs, Ph.D.

_____

Robert Smalley, Ph.D.

_____

Arch Johnston, Ph.D.

_____

Mitch Withers, Ph.D.

_____

Joan Schmelz, Ph.D.

Accepted for the Graduate Council:

_____

Karen D. Weddle-West, Ph.D.
Vice Provost for Graduate Programs

GLADWIN TENSOR STRAINMETER CALIBRATION USING SEISMIC DATA:

INSTRUMENT CALIBRATION METHODS AND WAVE GRADIOMETRY APPLICATIONS

by

Elige Buckhanan Grant V

A Dissertation

Submitted in Partial Fulfillment of the

Requirements for the Degree of

Doctor of Philosophy

Major: Earth Science – Geophysics

The University of Memphis

August 2010

ACKNOWLEDGEMENTS

I owe a great deal of thanks to a number of people and organizations that have assisted me in completing my dissertation.

- My advisor, Dr. Charles Langston, has been an important resource at every step in the research and development process of this body of work. I am deeply grateful for his guidance, patience, and encouragement.
- All of my committee members: Dr. Evelyn Roeloffs, Dr. Robert Smalley, Dr. Arch Johnston, Dr. Mitch Withers, and Dr. Joan Schmelz. I appreciate all their help and guidance, especially their help in preparing this manuscript.
- EarthScope and its sponsor, The National Science Foundation (NSF), for providing the strain data used in this study.
- Wessel and Smith (1998), as several figures were generated using the Generic Mapping Tool (GMT)
- Several institutions and organizations for the excellent level of financial support I enjoyed during the past four years:
    - During 2006 – 2007 and 2007 – 2008, my research and education was supported by the Center for Earthquake Research and Information (CERI) through the Palisades Geophysical Institute (PGI) Fellowship.
    - During 2008 – 2009 and 2009 – 2010, my research was supported by an NSF grant: EAR-0745898.
    - During 2007 – 2008 and 2008 – 2009, supplemental financial support was provided by a Federal Work-Study (FSW) program.
    - During 2008 – 2009 and 2009 – 2010, supplemental financial support was provided by a scholarship from the Chevron Corporation.
- The faculty, staff, and students of CERI for all the knowledge and support they shared with me.
- My friends and family for their love and support. Especially my parents, Elige and Julie, my sisters, Haley and Jordan, and my wife's parents, Gail and Jim. Additional thanks go to my wife's sister, Susan, for introducing me to several

optimization schemes in Matlab that proved to be very useful for quickly solving a variety of problems encountered during my work.

- My wife, Meredith, to whom I am eternally indebted – I would not have been able to accomplish this feat without her love, support, and encouragement.

ABSTRACT

Grant, Elige Buckhanan. Ph.D. The University of Memphis. August, 2010. Gladwin Tensor Strainmeter Calibration using Seismic Data: Instrument Calibration Methods and Wave Gradiometry Applications. Major Professor: Dr. Charles A. Langston.

Calibration coefficients yielding the borehole coupling parameters and corrections to misalignment errors have been calculated for seven borehole Gladwin Tensor Strainmeter (GTSM) instruments, in southern California, associated with the Plate Boundary Observatory (PBO). The calibration coefficients are derived from a linear relationship between the strain field measured in the borehole and the reference strain field derived at the surface. In this study, we derived the reference formation strains (i.e., areal strain, differential normal strain, and shear strain) at the surface from broadband data collected by the Anza Seismic Network in southern California. We find reasonable agreement between the calibration coefficients derived here using seismic data and the calibration coefficients derived elsewhere using theoretical earth tide measurements. We tested whether each strainmeter required different calibration coefficients over time and found no time dependency over a ~2 year period. We also investigated potential instrument orientation errors during the calibration process and determined that the seven borehole GTSM instruments in this study required correction factors ranging from 3 to 50 degrees.

Accurate reference formation strains are necessary to ensure accurate calibration of the borehole GTSM instruments. In order to derive accurate measurements of reference strain, we evaluate four different methods for estimating the spatial displacement gradient using broadband, teleseismic data. During these experiments we identified two methods, one derived from spatial gradient analysis in two-dimensions (2D) and one based on plane-wave polynomial interpolation, that appeared to perform well consistently. During the calibration process we combined these two methods in order to further increase the accuracy of our spatial displacement gradient estimates, and therefore the accuracy of our reference strain estimates.

Three interesting applications utilizing data collected by a calibrated borehole GTSM instrument co-located with a broadband seismic station and by a dense array of

calibrated borehole GTSM instruments are discussed. We find that important characteristics of the seismic wavefield, including the change in geometrical spreading, horizontal phase velocity, and propagation direction, can all be derived at a single location on the surface of the earth using techniques derived from spatial gradient analysis in 1D and 2D.

TABLE OF CONTENTS

LIST OF TABLES

LIST OF FIGURES

LIST OF ABBREVIATIONS

1D – One Dimensional

2D – Two Dimensional

3D – Three Dimensional

BSM – Borehole Strainmeter

CW – Clockwise

CCW – Counter-Clockwise

E. T. – Earth Tide

GPS – Global Positioning System

GTSM – Gladwin Tensor Strainmeter

IRIS – Incorporated Research for Seismology

LOSS – Leave Out Station Scenario

LSM – Laser Strainmeter

M – Magnitude

NSF – National Science Foundation

PBO – Plate Boundary Observatory

PDF – Probablity Density Function

SAFOD – San Andreas Fault Observatory at Depth

STD – Standard Deviation

UNAVCO – University NAVSTAR Consortium

LIST OF SYMBOLS

c – Propagation Velocity

C – Instrument Cross-Spectra Matrix

δ_{ij} – Kronerker Delta (0 if $i \neq j$ or 1 if $i=j$)

° – Degrees

e – Gauge Strain

ε – Strain

e_a – Areal Strain

f – Frequency

G_r – Radial Geometrical Spreading

γ_1 – Differential Normal Strain

γ_2 – Engineering Shear Strain

Hz – Hertz

I – Instrument

k – wavenumber

K – Coupling Model (or Coupling Matrix)

km – Kilometers

λ – Wavelength

m – Meters

μm – Micrometers

M – Matrix or Set

nm – Nanometers

N – Integer Number

O – Orientation Matrix

ω – Radial Frequency

r – Radial Distance or Reference

R – Radial or Reference

R – Reference Cross-Spectra Matrix

s – seconds

s – Formation Strain

s_r – Radial Slowness

S – Calibration Matrix

τ – Stress

t – Time

T – Transverse

T* – Conjugate Transpose

θ – Propagation Azimuth

u – Displacement

$u_{i,j}$ – Displacement Gradient ($\partial u_i / \partial u_j$)

v – Vector

v – Variable

CHAPTER 1

Introduction

The Plate Boundary Observatory (PBO) is an EarthScope project designed to measure and study plate deformation in the western part of North America. There are nearly 1300 stations that make up the PBO – they include Global Positioning System (GPS) stations, Borehole Strainmeter (BSM) stations, surface Laser Strainmeter (LSM) stations, tiltmeter stations, and seismometer stations [*EarthScope*, 2009]. Of the nearly 1300 instruments, there are currently 74 borehole Gladwin Tensor Strainmeter (GTSM) instruments that have been deployed [*UNAVCO*, 2010]. However, most (if not all) GTSM instruments that have been installed to date have experienced problems that have brought the quality of their data into question [*Roeloffs et al.*, 2004]. This body of work will focus on seismological calibration methods that mitigate these problems and on interesting applications that incorporate calibrated strainmeter data.

The Plate Boundary Observatory

The Plate Boundary Observatory was developed in order to study the four-dimensional (4D) characteristics of deformation across western North America – especially the deformation process leading up to a large earthquake or volcanic event [*Jackson and Bohnenstiehl*, 2005]. The PBO concept was presented to the National Science Foundation (NSF) after gathering input from a workshop conducted in October 1999. The Plate Boundary Observatory together with the USArray and the San Andreas Fault Observatory at Depth (SAFOD), collectively known as the EarthScope Project (see Figure 1), got underway in 2004 through financial support from the NSF. The

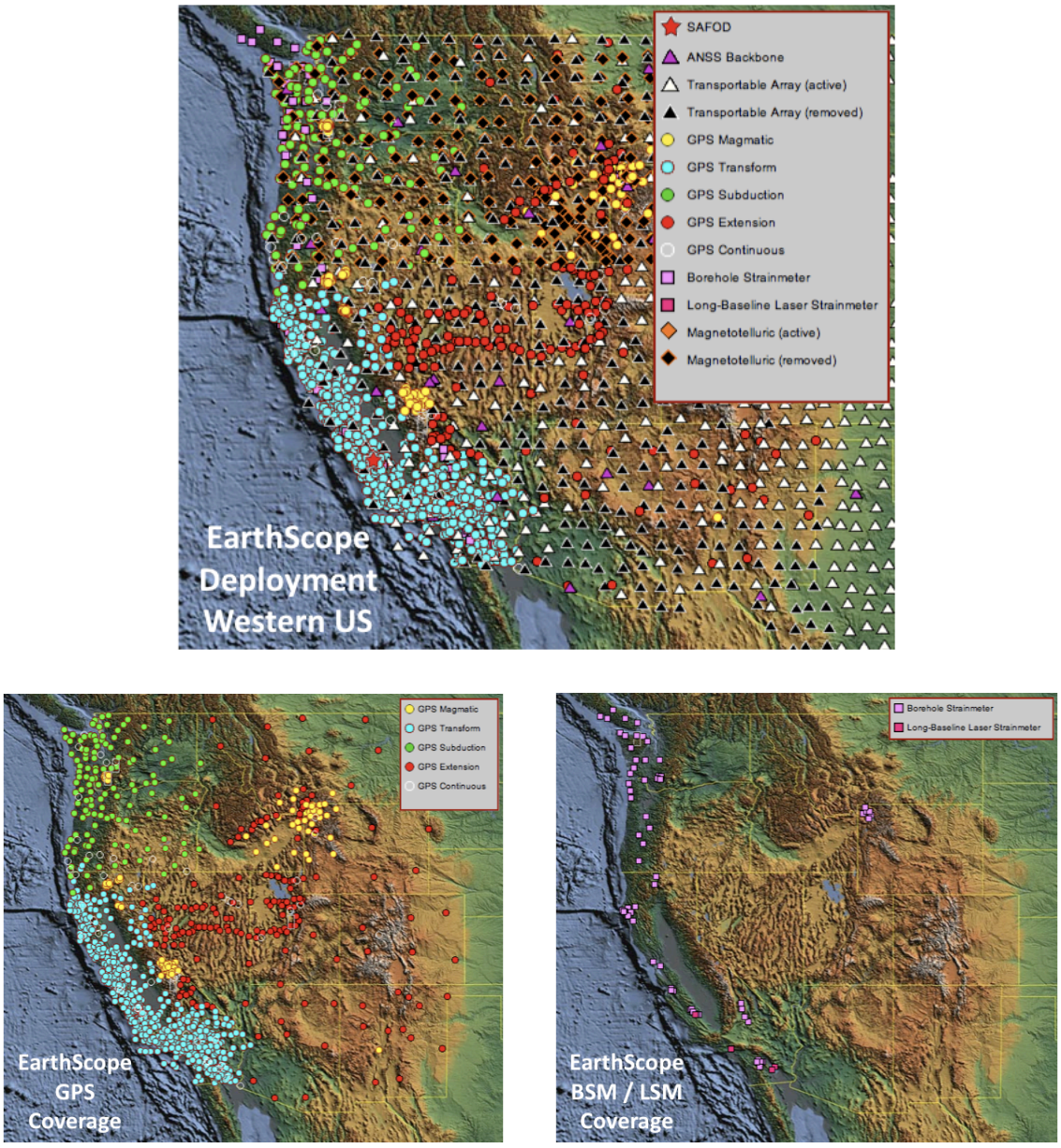

Figure 1. Illustration of the EarthScope deployment (PBO, USArray, and SAFOD) along western North America [*EarthScope*, 2009].

University NAVSTAR Consortium (UNAVCO) has been responsible for installing and maintaining all the instruments that make up the PBO.

The PBO is composed of a variety of sensors in order to measure deformation across a variety of time scales. The ~1100 GPS stations, which make up the largest fraction of the PBO instrumentation, measure deformation associated with characteristic event times ranging from several days to several decades [*Roeloffs et al.*, 2004]. In contrast, seismometer instruments measure deformation associated with characteristic event times ranging from several milliseconds to several minutes. BSM instruments bridge the gap between seismological and GPS technologies by measuring deformation associated with characteristic event times ranging from several seconds to several months (Figure 2).

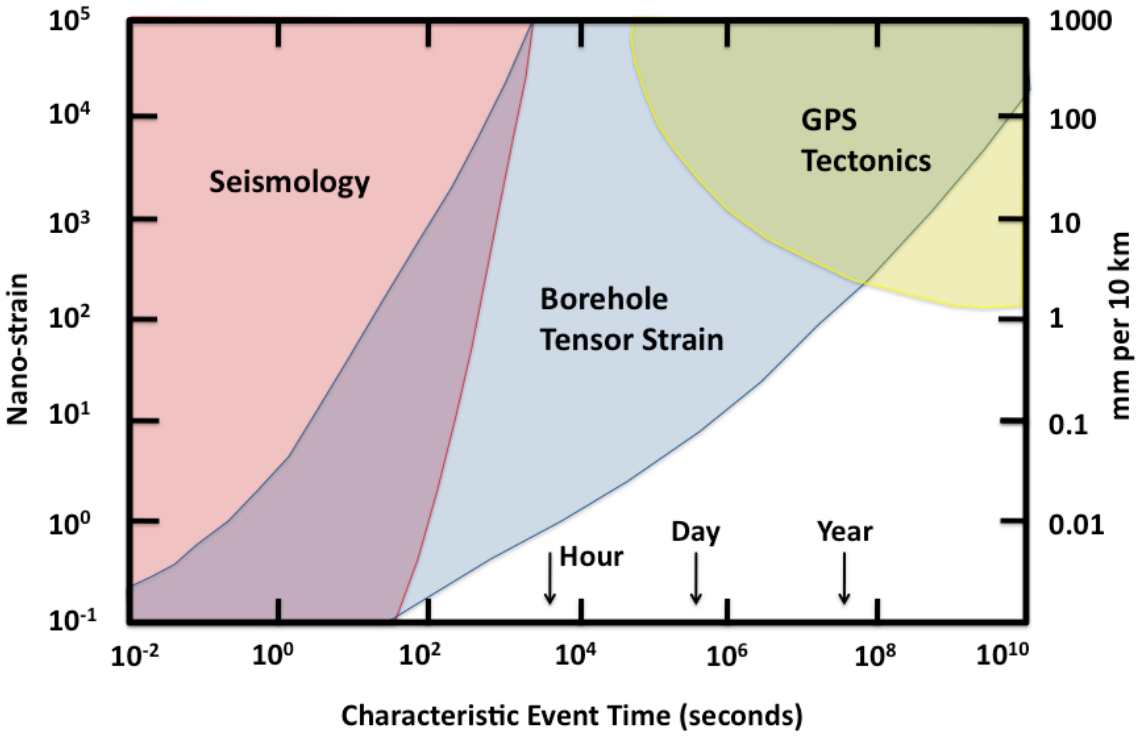

Figure 2. Illustration of the characteristic event time coverage for Seismological, GTSM and GPS Technologies (reproduced from *GTSM* [2010]).

In order to study the deformation processes that occur at time scales between that of the seismological and GPS technologies, it is important that the data collected by the BSM instruments accurately reflect the true local strain field resulting from a tectonic event. However, the default isotropic calibration parameters that have been adopted by the PBO do not take into account the local anisotropic effects associated with each borehole GTSM instrument [*Hart et al.*, 1996 and *Roeloffs*, 2010]. Therefore, in order to recover the true local strain field, it is necessary to provide accurate calibration parameters specific to each GTSM station.

Gladwin Tensor Strainmeter Instruments

Gladwin Tensor Strainmeter (GTSM) instruments are billed to be a high precision, high stability multi-component (tensor) tool for measuring tectonic strain inside a deep borehole. As of July 2010, 74 of the proposed 103 GTSM instruments have been installed (see bottom-right image in Figure 1 for current station coverage). Boreholes typically extend down to depths greater than 150m, where the GTSM instrument is emplaced using an expansive grout to ensure proper coupling. As an example, the schematic associated with the installation of GTSM station B081, located in southern California, is illustrated in Figure (3). Each GTSM instrument consists of 4 gauges – channel 1 is orientated 60 degrees Counter-Clockwise (CCW) from channel 0, channel 2 is orientated 120 degrees CCW from channel 0, and channel 3 is orientated 150 degrees CCW from channel 0. The fourth gauge is redundant for deriving strain information, but is important in identifying whether a gauge is operating inconsistently (or not at all). The four gauges measure the change in diameter of the instrument housing in response to various tectonic and non-tectonic (e.g., tide, atmosphere, and pore pressure) activities.

The deformation measured by the GTSM instrument downhole is different from the deformation that would have resulted in the same location had the borehole never been

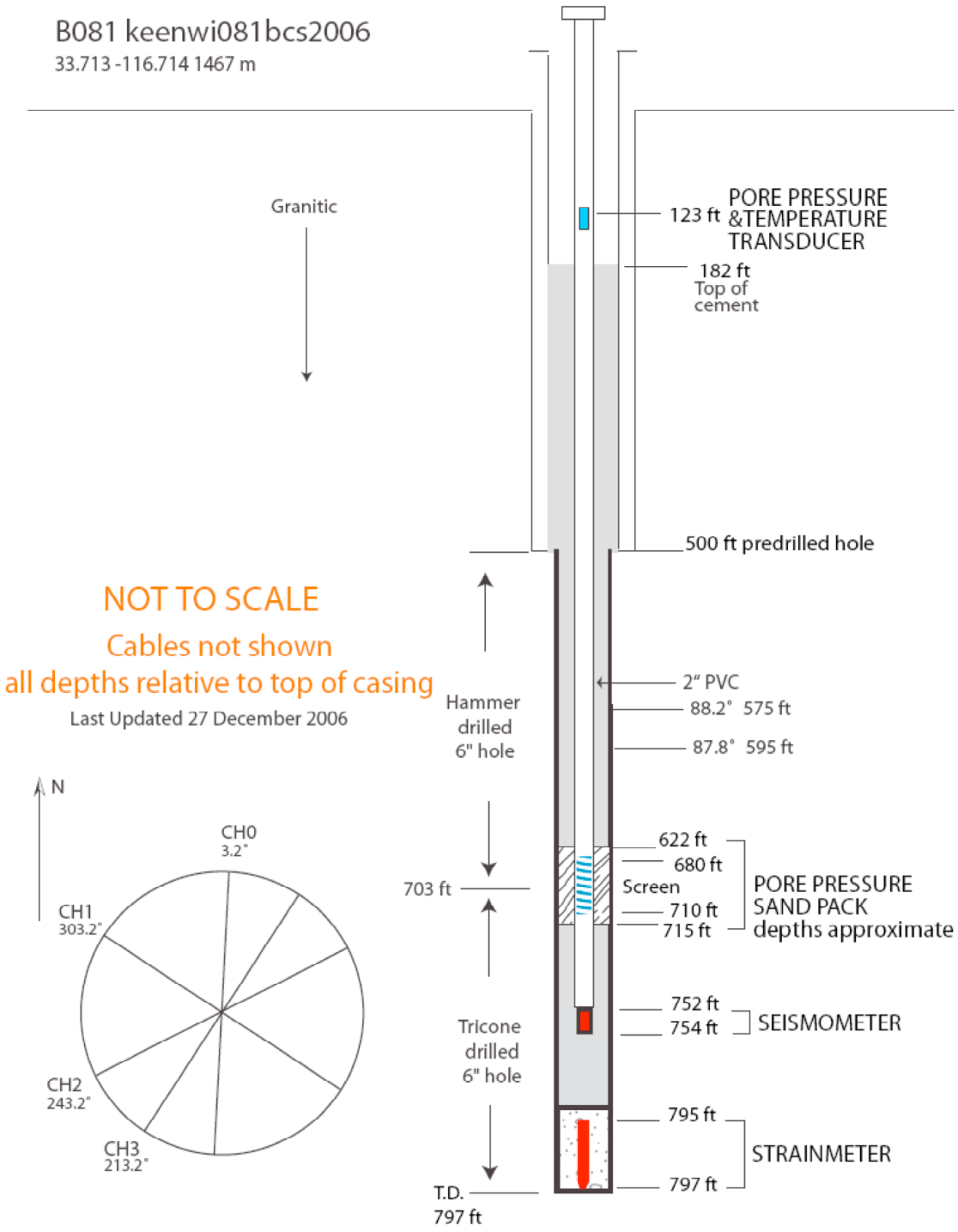

Figure 3. Installation schematic of PBO GTSM instrument B081 located in Southern California [*UNAVCO*, 2010]. Nearly all GTSM installations also include the installation of a seismometer and temperature transducer; only a few also include a pore pressure transducer.

drilled. The difference in the amount of deformation at the same location before/after installation is due, in part, to the large difference in elastic properties between the downhole geology and the borehole coupled instrument. The downhole location is transformed from a nearly isotropic medium to an anisotropic system composed of the borehole geology, expansive grout, and strainmeter housing. Since measured deformation is not the same as the "true" deformation, it is necessary to derive scale factors that attempt to transform the deformation measured downhole to the theoretical deformation that would have occurred had the instrument not been installed.

Previous Studies

Gladwin and Hart [1985] and *Shimada et al.* [1987] both attempted to directly estimate the elastic parameters associated with the borehole environment. The elastic parameters were derived separately for the borehole geology and the expansive grout used to couple the BSM to the borehole. The effective response of a BSM inside a specific borehole was then obtained by combining the derived elastic parameters with the known response of a BSM instrument to deformation under ideal (i.e., isotropic) conditions.

Hart et al. [1996] attempted to derive the effective response of a BSM inside a specific borehole by linearly relating the strain field measured by a BSM instrument to the strain field measured by a co-located LSM instrument. In that study, the strain field measured by each instrument was related to the earth's tide. Theoretical earth tide measurements were also considered, however the authors found the theoretical strain measurements were not able to compensate for the heterogeneous effects associated with each borehole environment.

Roeloffs [2010] attempted to derive the effective response of a BSM inside a specific borehole by linearly relating the strain field measured by a BSM instrument to the strain field derived from theoretical earth tide measurements. Only the theoretical strain

measurements at locations that were known to be consistent with previous strain measurements were used. That study reformulated the calibration equations, similar to those in *Hart et al.* [1996], in order to account for the effects caused by coupling between the vertical strain and the horizontal components of formation strain. That study also investigated both the relationship between the borehole GTSM and the changes in atmospheric pressure and the possible relationship between the borehole GTSM and the changes in pore fluid pressure.

Data provided by BSM instruments are critical to studies involving many different important tectonic processes – they include tectonic activity associated with aseismic fault movement [*Linde et al.*, 1996 and *McCausland et al.*, 2008], tectonic activity creating permanent displacement offsets [*Johnston et al.*, 2006], and tectonic activity indicating an imminent volcanic eruption [*Sturkell et al.*, 2006].

The Current Study

In this study, we make the hypothesis that the borehole GTSM instruments associated with the PBO can be calibrated using reference formation strain measurements derived from broadband seismic data. This hypothesis was motivated by *Langston and Liang* [2008], where formation strain measurements derived from 7 PBO GTSM instruments (B081, B082, B084, B086, B087, B088 and B089) were compared to each other and to the formation strain measurements derived from broadband seismic data collected by a dense, 10-element subset of the Anza Seismic Network in southern California (see Figure 4). It was observed that the formation strain measurements derived from the broadband seismic data showed excellent consistency in both waveshape and amplitude for the 1 April 2007 M8.1 Solomon Islands earthquake (see Figure 5). In contrast, formation strain measurements derived from borehole GTSM instrument data associated with the same event were highly inconsistent in both waveshape and amplitude despite the relative close proximity of each station (see Figure 6).

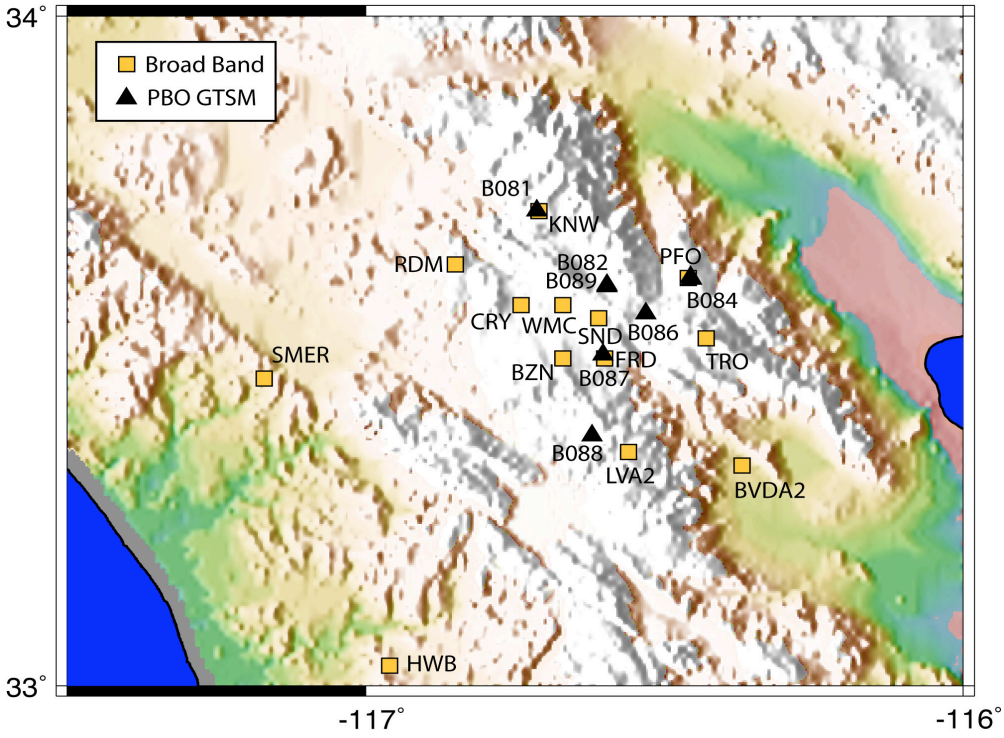

Figure 4. Location of Anza Seismic Network stations and PBO GTSM stations in the study area. ORANGE squares indicate the location of broadband seismic instruments – the subset of the Anza Seismic Network used in this study did not include BVDA2, HWB, and SMER. BLACK triangles indicate the location of GTSM instruments. Image from *Langston and Liang* [2008].

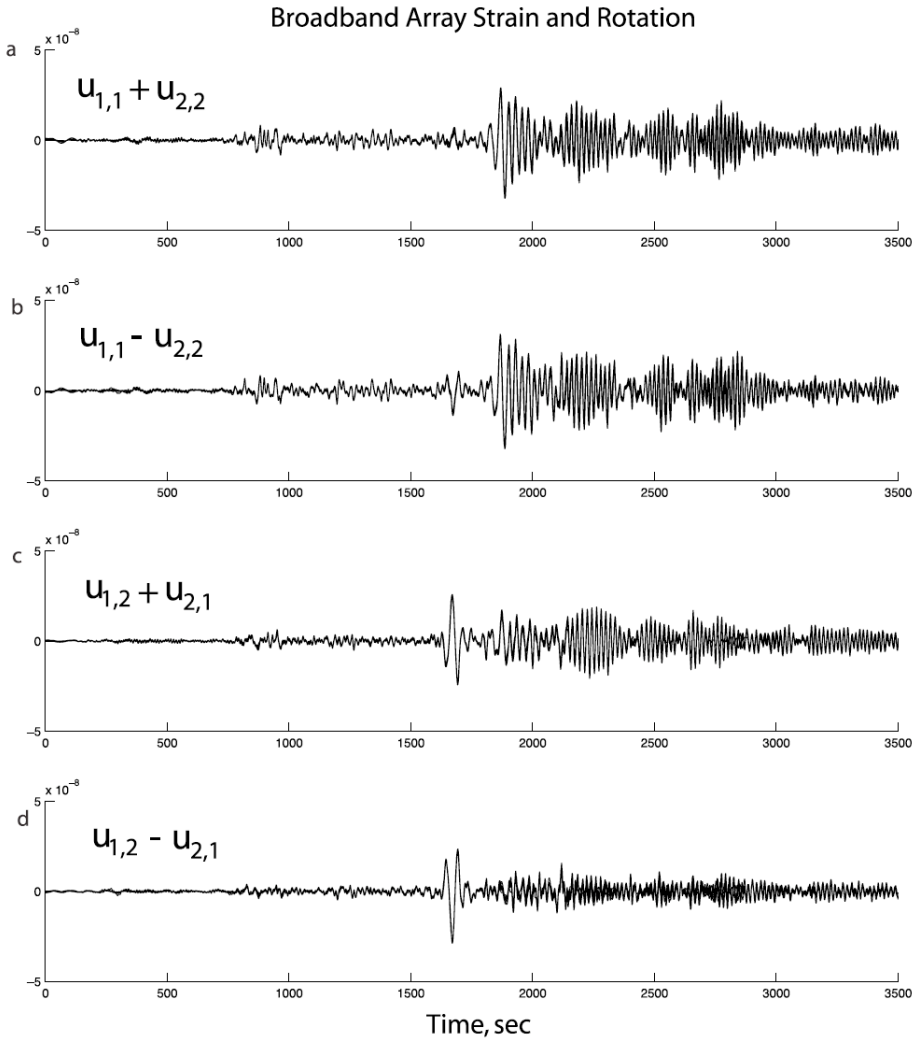

Figure 5. Illustration of the formation strain derived at each broadband seismic station in the 10-element subset of the Anza Seismic Network for the 1 April 2007 M8.1 Solomon Islands earthquake. The areal strain (a) is equal to the sum of displacement gradient elements $u_{1,1}$ and $u_{2,2}$. The differential normal strain (b) is equal to the difference between displacement gradient elements $u_{1,1}$ and $u_{2,2}$. The shear strain (c) is equal to the sum of displacement gradient elements $u_{1,2}$ and $u_{2,1}$. The rotation (d) is equal to the difference between displacement gradient elements $u_{1,2}$ and $u_{2,1}$. The vertical axis (i.e., *y*-axis) limits were set to ± $5x10^{-8}$ m/m in order to highlight the very consistent nature of strain measurements between all stations (i.e., the 10 traces overlap each other). Figure (9) from *Langston and Liang* [2008].

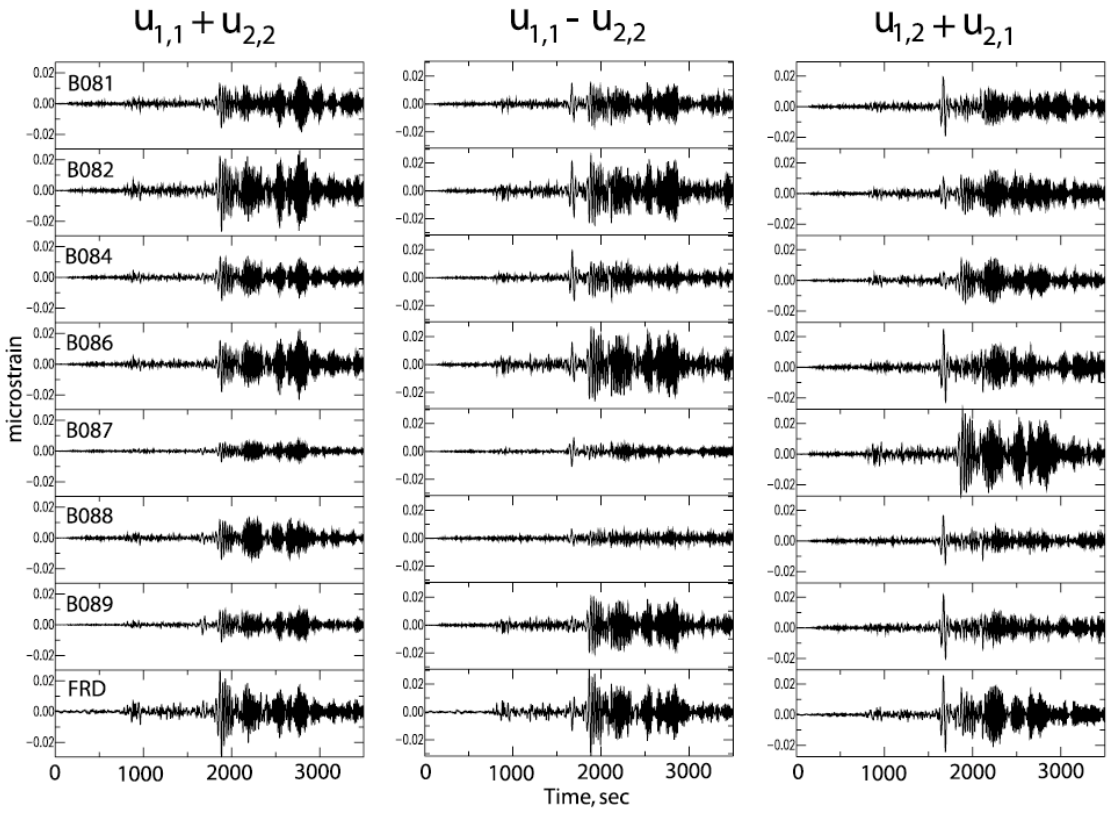

Figure 6. Illustration of the formation strain derived from seven PBO GTSM instruments, using advertised orientation angles, inside the Anza Seismic Network in Southern California. For comparison, the bottom row indicates the formation strain derived from one of the broadband seismometers (FRD) in Figure (5a, b, c). The vertical axis (i.e., *y*-axis) limits were set to ± 0.03 micro-strain (i.e., 10^{-6} m/m) in order to highlight the inconsistent nature of strain measurements between all stations. Figure (10) from *Langston and Liang* [2008].

The material in this study will cover three important aspects related to strainmeter calibration; in short, Chapter (2) will cover methods for deriving strain measurements from broadband seismic data, Chapter (3) will cover the method for calibrating borehole GTSM instruments using the reference strain measurements derived from seismic data, and Chapter (4) will cover three possible applications that incorporate the calibrated strainmeter data. More specifically, Chapter (2) will develop and describe several interpolation-based techniques to appropriately describe the formation strain at arbitrary locations inside an irregularly spaced seismic array. Chapter (3) will develop and describe the theory associated with strainmeter calibration using seismic data. This chapter will also illustrate the success of the calibration method. Chapter (4) will introduce and discuss several interesting applications based on standard array processing techniques and spatial gradient analysis, which both rely on data from a calibrated borehole instrument to work.

The results of this study demonstrate that seismic-based calibration techniques appear to be a useful way of resolving the borehole coupling model, assumed here to be frequency independent, and any orientation errors. Accurate estimates of these parameters enable the “true” crustal strain associated with a variety of tectonic and non-tectonic events to be resolved from the complex deformation signals measured by most borehole GTSM instruments. It should be a straightforward process to extend the procedure followed in this study to other borehole GTSM instruments in need of calibration when dense permanent or temporary broadband seismic networks are installed nearby.

CHAPTER 2

Estimating Spatial Displacement Gradients using Seismic Data

Abstract

We compare four methods for estimating the spatial displacement gradients across an arbitrary, two-dimensional (2D) seismic array. The first is the seismo-geodetic method of *Spudich et al.* [1995], the second is the biharmonic spline interpolation method of *Sandwell* [1987], the third method (developed here) is also interpolation-based, and the fourth method is based on the 2D spatial gradient analysis (or wave gradiometry) method of *Langston* [2007b]. The seismo-geodetic method may only be applied to seismic array displacement data that are the result of uniform strain at any instant in time. The biharmonic spline interpolation method does not make any assumptions about the mode of wave propagation across an arbitrary 2D seismic array, except that ground displacements at any instant in time are smoothly varying. The second interpolation-based method and the method based on spatial gradient analysis both assume plane-wave propagation and that displacements are smoothly varying across an arbitrary 2D seismic array. When the seismic displacements across an array are not the result of uniform strain, the results from the seismo-geodetic method appear to suffer from timing (or phase) errors. We find that these apparent timing (or phase) errors are sensitive to irregularities in the geometry of the seismic array. We also find that the last three methods can help mitigate the apparent timing (or phase) errors in the spatial displacement gradients.

Experiments conducted in this study demonstrate that the method based on spatial gradient analysis appears to offer more accurate and precise estimates of the spatial displacement gradients at a specific seismic station. However, when estimating the displacement gradient at an arbitrary reference position inside the seismic array, we find

that the preferred method should be combined with one of the interpolation methods in order to maintain the same level of accuracy and precision. This is important for analyses that depend on accurate measurements of strain and rotation.

Introduction

Accurate measurements of the spatial displacement gradient are an important component to many different areas of analyses that require accurate estimates of strain, stress, or rotation. Such areas of analyses include earthquake hazard mitigation [*Bodin et al.*, 1997 and *Gomberg et al.*, 1999], building and infrastructure engineering [*Trifunac*, 1982 and *Paolucci and Smerzini*, 2008], seismic phase velocity estimation [*Mikumo and Aki*, 1964 and *Langston and Liang*, 2008], and estimation of other wave propagation information [*Langston*, 2007a, b, c]. A short review of other studies may be found in *Gomberg and Agnew* [1996].

At the Earth's surface, horizontal spatial displacement gradient estimates yield all the information necessary to estimate the full 3D strain tensor and a rigid body rotation. Accurate measurements of the spatial displacement gradients at the surface have the potential to provide very valuable information associated not only with seismic wave propagation and Earth structure, but also with local/regional deformation. Recently, *Langston and Liang* [2008] proposed linking inertial seismometry with differential (strain and rotation) seismometry for the purpose of calibrating differential seismometry instruments (e.g., borehole strainmeter instruments, or BSM instruments). The reasons for needing the calibration, in addition to methods for performing the calibration, are explained in detail in the next chapter (Chapter 3). In short, BSM instruments measure deformation in the ground that is different from the deformation that would have resulted prior to drilling/instrumentation. However, the difference between the deformation measured by the downhole BSM and the deformation that theoretically should have been measured are linearly related. In order to ensure that the linear calibration parameters (in the following chapter) are as accurate as possible, we review four methods (and select the

best) for estimating the spatial displacement gradient from seismic data collected by a well-calibrated broadband array at the earth's surface.

The seismo-geodetic method of *Spudich et al.* [1995] assumes that the ground displacements across a seismic array are the result of rigid body rotation and uniform strain, which is associated with uniform spatial displacement gradients, at any instant in time. In order for the assumption of uniform strain to be valid, the ground displacements at a specific instant in time should vary linearly in the direction parallel to wave propagation. This assumption requires that the ground displacement data be filtered such that the effective wavelength of a wave propagating across an array is significantly larger than the aperture of the array. For waves produced by large (M>7) teleseismic events, the seismo-geodetic method is more than adequate when considering waves that propagate with wavelengths that are significantly larger (i.e., > 10 times) the aperture of the seismic array.

In the case involving band-limited data collected by a large aperture array, the effective wavelength of a wave that propagates across the array may not be large enough that the ground displacements vary linearly in the direction parallel to wave propagation. This can happen because the ground displacements derived from broadband seismic data are sometimes not well resolved below some low frequency limit. When the seismo-geodetic method is applied in this situation, the spatial displacement gradients at each station will be different (i.e., non-uniform) and will create the potential for bias to be introduced in the estimate of the spatial displacement gradients at stations located toward the perimeter of the array. The bias is manifested in the form of an apparent timing (or phase) error – perimeter stations that are furthest from the source will see positive time (or phase) errors (i.e., seismic phases appear to arrive earlier) and perimeter stations that are closest to the source will see negative time (or phase) errors (i.e., seismic phases appear to arrive later). The magnitude of the apparent timing (or phase) errors will depend on the effective wavelength of the seismic wave. Since the effective wavelength (λ_e) of a seismic wave depends on both the propagation velocity (c) and frequency (f), i.e., $\lambda_e = c/f$, the components of the wavefield with higher frequency and slower propagation velocity will suffer from the largest apparent timing (or phase) errors.

For a seismic record that contains a variety of seismic phases, which travel at different rates of apparent horizontal speed across an array, this means that the resulting spatial displacement gradients cannot be corrected by simply applying a time-shift to the result by some constant offset. If the spatial displacement gradient estimates are off by even a constant phase angle, then it may not be possible to estimate this angle without a known reference for comparison or *a priori* information. With respect to the problem of BSM calibration, significant timing (or phase) errors will lead to time-dependent calibration parameters, which are neither desired nor ideal. In this case, the calibration parameters would have to be convolved with, instead of simply multiplied to, the raw BSM data to yield calibrated results in the time domain. If the spatial displacement gradient estimates are accurate, then the calibration parameters should not be complex if computed in the frequency domain.

In order to avoid the apparent timing issues that may result from using the seismo-geodetic method, hereafter Method (1), we investigate three additional methods for estimating the spatial displacement gradients:

- Method (2) – The biharmonic spline interpolation technique developed in *Sandwell* [1987]
- Method (3) – A plane-wave polynomial interpolation technique, developed in this study based on findings in *Gomberg et al.* [1999]
- Method (4) – The spatial gradient analysis (wave gradiometry) method developed in both *Langston* [2007a] and *Gomberg et al.* [1999]

Each interpolation-based method attempts to fit a surface, instead of a plane, through each component of the ground displacement data, at a single instant in time, recorded at arbitrary positions within a 2D plane. In this manner, the displacements and displacement gradients can be described at virtually any reference position within an arbitrary 2D seismic array when the strain field is either uniform or non-uniform across the array. The first interpolation-based method, Method (2), was implemented in *Smerzini et al.* [2006],

and later in *Paolucci and Smerzini* [2008], where it was applied specifically to the problem of estimating spatial displacement gradients from dense seismic array data. This method allows the best-fit surface to vary both parallel to and perpendicular to the radial propagation direction. The second interpolation-based method, Method (3), is based on the argument, in *Gomberg et al.* [1999], that ground deformation across an array is primarily due to plane-wave propagation of waves (when below ~ 1Hz). In other words, the displacement gradients should be uniform between stations that are perpendicular to the radial propagation direction and should only vary between stations that are parallel to the radial propagation direction. Typically, the position differences between the source location and the receiver array location can provide an adequate estimate of the propagation direction across the array. If the source location is unknown, or independent estimates of the propagation direction across an array are desired, then there are additional techniques that may provide this information based on the cross-correlation of various seismic phases within the seismogram.

In addition to the interpolation-based methods introduced above, *Gomberg et al.* [1999] describes a technique, Method (4), for estimating the displacement gradients from three-component velocity seismograms at a single station when the propagation velocity and direction are known. The same result in *Gomberg et al.* [1999] can be derived from the spatial gradient analysis of *Langston* [2007b] by assuming plane-wave propagation from an isotropic source (see also *Langston and Liang* [2008]). If the single station in question is an element of a 2D seismic array, the propagation velocity and direction may also be derived using similar cross-correlation based techniques mentioned above.

We conduct several experiments using synthetic data to evaluate the performance of all the methods that estimate the spatial displacement gradients. In one experiment, we demonstrate the general performance characteristics of the seismo-geodetic method and the polynomial interpolation-based method (Method 3) using a simple three-element linear array. In the remaining experiments, we demonstrate specific performance characteristics of all methods using an array with geometry based on a subset of the Anza Seismic Network in southern California (see Figure 4). In these last experiments we test

the methods using a variety of synthetic data and real data, which are associated with the M8.1 Samoa Island Earthquake (2009/09/29).

Deriving the Spatial Displacement Gradients from Seismic Data

In this study, we discuss methods for obtaining the spatial displacement gradients from seismic data recorded by a two-dimensional (2D) array at the earth's surface. Therefore, in estimating the displacement gradients we assume a free surface boundary condition (i.e., zero stress in the vertical direction at the surface). The stress tensor (τ_{ij}) for an isotropic solid as a function of the displacement gradients ($u_{i,j}$) is given by:

$$i,j,k \in \{1,2,3\} : \tau_{ij} = \lambda \delta_{ij} u_{k,k} + \mu\left(u_{i,j} + u_{j,i}\right) \quad , \tag{1}$$

where λ and μ are the Lamé parameters,

$$\delta_{ij} = \begin{cases} 0 \text{ for } i \neq j \\ \\ 1 \text{ for } i = j \end{cases} \quad , \tag{2}$$

$$u_{i,j} = \frac{\partial u_i}{\partial x_j} \quad \text{, and} \tag{3}$$

$$u_{k,k} = \left(\frac{\partial u_1}{\partial x_1} + \frac{\partial u_2}{\partial x_2} + \frac{\partial u_3}{\partial x_3}\right) = \left(\frac{\partial u_x}{\partial x} + \frac{\partial u_y}{\partial y} + \frac{\partial u_z}{\partial z}\right) \quad . \tag{4}$$

Under the assumption of a free surface boundary condition at the surface, all components of the stress tensor in the vertical direction are equal to zero. As described in *Spudich et al.* [1995], this leads to the relationship:

$$\begin{bmatrix} u_{1,1} & u_{1,2} & u_{1,3} \\ u_{2,1} & u_{2,2} & u_{2,3} \\ u_{3,1} & u_{3,2} & u_{3,3} \end{bmatrix} = \begin{bmatrix} u_{1,1} & u_{1,2} & -u_{3,1} \\ u_{2,1} & u_{2,2} & -u_{3,2} \\ u_{3,1} & u_{3,2} & -\eta\left(u_{1,1} + u_{2,2}\right) \end{bmatrix} \quad , \tag{5}$$

where

$$\eta = \frac{\lambda}{(\lambda + 2\mu)} \quad . \tag{6}$$

In the next two sections, we will discuss general methods for obtaining the displacement gradients from seismic data. Each method is based on underlying assumptions that must be taken into account before application.

Uniform Displacement Gradients

The underlying assumption associated with the seismo-geodetic method of *Spudich et al.* [1995], Method (1), is that the displacement gradients are uniform across an array of seismometers at any instant in time. If we consider a *N*-element seismic array numbered according to the set $\mathbf{M} = \{0,1,\cdots,N-1\}$, then we can find the displacement gradients at a reference station (we will denote "0") by expanding the ground displacements $\mathbf{u}^i = \left[u_x^i \;\; u_y^i \;\; u_z^i\right]$, recorded at stations $i \in \mathbf{M} : i > 0$, in a truncated Taylor's series (to first order) about the reference ground displacement $\mathbf{u}^0 = \left[u_x^0 \;\; u_y^0 \;\; u_z^0\right]$:

$$\begin{aligned}
u_x^i &= u_x^0 + \left(\left.\frac{\partial u_x}{\partial x}\right|_{x^0} \left(x^i - x^0\right) + \left.\frac{\partial u_x}{\partial y}\right|_{y^0} \left(y^i - y^0\right) + \left.\frac{\partial u_x}{\partial z}\right|_{z^0} \left(z^i - z^0\right) \right) \\
u_y^i &= u_y^0 + \left(\left.\frac{\partial u_y}{\partial x}\right|_{x^0} \left(x^i - x^0\right) + \left.\frac{\partial u_y}{\partial y}\right|_{y^0} \left(y^i - y^0\right) + \left.\frac{\partial u_y}{\partial z}\right|_{z^0} \left(z^i - z^0\right) \right) \\
u_z^i &= u_z^0 + \left(\left.\frac{\partial u_z}{\partial x}\right|_{x^0} \left(x^i - x^0\right) + \left.\frac{\partial u_z}{\partial y}\right|_{y^0} \left(y^i - y^0\right) + \left.\frac{\partial u_z}{\partial z}\right|_{z^0} \left(z^i - z^0\right) \right)
\end{aligned} \quad , \tag{7}$$

where x^i, y^i, and z^i represent the horizontal and vertical locations of stations $i \in \mathbf{M}$ in a Cartesian coordinate system (variation of *Langston and Liang* [2008]). Since we only

consider seismic data from a 2D horizontal surface array (or at least approximately 2D), we may assume that the differences in vertical position are zero. With the differences in vertical position equal to zero, the problem above can be cast into a matrix equation of the form **Gm** = **d**, where

$$\mathbf{G} = \begin{bmatrix} \left.\frac{\partial u_x}{\partial x}\right|_{x^0} & \left.\frac{\partial u_x}{\partial y}\right|_{y^0} \\ \left.\frac{\partial u_y}{\partial x}\right|_{x^0} & \left.\frac{\partial u_y}{\partial y}\right|_{y^0} \\ \left.\frac{\partial u_z}{\partial x}\right|_{x^0} & \left.\frac{\partial u_z}{\partial y}\right|_{y^0} \end{bmatrix} ,$$

$$\mathbf{m} = \begin{bmatrix} \left(x^1 - x^0\right) & \left(x^2 - x^0\right) & \cdots & \left(x^{N-1} - x^0\right) \\ \left(y^1 - y^0\right) & \left(y^2 - y^0\right) & \cdots & \left(y^{N-1} - y^0\right) \end{bmatrix} \quad , \text{ and}$$

$$\mathbf{d} = \begin{bmatrix} \left(u_x^1 - u_x^0\right) & \left(u_x^2 - u_x^0\right) & \cdots & \left(u_x^{N-1} - u_x^0\right) \\ \left(u_y^1 - u_y^0\right) & \left(u_y^2 - u_y^0\right) & \cdots & \left(u_y^{N-1} - u_y^0\right) \\ \left(u_z^1 - u_z^0\right) & \left(u_z^2 - u_z^0\right) & \cdots & \left(u_z^{N-1} - u_z^0\right) \end{bmatrix} \quad .$$

The best-fit displacement gradients at the reference location are found, in a least-squares sense, by:

$$\mathbf{G} = \mathbf{d}\mathbf{m}^T\left(\mathbf{m}\mathbf{m}^T\right)^{-1} \quad . \tag{8}$$

Non-Uniform Displacement Gradients

In some cases it may not be appropriate to assume uniform displacement gradients across an array. For example, if the array dimension is significantly large enough, then it might not be possible to adequately filter the seismic displacement data below a certain

frequency threshold due to instrument limitations, low frequency noise, etc. Whatever the case, it has been recognized here and by others [e.g., *Smerzini et al.*, 2006 and *Paolucci and Smerzini*, 2008] that interpolating seismic displacement data may provide a quick way of estimating non-uniform displacement gradients across a seismic array. In addition to the methods based on interpolation, it is also possible to approximate the displacement gradients across a seismic array when the propagation velocity and propagation direction of each significant phase within the seismic record are known.

Biharmonic Spline Interpolation

The first interpolation-based method, Method (2), is an algorithm originally presented by *Sandwell* [1987] and is based on Green's functions of the biharmonic operator. This algorithm was initially used to interpolate between irregularly spaced GEOS-3 and SEASAT altimeter data, but was later adopted by *Paolucci and Smerzini* [2008] to interpolate between seismic displacement data collected by an irregular spaced, dense seismic array. This interpolation method does not make any assumptions about the mode of wave propagation across the array, although for better performance the data should be smoothly varying. Displacement gradients may be found at an arbitrary reference point in a separate step by using the formulation in *Sandwell* [1987] or by applying a second-order finite difference scheme to seismic displacement data that have been interpolated onto a regular grid around the reference point (see *Langston* [2007b] or *Paolucci and Smerzini* [2008]).

Method (2) produces stable results for data occupying up to three dimensions of space. The general solution for the ground displacement $\mathbf{u} = \begin{bmatrix} u_x & u_y & u_z \end{bmatrix}$ at an arbitrary position $\mathbf{p} = \begin{bmatrix} x & y & z \end{bmatrix}$ within a seismic array is:

$$\mathbf{u} = \sum_{j=0}^{N-1} \mathbf{a}^j \, \phi_m\left(\mathbf{p} - \mathbf{p}^j\right) \quad , \tag{9}$$

where the elements of $\mathbf{a}^j = \left[a_x^j \;\; a_y^j \;\; a_z^j\right] : j \in \mathbf{M}$ represent the point forces applied to a thin elastic beam (spline) passing through displacement data points at positions $\mathbf{p}^j : j \in \mathbf{M}$ and the operator ϕ_m is the biharmonic Green's function in $m \in \{1,2,3\}$ dimension(s) described by:

$$j \in \mathbf{M} : \phi_m\left(\mathbf{p} - \mathbf{p}^j\right) = \begin{cases} \left|\mathbf{p} - \mathbf{p}^j\right|^3 & \text{for } m = 1 \\ \left|\mathbf{p} - \mathbf{p}^j\right|^2 \left(\ln\left|\mathbf{p} - \mathbf{p}^j\right| - 1\right) & \text{for } m = 2 \\ \left|\mathbf{p} - \mathbf{p}^j\right| & \text{for } m = 3 \end{cases} . \tag{10}$$

The | |'s in Equation (10) indicate the magnitude of the vector between the two positions $\mathbf{p}$ and $\mathbf{p}^j$. The point forces ($\mathbf{a}^j : j \in \mathbf{M}$) are found by solving the system of linear equations such that:

$$\forall i \in \mathbf{M} : \mathbf{u}^i = \sum_{j=0}^{N-1} \mathbf{a}^j \; \phi_m\left(\mathbf{p}^i - \mathbf{p}^j\right) \quad . \tag{11}$$

For a 2D seismic array, the relationship above may be cast into a matrix equation of the form **Gm** = **d**,

$$\mathbf{G} = \begin{bmatrix} 0 & \phi_2\left(\mathbf{p}^0 - \mathbf{p}^1\right) & \cdots & \phi_2\left(\mathbf{p}^0 - \mathbf{p}^{N-1}\right) \\ \phi_2\left(\mathbf{p}^1 - \mathbf{p}^0\right) & 0 & \ddots & \vdots \\ \vdots & \ddots & \ddots & \phi_2\left(\mathbf{p}^{N-2} - \mathbf{p}^{N-1}\right) \\ \phi_2\left(\mathbf{p}^{N-1} - \mathbf{p}^0\right) & \cdots & \phi_2\left(\mathbf{p}^{N-1} - \mathbf{p}^{N-2}\right) & 0 \end{bmatrix} ,$$

$$\mathbf{m} = \begin{bmatrix} a_x^0 & a_y^0 & a_z^0 \\ a_x^1 & a_y^1 & a_z^1 \\ \vdots & \vdots & \vdots \\ a_x^{N-1} & a_y^{N-1} & a_z^{N-1} \end{bmatrix} , \quad \text{and}$$

$$\mathbf{d} = \begin{bmatrix} u_x^0 & u_y^0 & u_z^0 \\ u_x^1 & u_y^1 & u_z^1 \\ \vdots & \vdots & \vdots \\ u_x^{N-1} & u_y^{N-1} & u_z^{N-1} \end{bmatrix} \quad .$$

The best-fit estimate for the point forces are found, in a least-squares sense, by:

$$\mathbf{m} = \left(\mathbf{G}^T\mathbf{G}\right)^{-1}\mathbf{G}^T\mathbf{d} \qquad . \tag{12}$$

In order to describe the displacement gradient at an arbitrary reference point $\mathbf{p}^r = \begin{bmatrix} x^r & y^r & z^r \end{bmatrix}$, the point forces obtained above may be applied, using *Sandwell* [1987], to the following:

$$\left.\frac{\partial \mathbf{u}}{\partial x}\right|_{x^r} = \sum_{j=0}^{N-1} \mathbf{a}^j \left(\nabla\phi_m\left(\mathbf{p}^r - \mathbf{p}^j\right)\cdot \mathbf{n}_x\right)$$
$$\left.\frac{\partial \mathbf{u}}{\partial y}\right|_{y^r} = \sum_{j=0}^{N-1} \mathbf{a}^j \left(\nabla\phi_m\left(\mathbf{p}^r - \mathbf{p}^j\right)\cdot \mathbf{n}_y\right) \quad , \tag{13}$$

where

$$j \in \mathbf{M} : \nabla\phi_m\left(\mathbf{p}^r - \mathbf{p}^j\right) = \begin{cases} 3\left(\mathbf{p}^r - \mathbf{p}^j\right)\left|\mathbf{p}^r - \mathbf{p}^j\right| & \text{for } m = 1 \\ \left(\mathbf{p}^r - \mathbf{p}^j\right)\left(2\ln\left|\mathbf{p}^r - \mathbf{p}^j\right| - 1\right) & \text{for } m = 2 \\ \left(\mathbf{p}^r - \mathbf{p}^j\right)\left|\mathbf{p}^r - \mathbf{p}^j\right|^{-1} & \text{for } m = 3 \end{cases} \quad , \tag{14}$$

$\mathbf{n}_x$ and $\mathbf{n}_y$ are unit vectors in the *x*- and *y*-direction, respectively, and the "·" indicates the dot product.

Alternatively, seismic displacement data can be described at locations that correspond to a regular, symmetric arrangement around an arbitrary reference point. For example, one could follow *Langston* [2007b] and describe the displacements:

$$k \in \{1,2,3,4\} : \mathbf{u}^k = \begin{bmatrix} u_x^k & u_y^k & u_z^k \end{bmatrix} \quad , \tag{15}$$

around an arbitrary reference point $\mathbf{p}^r = \begin{bmatrix} x^r & y^r & z^r \end{bmatrix}$, within the original 2D array, at positions corresponding to:

$$k \in \{1,2,3,4\} : \mathbf{p}^k = \begin{cases} \begin{bmatrix} x^r + \Delta h & y^r + \Delta h \end{bmatrix} & \text{for } k = 1 \\ \begin{bmatrix} x^r + \Delta h & y^r - \Delta h \end{bmatrix} & \text{for } k = 2 \\ \begin{bmatrix} x^r - \Delta h & y^r - \Delta h \end{bmatrix} & \text{for } k = 3 \\ \begin{bmatrix} x^r - \Delta h & y^r + \Delta h \end{bmatrix} & \text{for } k = 4 \end{cases} \quad , \tag{16}$$

and then compute the displacement gradients at the center of the array through:

$$\begin{aligned} \left.\frac{\partial \mathbf{u}}{\partial x}\right|_{x^r} &= \frac{1}{4\Delta h}\left(\mathbf{u}^1 + \mathbf{u}^2 - \mathbf{u}^3 - \mathbf{u}^4\right) \\ \left.\frac{\partial \mathbf{u}}{\partial y}\right|_{y^r} &= \frac{1}{4\Delta h}\left(\mathbf{u}^1 - \mathbf{u}^2 - \mathbf{u}^3 + \mathbf{u}^4\right) \end{aligned} \quad . \tag{17}$$

The surface created by this method exactly fits the data at the data locations. This is a potential drawback for spatial displacement gradient estimates if the seismic ground displacement data contain average or above average levels of noise. A potential workaround is to compute the spatial displacement gradients using different station combinations in order to check for data consistency or in order to compute the mean spatial displacement gradient estimate.

Plane Wave Interpolation

The second interpolation method, hereafter Method (3), is an algorithm that assumes the observed seismic displacements are both smoothly varying across the array and the result of plane wave propagation at any instant in time. Instead of attempting to fit the observed 2D array displacement data with a 2D surface whose shape is allowed to vary both parallel to and perpendicular to the propagation direction (i.e., Method 2), this method attempts to fit the observed displacement data with a 2D surface whose shape is only allowed to vary parallel to the propagation direction. This essentially converts the problem from a 2D interpolation problem to a 1D interpolation problem.

The best-fit 2D polynomials, of order Q, which describe the radial (R), transverse (T) and vertical components of ground displacement $\mathbf{u}^i = \left[u_T^i \;\; u_R^i \;\; u_z^i\right] : i \in \mathbf{M}$, are found by solving the system of linear equations such that:

$$\forall i \in \mathbf{M} : \mathbf{u}^i = \sum_{j=0}^{Q} \mathbf{a}^j \left(r_d^i(\theta)\right)^j \quad , \tag{18}$$

where the elements of $\mathbf{a}^j = \left[a_T^j \;\; a_R^j \;\; a_z^j\right] : j \in \{0,1,...,Q\}$ represent the polynomial coefficients and the elements $r_d^i(\theta) : i \in \mathbf{M}$ represent the relative radial positions between each station $i \in \mathbf{M}$ and an arbitrary reference point $\mathbf{p}^r = \left[x^r \;\; y^r \;\; z^r\right]$, within the original 2D array. The relative radial distances along a propagation path according to the propagation direction (θ) may be found using the dot product:

$$i \in \mathbf{M} : r_d^i(\theta) = \left[\sin\theta \quad \cos\theta\right] \cdot \left[x^i - x^r \quad y^i - y^r\right] \quad . \tag{19}$$

It is possible to cast the relationship in Equation (18) into a matrix equation of the form **Gm** = **d**, for example the best fit 3rd order polynomial may be found by setting:

$$\mathbf{G} = \begin{bmatrix} \left(r_d^0\right)^3 & \left(r_d^0\right)^2 & r_d^0 & 1 \\ \left(r_d^1\right)^3 & \left(r_d^1\right)^2 & r_d^1 & 1 \\ \vdots & \vdots & \vdots & \vdots \\ \left(r_d^{N-1}\right)^3 & \left(r_d^{N-1}\right)^2 & r_d^{N-1} & 1 \end{bmatrix},$$

$$\mathbf{m} = \begin{bmatrix} a_T^3 & a_R^3 & a_z^3 \\ a_T^2 & a_R^2 & a_z^2 \\ a_T^1 & a_R^1 & a_z^1 \\ a_T^0 & a_R^0 & a_z^0 \end{bmatrix}, \quad \text{and}$$

$$\mathbf{d} = \begin{bmatrix} u_R^0 & u_T^0 & u_z^0 \\ u_R^1 & u_T^1 & u_z^1 \\ \vdots & \vdots & \vdots \\ u_R^{N-1} & u_T^{N-1} & u_z^{N-1} \end{bmatrix}.$$

The best-fit estimate for the polynomial coefficients are found, in a least-squares sense, by:

$$\mathbf{m} = \left(\mathbf{G}^T\mathbf{G}\right)^{-1}\mathbf{G}^T\mathbf{d} \quad . \tag{20}$$

For any $Q > 0$, the displacement gradients at the arbitrary reference point $\mathbf{p}^r = \begin{bmatrix} x^r & y^r & z^r \end{bmatrix}$ are simply:

$$\begin{bmatrix} \left.\frac{\partial u_x}{\partial x}\right|_{x^r} & \left.\frac{\partial u_x}{\partial y}\right|_{y^r} \\ \left.\frac{\partial u_y}{\partial x}\right|_{x^r} & \left.\frac{\partial u_y}{\partial y}\right|_{y^r} \\ \left.\frac{\partial u_z}{\partial x}\right|_{x^r} & \left.\frac{\partial u_z}{\partial y}\right|_{y^r} \end{bmatrix} = \begin{bmatrix} \cos\theta & \sin\theta & 0 \\ -\sin\theta & \cos\theta & 0 \\ 0 & 0 & 1 \end{bmatrix} \begin{bmatrix} a_T^1 \sin\theta & a_T^1 \cos\theta \\ a_R^1 \sin\theta & a_R^1 \cos\theta \\ a_z^1 \sin\theta & a_z^1 \cos\theta \end{bmatrix} . \quad (21)$$

The drawback of Method (3) is that the propagation direction must be known prior to application. In general, the propagation direction can be derived from the relative location between the origin source location and the reference location on an ellipsoidal earth. If the source location is unknown, cross-correlation methods may be used to determine the propagation direction of specific seismic phases across an array.

Plane Wave Gradiometry

Spatial gradient theory for 2D seismic arrays [*Langston*, 2007b] describes a relationship between the radial displacement gradient, the radial displacement, and the radial slowness at any instant in time during the seismic record. Following *Langston* [2007a], the displacement of a propagating wave may be described as:

$$u(t,r,\theta) = G_r(r)R(\theta)f(t-t_0) = G_r(r)R(\theta)f\left(t - s_r(r)(r-r_0)\right) , \quad (22)$$

where t is the time relative to the origin time (t_0), r is the radial distance relative to the origin location (r_0), θ is the radial propagation direction, G_r is the geometrical spreading term, R is the radiation pattern term, and s_r is the radial slowness. The corresponding radial and azimuthal derivatives may then be described, respectively, as:

$$\begin{aligned}\frac{\partial u(t,r,\theta)}{\partial r} &= u'(t,r,\theta) = \frac{G_r'(r)}{G_r(r)}u(t,r,\theta) - \left[s_r(r) + s_r'(r)(r-r_0)\right]\dot{u}(t,r,\theta) \\ \frac{\partial u(t,r,\theta)}{\partial \theta} &= \frac{R'(\theta)}{R(\theta)}u(t,r,\theta)\end{aligned} \quad . \tag{23}$$

Under the assumption of plane wave propagation, isotropic source, and constant horizontal slowness, the above relationship simplifies to:

$$\begin{aligned}\frac{\partial u(t,r,\theta)}{\partial r} &= -s_r\,\dot{u}(t,r,\theta) \\ \frac{\partial u(t,r,\theta)}{\partial \theta} &= 0\end{aligned} \quad , \tag{24}$$

because the functions describing the geometrical spreading, radiation pattern, and radial slowness are assumed constant for all r (i.e., their rate of change as a function of distance is naught). Under these assumptions, the displacement gradients at the arbitrary reference point $\mathbf{p}^r = \left[x^r \;\; y^r \;\; z^r\right]$ may be described by:

$$\begin{bmatrix} \left.\frac{\partial u_x}{\partial x}\right|_{x^r} & \left.\frac{\partial u_x}{\partial y}\right|_{y^r} \\ \left.\frac{\partial u_y}{\partial x}\right|_{x^r} & \left.\frac{\partial u_y}{\partial y}\right|_{y^r} \\ \left.\frac{\partial u_z}{\partial x}\right|_{x^r} & \left.\frac{\partial u_z}{\partial y}\right|_{y^r} \end{bmatrix} = \begin{bmatrix} \cos\theta & \sin\theta & 0 \\ -\sin\theta & \cos\theta & 0 \\ 0 & 0 & 1 \end{bmatrix} \begin{bmatrix} -s_T\,\dot{u}_T^r \sin\theta & -s_T\,\dot{u}_T^r \cos\theta \\ -s_R\,\dot{u}_R^r \sin\theta & -s_R\,\dot{u}_R^r \cos\theta \\ -s_z\,\dot{u}_z^r \sin\theta & -s_z\,\dot{u}_z^r \cos\theta \end{bmatrix} \quad . \tag{25}$$

This is the result of Method (4) and should resemble the result from Method (3) – this is because the first-order polynomial coefficients ($\mathbf{a}^1$) are attempting to describe the same result. This is essentially the same result in *Gomberg et al.* [1999].

The drawback of Method (4) is that both the propagation direction and propagation slowness must be known prior to application. In general, the propagation direction can be derived from the relative location between the origin source location and the reference

location on an ellipsoidal earth. However, in order to determine the propagation slowness, it is necessary to employ techniques such as beam-forming or cross-correlation. One method is to assume that the time offsets (T), relative to a reference station/location ($\mathbf{p}^0$), are related to the relative x and y position differences and horizontal slowness in the x and y directions:

$$\begin{bmatrix} (x_0 - x_1) & (y_0 - y_1) \\ (x_0 - x_2) & (y_0 - y_2) \\ \vdots & \vdots \\ (x_0 - x_{N-1}) & (y_0 - y_{N-1}) \end{bmatrix} \begin{bmatrix} s_x \\ s_y \end{bmatrix} = \begin{bmatrix} T_0^1 \\ T_0^2 \\ \vdots \\ T_0^{N-1} \end{bmatrix} . \quad (26)$$

The appropriate time offsets, at any instant in time, may be obtained by attempting to find those offsets that lead to the best correlation between a suitable window of data from a reference location (for a single component of motion) and the seismogram data from the remaining stations within an array. For example, one could define a window of data such that the length $W = V*2+1$, where V represents the number of data samples to the "left" and "right" of a data sample at a specific instant in time. As this window slides in the direction of increasing time (i.e., from "left" to "right"), the appropriate time lags at each instant in time are expected to change since the window will begin to sample different seismic phases, which generally travel at different rates of apparent horizontal slowness across a 2D array. In addition to conventional grid-search based correlation techniques in the time domain, one can utilize optimization algorithms (such as those found in the Optimization Toolbox within MATLAB) in order to quickly converge to an optimum time lag for each station pair (see Appendix 1 for an implementation example) or a set of optimum time lags for a group of stations at each instant in time.

Hybrid Methods

In order to provide more constraint on the estimates of the spatial displacement gradients at arbitrary locations inside a seismic array, it may be useful to combine a few of the methods described above. For example, estimates of the spatial displacement gradients derived at each seismometer location using Method (4) can be combined with the observed ground displacements, also at each seismometer location, in order to provide better constraint on the point forces or the polynomial coefficients when using Method (2) or Method (3), respectively. Another possibility is to use the propagation direction and slowness information in conjunction with a small time window of ground displacements at a single station, to create a virtual linear seismic array aligned in the propagation direction. Method (3) is potentially the only method suitable for performing interpolation on the data derived from the virtual linear seismic array. The second option also lends itself to a useful way of estimating the potential error in the spatial displacement gradient – namely because creating a virtual array using data from all the stations within the seismic array can create independent estimates of the displacement gradient at an arbitrary location. The variance, weighted variance, or standard deviation of the independent estimates can be used to describe the potential error about some mean, or weighted mean, displacement gradient estimate at a specific instant in time.

Performance Tests

A series of experiments were developed in order to determine the performance of each method for both simplified synthetic data and real data. We use synthetic data that are very simplistic in nature and without added noise because we felt it necessary to first gauge the performance of each method under ideal/perfect conditions. With the exception of the 1D tests, we perform our analysis using synthetic data under the assumption that the data were collected by a 2D array with essentially the same dimensions/geometry as a

sub-set of the Anza seismic network and the Plate Boundary Observatory (PBO) Gladwin Tensor Strain-Meter (GTSM) instruments in southern California (see Figure 4). The real data are associated with the M8.1 Somoa Islands Earthquake of 2009 September 29.

Synthetic Data: One-Dimensional (1D) Tests

This particular experiment is meant to illustrate the behavior of the errors in accuracy of the displacement gradients, which are estimated using either Method (1) or Method (3), from synthetic displacement data "recorded" by a 3-element linear array. The array is designed such that the reference station (station "0"), where the displacement gradient is calculated, is always situated between the other two stations (stations "1" and "2"). The synthetic displacement data correspond to a sinusoidal wave with unit amplitude and unit wavelength. The array dimension (Δ = distance between station "1" and "2" in percent of wavelength) and the array geometry (A/B, where A [or B] represents the distance between station "1" [or "2"] and "0" in percent of Δ) are allowed to vary over a specified range in order to determine the errors in displacement gradient accuracy using either Method (1) or (3). In order for either method to work properly, it is important that the smallest wavelength of a seismic disturbance is much greater than the largest dimension of an array. The following examples illustrate how the errors in accuracy depend on both the dimension of the array as well as the irregularity of the array geometry. The 3-element array of a particular dimension/geometry scenario is allowed to sample one complete wave cycle before the mean error and standard deviation (STD) of the errors along this cycle are computed.

Figures (7) and (8) illustrate the expected errors, using Method (1), in displacement gradient accuracy for 50×4 different array dimension/geometry scenarios (i.e., 200 combinations from 50 different array dimensions and 4 different geometry scenarios) for the 3-element linear array. The chief result of this simple example is that the expected errors in accuracy are expected to increase under two general circumstances when using this method: 1) when the array dimension becomes an increasingly

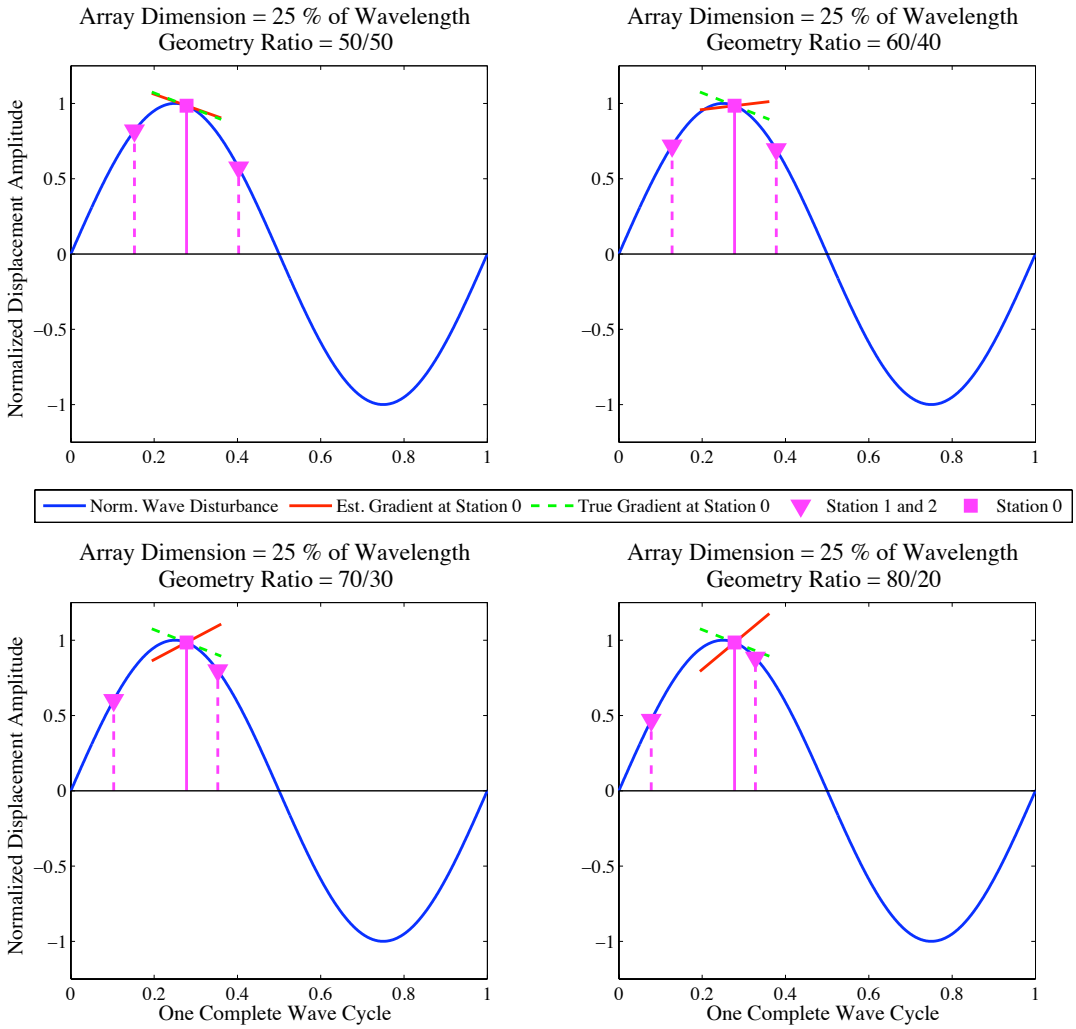

Figure 7. Example illustrating the different displacement gradient results obtained from different one-dimensional (1D) array geometry scenarios. In this example the largest array dimension (length between Station 1 and 2) is 25% of the wavelength of the simulated seismic disturbance (a sine wave). The array geometry ratio is indicated in terms of the relative percent distance between station 0 and (station 1)/(station 2). The BLUE line indicates the normalized displacement amplitude over the course of one complete wave cycle. The MAGENTA triangles indicate the displacement amplitude at stations 1 and 2 for the different array geometry ratios. The MAGENTA square indicates the displacement amplitude at station 0. Given the displacement data recorded at the 3-element array for the different array geometry ratios, the RED line indicates the displacement gradient one would find at station 0 using the method based on uniform displacement gradients.

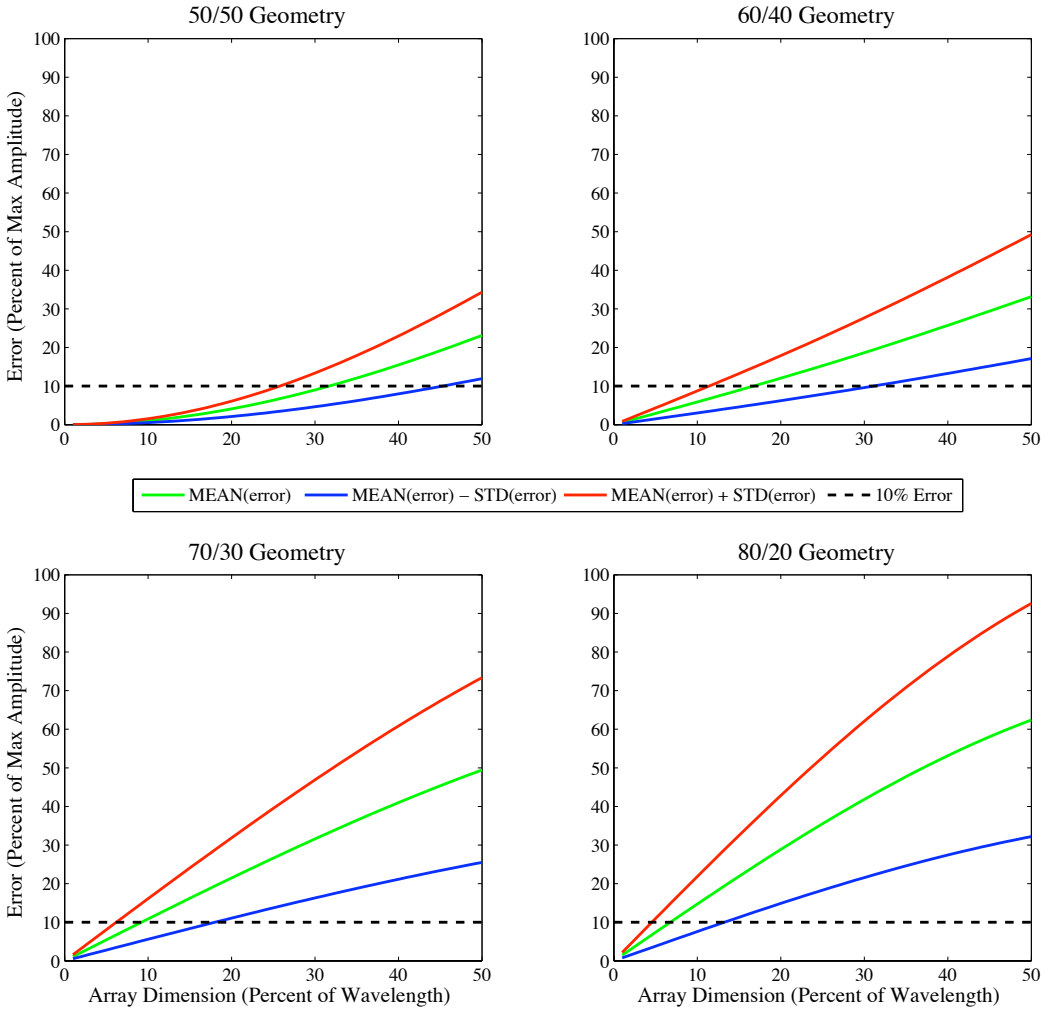

Figure 8. The above figure illustrates the expected errors in accuracy if the example experiment in Figure (7) were repeated for the same geometry ratios, but for a variety of array dimensions and relative array locations (i.e., different array sample locations along the wave cycle). A single array configuration consists of a constant array dimension and geometry ratio. As an array configuration samples different parts of the wave cycle the error in the accuracy can either improve or become worse. Therefore, the performance of each array configuration is evaluated by running statistics on the set of errors associated with the errors in displacement gradients computed at each location along the wave cycle. The GREEN lines plotted above indicate the expected normalized average errors in displacement gradient, after sampling an entire wave cycle, as the array dimension increases for a given array geometry ratio. Similarly, the RED / BLUE lines plotted above indicate the expected normalized average errors in displacement gradient ± one standard deviation (STD), respectively.

significant fraction of the smallest apparent wavelength, and 2) when the array geometry is irregular. Noise was not considered in the example, but is expected to result in yet additional increases to the errors in accuracy.

Figures (9) and (10) illustrate the expected errors, using Method (3), in displacement gradient accuracy for 50×4 different array dimension/geometry scenarios for the 3-element linear array (same scenarios as above). In this example, the displacement gradients are estimated after obtaining the best quadratic fit (i.e., $y=Ax^2+Bx+C$) through the synthetic displacement data. The chief result of this simple example is that, like Method (1), the expected errors in accuracy are expected to increase when the array dimension becomes an increasingly significant fraction of the smallest apparent wavelength. However, unlike Method (1), it appears that the errors in accuracy decrease when the array geometry becomes more irregular. Noise was also not considered in the example, but is expected to result in an increase to the errors in accuracy.

Synthetic Data: Two-Dimensional (2D) Tests

The geometry of most 2D seismic arrays at the surface is irregular. Therefore, an array will sample different parts of an incoming wave when the wave propagates across that array in different directions – even if the other properties of the wave (i.e., amplitude, wavelength, etc.) are virtually identical. This set of experiments is meant to illustrate the behavior of the errors in accuracy of the displacement gradients and interpolated ground displacements, which are both estimated using the first 3 methods, from synthetic displacement data "recorded" by a 10-element 2D sub-array of the Anza seismic network. The synthetic displacement data correspond to a sinusoidal plane wave with unit amplitude that propagates across the array in different directions (θ) and with different wavenumbers ($k = \omega/c = 2\pi/\lambda$: where ω is the radial frequency, c is the apparent horizontal velocity, and λ is the apparent horizontal wavelength). In order to simplify the

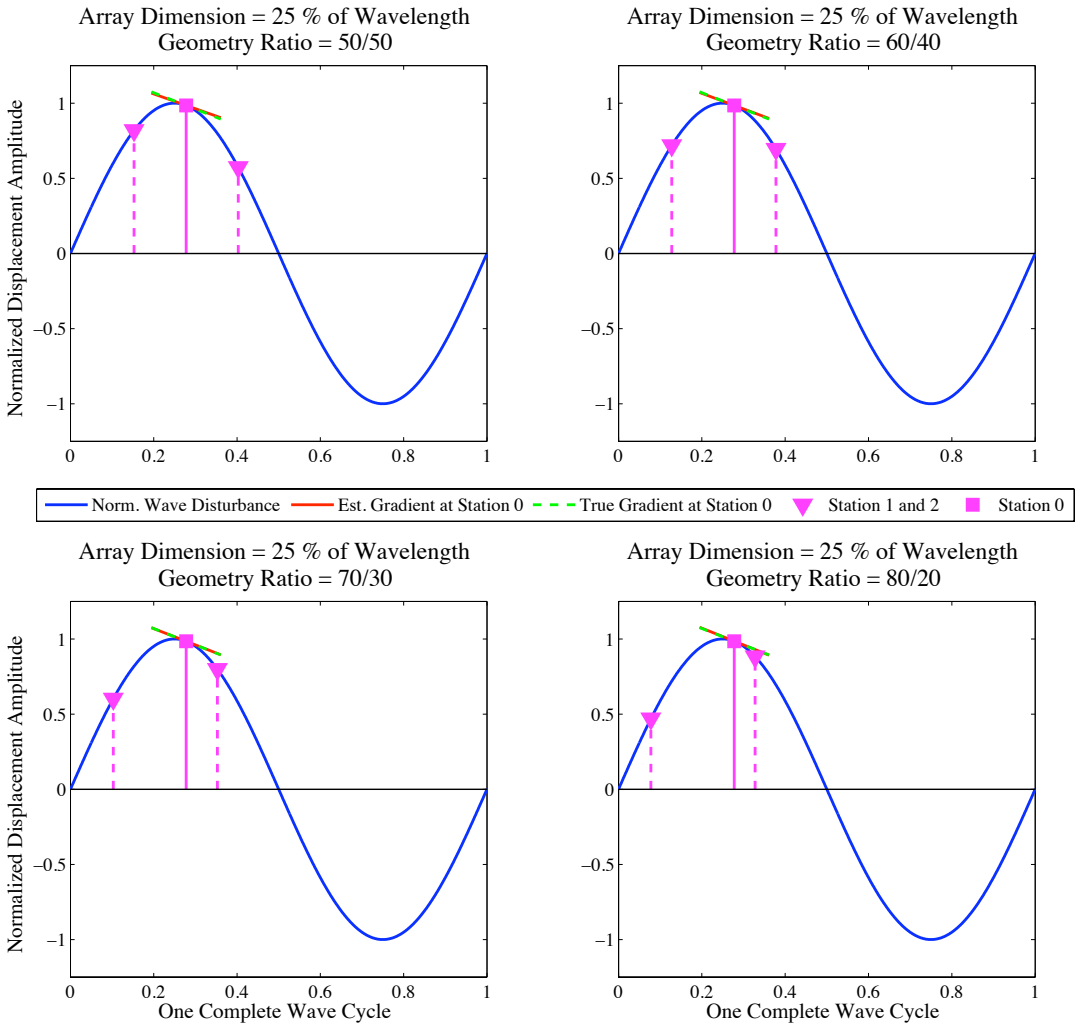

Figure 9. Example illustrating the different displacement gradient results obtained from different one-dimensional (1D) array geometry scenarios. In this example the largest array dimension (length between Station 1 and 2) is 25% of the wavelength of the simulated seismic disturbance (a sine wave). The array geometry ratio is indicated in terms of the relative percent distance between station 0 and (station 1)/(station 2). The BLUE line indicates the normalized displacement amplitude over the course of one complete wave cycle. The MAGENTA x's indicate the displacement amplitude at stations 1 and 2 for the different array geometry ratios. The MAGENTA square indicates the displacement amplitude at station 0. Given the displacement data recorded at the 3-element array for the different array geometry ratios, the RED line indicates the displacement gradient one would find at station 0 using the method based on non-uniform displacement gradients where the best-fit quadratic function ($y=Ax^2 + Bx + C$), in a least-squares sense, is found through the displacement data points.

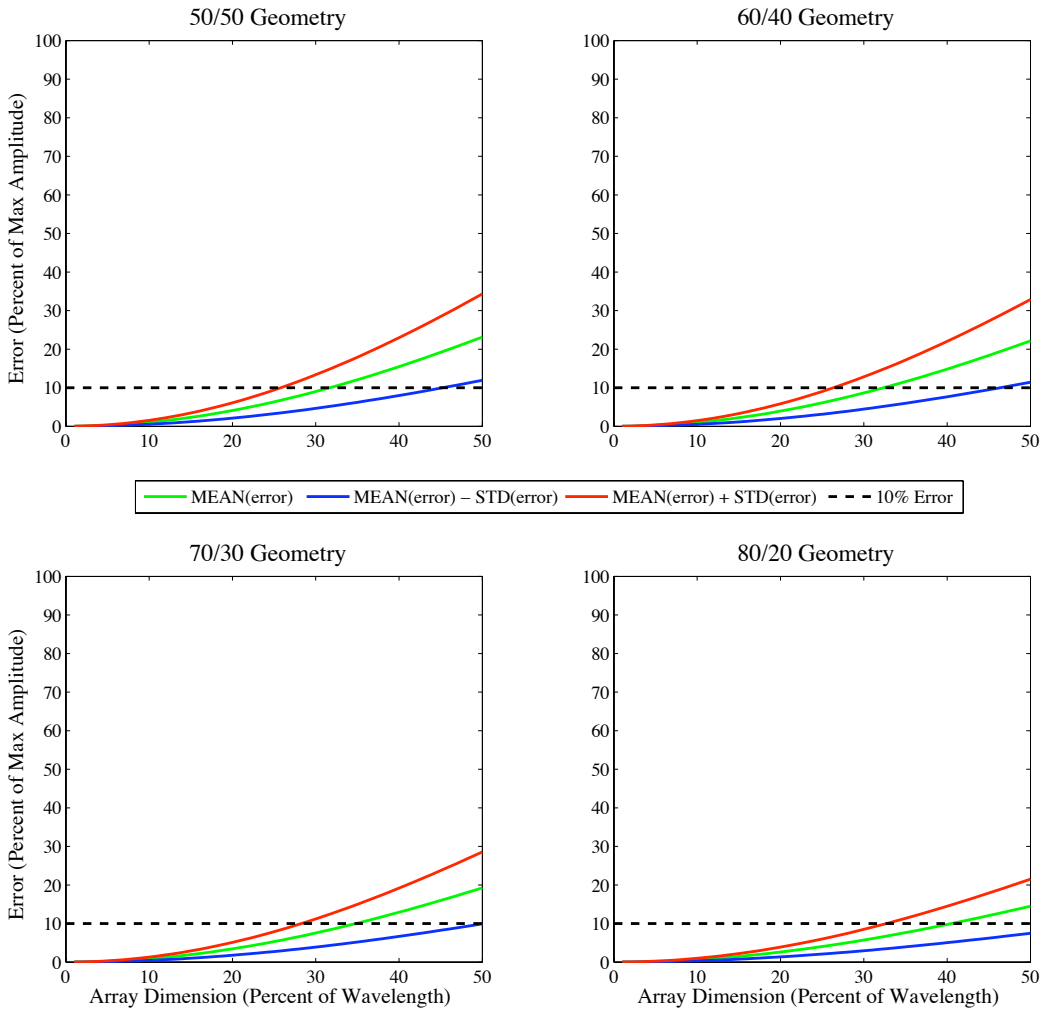

Figure 10. The above figure illustrates the expected errors in accuracy if the example experiment in Figure (9) were repeated for the same geometry ratios, but for a variety of array dimensions and relative array locations (i.e., different array sample locations along the wave cycle). A single array configuration consists of a constant array dimension and geometry ratio. As an array configuration samples different parts of the wave cycle the error in the accuracy can either improve or become worse. Therefore, the performance of each array configuration is evaluated by running statistics on the set of errors associated with the errors in displacement gradients computed at each location along the wave cycle. The GREEN lines plotted above indicate the expected normalized average errors in displacement gradient, after sampling an entire wave cycle, as the array dimension increases for a given array geometry ratio. Similarly, the RED / BLUE lines plotted above indicate the expected normalized average errors in displacement gradient ± one standard deviation (STD), respectively.

example, we only consider the vertical component of ground displacement. The equation used to describe the vertical ground displacement at each station in our experiments is:

$$\forall i \in \{0,1,...,9\} : u_z^i(t,k,c,\theta) = \sin\left(k\left(ct - r_d^i(\theta)\right)\right) \quad , \tag{27}$$

where k = 0.001, 0.002, … , 0.1 radians/kilometer, c = 2 kilometers/second, and θ = 0, 1, … ,180 degrees.

The main concern with the following experiments, is that real data have low-frequency limitations (e.g., low-frequency noise, instrumentation sensitivity, etc.) that, in turn, limit the effectiveness of each method for estimating the displacement gradients. With real data, the most practical way to empirically determine the optimum method for estimating displacement gradients consists of determining the optimum method for estimating the ground displacements. As in *Paolucci and Smerzini* [2008], we can ignore the ground displacement data at one station and then use the ground displacement data from the remaining stations to "predict" the ground displacements at the omitted (or leave-out) station. By conducting this Leave-Out Station Scenario (LOSS) for each of the stations in the array using each method for a particular data set, one can get a rough idea of how well that particular method will work when used to estimate the spatial displacement gradients at arbitrary positions within the array. In this experiment we perform a LOSS for two stations within the Anza seismic network (LVA2 and FRD) for the range in k and θ, discussed above, using the first three methods. The results of this experiment are briefly described below. For a visual aid to the description below, supplemental Figures (A1) – (A8) are available in Appendix (1).

In the LOSS experiment, the spatial displacement gradients derived from each method were used to predict the ground displacements at LVA2 or FRD (depending on which was left out). The errors between the "predicted" ground displacements and the "observed" ground displacements are compared for each LOSS. The errors associated with each method are used to predict the largest resolvable wavenumber at Anza stations LVA2 and FRD. The largest resolvable wavenumber corresponds to the point where the mean error between the "predicted" ground displacements and the "observed" ground displacements exceeds 10%. Before we list the results, it may be helpful to describe the

range in k, discussed above, in terms of the frequency by assuming some lower bound on the propagation velocity. If we assume this lower bound is equal to 3 km/s, then the range in k becomes the range $f = 0.0005, 0.001, \ldots, 0.05$ Hz. The results from performing the LOSS for LVA2 and FRD using Method (1), Method (2), Method (3) based on a quadratic fit (hereafter Method 3a), and Method (3) based on a cubic fit (hereafter Method 3b), and Method (4), are indicated in Table (1). The chief results of this experiment are that each method appears to perform better than the last, in terms of predicting the ground displacements for each LOSS, but Method (2) appears to perform much worse than the other methods under extrapolation, even with "perfect" data. The results of this experiment using Method (4) are not shown in Appendix (1) because, due to the simplicity of the synthetic waveforms, the "predicted" ground displacements were virtually identical to the "observed" ground displacements, for the range in k and θ discussed above, for each LOSS.

We find that the predicted largest resolvable wavenumber (or frequency), using the results from the previous experiment, are often over-estimated. Therefore, in this next experiment we attempt to determine the high-frequency limitations of each method specifically for a sub-set of the Anza seismic array surrounding a selected group of PBO GTSM instruments in southern California. In other words, although the lowest wave-number limit will be dictated by the quality of data, this experiment should immediately identify the largest wave-number limit because of the simplicity of the synthetic waveforms. We chose PBO GTSM station B087, which is approximately co-located with Anza seismic station FRD, and station B088, which is approximately 5 km from Anza seismic station LVA2.

Similar to the previous experiment, Table (2) lists the largest resolvable wavenumber and frequency results (assuming a propagation velocity of 3 km/s) from computing the displacement gradients at B087 and B088 using Method (1), Method (2), Method (3a), Method (3b), and Method (4). For a visual aid to the description below, supplemental Figures (A9) – (A16) are available in Appendix (1). The chief results of this experiment are similar (in a relative sense) to the results from the previous experiment, except that the errors in accuracy are greater for the same range in k and θ.

Table 1. A list of the largest resolvable wavenumber (k) estimates and frequency (f) estimates (assuming propagation velocity of 3 km/s) that result from performing a Leave Out Station Scenario (LOSS) experiment for Anza stations LVA2 and FRD. The largest resolvable wavenumber and frequency corresponds to the point where the mean error between the "predicted" ground displacements and the "observed" ground displacements exceeds 10% at each LOSS. The wavenumber range studied here was between 0.001 rad/km and 0.1 rad/km. In some cases the error did not exceed 10% within the range specified, however, the list indicates whether the largest resolvable wavenumber and frequency was greater than or less than the range in this study.

Estimation Method	**LVA2**		**FRD**	
	***k* @ 10%**	**$f_{3\ km/s}$ @ 10%**	***k* @ 10%**	**$f_{3\ km/s}$ @ 10%**
Method 1	0.045 rad/km	0.02 Hz	0.083 rad/km	0.04 Hz
Method 2	< 0.001 rad/km	< 0.0005 Hz	> 0.1 rad/km	> 0.5 Hz
Method 3a	0.054 rad/km	0.026 Hz	0.091 rad/km	0.043 Hz
Method 3b	0.073 rad/km	0.035 Hz	> 0.1 rad/km	> 0.5 Hz
Method 4	> 0.1 rad/km	> 0.5 Hz	> 0.1 rad/km	> 0.5 Hz

Table 2. A list of the largest resolvable wavenumber (k) estimates and frequency (f) estimates (assuming propagation velocity of 3 km/s) that result from estimating the spatial displacement gradients at PBO GTSM stations B088 and B087. The largest resolvable wavenumber and frequency corresponds to the point where the mean error between the "predicted" spatial displacement gradients and the "observed" spatial displacement gradients exceeds 10% at each PBO GTSM. The wavenumber range studied here was between 0.001 rad/km and 0.1 rad/km. In some cases the error did not exceed 10% within the range specified, however, the list indicates whether the largest resolvable wavenumber and frequency was greater than or less than the range in this study.

Estimation Method	**B088**		**B087**	
	***k* @ 10%**	**$f_{3\ km/s}$ @ 10%**	***k* @ 10%**	**$f_{3\ km/s}$ @ 10%**
Method 1	0.014 rad/km	0.007 Hz	0.037 rad/km	0.018 Hz
Method 2	< 0.001 rad/km	< 0.0005 Hz	> 0.1 rad/km	> 0.5 Hz
Method 3a	0.051 rad/km	0.024 Hz	0.068 rad/km	0.032 Hz
Method 3b	0.099 rad/km	0.047 Hz	> 0.1 rad/km	> 0.5 Hz
Method 4	> 0.1 rad/km	> 0.5 Hz	> 0.1 rad/km	> 0.5 Hz

Again, the results of this experiment using Method (4) are not shown in Appendix (1) because, due to the simplicity of the synthetic waveforms, the "predicted" displacement gradients were virtually identical to the "observed" displacement gradients, for the range in k and θ discussed above, at each PBO GTSM.

Real Data: M8.1 Samoa Islands Earthquake (2009/09/29)

Data collected by seismic instruments are never perfect. Instead of introducing random errors – associated with differences in the propagation velocity, propagation angle, contamination from scattered waves, instrument response irregularities, etc. – into the synthetic data sets above, we illustrate the performance of each method as they are applied to real data, collected by the same 10-element subset of the Anza Seismic Network, that correspond to the M8.1 Samoa Islands Earthquake (2009/09/29). In this experiment, we again attempt to first predict the ground displacements for the same two LOSS experiments (for FRD and LVA2) described in the previous experiment. After gauging the performance of each method for each LOSS, we compare the predicted displacement gradient estimates for all four methods at stations FRD and LVA2.

Figures (11) and (12) are histograms that illustrate the distribution of errors associated with performing the LOSS experiment using each method at stations FRD and LVA2, respectively. Supplemental Figures (A17) – (A19) and (A20) – (A22) that illustrate all three components of the predicted ground displacement for stations FRD and LVA2, respectively, are located in Appendix (1). The example involving station FRD demonstrates that all four methods are able to predict the ground displacements at a station with several other seismic stations nearby. However, the example involving station LVA2 demonstrates that Method (2), and to some extent Method (1), is not well suited for predicting the ground displacements at a relatively isolated station that is located towards the perimeter of the seismic array.

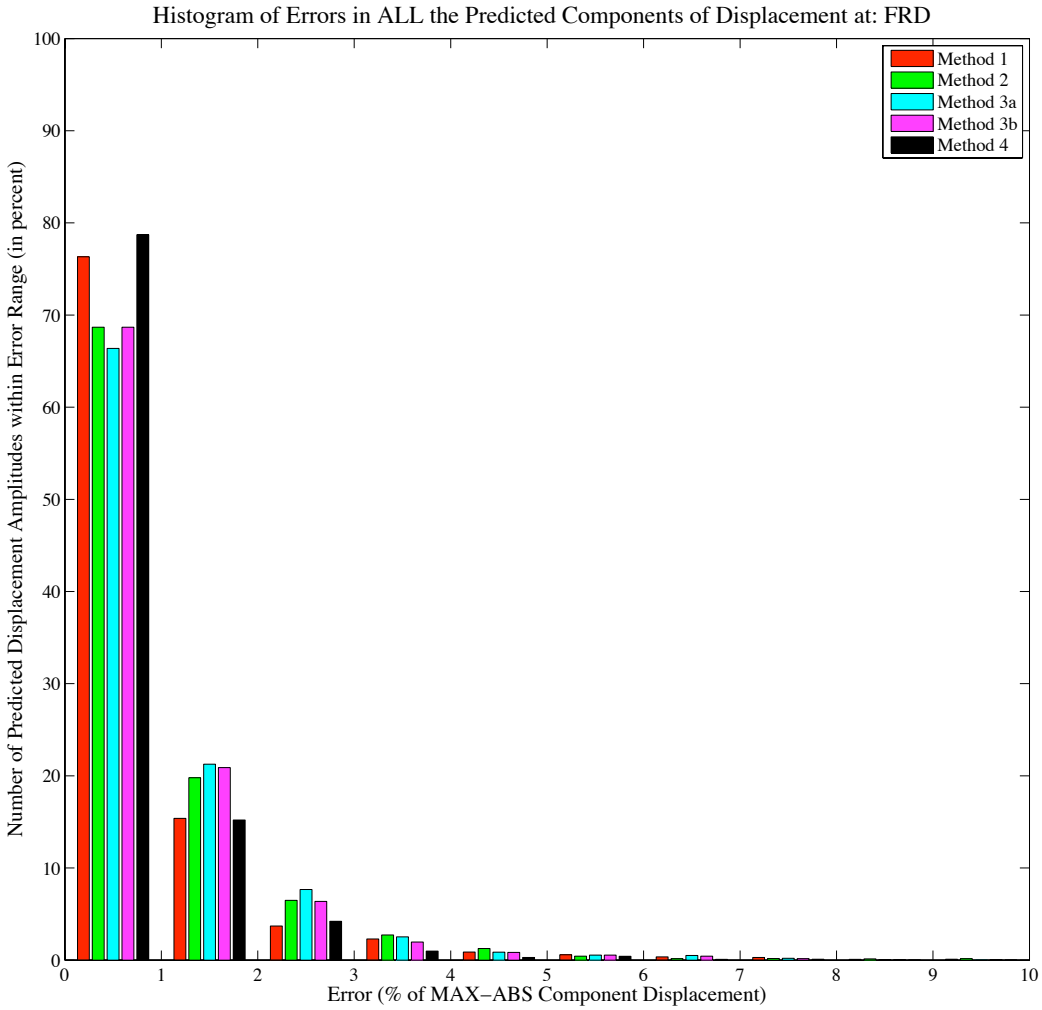

Figure 11. Illustrates a histogram of the errors in all three components of the predicted ground displacement at FRD, illustrated in Figures (A17) – (A19), after comparing the results from Methods (1), (2), (3a), (3b) and (4) to the actual ground displacements observed at FRD. The size of the error is expressed in percent of the maximum, absolute amplitude associated with each component of motion. The size of each histogram bar represents the total number of predicted amplitudes, expressed in percent of the total number of amplitudes in the time window (1701 samples), that occur within that specific error range (i.e., between 0 and 1 percent error, or between 1 and 2 percent error, etc.).

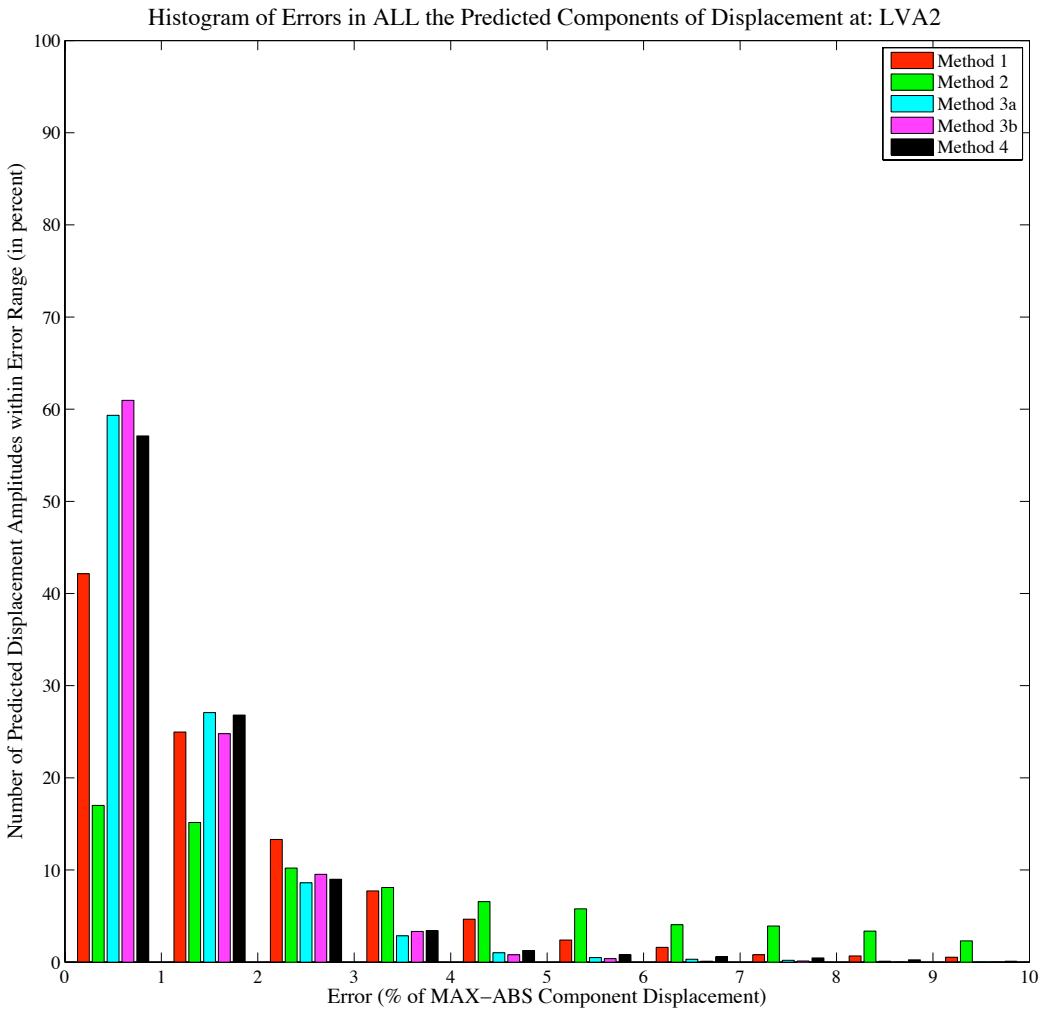

Figure 12. Illustrates a histogram of the errors in all three components of predicted ground displacement at LVA2, illustrated in Figures (A20) – (A22), after comparing the results from Methods (1), (2), (3a), (3b) and (4) to the actual ground displacements observed at LVA2. The size of the error is expressed in percent of the maximum, absolute amplitude associated with each component of motion. The size of each histogram bar represents the total number of predicted amplitudes, expressed in percent of the total number of amplitudes in the time window (1701 samples), that occur within that specific error range (i.e., between 0 and 1 percent error, or between 1 and 2 percent error, etc.).

Unlike the synthetic experiment immediately above, we do not have independent displacement gradient data at each station in order to compare the performance of each method. However, since Method (4) appears to be the most consistent in terms of yielding low errors for each LOSS, we choose to compare the performance of each of the first three methods for estimating the displacement gradient against the result from Method (4). Figures (13) – (15) illustrate the horizontal displacement gradients that correspond to each component of the ground displacement for station FRD using all four methods. Supplemental Figures (A22) – (A24) illustrate the result for station LVA2. Figures (16) and (17) are histograms that illustrate the distribution of errors associated with the difference between the result of each of the first three methods and the result of Method (4) at stations FRD and LVA2, respectively. The example involving station FRD demonstrates that all four methods are somewhat consistent at a station toward the interior of a seismic array. Nearly all the displacement gradient amplitudes are within ± %10 of the result from Method (4). The example involving station LVA2 demonstrates, again, that Method (2) is not well suited when applied to a station toward the perimeter of a seismic array. The distribution in Figure (17) appears to indicate that the results from Method (1) and Method (3) differ from the result of Method (4) to a similar degree. However, the reasons for these differences are not so similar. Figures (18) and (19) illustrate a good example of the type of expected differences between the result of Method (1) and the result of Method (4). The amplitude result of Method (1) appears to be reasonably accurate compared to Method (4), however the result is out of phase. As mentioned previously, this timing error (or phase error) is due to the bias in the estimate of the displacement gradient caused by an uneven amount of stations to the "left" and "right" of the reference station relative to the radial propagation direction. The differences related to the estimates resulting from Method (3), illustrated in the BOTTOM-LEFT panel in Figure (19), are likely due to the irregularities/ inconsistencies in the ground displacements across the seismic array caused by any combination of the reasons described above (i.e., local site effects, instrumentation, response, calibration, etc.).

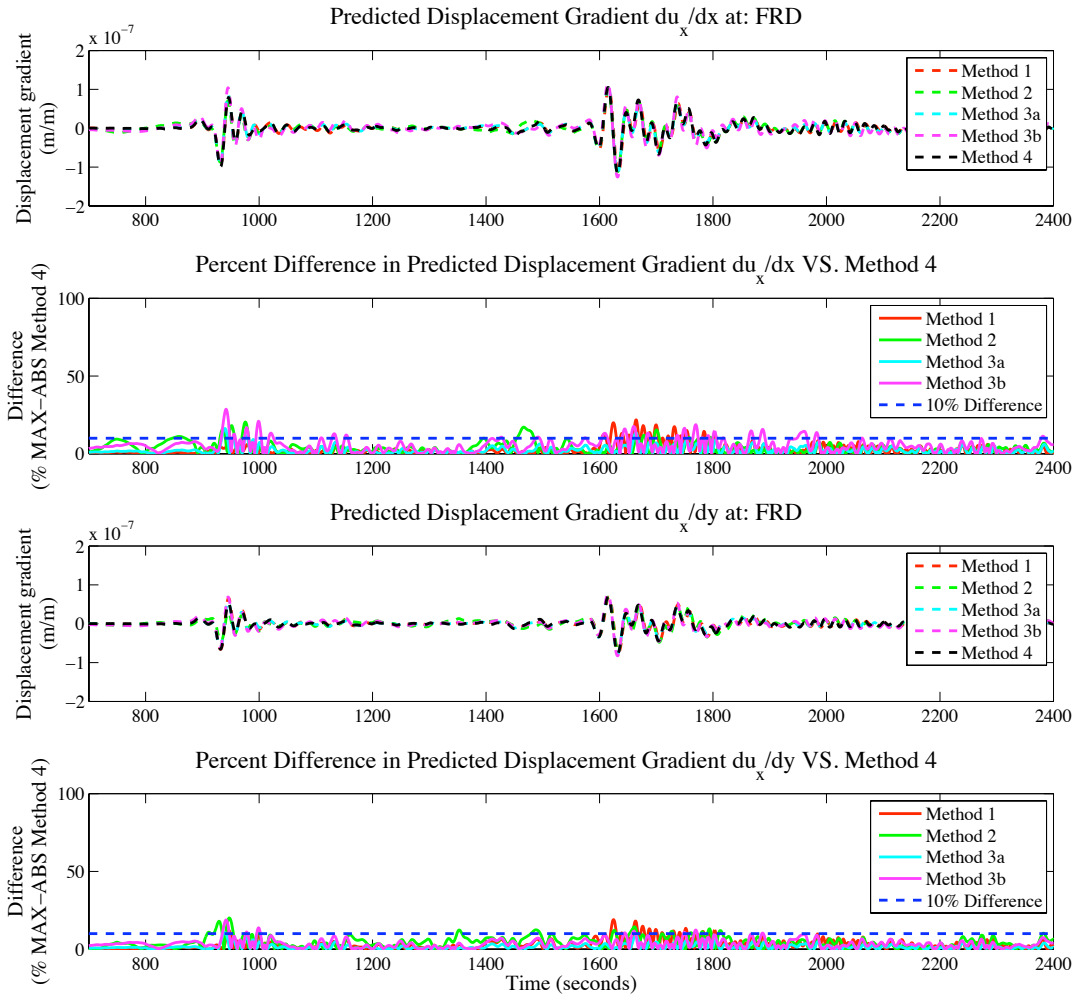

Figure 13. Illustrates the horizontal displacement gradients (i.e., $\partial/\partial x$ and $\partial/\partial y$) associated with the east-west component of ground displacement (i.e., u_x) at FRD using Methods (1), (2), (3a), (3b), and (4). The error plots indicate the difference between each of the results from the first three methods and the result from Method (4). The original seismograms correspond to the 29 September 2009 M8.1 Samoa Island earthquake band-pass filtered between 0.005 Hz and 0.05 Hz with a 4-pole Butterworth acausal filter.

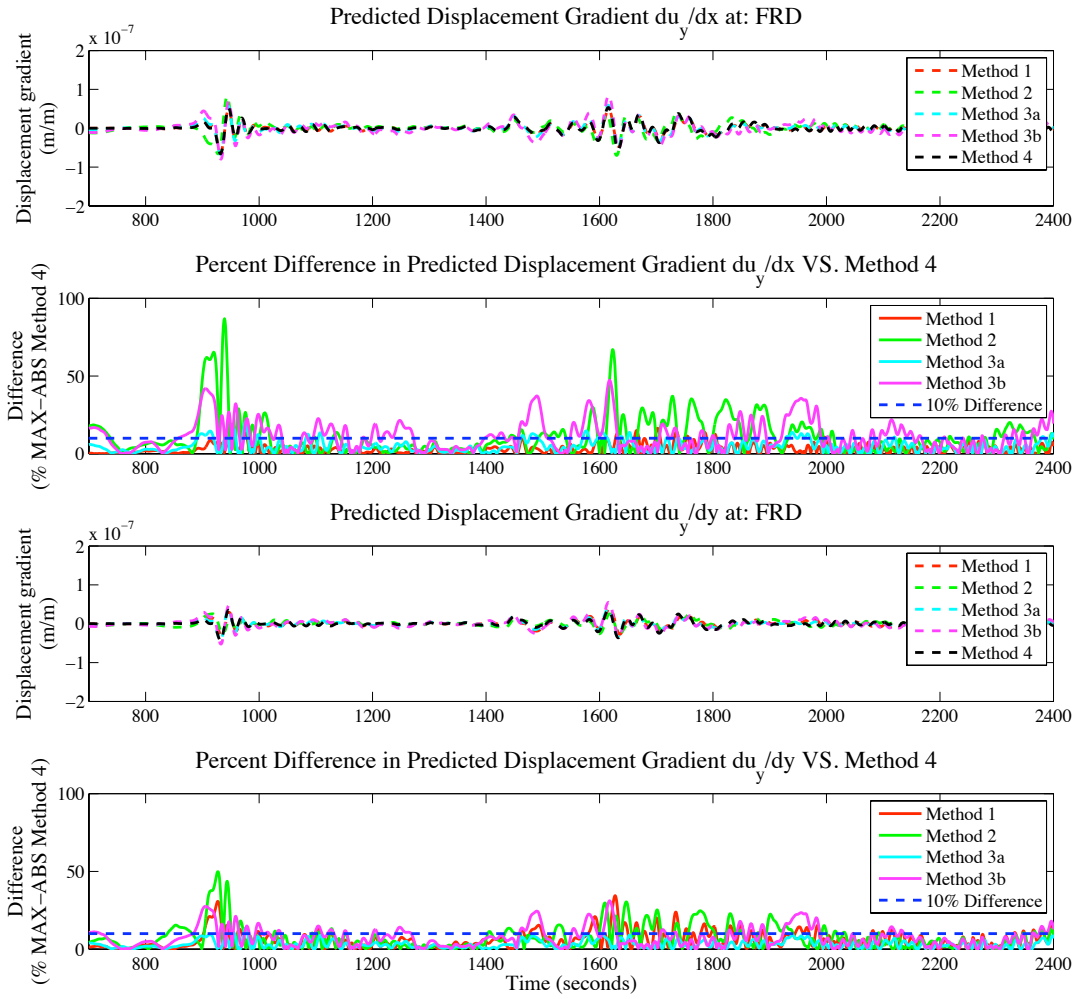

Figure 14. Illustrates the horizontal displacement gradients (i.e., $\partial/\partial x$ and $\partial/\partial y$) associated with the north-south component of ground displacement (i.e., u_y) at FRD using Methods (1), (2), (3a), (3b), and (4). The error plots indicate the difference between each of the results from the first three methods and the result from Method (4). The original seismograms correspond to the 29 September 2009 M8.1 Samoa Island earthquake band-pass filtered between 0.005 Hz and 0.05 Hz with a 4-pole Butterworth acausal filter.

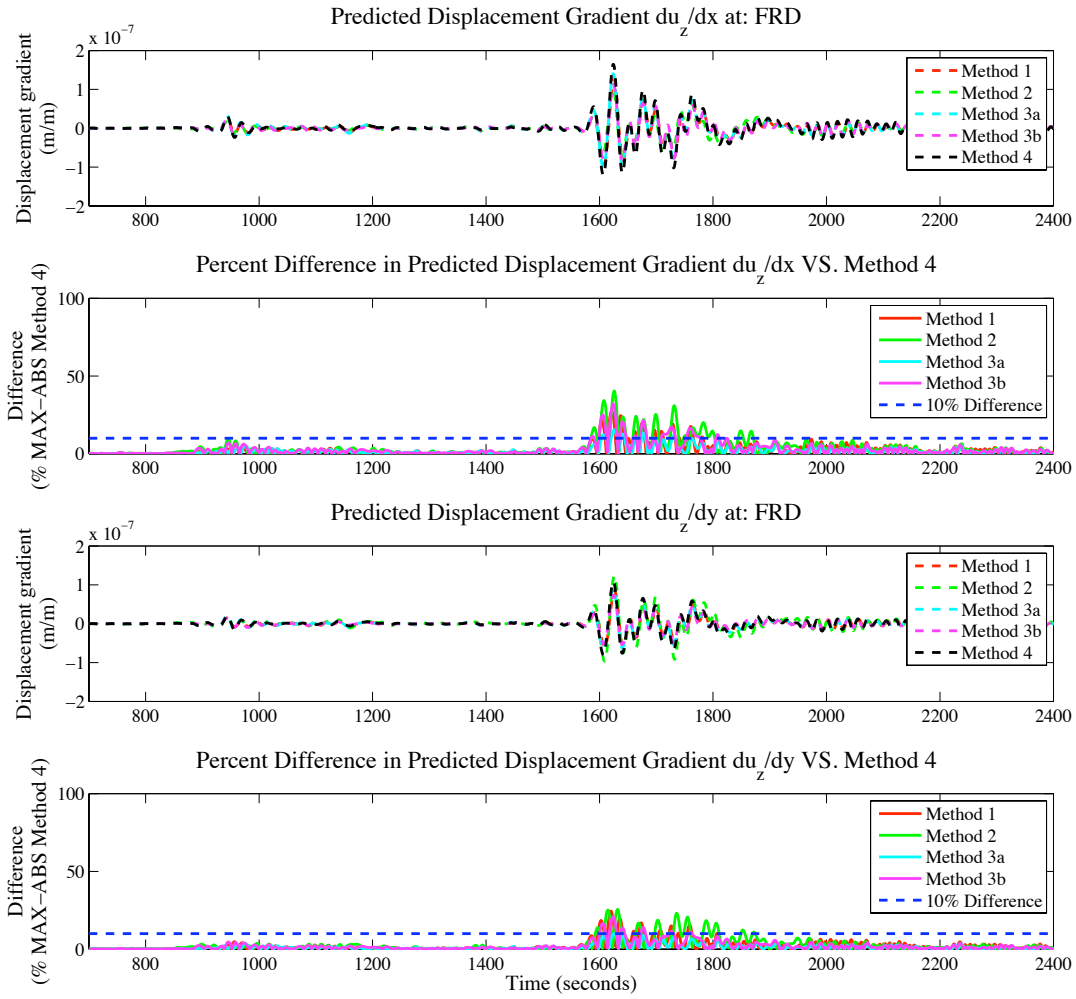

Figure 15. Illustrates the horizontal displacement gradients (i.e., $\partial/\partial x$ and $\partial/\partial y$) associated with the vertical component of ground displacement (i.e., u_z) at FRD using Methods (1), (2), (3a), (3b), and (4). The error plots indicate the difference between each of the results from the first three methods and the result from Method (4). The original seismograms correspond to the 29 September 2009 M8.1 Samoa Island earthquake band-pass filtered between 0.005 Hz and 0.05 Hz with a 4-pole Butterworth acausal filter.

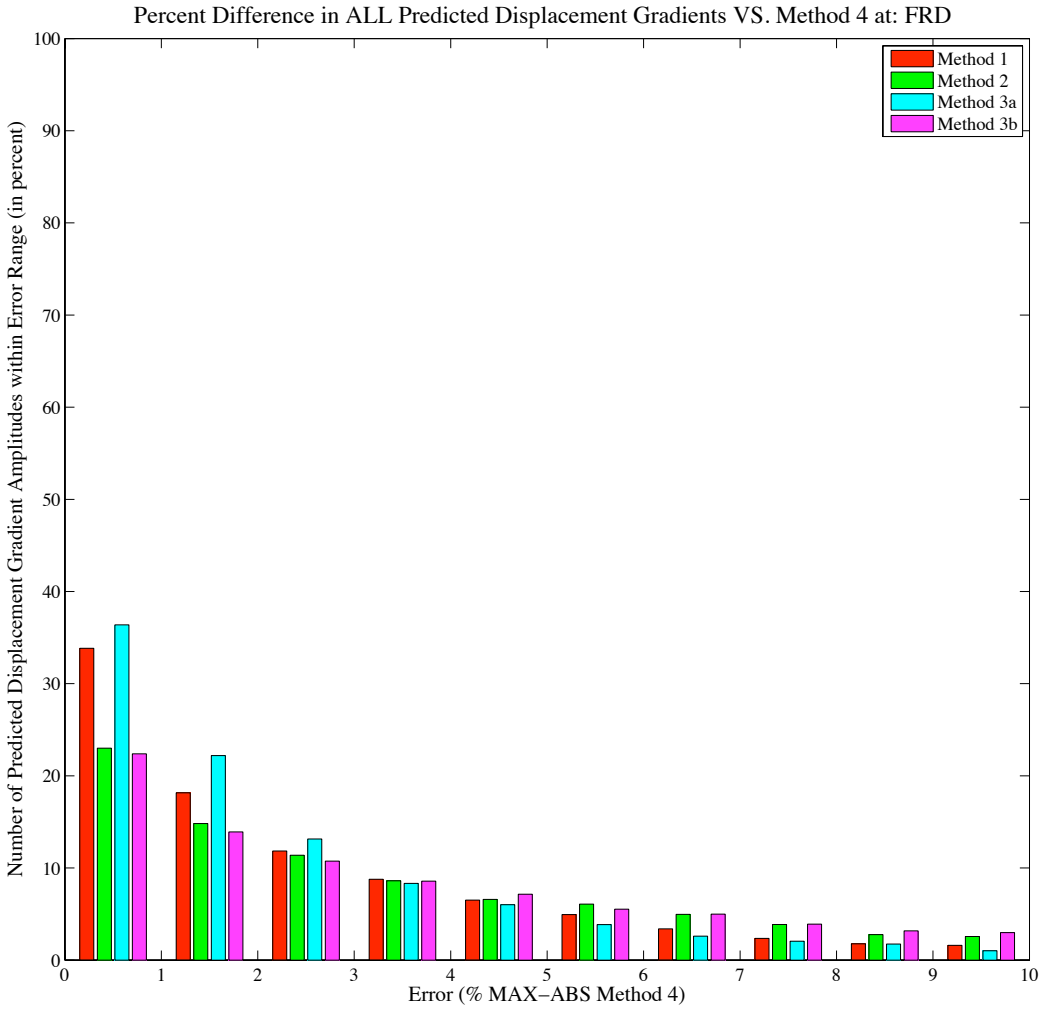

Figure 16. Illustrates a histogram of the errors associated with the differences in the estimated horizontal displacement gradients at FRD, illustrated in Figures (13) – (15), after comparing the results from the first three methods to the results from Method (4). The size of the error is expressed in percent of the maximum, absolute amplitude associated with the result from Method (4). The size of each histogram bar represents the total number of predicted amplitudes, expressed in percent of the total number of amplitudes in the time window (1701 samples), that occur within that specific error range (i.e., between 0 and 1 percent error, or between 1 and 2 percent error, etc.).

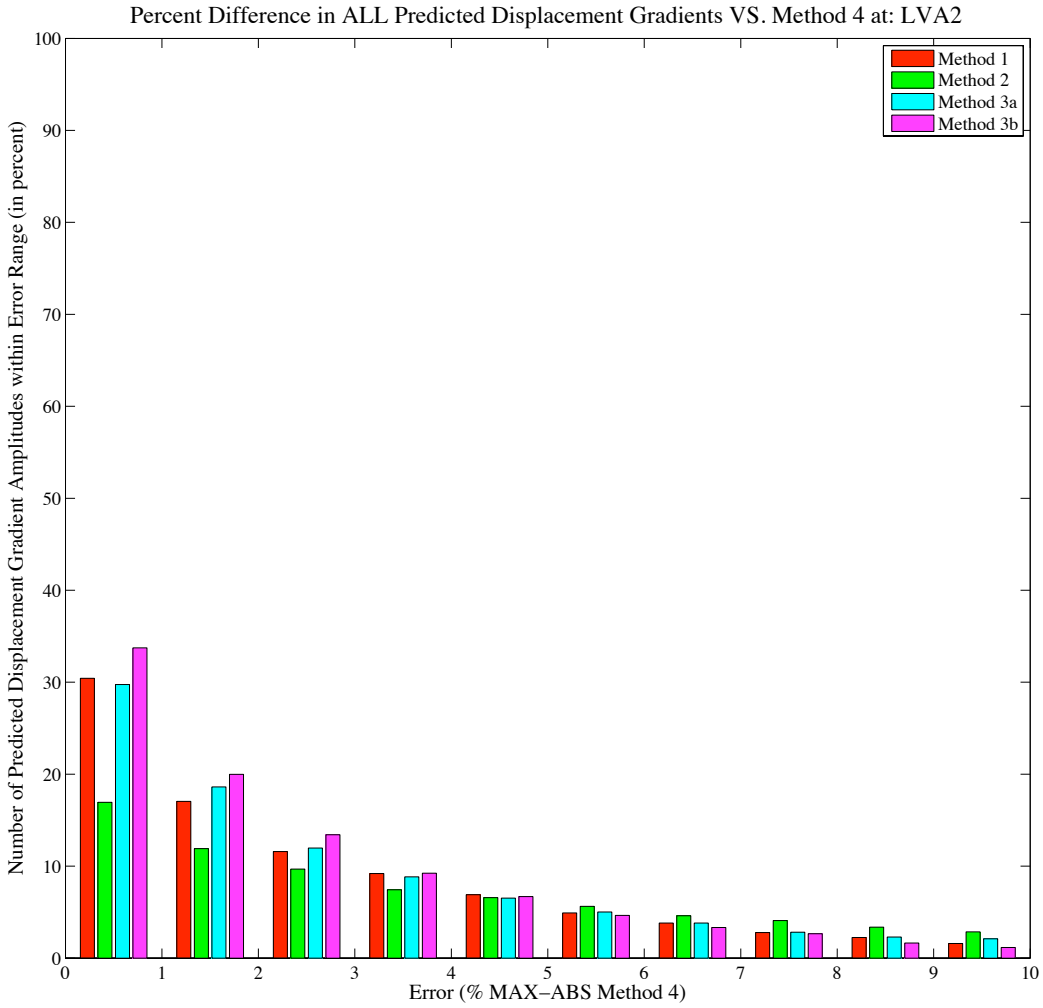

Figure 17. Illustrates a histogram of the errors associated with the differences in the estimated horizontal displacement gradients at LVA2, illustrated in Figures (A22) – (A24), after comparing the results from the first three methods to the results from Method (4). The size of the error is expressed in percent of the maximum, absolute amplitude associated with the result from Method (4). The size of each histogram bar represents the total number of predicted amplitudes, expressed in percent of the total number of amplitudes in the time window (1701 samples), that occur within that specific error range (i.e., between 0 and 1 percent error, or between 1 and 2 percent error, etc.).

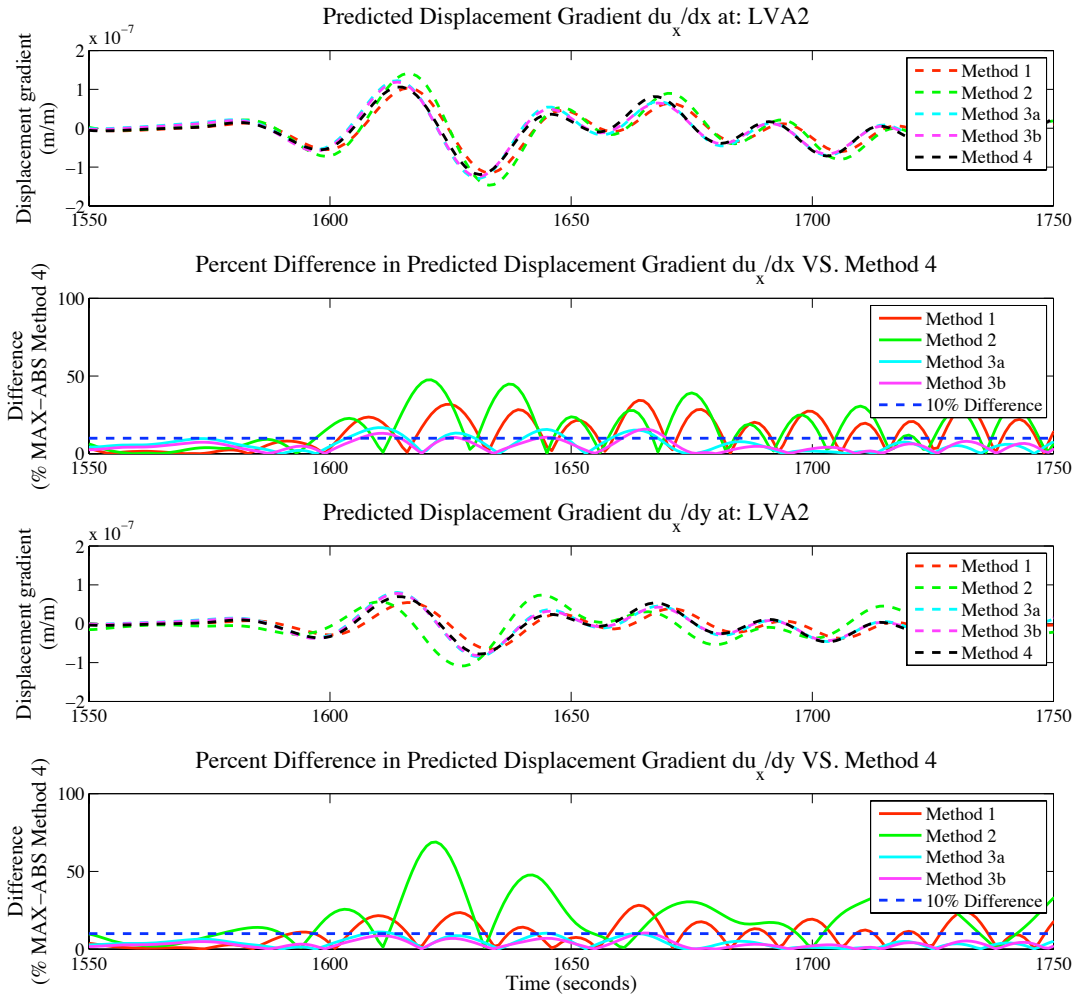

Figure 18. Illustrates a version of Figure (A22) that has been zoomed in around the Rayleigh wave. Notice that the result from Method (1) appears to be consistent in amplitude, but inconsistent in phase, when compared to the result from Method (4). The result from Method (2) appears to be inconsistent with respect to both amplitude and phase, when compared to the result from Method (4). In this time window, nearly all the displacement gradient estimates predicted by Method (3a) and (3b) are consistent with respect to both amplitude and phase, when compared to the result from Method (4).

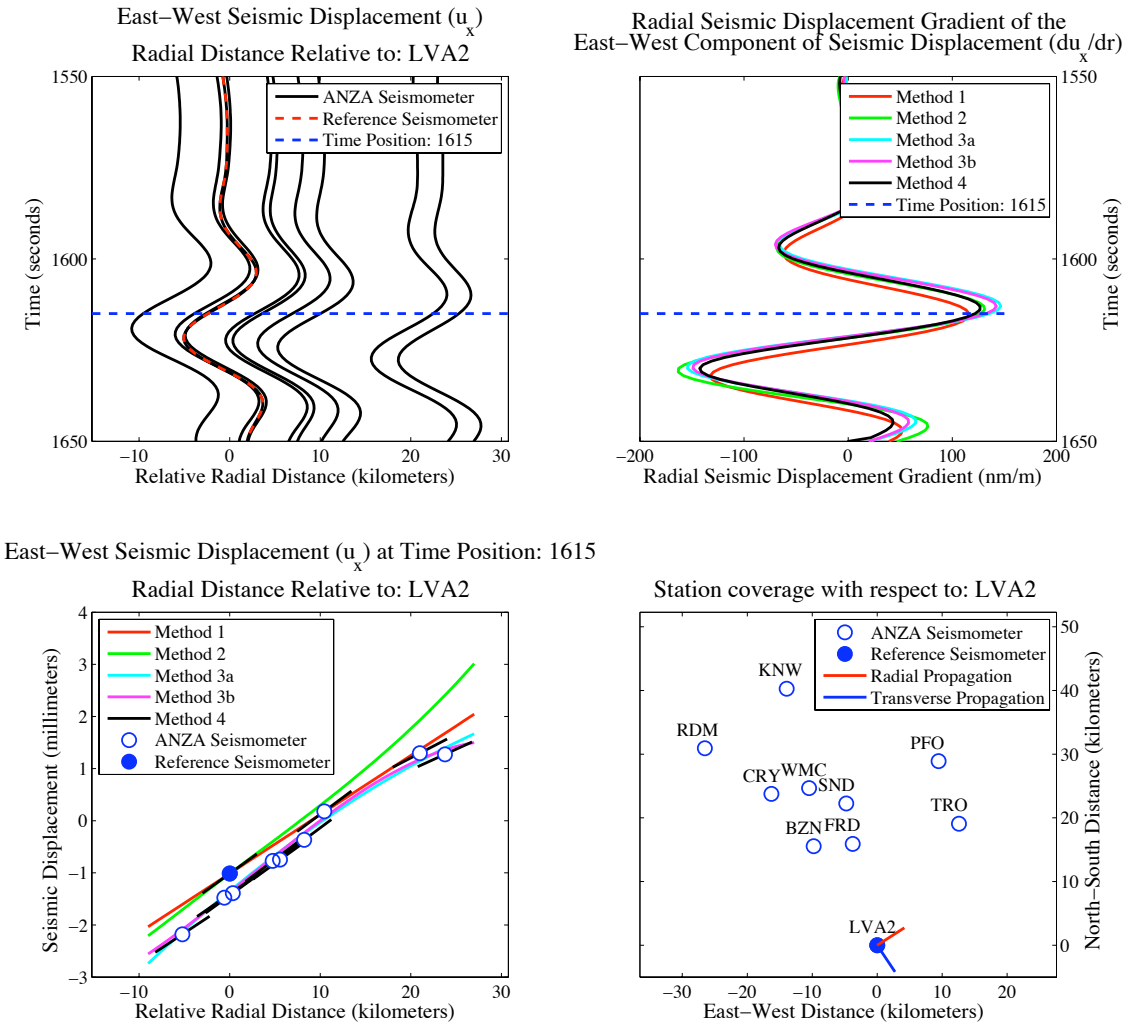

Figure 19. (TOP-LEFT) Illustration of the seismograms representing the east-west component of the ground displacement arranged according to radial distance relative to Anza station LVA2. (TOP-RIGHT) Illustration of the estimates of the radial displacement gradient, associated with the east-west component of the ground displacement for the same time-window in the adjacent figure, according to each of the four methods. (BOTTOM-LEFT) Illustration of the ground displacement at each of the Anza seismic stations (open and close BLUE circles) according to the radial distance relative to LVA2. (BOTTOM-RIGHT) Illustration of the sub-set of the Anza seismic array used to compute displacement gradients and approximate propagation direction of the Rayleigh wave at the reference seismic station: LVA2.

Discussion

Four methods for deriving the spatial displacement gradient from seismic data across a 2D surface array have been reviewed in this paper. We reviewed each method with specific interest to their performance after being applied to both synthetic and real seismic data collected by a large aperture (> 10km) surface array. Under these conditions we find that Method (4), based on the findings in *Gomberg et al.* [1999] and the spatial gradient analysis of *Langston* [2007b], is likely to offer the most accurate estimate of the spatial displacement gradient when the assumption of plane-wave propagation is valid and the propagation slowness / direction can be determined accurately. However, when estimating the displacement gradient at arbitrary locations inside the seismic array, it may be necessary to implement a hybrid method that consists of using Method (4) to determine the displacement gradients at each seismic station location and then using either Method (2) or (3) to interpolate the displacement gradient result to the arbitrary location with the array.

The results of this study will directly impact the way borehole Gladwin Tensor Strain-meter (GTSM) instruments are calibrated in the future. Currently borehole GTSM instruments, which make up a significant portion of the Plate Boundary Observatory (PBO) facility, are calibrated based on the strain information associated with the earth's tides. The raw strain information derived from the borehole GTSM instrument is compared to known/theoretical earth tide strain and the linear relationship, between the two sets of data, is used to calibrate future GTSM instrument recordings. Instead of using data associated with the earth's tidal forces, it is now possible to derive much of the necessary calibration information using data associated with large teleseismic earthquakes and applying the methods reviewed in this paper. In order to simplify the calibration process, the linear relationship between the raw strain information derived from the borehole GTSM instrument and the reference strain information derived from seismic data is determined in the frequency domain. If the reference strain information

derived from the seismic data contain timing (or phase) errors, then the calibration coefficients that linearly relate the raw GTSM instrument data to the reference strain may be complex, instead of real. The imaginary parts will lead to timing (or phase) errors in the calibrated GTSM instrument data that may affect the accuracy of any physical relationships (i.e., phase velocity) derived from their data in the future. The necessary information for implementing this type of borehole GTSM instrument calibration may be found in the next chapter (Chapter 3).

CHAPTER 3

Calibrating Gladwin Tensor Strainmeters using Seismic Data

Abstract

Teleseismic data collected by the southern California Anza seismic network have been used for calibrating nearby borehole GTSM instruments of the Plate Boundary Observatory (PBO). We find reasonable agreement between the calibration coefficients derived here using seismic data and the coupling coefficients derived in other studies using theoretical calculations of earth tides. This study investigates whether the coupling coefficients necessary to calibrate the borehole instrument have changed since each station has been installed. We find that the coefficients necessary for calibrating data collected over the course of 2 years are remarkably stable. During the course of calibration, we discovered that some stations had misalignment errors approaching 50 degrees.

This study provides an overview of the process necessary to compute the necessary calibration coefficients that linearly relate the raw instrument gauge strains, recorded by borehole GTSM instruments, to the reference formation strains derived from seismic data. The calibration method implemented here is based on the method developed in *Hart et al.* [1996]. We also discuss several methods for performing the necessary first step of deriving formation strain information from seismic data, including the assumptions and limitations associated with each. The process used to derive formation strain information is a hybrid method based on the methods developed in *Gomberg et al.* [1999], *Langston* [2007b], and the previous chapter. We also discuss two general methods – a multi-station seismic approach and a single-station seismic approach – for deriving the coupling coefficients necessary for GTSM calibration, including error analysis. The results of this study suggests that it should be possible to calibrate the remaining GTSM instruments

inside the PBO network that also have either a nearby array of seismic instruments or a single, co-located seismic instrument.

Introduction

The goal of the Plate Boundary Observatory (PBO) is to monitor and study the strain field associated with the interaction between the Pacific, the Juan de Fuca, and the North American plates along the west coast of the United States. The PBO is composed of a variety of sensors to measure the ongoing deformation; these include Global Positioning System (GPS) receivers and several types of strain-meter instruments (see Figure 1). In this study we concentrate on borehole Gladwin Tensor Strain-Meter (GSTM) instruments, which make up a significant portion of the PBO strain-meter network. Borehole GTSM instruments obtain measurements that may be related to the areal strain, differential normal strain, and shear strain – collectively known as the formation strain – from any three of the four built-in strain gauges [*GTSM*, 2010]. Areal strain describes two-dimensional (2D) isotropic deformation – deformation is equal in every direction with respect to the horizontal plane. Differential normal strain and shear strain describe 2D anisotropic deformation – deformation is *not* the same in every direction with respect to a reference plane. One of the intended purposes of the borehole GTSM instruments is to provide very important information regarding the source mechanisms of tectonic events, such as aseismic slip, that would otherwise be undetected (see Figure 2) by current seismological and/or geodetic instruments [*Wyatt*, 1988]. Unfortunately, these instruments have proved to be problematic because of the inconsistent nature of the measurements recorded by the borehole GTSM instruments.

As with any instrument, it is important that the measurements are as accurate as possible in order to reduce the amount of uncertainty associated with their physical meaning – this is especially the case with the borehole GTSM instruments. In order to eliminate any potential accuracy problems related to the coupling of the GTSM instruments with the inside of a borehole, the sensors are often emplaced using expansive grout to ensure a constant state of compression [*GTSM*, 2010]. However, as discussed in

Hart et al. [1996], the combination of several factors – the expansive grout, misalignment during the emplacement process, and heterogeneities associated with local borehole geology – can cause the instruments to measure a distorted version of the true local strain field. Figure (20) illustrates a good example of processed long-period strain data that are largely inconsistent despite being collected from an array with aperture significantly smaller than the wavelength of the recorded disturbance. At these wavelengths, the inconsistencies are more likely related to effects associated with local small-scale heterogeneities than to effects associated with wave propagation. Since the measurements collected by borehole GTSM instruments do not always reflect actual local strains, they rely on accurate calibration methods to relate what *is* measured to what *ought* to be measured.

One approach to calibrating borehole GTSM instruments, offered by *Gladwin and Hart* [1985] and *Shimada et al.* [1987], is to attempt direct estimation of the elastic properties associated with the borehole coupling environment. However, as noted by *Hart et al.* [1996], this approach is complicated and tends to increase uncertainty, rather than reduce it. The second approach, offered in *Hart et al.* [1996] and reformulated here, is based on the assumption that the "true" reference formation strain can be linearly related to the instrument strain measured by the GTSM gauges. In the study by *Hart et al.* [1996], borehole GTSM instruments were calibrated by using earth tide measurements, collected by a co-located laser strain-meter (LSM) instrument, as the "true" reference strains. However, not all borehole GTSM instruments are co-located with an LSM instrument to facilitate the calibration process. Instead, other studies rely on theoretical earth tide calculations in order to serve as the reference strains during calibration (see *Roeloffs* [2010]).

In some cases, several additional corrections must be accounted for prior to analyzing strain data. These include corrections to the strain data for effects caused by an error in the instrument alignment (if the borehole coupling model is derived independently), by earth tide or ocean loading, by changes in atmospheric pressure, and by changes in pore fluid pressure [*Roeloffs*, 2010]. Corrections for the strain caused by the earth's tide and ocean loading are collectively known as the theoretical tides. The

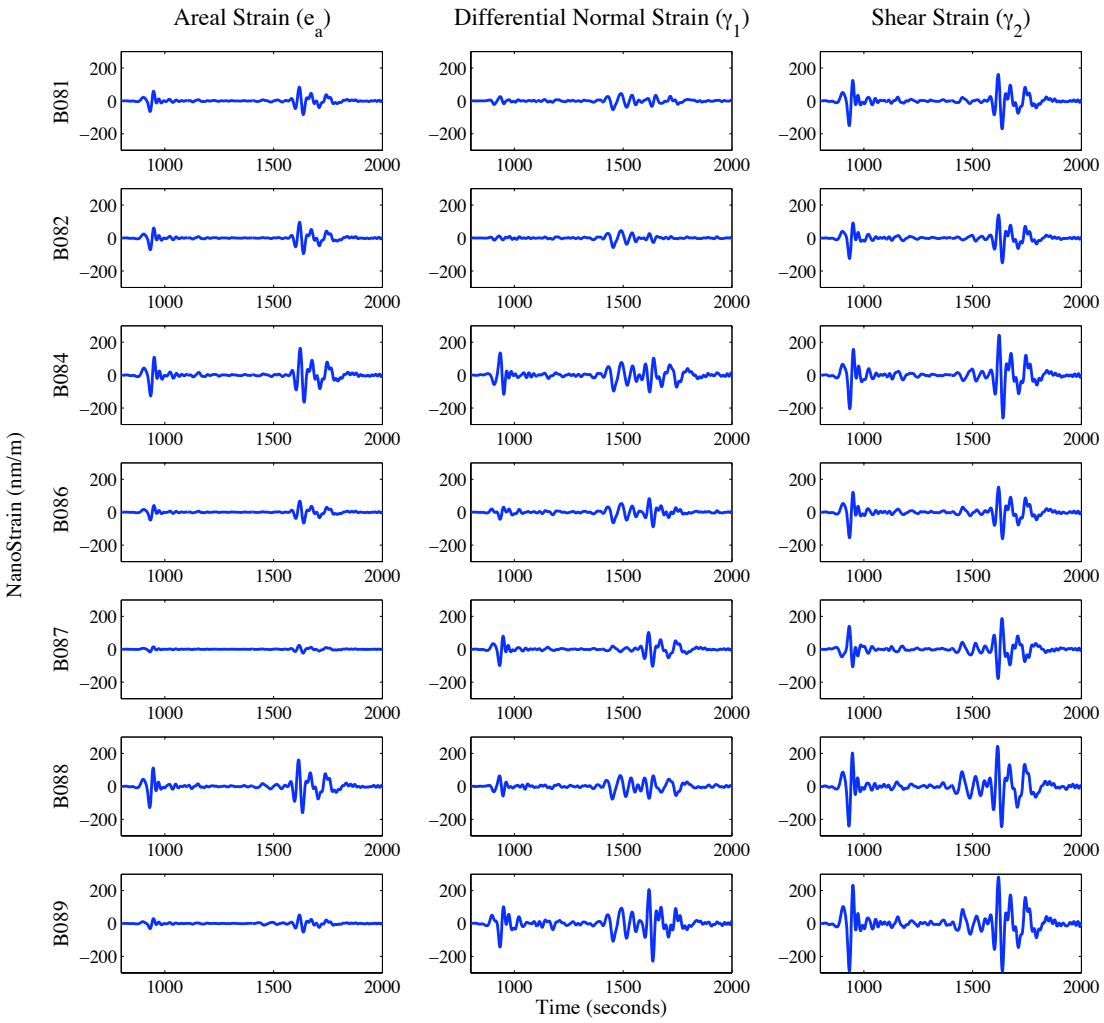

Figure 20. Illustration of the formation strain derived from seven PBO GTSM instruments, using Equation (34) and the advertised orientation angles, inside the Anza Seismic Network in Southern California. The areal strain is equal to the sum of strain tensor elements ε_{11} and ε_{22}. The differential normal strain is equal to the difference between strain tensor elements ε_{11} and ε_{22}. The shear strain is equal to the sum of strain tensor elements ε_{12} and ε_{21}. Formation strain in the above figure corresponds to the 29 September 2009 M8.1 Samoa Island earthquake band-pass filtered between 0.01 Hz and 0.03 Hz with a 4-pole Butterworth acausal filter. The vertical axis (i.e., *y*-axis) limits were set to ± 300 nm/m in order to highlight the inconsistent nature of strain measurements between all stations.

strain estimates associated with the theoretical tides can be computed, using software such as the SPOTL package [*Agnew*, 1996], at a particular location and removed from the calibrated strain data (i.e., strain data that has had the coupling response and orientation error removed). Corrections for the strain caused by changes in atmospheric pressure are found by linearly relating these pressure changes to the changes in strain measured by the instrument downhole (a brief description of software available for this type of correction may be found in *UNAVCO* [2004]). Corrections for the strain caused by changes in the pore fluid pressure may be found by deriving a relationship between these pressure changes and the changes in the strain measured by the instrument downhole [*Roeloffs*, 2010]. However, depending on fluid flow conditions, this set of corrections could affect not only the amplitude of the strain traces, but also the phase of the strain traces. Only a few borehole PBO GTSM instruments have co-located instruments that measure these changes in pore fluid pressure (personal communication with *E. Roeloffs* [2010]), so removing this effect (if it is present) is possible only at those select GTSM site locations.

In this study, we present a novel approach to borehole GTSM calibration by deriving the reference strain information from broadband seismic data. Recently, *Langston and Liang* [2008] discovered that strain information derived from seismic data collected by the Anza Seismic Network, using techniques similar to that of *Spudich et al.* [1995], were much more consistent than the strain information derived from the PBO GTSM instruments located inside the same network (see Figure 21). This realization led to the hypothesis that the "true" reference strain information necessary to calibrate the borehole GTSM instruments could be obtained from seismic data. We test this hypothesis by determining whether the linear relationship between the reference strains and the borehole GTSM instrument strains are consistent between the method of calibration in this study and the previous methods of calibration. Since the other methods of calibration involve waves with oscillation periods several orders of magnitude greater than even the largest associated with teleseismic waves, we assume that the linear relationship between the reference strains and the instrument strains are frequency independent.

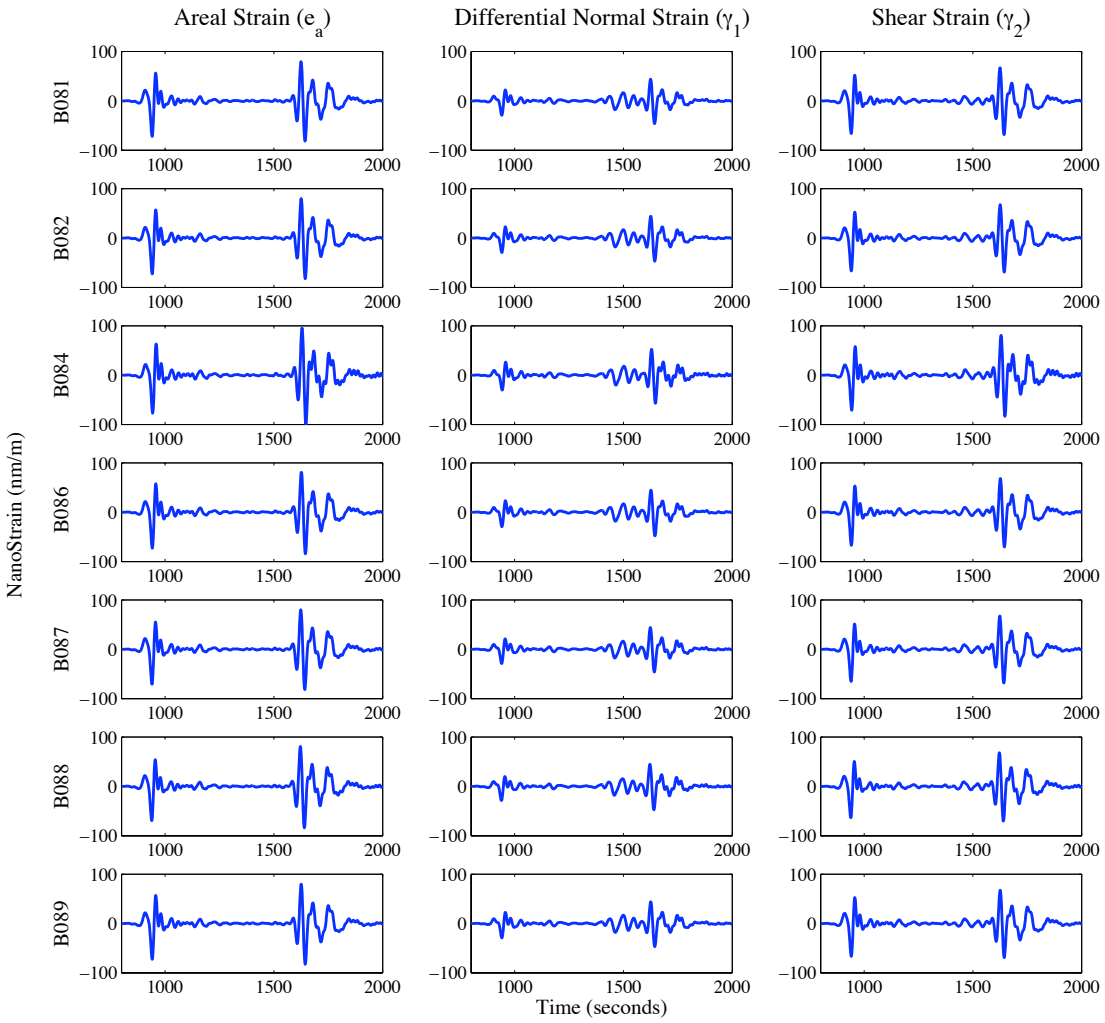

Figure 21. Illustration of the formation strain derived/predicted from broadband seismic data, collected by the Anza Seismic Network, at the same seven PBO GTSM instrument locations described in Figure (20). The areal strain is equal to the sum of strain tensor elements ε_{11} and ε_{22}. The differential normal strain is equal to the difference between strain tensor elements ε_{11} and ε_{22}. The shear strain is equal to the sum of strain tensor elements ε_{12} and ε_{21}. Formation strain in the above figure corresponds to the 29 September 2009 M8.1 Samoa Island earthquake band-pass filtered between 0.01 Hz and 0.03 Hz with a 4-pole Butterworth acausal filter. The vertical axis (i.e., *y*-axis) limits were set to ± 100 nm/m in order to highlight the very consistent nature of strain measurements derived from broadband seismic data.

Previously, in Chapter (2), we discussed several methods related to estimating the spatial displacement gradient in order to obtain the reference formation strain necessary for calibration. We also discussed potential timing (or phase) errors that can be introduced into the spatial displacement gradient estimates from using the seismo-geodetic technique of *Spudich et al.* [1995]. In this study, we chose to develop a hybrid process consisting of a mix between the methods based on the results from *Gomberg et al.* [1999] and *Langston* [2007b], and the polynomial interpolation method described in the previous chapter. The purpose of this hybrid process is to eliminate as much of the timing (or phase) errors that might have been introduced as a result of using the seismo-geodetic technique.

Data and Processing

As previously noted in *Langston and Liang* [2008], the Anza Seismic Network in southern California provides a dense 2D seismic array excellent for deriving long-period strain measurements associated with large teleseismic events. We select a 10-element sub-set of the Anza broadband seismic stations that surround 7 borehole GTSM instruments. The instruments associated with the Anza Seismic Network are three-component Streckeisen STS-2 seismometers with Reftek 24-bit digitizers. At each site location, where the local geology may consist of either crystalline plutonic or metamorphic basement rocks, the seismometers are secured to a concrete pad that is either poured directly on the crystalline rock outcropping (KNW, RDM, TRO) or poured over rebar stakes inside a hole dug from the top weathered layer [*Vernon*, 1989]. Specific information for each Anza seismic station is listed inside Table (3). The general process for emplacing each GTSM instrument includes drilling a borehole to ~150m, logging the geological/geophysical properties of the borehole, protecting the borehole with steel casing, pumping expansive grout to the bottom of the borehole, and finally lowering the GTSM instrument into the expansive grout [*UNAVCO*, 2010]. Specific information for each PBO borehole station location is listed inside Table (4). Additionally, the orientations of each of the four instrument gauges for each station are listed in Table (5).

Table 3. List of station names, location, and local geology associated with a sub-set of the Anza Seismic Network in southern California. Except for station TRO, all the stations are located at an elevation of 1321m ± 200m. Since the smallest wavelengths of interest are on the order of 500 times larger than the differences in elevation, the array is assumed to have uniform elevation. Information from *Vernon* [1989].

Station Name	Location (Lat. / Lon. / Elev.)	Geology
BZN	33.4915° / -116.6662° / 1314m	Decomposed tonalite, part of the Coahuila Valley Pluton
CRY	33.5653° / -116.7365° / 1151m	Tonalite, part of the Coahuila Valley Pluton
FRD	33.4947° / -116.6014° / 1176m	Tonalite, part of the Coahuila Valley Pluton
KNW	33.7141° / -116.7111° / 1521m	Tonalite, part of the San Jacinto Mountain Intrusive Complex
LVA2	33.3492° / -116.5694° / 1439m	Granodiorite, part of the Collins Valley Pluton
PFO	33.6116° / -116.4586° / 1288m	Decomposed quartz diorite-granodiorite, part of the Haystack Pluton
RDM	33.6299° / -116.8470° / 1390m	Larded gneiss, part of the Coahuila Valley Pluton
SND	33.5519° / -116.6121° / 1396m	Decomposed tonalite, part of the Coahuila Valley Pluton
TRO	33.5234° / -116.4248° / 2655m	Quartz diorite-granodiorite, part of the Santa Rosa Pluton
WMC	33.5736° / -116.6734° / 1280m	Alluvium and sediment, approximately 60m thick

Table 4. List of station names, location and local geology associated with a sub-set of the PBO borehole GTSM instruments inside the Anza Seismic Network. All seven borehole GTSM instruments were installed on dates between 2006 June 10 and 2007 January 28. Information from *UNAVCO* [2010].

Station Name	Location (Lat. / Lon. / Elev. / Install Depth)	Borehole Geology / P-wave Velocity at Install Depth
B081	33.7111° / -116.7142° / 1467m / 243m	Granite ~5500 m/s
B082	33.5982° / -116.5960° / 1375m / 243m	Gneiss ~4000 m/s
B084	33.6116° / -116.4564° / 1271m / 159m	Granite ~5000 m/s
B086	33.5575° / -116.5310° / 1392m / 240m	Granite ~4800 m/s
B087	33.4955° / -116.6027° / 1139m / 161m	Granite ~5000 m/s
B088	33.3750° / -116.6205° / 1404m / 160m	Granite/Gneiss ~4400 m/s
B089	33.5999° / -116.5961° / 1362m / 133m	Folded Gneiss ~4000 m/s

Table 5. List of orientation angles associated with each of the four gauges built into the GTSM instrument. The angles are measured clockwise from north (i.e., 0°). The orientation of all the gauges relative to Channel 0 are the same – Channel 1 is 60° counter-clockwise from Channel 0, Channel 2 is 120° counter-clockwise from Channel 0, and Channel 3 is 150° counter-clockwise from Channel 0. Information from *UNAVCO* [2010].

Station Name	Channel 0 Orientation	Channel 1 Orientation	Channel 2 Orientation	Channel 3 Orientation
B081	3.2°	303.2°	243.2°	213.2°
B082	324.8°	264.8°	204.8°	174.8°
B084	197°	137°	77°	47°
B086	316.5°	256.5°	196.5°	166.5°
B087	340.7°	280.7°	220.7°	190.7°
B088	216.2°	156.2°	96.2°	66.2°
B089	291°	231°	171°	141°

The raw broadband seismic velocity data and broadband GTSM instrument data are initially corrected to remove the response of each instrument (see Table 6 and 7). The broadband data are then low-pass filtered and decimated to one sample per second before cutting the traces to equal length, removing the mean, and applying a two-pole Butterworth band-pass filter in both the forward and backward direction (i.e., acausal). The low-frequency cut-off used in the band-pass filter depends on the signal-to-noise ratio, which is related to both the size of the teleseismic event and its relative distance from southern California (see Table 8). All data were band-pass filtered between 0.01 and 0.03 Hz, in order to avoid low-frequency noise on the low-end and spatial aliasing on the high-end, during the process of deriving the necessary strain information from the seismic data. The "cleaned" seismic velocity data are then integrated once in the frequency domain to obtain the ground displacements. Size, location, and other information associated with the teleseismic events used in this study are tabulated in Table (8). Table (9) and Table (10) indicate whether data were available for each station-event pair during the calibration process.

Methods

In continuum mechanics, the strain tensor (**ε**) describes the deformation resulting from differential motion within a body. For three-dimensional (3D) deformation, the tensor is a symmetric 3x3 square matrix described by spatial derivatives of the displacement field (**u**) with respect to the coordinate system (**x**) and is defined by

$$\varepsilon_{ij} = \frac{1}{2}\left(\frac{\partial u_i}{\partial x_j} + \frac{\partial u_j}{\partial x_i} + \frac{\partial u_k}{\partial x_i}\frac{\partial u_k}{\partial x_j} \right) \quad , \tag{28}$$

where i, j, and k are indices that range from 1 to 3. However, if the displacement gradients are small, then the higher order term ($\partial u_k/\partial x_i \cdot \partial u_k/\partial x_j$), in Equation (28), is often neglected. Following *Frank* [1966] and *Hart et al.* [1996], the formation strain (**s**) describes 2D horizontal deformation through the areal strain (e_a), the differential normal

Table 6. Instrument response information corresponding to the broadband Anza seismic instruments used in this study. Removing the instruments response from the raw broadband data yields the corrected velocity time-series in units of meters per second (m/s). Information from *IRIS* [2010].

Stations	Zeros	Poles	Gain Constant
BZN KNW	0.00 + i0.00 0.00 + i0.00 -15.15 + i0.00 -318.6 + i401.2 -318.6 – i401.2	-0.037 + i0.037 -0.037 – i0.037 -15.99 + i0.00 -417.1 + i0.00 -187.2 + i0.00 -100.9 + i401.9 -100.9 – i401.9 -7454.0 + i7142.0 -7454.0 – i7142.0	+3.614501958E+21
CRY FRD LVA2 PFO RDM SND TRO WMC	0.00 + i0.00 0.00 + i0.00 -15.15 + i0.00 -318.6 + i401.2 -318.6 – i401.2	-0.037 + i0.037 -0.037 – i0.037 -15.99 + i0.00 -417.1 + i0.00 -187.2 + i0.00 -100.9 + i401.9 -100.9 – i401.9 -7454.0 + i7142.0 -7454.0 – i7142.0	+4.535642826E+21

Table 7. Instrument response information corresponding to the PBO borehole GTSM instruments. Removing the instruments response from the raw broadband data yields the corrected strain time-series in units of meters per meter (m/m). Information from *IRIS* [2010].

Stations	Zeros	Poles	Gain Constant
B081			
B082			
B084			
B086	0.00 + i0.00	0.00 + i0.00	+1.00E+10
B087			
B088			
B089			

Table 8. Teleseismic waves from 20 events were used to perform strainmeter calibration. The date, location, and magnitude are indicated for each of the events. The approximate great circle propagation distance between the source and array network, in addition to the approximate wave propagation direction across the array, are also indicated.

EQ No.	Date (YYYY / MM / DD)	Location (Lat. / Lon. / Depth)	EQ Mag.	Prop. Dist.	Prop. Azi.
1	2007 / 01 / 13	46.24° / 154.52° / 10 km	8.1	7707 km	131°
2	2007 / 08 / 01	-15.60° / 167.68° / 120 km	7.2	9400 km	69°
3	2007 / 08 / 15	-13.39° / -76.60° / 39 km	8.0	6621 km	314°
4	2007 / 09 / 02	-11.61° / 165.76° / 35 km	7.2	9414 km	74°
5	2007 / 09 / 10	2.97° / -77.96° / 15 km	6.8	5309 km	302°
6	2007 / 09 / 28	22.01° / 142.67° / 260 km	7.5	9985 km	114°
7	2007 / 11 / 14	-22.25° / -69.89° / 40 km	7.7	7713 km	315°
8	2007 / 11 / 16	-2.31° / -77.84° / 122 km	6.8	5717 km	307°
9	2007 / 11 / 29	14.94° / -61.27° / 156 km	7.4	5976 km	276°
10	2007 / 12 / 09	-26.00° / -177.51° / 152 km	7.8	8848 km	52°
11	2008 / 04 / 09	-20.07° / 168.89° / 33 km	7.3	9492 km	65°
12	2008 / 07 / 05	53.88° / 152.89° / 632 km	7.7	7611 km	139°
13	2008 / 11 / 24	54.20° / 154.32° / 492 km	7.3	7495 km	139°
14	2009 / 03 / 19	-23.04° / -174.66° / 31 km	7.6	8474 km	53°
15	2009 / 05 / 28	16.73° / -86.22°/ 19 km	7.3	3583 km	294°
16	2009 / 09 / 29	-15.49° / -172.10° / 18 km	8.1	7821 km	57°
17	2009 / 10 / 07	-13.01° / 166.51° / 45 km	7.7	9399 km	72°
18	2009 / 10 / 07	-12.52° / 166.38° / 35 km	7.8	9393 km	72°
19	2010 / 01 / 12	18.44° / -72.57° / 13 km	7.0	4708 km	280°
20	2010 / 02 / 27	-36.12° / -72.90° / 22 km	8.8	8708 km	326°

Table 9. In some cases, data corresponding to a teleseismic event was not available for all Anza Seismic Array stations used in this study. Stations that did (or did not) have data for a particular event are indicated with a "●" (or a "○").

EQ No.	BZN	CRY	FRD	KNW	LVA2	PFO	RDM	SMER	SND	TRO	WMC
1	○	●	●	●	●	●	●	○	●	●	●
2	●	●	●	●	●	●	●	●	●	●	●
3	●	●	●	●	●	●	●	○	●	●	●
4	●	●	●	●	●	●	●	●	●	●	●
5	●	●	●	●	●	●	●	○	●	○	●
6	●	●	●	●	●	●	●	○	●	●	●
7	●	●	●	●	●	●	●	○	○	○	●
8	●	●	●	●	●	●	●	○	○	○	●
9	●	●	●	●	●	●	●	●	●	○	●
10	●	●	●	●	●	●	●	●	●	●	●
11	○	●	●	●	●	●	●	○	●	●	●
12	●	●	●	●	●	●	●	●	●	●	●
13	●	●	●	●	●	●	○	○	●	●	●
14	●	●	●	●	●	●	●	●	●	●	●
15	●	●	●	●	●	●	○	●	●	●	●
16	●	●	●	●	●	●	●	●	●	●	●
17	●	●	●	●	●	●	●	●	●	●	●
18	●	●	●	●	●	●	●	●	●	●	●
19	●	●	●	●	●	○	●	●	●	●	●
20	●	●	●	●	●	●	●	●	●	●	●

Table 10. In some cases, data corresponding to a teleseismic event was not available for all PBO GTSM stations inside the Anza Seismic Array used in this study. Stations that did (or did not) have data for a particular event are indicated with a "●" (or a "○").

EQ No.	B081	B082	B084	B086	B087	B088	B089
1	○	●	●	○	●	○	○
2	●	●	●	●	●	●	●
3	●	●	●	●	●	●	●
4	●	●	●	○	●	●	●
5	○	●	●	●	●	●	●
6	●	●	●	●	○	●	●
7	●	●	●	●	○	●	●
8	●	●	●	●	●	●	●
9	●	●	○	○	●	●	●
10	○	●	○	○	●	●	●
11	●	○	●	○	●	●	●
12	○	○	●	●	●	●	●
13	●	●	●	●	●	●	●
14	●	●	●	●	●	●	●
15	○	●	●	●	●	●	●
16	●	●	●	●	●	●	●
17	●	●	●	●	●	○	●
18	●	●	●	●	●	○	●
19	●	●	●	●	●	●	●
20	●	●	●	●	●	●	●

strain (γ_1), and the shear strain (γ_2). The formation strain is related to the components of the strain tensor by

$$\mathbf{s} = \begin{bmatrix} e_a \\ \gamma_1 \\ \gamma_2 \end{bmatrix} = \begin{bmatrix} \varepsilon_{11} + \varepsilon_{22} \\ \varepsilon_{11} - \varepsilon_{22} \\ \varepsilon_{12} + \varepsilon_{21} \end{bmatrix} \quad . \tag{29}$$

Process for Estimating the Formation Strain using Seismic Data

The result of Chapter (2) was that the spatial displacement gradients estimated using the method based on Spatial Gradient Analysis (i.e., Method 4) were consistently more accurate, especially in the frequency band necessary for strainmeter calibration in this study. However, this was the case only when the spatial displacement gradients were calculated at specific seismometer station locations. In order to ensure the accuracy of the spatial displacement gradients at locations between broadband seismometers, it is necessary to incorporate additional methods, such as interpolation-based methods (i.e., Methods 2 and 3 discussed in the previous chapter).

In this study, we developed a 4-step process for obtaining accurate displacement gradient estimates at PBO GTSM station locations inside the Anza Seismic Network. The first step consisted of identifying the propagation slowness and propagation direction of the major seismic phases as they moved across the seismic network. We chose to implement a time-domain cross-correlation method, similar to that described in Chapter (2). The time-domain cross-correlation method consisted of identifying and picking windows around major seismic phases, and then solving for the propagation slowness and propagation azimuth that resulted in the best alignment of the seismograms. This process was repeated for all the seismic phases that appeared to yield the largest levels of strain.

The second step consisted of calculating the radial displacement gradients at every instant in time, within a selected time window, at each station using formulation similar to Method (4) from the previous chapter, i.e.,

$$\begin{bmatrix} \left.\frac{\partial u_x}{\partial x}\right|_{x^r} & \left.\frac{\partial u_x}{\partial y}\right|_{y^r} \\ \left.\frac{\partial u_y}{\partial x}\right|_{x^r} & \left.\frac{\partial u_y}{\partial y}\right|_{y^r} \end{bmatrix} = \begin{bmatrix} \cos\theta & \sin\theta \\ -\sin\theta & \cos\theta \end{bmatrix} \begin{bmatrix} -s_T \dot{u}_T^r \sin\theta & -s_T \dot{u}_T^r \cos\theta \\ -s_R \dot{u}_R^r \sin\theta & -s_R \dot{u}_R^r \cos\theta \end{bmatrix} \quad , \tag{30}$$

where the position $\mathbf{p}^r = \begin{bmatrix} x^r & y^r & z^r \end{bmatrix}$ describes the location of a specific seismometer, s_T and s_R describe the transverse and radial propagation slowness, and θ is the propagation direction.

In the third step, we determine the relative radial distances associated with each of the $i \in \mathbf{M} = \{0,1,\cdots,N-1\}$ seismometers, with respect to the reference GTSM station in question, along the propagation path according to the propagation direction information, derived above, using

$$i \in \mathbf{M} : r_d^i(\theta) = \begin{bmatrix} \sin\theta & \cos\theta \end{bmatrix} \cdot \begin{bmatrix} x^i - x^r & y^i - y^r \end{bmatrix} \quad . \tag{31}$$

In the last step, we construct a matrix equation of the form **WGm** = **Wd**, where

$$\mathbf{G} = \begin{bmatrix} \left(r_d^0\right)^3 & \left(r_d^0\right)^2 & r_d^0 & 1 \\ \left(r_d^1\right)^3 & \left(r_d^1\right)^2 & r_d^1 & 1 \\ \vdots & \vdots & \vdots & \vdots \\ \left(r_d^{N-1}\right)^3 & \left(r_d^{N-1}\right)^2 & r_d^{N-1} & 1 \\ 3\left(r_d^0\right)^2 & 2\left(r_d^0\right) & 1 & 0 \\ 3\left(r_d^1\right)^2 & 2\left(r_d^1\right) & 1 & 0 \\ \vdots & \vdots & \vdots & \vdots \\ 3\left(r_d^{N-1}\right) & 2\left(r_d^{N-1}\right) & 1 & 0 \end{bmatrix} \quad , \qquad \mathbf{m} = \begin{bmatrix} a_T^3 & a_R^3 \\ a_T^2 & a_R^2 \\ a_T^1 & a_R^1 \\ a_T^0 & a_R^0 \end{bmatrix} \quad ,$$

$$\mathbf{d} = \begin{bmatrix} u_R^0 & u_T^0 \\ u_R^1 & u_T^1 \\ \vdots & \vdots \\ u_R^{N-1} & u_T^{N-1} \\ -s_R \dot{u}_R^0 & -s_T \dot{u}_T^0 \\ -s_R \dot{u}_R^1 & -s_T \dot{u}_T^1 \\ \vdots & \vdots \\ -s_R \dot{u}_R^{N-1} & -s_T \dot{u}_T^{N-1} \end{bmatrix} \quad \text{, and}$$

W is a diagonal matrix containing the inversion weights. The reason the weights are important is because the ground displacement amplitudes in the upper half of **d** may be an order of magnitude different than the corresponding displacement gradient amplitudes in the lower half of **d**. Therefore, it is necessary to weight the data matrix such that the ground displacements and the corresponding displacement gradients equally contribute to the final polynomial coefficients. For a GTSM instrument at an arbitrary reference point $\mathbf{p}^r = \begin{bmatrix} x^r & y^r & z^r \end{bmatrix}$ inside the seismic network, the displacement gradients necessary for deriving the formation strains in Equation (29) are found by:

$$\begin{bmatrix} \left.\frac{\partial u_x}{\partial x}\right|_{x^r} & \left.\frac{\partial u_x}{\partial y}\right|_{y^r} \\ \left.\frac{\partial u_y}{\partial x}\right|_{x^r} & \left.\frac{\partial u_y}{\partial y}\right|_{y^r} \end{bmatrix} = \begin{bmatrix} \cos\theta & \sin\theta \\ -\sin\theta & \cos\theta \end{bmatrix} \begin{bmatrix} a_T^1 \sin\theta & a_T^1 \cos\theta \\ a_R^1 \sin\theta & a_R^1 \cos\theta \end{bmatrix} \quad . \tag{32}$$

Process for Performing Strainmeter Calibration

The basic assumption made in *Hart et al.* [1996], is that the strain is small enough to assume that a linear relationship exists between the instrument strain measured by each gauge (**e**) and the reference formation strains ($\mathbf{s^R}$) through the model

$$\mathbf{e} = \mathbf{S}\mathbf{s}^{\mathbf{R}} \quad , \tag{33}$$

where **S** is the calibration matrix. Ideally, if the borehole GTSM instruments required no calibration, the instrument strain measured by each gauge would be related to the formation strain through an orientation matrix (**O**) by

$$\mathbf{e} = \begin{bmatrix} e_1 \\ e_2 \\ e_3 \\ e_4 \end{bmatrix} = \frac{1}{2} \begin{bmatrix} 1 & \cos(2\theta_1) & \sin(2\theta_1) \\ 1 & \cos(2\theta_2) & \sin(2\theta_2) \\ 1 & \cos(2\theta_3) & \sin(2\theta_3) \\ 1 & \cos(2\theta_4) & \sin(2\theta_4) \end{bmatrix} \begin{bmatrix} e_a \\ \gamma_1 \\ \gamma_2 \end{bmatrix} = \mathbf{O}\mathbf{s}^R \quad , \tag{34}$$

where the angles ($\boldsymbol{\theta}$) represent the orientation of the strain-meter gauge measured counter-clockwise from the x_1-axis (i.e., east). However, if the instrument strain measured by each gauge is not exactly related to the reference formation strain through **O**, and there is high confidence that the orientation angles are correct, then it is likely that a linear set of coupling coefficients (**K**) are needed to properly relate what *is* measured by each gauge to what *should* be measured by each gauge. The calibration matrix (**S**) necessary for relating the instrument strain (**e**) to reference strain ($\mathbf{s^R}$), in this case, is the result from taking the product between the orientation matrix (**O**) and the linear coupling coefficients (**K**):

$$\mathbf{O}\mathbf{K}\mathbf{s}^{\mathbf{R}} = \mathbf{S}\mathbf{s}^{\mathbf{R}} = \mathbf{e} \quad . \tag{35}$$

Conceptually, the calibration coefficients in **S** are like an additional instrument response that needs to be removed from the GTSM instrument data in order to yield the "true" formation strain data. We make the assumption that the necessary calibration coefficients in **S** are real, constant through time, and independent of frequency. This assumption allows the necessary calibration coefficients to be found in either the time domain or the frequency domain using the same simple mathematical relationship – namely multiplication/division. In this study, we choose to compute **S** in the frequency domain because the inversion process and the error analysis associated with finding the calibration coefficients are much easier to implement. In the frequency domain (strain terms in the frequency domain are denoted by "^"), the system of linear equations to be solved is:

$$\begin{bmatrix} S_{11} & S_{12} & S_{13} \\ S_{21} & S_{22} & S_{23} \\ S_{31} & S_{32} & S_{33} \\ S_{41} & S_{42} & S_{43} \end{bmatrix} \begin{bmatrix} \hat{e}_a^R(\omega) \\ \hat{\gamma}_1^R(\omega) \\ \hat{\gamma}_2^R(\omega) \end{bmatrix} = \begin{bmatrix} \hat{e}_1(\omega) \\ \hat{e}_2(\omega) \\ \hat{e}_3(\omega) \\ \hat{e}_4(\omega) \end{bmatrix} \quad . \tag{36}$$

The components of the calibration matrix can be found by regularizing the inversion using strain amplitudes corresponding not only to several different frequencies, but to several different strain-inducing events, i.e., earthquakes, as well (explained in Appendix 2). For example, if we consider the formation strain amplitudes for M frequency increments $(\omega_1, \omega_2, \cdots, \omega_M)$ and N strain-inducing events, then we can horizontally concatenate the $M \cdot N$ 3-element column vectors such that:

$$\hat{\mathbf{R}} = \left[\hat{\mathbf{s}}^{\mathbf{R}}_{(1,2,\cdots,M),\,1} \;\; \hat{\mathbf{s}}^{\mathbf{R}}_{(1,2,\cdots,M),\,2} \;\; \cdots \;\; \hat{\mathbf{s}}^{\mathbf{R}}_{(1,2,\cdots,M),\,N} \right] \quad , \tag{37}$$

where, for example:

$$\hat{\mathbf{s}}^{\mathbf{R}}_{(1,2,\cdots,M),N} = \begin{bmatrix} \hat{e}_a^N(\omega_1) & \hat{e}_a^N(\omega_2) & \cdots & \hat{e}_a^N(\omega_M) \\ \hat{\gamma}_1^N(\omega_1) & \hat{\gamma}_1^N(\omega_2) & \cdots & \hat{\gamma}_1^N(\omega_M) \\ \hat{\gamma}_2^N(\omega_1) & \hat{\gamma}_2^N(\omega_2) & \cdots & \hat{\gamma}_2^N(\omega_M) \end{bmatrix} \quad . \tag{38}$$

The same process is repeated for the instrument strain amplitudes for the same M frequency increments and N strain-inducing events (i.e., earthquakes) such that:

$$\hat{\mathbf{C}} = \left[\hat{\mathbf{e}}_{(1,2,\cdots,M),1} \;\; \hat{\mathbf{e}}_{(1,2,\cdots,M),2} \;\; \cdots \;\; \hat{\mathbf{e}}_{(1,2,\cdots,M),N} \right] \quad , \tag{39}$$

and the new system of equations to be solved is:

$$\mathbf{S}\hat{\mathbf{R}} = \hat{\mathbf{C}} \quad . \tag{40}$$

The calibration coefficients in **S** are then found by performing the following set of operations:

$$\mathbf{S} = \hat{\mathbf{C}}\hat{\mathbf{C}}^{T*}\left(\hat{\mathbf{R}}\hat{\mathbf{C}}^{T*}\right)^{-1} \quad , \tag{41}$$

where "T*" denotes the complex conjugate transpose.

Our original assumption that **S** is both real and constant means that an appropriate estimate of **S** may be applied in either the time or frequency domain. However, when computing the calibration coefficients in the frequency domain, it is possible that consistent timing (or phase) errors between the instrument strain and the reference strain will cause **S** to be complex. In order to ensure that no erroneous timing (or phase) errors are introduced into the calibration coefficients, it is important to not only compute the reference strains accurately, but also compute **S** for a large number and diverse set of teleseismic events.

Results and Analysis

The results in this section will focus on PBO GTSM station B081, because it is the only borehole instrument (of the 7 in this study) that has a set of calibration coefficients derived through independent analysis (see *Roeloffs* [2010]). A brief overview of the results from the remaining 6 borehole instruments will follow. The results in each section will focus on three issues: 1) alignment and phase errors, 2) the derived calibration coefficients, and 3) anisotropic-coupling (or cross-coupling) versus isotropic-coupling models.

Alignment errors were calculated in two different ways. The first method involves a process where the "cleaned" instrument gauge strains were converted to formation strains, using a variety of increments to the advertised orientation angles, then normalized before comparing them to the normalized, "cleaned" reference formation strains. The increment angle that resulted in the smallest difference between the normalized, adjusted instrument formation strains and the normalized reference formation strains were stored for each teleseismic event. Finally the mean and standard deviation of all the estimated angle adjustments for a specific station were computed. The list of the adjustment angles associated with each teleseismic event and borehole instrument are list in Table (11). The second method involves a process where the orientation angles are incrementally changed until the trace of $\mathbf{K} = \text{inv}(\mathbf{O}^T \mathbf{O})\, \mathbf{O}^T \mathbf{S}$ is maximized, where $\mathbf{K}$ is the coupling model.

The coupling model ($\mathbf{K}$) is an important consideration during the calibration process because it identifies the nature of the instrument coupling inside the borehole. If the instrument were isotropically coupled inside the borehole, then each component of the formation strain derived from the borehole instrument would scale by a constant. However, if the instrument were anisotropically coupled inside the borehole, then each component of the formation strain derived from the borehole instrument would scale by some linear combination of the reference formation strains. The default calibration

Table 11. Angle adjustments (a), measured counter-clockwise, for each station were derived from each teleseismic event based on the alignment fit between the normalized instrument formation strains with the normalized reference formation strains. Also, the phase angles (b) necessary to promote alignment are indicated to the right of the back-slash. Stations that did not have data for a particular event are indicated with a "○".

EQ No.	B081 a°/ b°	B082 a°/ b°	B084 a°/ b°	B086 a°/ b°	B087 a°/ b°	B088 a°/ b°	B089 a°/ b°
1	○	19°/ 13°	22°/ 12°	○	-47°/ 10°	○	○
2	10°/ 14°	14°/ 11°	26°/ 7°	0°/ 10°	-45°/ 11°	10°/ 2°	-4°/ 9°
3	4°/ 6°	22°/ 10°	24°/ 6°	5°/ 8°	-50°/ 0°	-19°/ 9°	-7°/ 8°
4	8°/ 13°	15°/ 12°	22°/ 10°	○	-45°/ 11°	9°/ 3°	-6°/ 10°
5	○	18°/ 5°	21°/ 7°	5°/ 17°	-47°/ 8°	-30°/ 7°	-13°/ 8°
6	3°/ 16°	20°/ 9°	24°/ 9°	5°/ 17°	○	-21°/ 1°	-12°/ 10°
7	2°/ 14°	21°/ 8°	25°/ 8°	6°/ 7°	○	-24°/ 8°	-13°/ 8°
8	1°/ 4°	18°/ 5°	23°/ 4°	3°/ 7°	-44°/ 7°	-19°/ 7°	-8°/ 8°
9	4°/ 0°	16°/ 3°	○	○	-44°/ 7°	-15°/ 5°	-10°/ 4°
10	○	16°/ 0°	○	○	-49°/ 1°	-19°/ 0°	-5°/ 2°

CONTINUED ON NEXT PAGE

Table 11. (cont.) Angle adjustments (a), measured counter-clockwise, for each station were derived from each teleseismic event based on the alignment fit between the normalized instrument formation strains with the normalized reference formation strains. Also, the phase angles (b) necessary to promote alignment are indicated to the right of the back-slash. Stations that did not have data for a particular event are indicated with a "O".

EQ No.	B081 a°/ b°	B082 a°/ b°	B084 a°/ b°	B086 a°/ b°	B087 a°/ b°	B088 a°/ b°	B089 a°/ b°
11	11°/ 7°	O	28°/ 9°	O	-45°/ 12°	10°/ 7°	-3°/ 12°
12	O	O	22°/ 9°	4°/ 17°	-51°/ 11°	-27°/ 12°	-14°/ 9°
13	3°/ 9°	21°/ 9°	21°/ 8°	2°/ 6°	-51°/ 10°	-19°/ 9°	-8°/ 9°
14	9°/ 14°	17°/ 11°	26°/ 10°	0°/ 10°	-57°/ 15°	13°/ 9°	-4°/ 8°
15	O	18°/ 12°	23°/ 10°	3°/ 33°	-49°/ 7°	18°/ 7°	-9°/ 11°
16	16°/ 4°	19°/ 10°	29°/ 6°	6°/ 9°	-53°/ 8°	15°/ 4°	0°/ 6°
17	11°/ 13°	18°/ 21°	26°/ 17°	2°/ 16°	-47°/ 19°	O	-3°/ 21°
18	11°/ 13°	18°/ 21°	26°/ 17°	2°/ 16°	-47°/ 19°	O	-3°/ 21°
19	3°/ 4°	15°/ 3°	22°/ 9°	1°/ 6°	-43°/ 5°	-10°/ 5°	-10°/ 6°
20	4°/ 3°	22°/ 5°	25°/ 2°	6°/ 4°	-52°/ -4°	-18°/ 5°	-5°/ 6°
(a) MEAN ± STD	6.6° ± 4.4°	18° ± 2.4°	25° ± 3.5°	3.3° ± 2.0°	-48° ± 3.8°	-10° ± 16°	-7.3° ± 4°
(b) MEAN ± STD	8.9° ± 5.2°	9.3° ± 5.6°	8.9° ± 3.7°	12° ± 5.5°	8.7° ± 5.9°	5.8° ± 3.2°	9.3° ± 4.9°

coefficients provided by PBO assumes an isotropic coupling model for all borehole instruments in the network, which correspond to the following relationship:

$$\mathbf{e} = \begin{bmatrix} e_1 \\ e_2 \\ e_3 \\ e_4 \end{bmatrix} = \frac{1}{2} \begin{bmatrix} 1 & \cos(2\theta_1) & \sin(2\theta_1) \\ 1 & \cos(2\theta_2) & \sin(2\theta_2) \\ 1 & \cos(2\theta_3) & \sin(2\theta_3) \\ 1 & \cos(2\theta_4) & \sin(2\theta_4) \end{bmatrix} \begin{bmatrix} 1.5 & 0 & 0 \\ 0 & 3 & 0 \\ 0 & 0 & 3 \end{bmatrix} \begin{bmatrix} e_a \\ \gamma_1 \\ \gamma_2 \end{bmatrix} = \mathbf{OKs}^R = \mathbf{Ss}^R \quad . \qquad (42)$$

The validity of an isotropic coupling model is tested for each borehole instrument below.

Calibration for PBO GTSM instrument: B081

An example of the level of disagreement between the "cleaned" raw instrument formation strain and the "cleaned" reference formation strain is illustrated in Figure (22). The amplitudes and phase associated with both areal strain estimates are remarkably similar. When we normalize the "cleaned" raw instrument formation strain and compare to the normalized reference formation strain, there is very close agreement with the areal strain and reasonable agreement with the shear strain (see Figure 23). However, the amplitudes and phase associated with the differential normal strain are quite different.

There are 1162 sets of 4 complex instrument gauge strain and 3 complex reference formation strain amplitudes from 15 teleseismic events that were compiled together, inside the frequency band between 0.01 and 0.03 Hz, before inverting for the calibration coefficients. The normalized probability density function in Figures (24) and (25) illustrate the real and imaginary components, respectively, resulting from repeatedly (1000 realizations) selecting a random subset of 58 (~5%) of the 1162 sets of instrument and reference strain amplitudes before inverting for the calibration

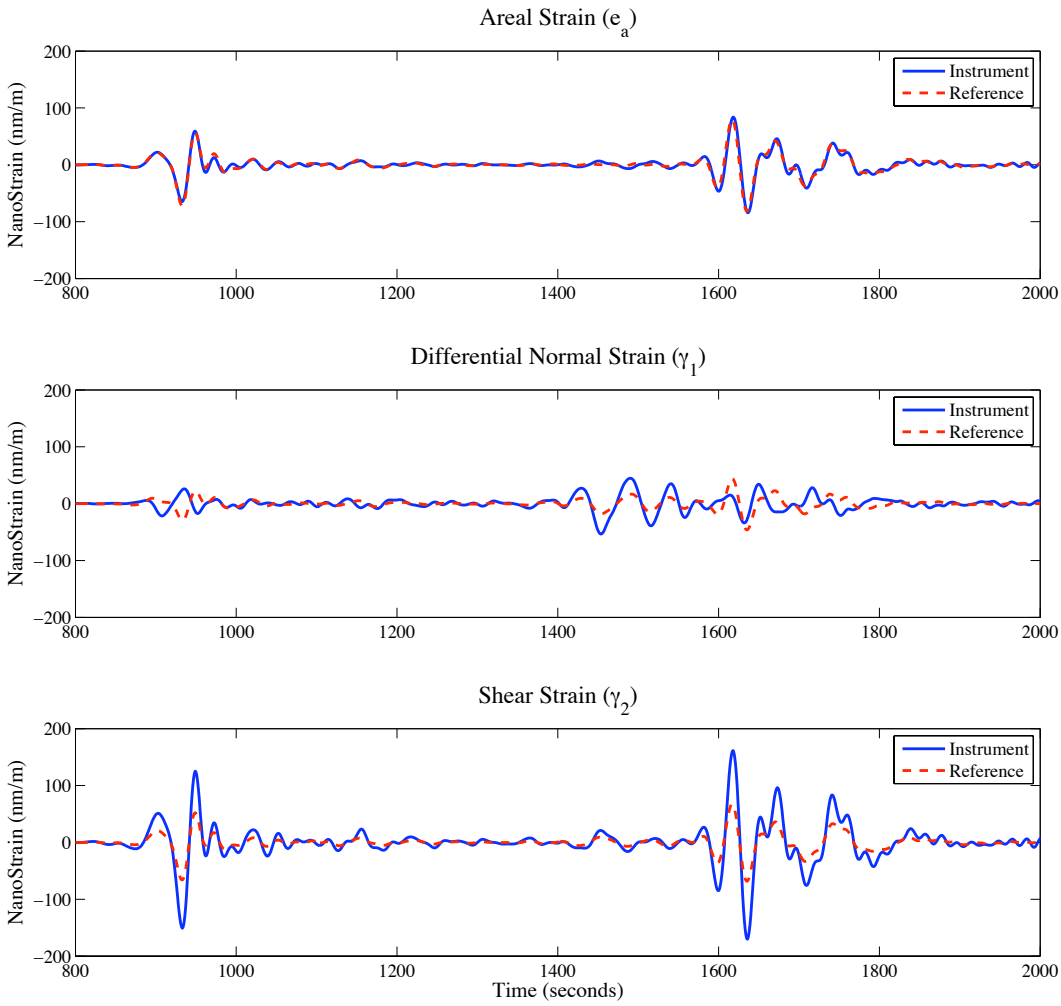

Figure 22. Example of the difference between the "cleaned" instrument formation strain at B081 and the "cleaned" reference formation strain derived from seismic data at the same GTSM location. Formation strain in the above figure corresponds to the 29 September 2009 M8.1 Samoa Island earthquake band-pass filtered between 0.01 Hz and 0.03 Hz with a 4-pole Butterworth acausal filter. The vertical axis (i.e., *y*-axis) limits were set to ± 200 nm/m in order to highlight the consistencies/inconsistencies between the two measurements of the formation strain.

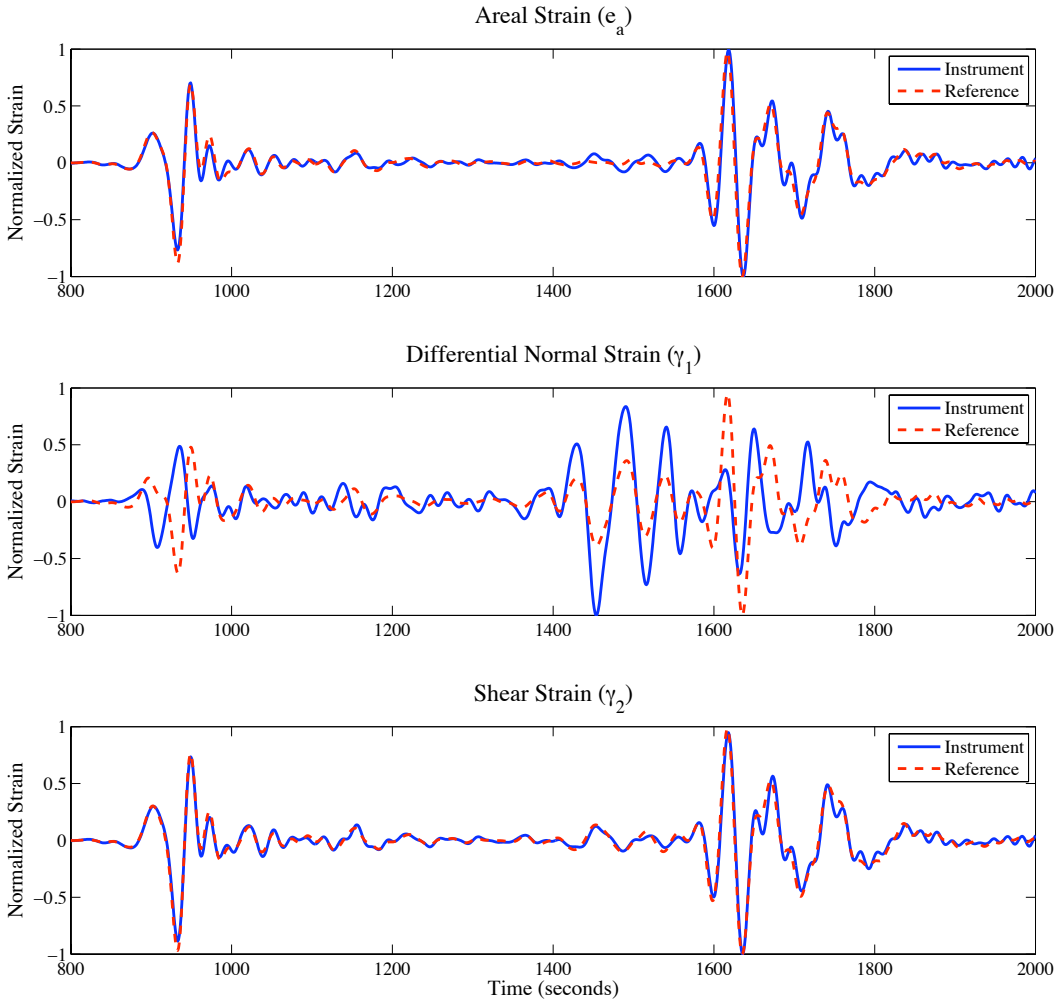

Figure 23. Example of the difference between the normalized, "cleaned" instrument formation strain at B081 and the normalized, "cleaned" reference formation strain derived from seismic data at the same GTSM location. Formation strain in the above figure corresponds to the 29 September 2009 M8.1 Samoa Island earthquake band-pass filtered between 0.01 Hz and 0.03 Hz with a 4-pole Butterworth acausal filter.

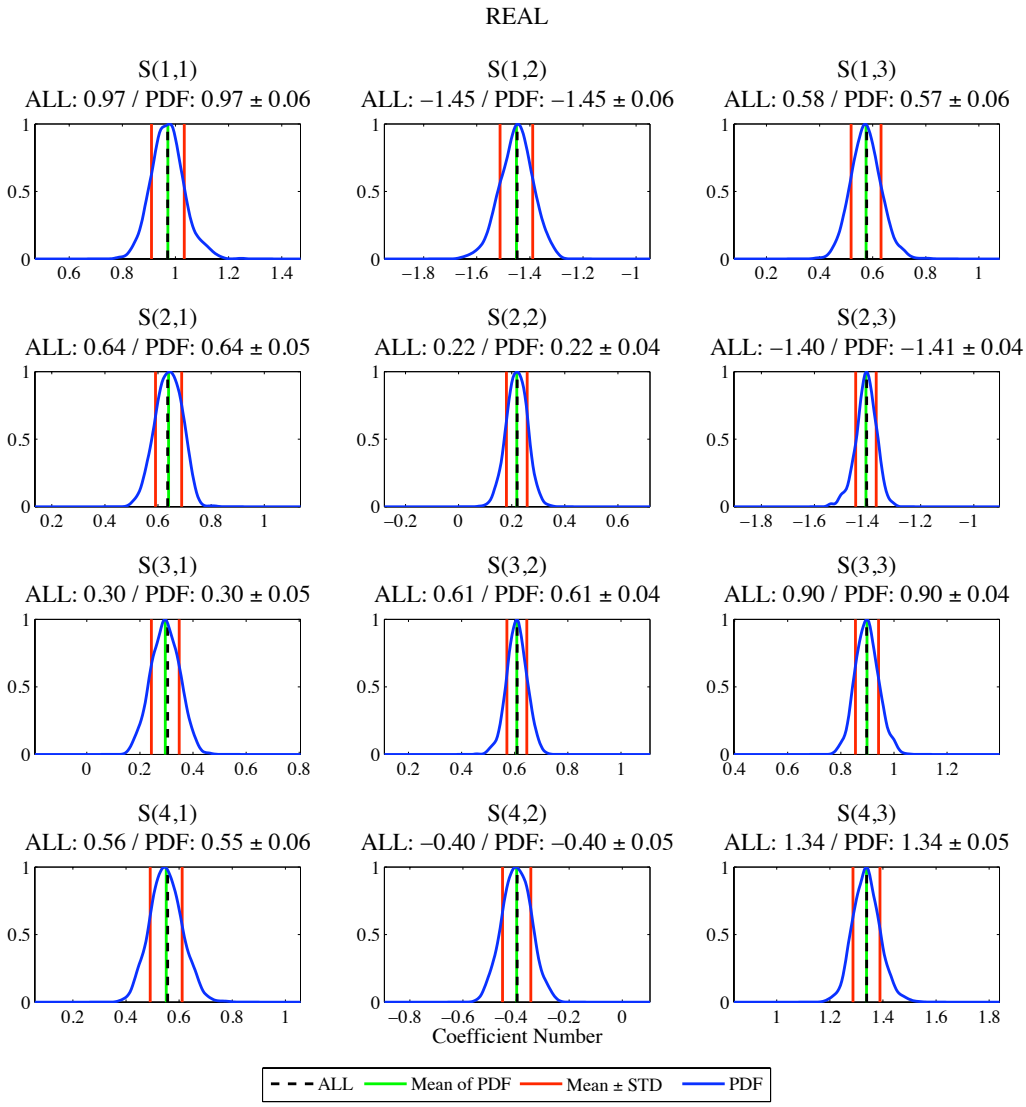

Figure 24. Illustration of the normalized probability density functions (PDF) associated with the REAL calibration coefficients derived for B081 using seismic data. The normalized PDF (BLUE line) about each coefficient value is the result from randomly selecting 58 (~5%) of the available 1162 sets of instrument and reference strain amplitudes, performing an inversion (similar to Equation 41) using these data, and repeating (1000 iterations total). The mean of the normalized PDF is indicated by the GREEN solid line, while the standard deviation about the mean is indicated by RED solid lines. The result from inverting all 1162 sets of strain information is indicated by the BLACK dashed line.

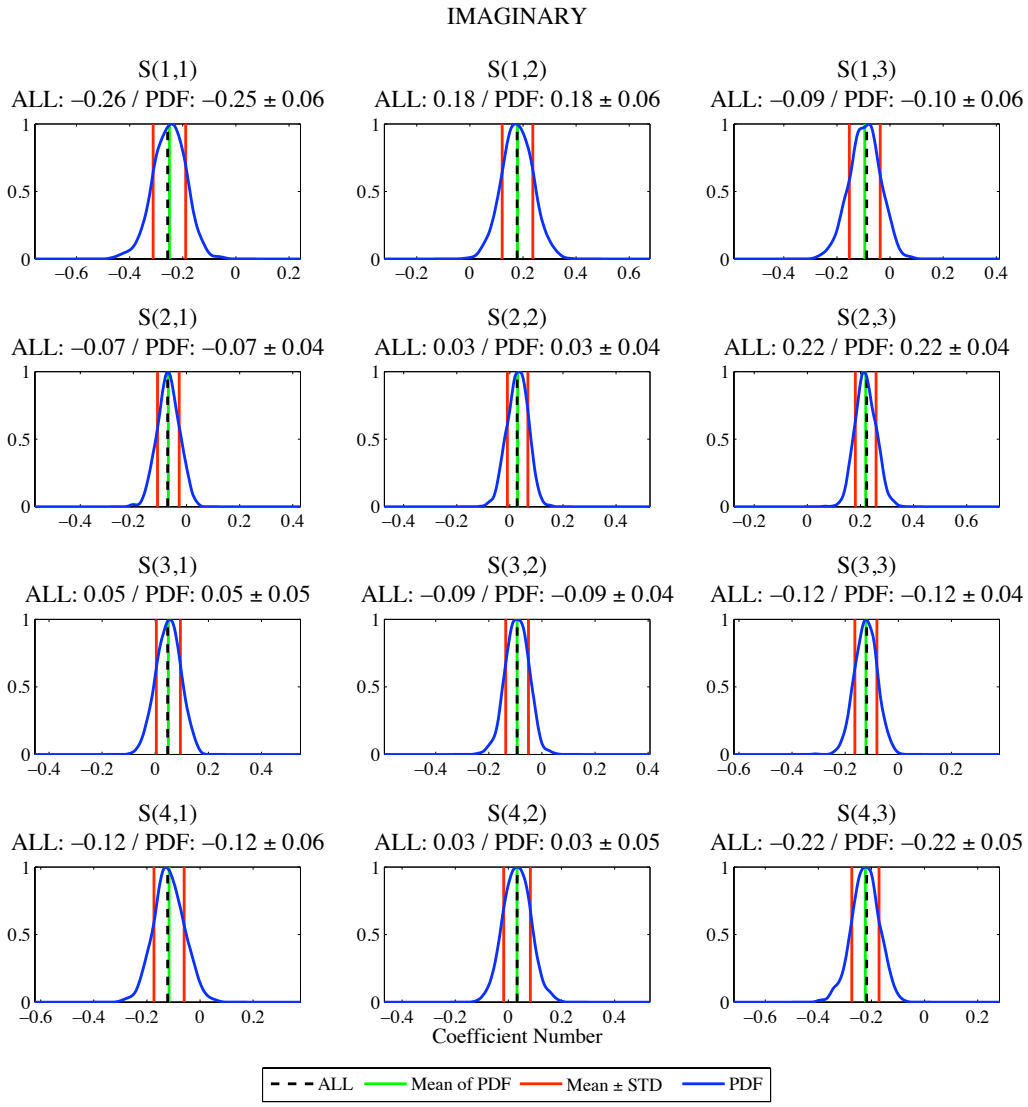

Figure 25. Illustration of the normalized probability density functions (PDF) associated with the IMAGINARY calibration coefficients derived for B081 using seismic data. The normalized PDF (BLUE line) about each coefficient value is the result from randomly selecting 58 (~5%) of the available 1162 sets of instrument and reference strain amplitudes, performing an inversion (similar to Equation 41) using these data, and repeating (1000 iterations total). The mean of the normalized PDF is indicated by the GREEN solid line, while the standard deviation about the mean is indicated by RED solid lines. The result from inverting all 1162 sets of strain information is indicated by the BLACK dashed line.

coefficients. The calibration coefficients, along with their standard deviation, are summarized in Table (12).

In addition to the calibration process, we attempted to derive the alignment error associated with B081 using the second method described above. We found that the second method yielded an alignment error of 6.8 degrees (compare to 6.6 degrees derived from the first method). After properly accounting for the alignment error we observed that the diagonal elements of the coupling model are very similar to those in the nominal isotropic coupling model provided by PBO (see Table 13). However, there are also significant cross-coupling terms, which indicate that an isotropic coupling model is not valid for station B081. Other evidence that an isotropic coupling model is not valid is illustrated in Figure (26), where the cross-coupling terms in Table (13) were neglected and the strainmeter result calibrated assuming an isotropic coupling model. Poor fit is clearly observed between the differential normal strain traces.

Figure (27) illustrates a remarkable finding that the coefficients necessary to calibrate B081 over the past two years are reasonably similar. The point at each group number, in this figure, represents the calibration coefficients derived for a specific set of 4 teleseismic events. Group number 1 consists of events 2, 3, 4, and 6; Group number 2 consists of events 3, 4, 6, and 7; etc. according to the data coverage listed in Table (10). To further illustrate the consistency of the derived calibration coefficients, we calibrated events 3 and 16 and displayed their results in Figures (28) and (29) to demonstrate that the calibration coefficients in Table (12) are in fact stable over the last 2 years.

Next we compared our calibration result with the result obtained in *Roeloffs* [2010], which is listed in Table (14). Although the calibration coefficients are very similar, only 1 of the calibration coefficients predicted by earth tide strains fall within one standard deviation of the result presented here. In Figure (30), we illustrate the relative consistency between using our result and the result obtain in *Roeloffs* [2010] and find reasonably good agreement.

Table 12. Derived calibration coefficients for B081 using seismic data. Calibration coefficients with imaginary parts are neglected. The coefficient values are the result from inverting 1162 sets of instrument strain and reference strain amplitudes. The standard deviation associated with each distribution in Figure (24) is indicated to the right of each respective coefficient value. The 4x3 calibration coefficient matrix relates the 3x1 reference formation strain to the 4x1 instrument gauge strain through Equation (36).

B081 Derived Calibration Coefficients	Areal Strain (e_a)	Differential Normal Strain (γ_1)	Shear Strain (γ_2)
Gauge 0	0.963 ± 0.056	-1.455 ± 0.056	0.557 ± 0.051
Gauge 1	0.647 ± 0.041	0.211 ± 0.037	-1.405 ± 0.034
Gauge 2	0.284 ± 0.046	0.609 ± 0.037	0.902 ± 0.041
Gauge 3	0.538 ± 0.056	-0.397 ± 0.053	1.329 ± 0.047

Table 13. Derived coupling model associated with B081. The 3x3 coupling model relates the 3x1 reference formation strain to the 3x1 instrument formation strain through Equation (35). Two standard deviations (a , b) are listed for each coupling coefficient, where "a" is related to the standard deviation in each calibration coefficient presented in the table above and "b" is related to the uncertainty in the alignment correction listed in Table (11).

B081 Derived Coupling Model	Reference Areal Strain (e_a)	Reference Differential Normal Strain (γ_1)	Reference Shear Strain (γ_2)
Instrument Areal Strain (e_a)	1.237 ± (0.040 , 0.000)	-0.344 ± (0.044 , 0.000)	-0.001 ± (0.036 , 0.000)
Instrument Differential Normal Strain (γ_1)	-0.757 ± (0.083 , 0.043)	2.468 ± (0.084 , 0.067)	-0.109 ± (0.075 , 0.429)
Instrument Shear Strain (γ_2)	-0.224 ± (0.084 , 0.118)	-0.247 ± (0.081 , 0.380)	2.797 ± (0.071 , 0.050)

Table 14. Derived calibration coefficients for B081 from *Roeloffs* [2010] using theoretical earth tides (E. T.) as the reference strain. The 4x3 calibration coefficient matrix relates the 3x1 reference formation strain to the 4x1 instrument gauge strain through Equation (36).

B081 Derived Calibration Coefficients (E. T.)	Areal Strain (e_a)	Differential Normal Strain (γ_1)	Shear Strain (γ_2)
Gauge 0	0.84	-1.35	0.18
Gauge 1	0.43	0.62	-0.98
Gauge 2	0.12	0.72	0.73
Gauge 3	0.51	-0.56	0.96

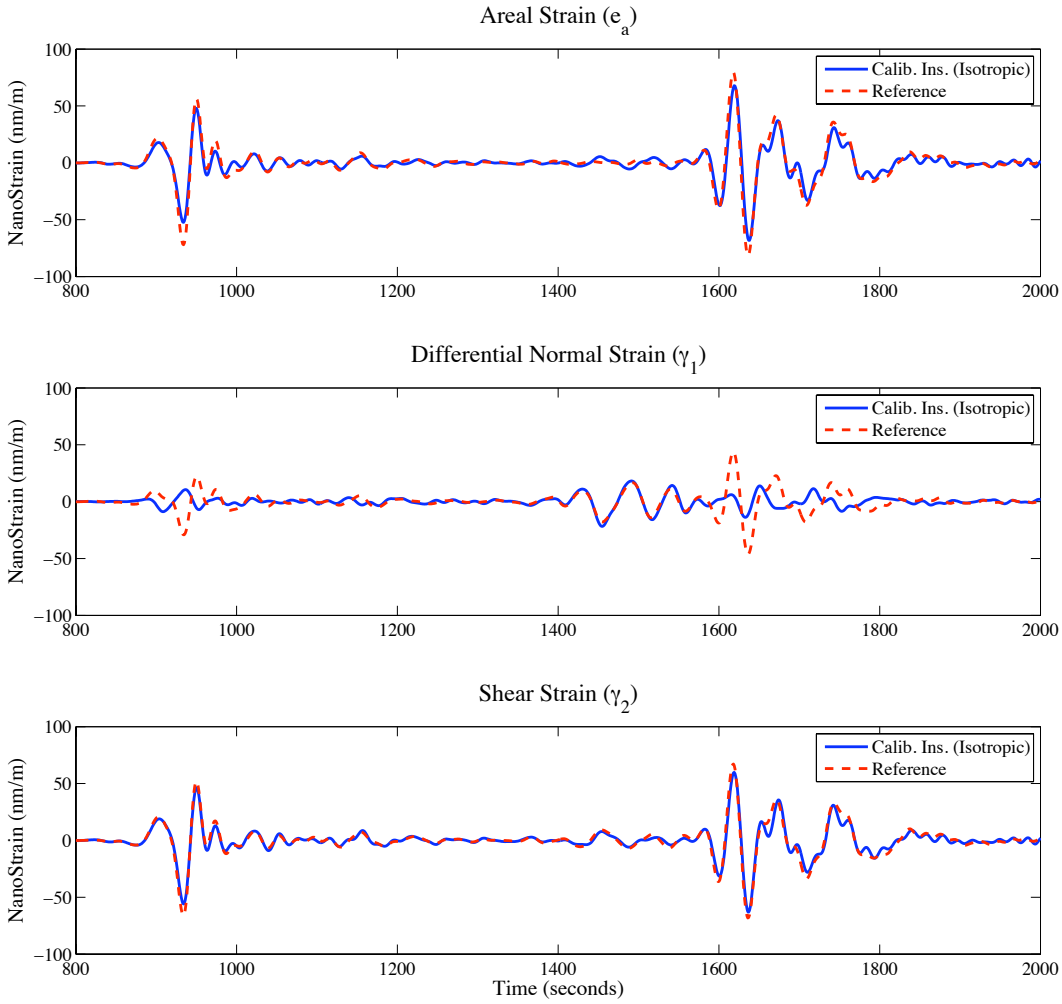

Figure 26. Illustration of the result from calibrating the instrument data associated with event 16 (2009/09/29) recorded by B081 using the calibration coefficients obtained from neglecting the cross-coupling terms in the coefficients listed in Table (13), GREEN solid line. The reference formation strains derived in this study are also illustrated for comparison, RED dashed line.

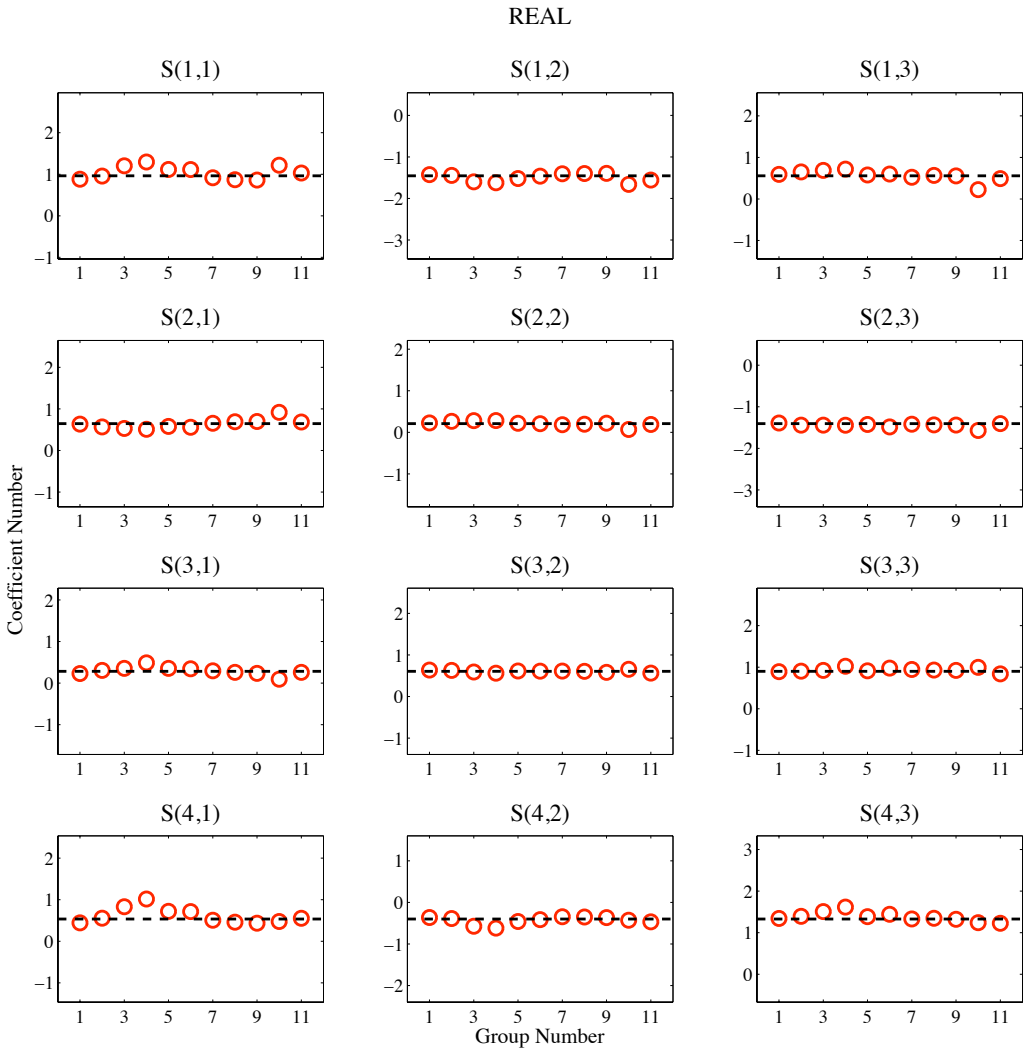

Figure 27. Illustration of the consistency between the REAL calibration coefficients derived for B081 at different periods of time over a 2-year period. The calibration coefficient result from each group (RED circle) represents 332 strain amplitude sets associated with 4 teleseismic events. The groups are organized such that group number 1 represents events 2, 3, 4, and 6; group number 2 represents events 3, 4, 6, and 7; etc. according to data coverage listed in Table (10). The result from inverting all 1162 sets of strain information is indicated by the BLACK dashed line.

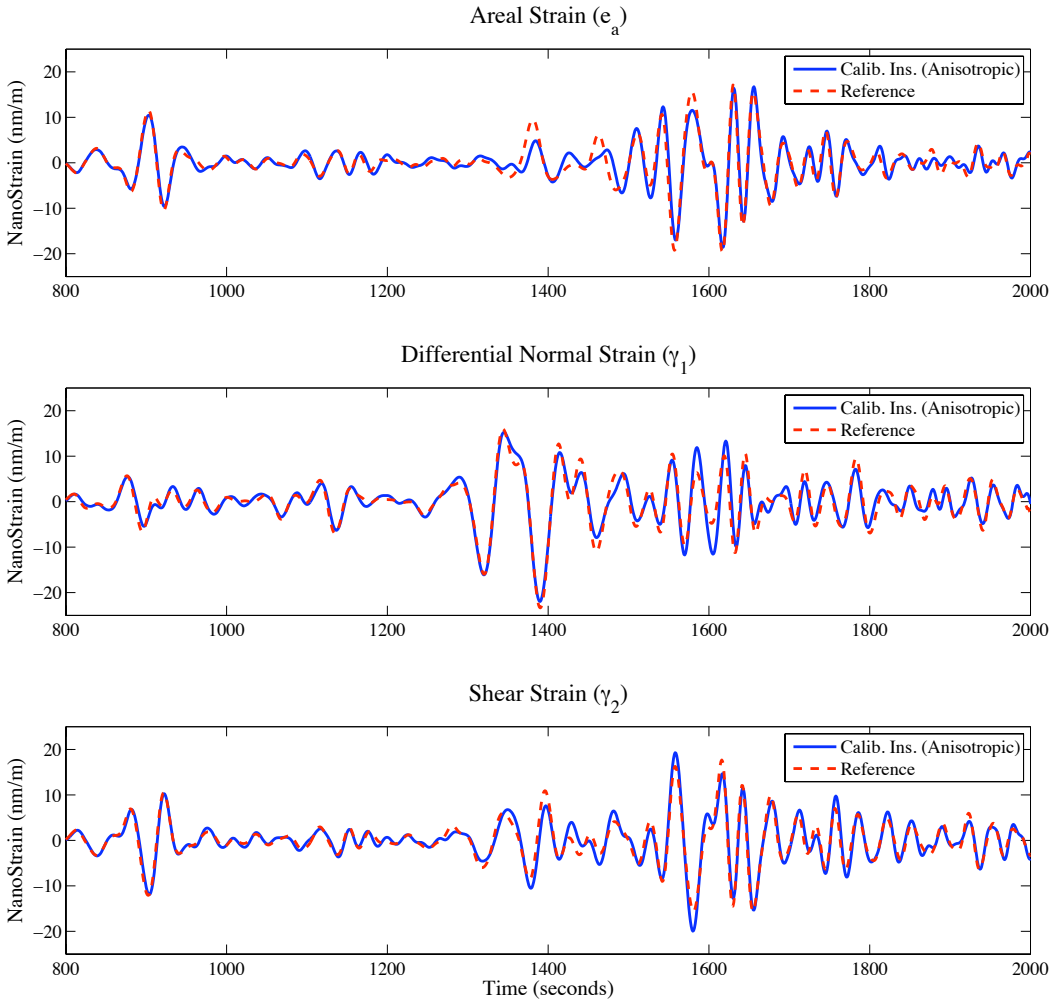

Figure 28. Illustration of the result from calibrating the instrument data associated with event 3 (2007/08/15) recorded by B081 using the calibration coefficients listed in Table (12).

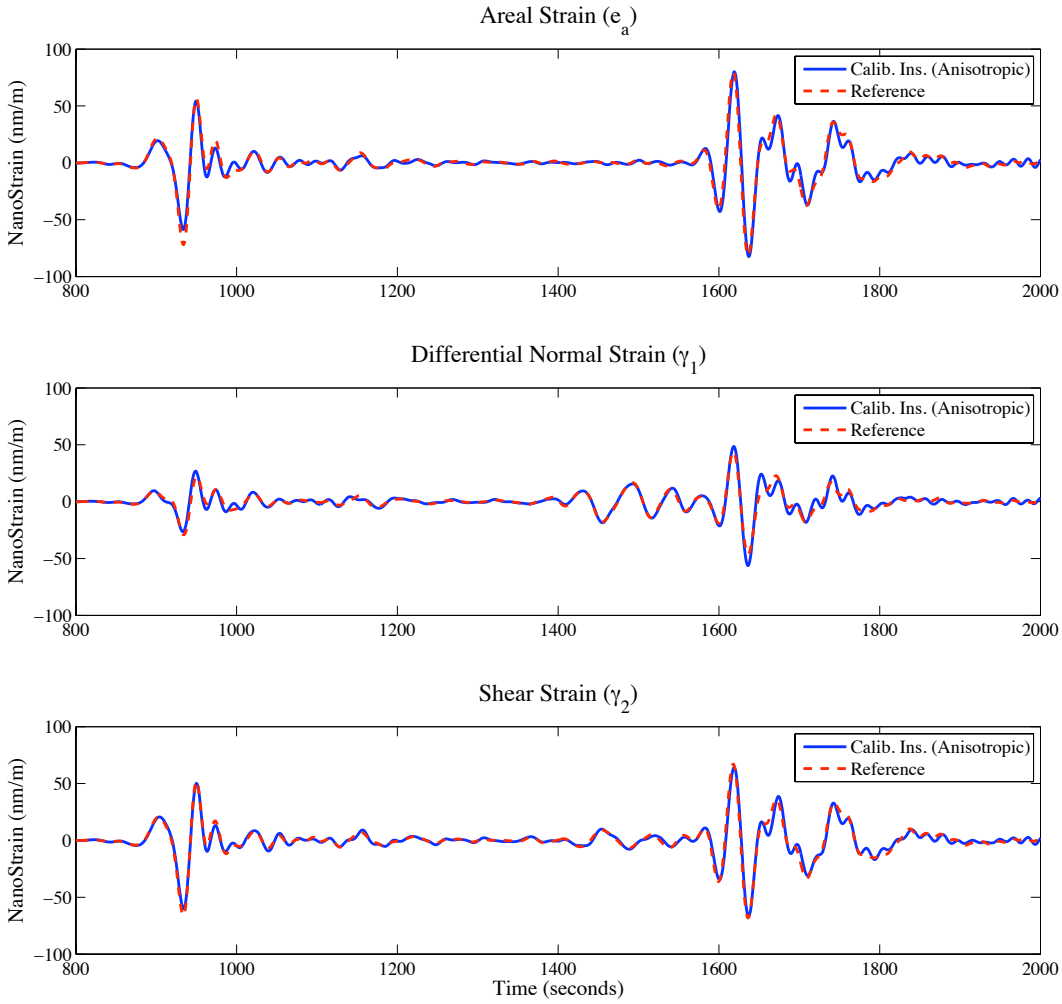

Figure 29. Illustration of the result from calibrating the instrument data associated with event 16 (2009/09/29) recorded by B081 using the calibration coefficients listed in Table (12).

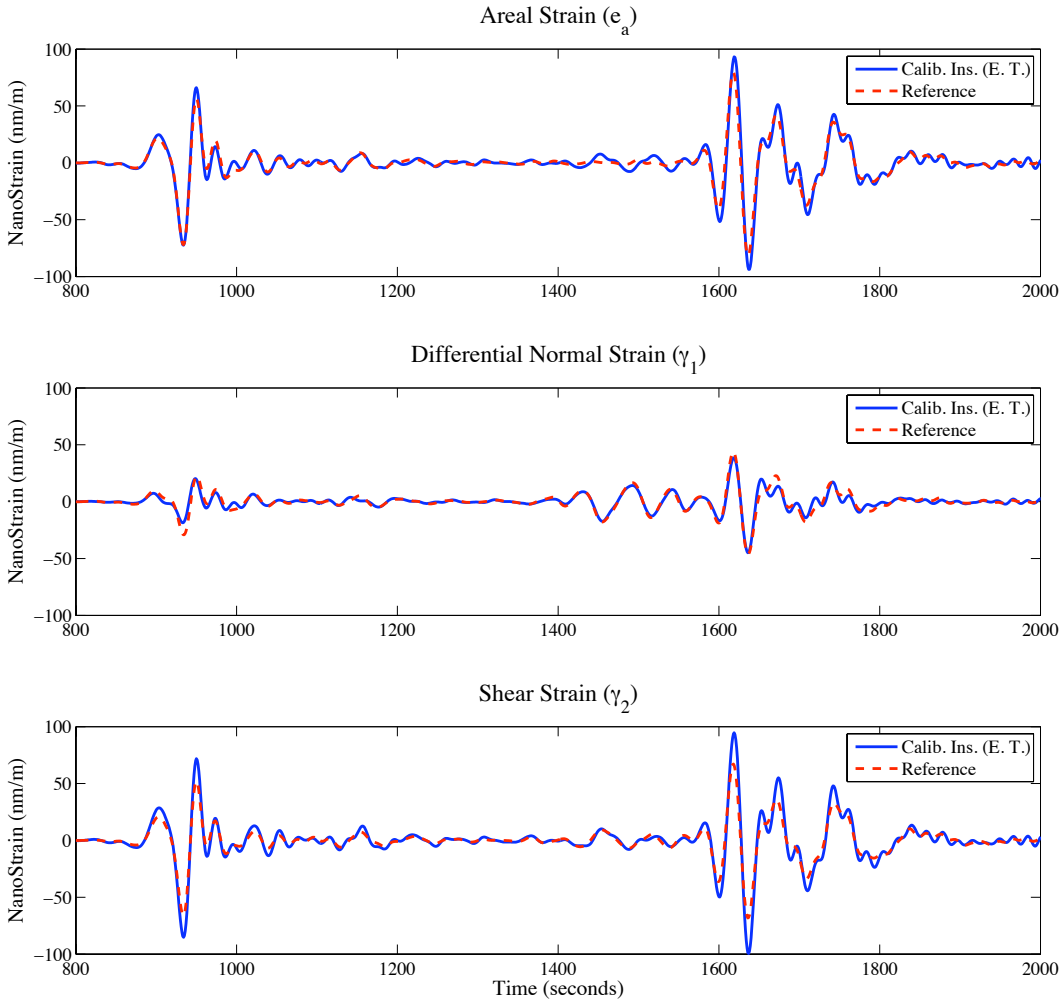

Figure 30. Illustration of the result from calibrating the instrument data associated with event 16 (2009/09/29) recorded by B081 using the calibration coefficients obtained from *Roeloffs* [2010] in Table (14), BLUE solid line. The reference formation strains derived in this study are also illustrated for comparison, RED dashed line.

Calibration for PBO GTSM instrument: B082

There are 1411 sets of 4 complex instrument strain and 3 complex reference strain amplitudes from 18 teleseismic events that were compiled together, inside the frequency band between 0.01 and 0.03 Hz, before inverting for the calibration coefficients. Supplemental Figures (A26) and (A27) associated with the normalized probability density function illustrate the real and imaginary components, respectively, resulting from repeatedly (1000 realizations) selecting a random subset of 71 (~5%) of the 1411 sets of instrument and reference strain amplitudes before inverting for the calibration coefficients. The calibration coefficients, along with their standard deviation, are summarized in Table (15).

In addition to the calibration process, we attempted to derive the alignment error associated with B082 using the second method described above. We found that the second method yielded an alignment error of 20.3 degrees (compare to 18 degrees derived from the first method). After properly accounting for the alignment error we observed that the diagonal elements of the coupling model are very similar to those in the nominal isotropic coupling model provided by PBO (see Table 16). However, there are also significant cross-coupling terms, which indicate that an isotropic coupling model is not valid for station B082.

Table 15. Derived calibration coefficients for B082 using seismic data. Calibration coefficients with imaginary parts are neglected. The coefficient values are the result from inverting 1411 sets of instrument strain and reference strain amplitudes. The standard deviation associated with each distribution in Figure (A26) is indicated to the right of each respective coefficient value. The 4x3 calibration coefficient matrix relates the 3x1 reference formation strain to the 4x1 instrument gauge strain through Equation (36).

B082 Derived Calibration Coefficients	Areal Strain (e_a)	Differential Normal Strain (γ_1)	Shear Strain (γ_2)
Gauge 0	1.125 ± 0.103	-1.329 ± 0.112	-0.938 ± 0.092
Gauge 1	0.947 ± 0.064	1.089 ± 0.052	-0.797 ± 0.047
Gauge 2	0.168 ± 0.043	0.017 ± 0.041	1.309 ± 0.037
Gauge 3	0.354 ± 0.042	-1.337 ± 0.038	0.723 ± 0.039

Table 16. Derived coupling model associated with B082. The 3x3 coupling model relates the 3x1 reference formation strain to the 3x1 instrument formation strain through Equation (35). Two standard deviations (a , b) are listed for each coupling coefficient, where "a" is related to the standard deviation in each calibration coefficient presented in the table above and "b" is related to the uncertainty in the alignment correction listed in Table (11).

B082 Derived Coupling Model	Reference Areal Strain (e_a)	Reference Differential Normal Strain (γ_1)	Reference Shear Strain (γ_2)
Instrument Areal Strain (e_a)	1.425 ± (0.046 , 0.000)	-0.183 ± (0.046 , 0.000)	-0.216 ± (0.038 , 0.000)
Instrument Differential Normal Strain (γ_1)	0.032 ± (0.113 , 0.010)	2.836 ± (0.111 , 0.041)	-0.173 ± (0.097 , 0.250)
Instrument Shear Strain (γ_2)	-1.192 ± (0.122 , 0.007)	0.375 ± (0.134 , 0.239)	2.982 ± (0.106 , 0.025)

Calibration for PBO GTSM instrument: B084

There are 1411 sets of 4 complex instrument strain and 3 complex reference strain amplitudes from 18 teleseismic events that were compiled together, inside the frequency band between 0.01 and 0.03 Hz, before inverting for the calibration coefficients. Supplemental Figures (A30) and (A31) associated with the normalized probability density function illustrate the real and imaginary components, respectively, resulting from repeatedly (1000 realizations) selecting a random subset of 71 (~5%) of the 1411 sets of instrument and reference strain amplitudes before inverting for the calibration coefficients. The calibration coefficients, along with their standard deviation, are summarized in Table (17).

In addition to the calibration process, we attempted to derive the alignment error associated with B084 using the second method described above. We found that the second method yielded an alignment error of 26.8 degrees (compare to 25 degrees derived from the first method). After properly accounting for the alignment error we observed that the diagonal elements of the coupling model are a lot larger than those in the nominal isotropic coupling model provided by PBO (see Table 18). In addition, there are also significant cross-coupling terms, which indicate that an isotropic coupling model is not valid for station B084.

Table 17. Derived calibration coefficients for B084 using seismic data. Calibration coefficients with imaginary parts are neglected. The coefficient values are the result from inverting 1411 sets of instrument strain and reference strain amplitudes. The standard deviation associated with each distribution in Figure (A30) is indicated to the right of each respective coefficient value. The 4x3 calibration coefficient matrix relates the 3x1 reference formation strain to the 4x1 instrument gauge strain through Equation (36).

B084 Derived Calibration Coefficients	Areal Strain (e_a)	Differential Normal Strain (γ_1)	Shear Strain (γ_2)
Gauge 0	0.723 ± 0.082	-0.658 ± 0.071	2.367 ± 0.081
Gauge 1	1.438 ± 0.055	-1.824 ± 0.055	-1.064 ± 0.046
Gauge 2	0.661 ± 0.062	1.949 ± 0.052	-1.029 ± 0.054
Gauge 3	0.393 ± 0.069	1.796 ± 0.060	1.136 ± 0.064

Table 18. Derived coupling model associated with B084. The 3x3 coupling model relates the 3x1 reference formation strain to the 3x1 instrument formation strain through Equation (35). Two standard deviations (a , b) are listed for each coupling coefficient, where "a" is related to the standard deviation in each calibration coefficient presented in the table above and "b" is related to the uncertainty in the alignment correction listed in Table (11).

B084 Derived Coupling Model	Reference Areal Strain (e_a)	Reference Differential Normal Strain (γ_1)	Reference Shear Strain (γ_2)
Instrument Areal Strain (e_a)	1.865 ± (0.061 , 0.000)	-0.247 ± (0.056 , 0.000)	0.145 ± (0.056 , 0.000)
Instrument Differential Normal Strain (γ_1)	-0.874 ± (0.122 , 0.073)	4.610 ± (0.106 , 0.080)	-0.495 ± (0.106 , 0.551)
Instrument Shear Strain (γ_2)	-0.547 ± (0.118 , 0.111)	-0.372 ± (0.112 , 0.565)	4.487 ± (0.119 , 0.094)

Calibration for PBO GTSM instrument: B086

There are 1162 sets of 4 complex instrument strain and 3 complex reference strain amplitudes from 15 teleseismic events that were compiled together, inside the frequency band between 0.01 and 0.03 Hz, before inverting for the calibration coefficients. Supplemental Figures (A34) and (A35) associated with the normalized probability density function illustrate the real and imaginary components, respectively, resulting from repeatedly (1000 realizations) selecting a random subset of 58 (~5%) of the 1162 sets of instrument and reference strain amplitudes before inverting for the calibration coefficients. The calibration coefficients, along with their standard deviation, are summarized in Table (19).

In addition to the calibration process, we attempted to derive the alignment error associated with B086 using the second method described above. We found that the second method yielded an alignment error of 2.3 degrees (compare to 3.3 degrees derived from the first method). After properly accounting for the alignment error we observed that the diagonal elements of the coupling model are slightly different than those in the nominal isotropic coupling model provided by PBO (see Table 20). However, there are also significant cross-coupling terms, which indicate that an isotropic coupling model is not valid for station B086.

Table 19. Derived calibration coefficients for B086 using seismic data. Calibration coefficients with imaginary parts are neglected. The coefficient values are the result from inverting 1162 sets of instrument strain and reference strain amplitudes. The standard deviation associated with each distribution in Figure (A34) is indicated to the right of each respective coefficient value. The 4x3 calibration coefficient matrix relates the 3x1 reference formation strain to the 4x1 instrument gauge strain through Equation (36).

B086 Derived Calibration Coefficients	Areal Strain (e_a)	Differential Normal Strain (γ_1)	Shear Strain (γ_2)
Gauge 0	1.099 ± 0.047	-0.131 ± 0.052	-1.641 ± 0.037
Gauge 1	0.305 ± 0.045	1.242 ± 0.039	0.233 ± 0.043
Gauge 2	0.635 ± 0.083	-1.310 ± 0.065	1.164 ± 0.072
Gauge 3	0.481 ± 0.053	-1.626 ± 0.047	-0.510 ± 0.047

Table 20. Derived coupling model associated with B086. The 3x3 coupling model relates the 3x1 reference formation strain to the 3x1 instrument formation strain through Equation (35). Two standard deviations (a , b) are listed for each coupling coefficient, where "a" is related to the standard deviation in each calibration coefficient presented in the table above and "b" is related to the uncertainty in the alignment correction listed in Table (11).

B086 Derived Coupling Model	Reference Areal Strain (e_a)	Reference Differential Normal Strain (γ_1)	Reference Shear Strain (γ_2)
Instrument Areal Strain (e_a)	1.165 ± (0.048 , 0.000)	-0.216 ± (0.042 , 0.000)	-0.202 ± (0.042 , 0.000)
Instrument Differential Normal Strain (γ_1)	-0.150 ± (0.100 , 0.045)	3.083 ± (0.086 , 0.029)	-0.464 ± (0.089 , 0.230)
Instrument Shear Strain (γ_2)	-0.634 ± (0.105 , 0.012)	-0.304 ± (0.091 , 0.216)	3.279 ± (0.091 , 0.040)

Calibration for PBO GTSM instrument: B087

There are 1411 sets of 4 complex instrument strain and 3 complex reference strain amplitudes from 18 teleseismic events that were compiled together, inside the frequency band between 0.01 and 0.03 Hz, before inverting for the calibration coefficients. Supplemental Figures (A38) and (A39) associated with the normalized probability density function illustrate the real and imaginary components, respectively, resulting from repeatedly (1000 realizations) selecting a random subset of 71 (~5%) of the 1411 sets of instrument and reference strain amplitudes before inverting for the calibration coefficients. The calibration coefficients, along with their standard deviation, are summarized in Table (21).

In addition to the calibration process, we attempted to derive the alignment error associated with B087 using the second method described above. We found that the second method yielded an alignment error of -51.5 degrees (compare to -48 degrees derived from the first method). After properly accounting for the alignment error we observed that the diagonal elements of the coupling model are smaller than those in the nominal isotropic coupling model provided by PBO (see Table 22). In addition, there are also significant cross-coupling terms, which indicate that an isotropic coupling model is not valid for station B087.

Table 21. Derived calibration coefficients for B087 using seismic data. Calibration coefficients with imaginary parts are neglected. The coefficient values are the result from inverting 1411 sets of instrument strain and reference strain amplitudes. The standard deviation associated with each distribution in Figure (A38) is indicated to the right of each respective coefficient value. The 4x3 calibration coefficient matrix relates the 3x1 reference formation strain to the 4x1 instrument gauge strain through Equation (36).

B087 Derived Calibration Coefficients	Areal Strain (e_a)	Differential Normal Strain (γ_1)	Shear Strain (γ_2)
Gauge 0	0.184 ± 0.025	0.944 ± 0.022	-0.403 ± 0.020
Gauge 1	0.578 ± 0.025	0.169 ± 0.025	0.583 ± 0.025
Gauge 2	0.166 ± 0.036	-1.246 ± 0.031	-0.598 ± 0.031
Gauge 3	-0.165 ± 0.022	-0.442 ± 0.022	-0.663 ± 0.020

Table 22. Derived coupling model associated with B087. The 3x3 coupling model relates the 3x1 reference formation strain to the 3x1 instrument formation strain through Equation (35). Two standard deviations (a , b) are listed for each coupling coefficient, where "a" is related to the standard deviation in each calibration coefficient presented in the table above and "b" is related to the uncertainty in the alignment correction listed in Table (11).

B087 Derived Coupling Model	Reference Areal Strain (e_a)	Reference Differential Normal Strain (γ_1)	Reference Shear Strain (γ_2)
Instrument Areal Strain (e_a)	0.551 ± (0.013 , 0.000)	-0.150 ± (0.014 , 0.000)	-0.213 ± (0.014 , 0.000)
Instrument Differential Normal Strain (γ_1)	0.202 ± (0.071 , 0.087)	2.583 ± (0.061 , 0.042)	0.565 ± (0.060, 0.164)
Instrument Shear Strain (γ_2)	0.645 ± (0.039 , 0.032)	-0.142 ± (0.039 , 0.343)	1.206 ± (0.037, 0.085)

Calibration for PBO GTSM instrument: B088

There are 1411 sets of 4 complex instrument strain and 3 complex reference strain amplitudes from 18 teleseismic events that were compiled together, inside the frequency band between 0.01 and 0.03 Hz, before inverting for the calibration coefficients. Supplemental Figures (A42) and (A43) associated with the normalized probability density function illustrate the real and imaginary components, respectively, resulting from repeatedly (1000 realizations) selecting a random subset of 71 (~5%) of the 1411 sets of instrument and reference strain amplitudes before inverting for the calibration coefficients. The calibration coefficients, along with their standard deviation, are summarized in Table (23).

In addition to the calibration process, we attempted to derive the alignment error associated with B088 using the second method described above. We found that the second method yielded an alignment error of -14.1 degrees (compare to -10 degrees derived from the first method). After properly accounting for the alignment error we observed that the diagonal elements of the coupling model are larger than those in the nominal isotropic coupling model provided by PBO (see Table 24). In addition, there are also significant cross-coupling terms, which indicate that an isotropic coupling model is not valid for station B088.

Table 23. Derived calibration coefficients for B088 using seismic data. Calibration coefficients with imaginary parts are neglected. The coefficient values are the result from inverting 1411 sets of instrument strain and reference strain amplitudes. The standard deviation associated with each distribution in Figure (A42) is indicated to the right of each respective coefficient value. The 4x3 calibration coefficient matrix relates the 3x1 reference formation strain to the 4x1 instrument gauge strain through Equation (36).

B088 Derived Calibration Coefficients	Areal Strain (e_a)	Differential Normal Strain (γ_1)	Shear Strain (γ_2)
Gauge 0	2.911 ± 0.106	-2.616 ± 0.102	1.619 ± 0.095
Gauge 1	1.360 ± 0.041	-0.565 ± 0.048	-1.322 ± 0.036
Gauge 2	-0.380 ± 0.046	1.781 ± 0.041	-0.087 ± 0.038
Gauge 3	0.389 ± 0.050	0.265 ± 0.046	1.426 ± 0.045

Table 24. Derived coupling model associated with B088. The 3x3 coupling model relates the 3x1 reference formation strain to the 3x1 instrument formation strain through Equation (35). Two standard deviations (a , b) are listed for each coupling coefficient, where "a" is related to the standard deviation in each calibration coefficient presented in the table above and "b" is related to the uncertainty in the alignment correction listed in Table (11).

B088 Derived Coupling Model	Reference Areal Strain (e_a)	Reference Differential Normal Strain (γ_1)	Reference Shear Strain (γ_2)
Instrument Areal Strain (e_a)	2.316 ± (0.063 , 0.000)	-0.722 ± (0.058 , 0.000)	0.128 ± (0.058 , 0.000)
Instrument Differential Normal Strain (γ_1)	-3.776 ± (0.150 , 1.004)	4.930 ± (0.140 , 1.471)	-0.769 ± (0.129 , 1.867)
Instrument Shear Strain (γ_2)	0.812 ± (0.088 , 2.124)	-1.362 ± (0.094 , 2.819)	3.302 ± (0.078 , 0.910)

Calibration for PBO GTSM instrument: B089

There are 1494 sets of 4 complex instrument strain and 3 complex reference strain amplitudes from 19 teleseismic events that were compiled together, inside the frequency band between 0.01 and 0.03 Hz, before inverting for the calibration coefficients. Supplemental Figures (A46) and (A47) associated with the normalized probability density function illustrate the real and imaginary components, respectively, resulting from repeatedly (1000 realizations) selecting a random subset of 75 (~5%) of the 1494 sets of instrument and reference strain amplitudes before inverting for the calibration coefficients. The calibration coefficients, along with their standard deviation, are summarized in Table (25).

In addition to the calibration process, we attempted to derive the alignment error associated with B089 using the second method described above. We found that the second method yielded an alignment error of -6.5 degrees (compare to -7.3 degrees derived from the first method). After properly accounting for the alignment error we observed that the last two diagonal elements of the coupling model are significantly larger than those in the nominal isotropic coupling model provided by PBO (see Table 26). In addition, there are also significant cross-coupling terms, which indicate that an isotropic coupling model is not valid for station B089.

Table 25. Derived calibration coefficients for B089 using seismic data. Calibration coefficients with imaginary parts are neglected. The coefficient values are the result from inverting 1494 sets of instrument strain and reference strain amplitudes. The standard deviation associated with each distribution in Figure (A46) is indicated to the right of each respective coefficient value. The 4x3 calibration coefficient matrix relates the 3x1 reference formation strain to the 4x1 instrument gauge strain through Equation (36).

B089 Derived Calibration Coefficients	Areal Strain (e_a)	Differential Normal Strain (γ_1)	Shear Strain (γ_2)
Gauge 0	-0.239 ± 0.087	3.130 ± 0.065	-1.460 ± 0.071
Gauge 1	0.242 ± 0.134	0.011 ± 0.073	2.607 ± 0.098
Gauge 2	1.432 ± 0.075	-2.506 ± 0.064	-1.542 ± 0.058
Gauge 3	0.655 ± 0.082	-0.010 ± 0.071	-3.317 ± 0.065

Table 26. Derived coupling model associated with B089. The 3x3 coupling model relates the 3x1 reference formation strain to the 3x1 instrument formation strain through Equation (35). Two standard deviations (a , b) are listed for each coupling coefficient, where "a" is related to the standard deviation in each calibration coefficient presented in the table above and "b" is related to the uncertainty in the alignment correction listed in Table (11).

B089 Derived Coupling Model	Reference Areal Strain (e_a)	Reference Differential Normal Strain (γ_1)	Reference Shear Strain (γ_2)
Instrument Areal Strain (e_a)	0.947 ± (0.077 , 0.000)	0.282 ± (0.037 , 0.000)	-0.408 ± (0.053 , 0.000)
Instrument Differential Normal Strain (γ_1)	-1.908 ± (0.169 , 0.089)	6.506 ± (0.136 , 0.088)	-0.167 ± (0.142 , 0.806)
Instrument Shear Strain (γ_2)	-0.505 ± (0.216 , 0.270)	0.175 ± (0.131 , 0.907)	5.780 ± (0.164 , 0.079)

Discussion

The results from this study suggest that borehole strainmeter instruments can be successfully calibrated using reference strain information derived from seismic data. We demonstrated for one PBO GTSM instrument, i.e., B081, that the calibration coefficients derived here can give results similar to those derived by other studies that may use theoretical earth tide strain measurements as the reference (see *Roeloffs* [2010]). This suggests that the coefficients necessary for calibration are remarkably stable for a large range of characteristic event times that span many orders of magnitude. We also developed and implemented processes for identifying problems with borehole readings associated with instrument misalignment. Although most PBO GTSM stations inside the Anza Seismic Network were within ± 10 degrees of the advertised orientation angles, there were 3 stations (B082, B084, and B087) with orientation errors that ranged between 18 and 54 degrees.

We also introduced a potentially useful method of empirically estimating the uncertainty in the calibrated strainmeter result by selecting random subsets of the raw instrument strain and reference strain amplitudes, in the frequency domain, and creating a statistical distribution of the predicted calibration coefficients. However, special care must be taken in selecting an appropriate subset size – a subset size that is too large will create an unreasonably tight distribution, while a subset size that is too small will create an unreasonably broad distribution (not to mention numerical instability in the inversion process). In this study, we selected and had reasonable success with a subset size that was approximately equal to 5% of the total dataset.

We also found that the PBO's default isotropic coupling model is not supported by the calibration parameters derived here. Due to the nature of the emplacement process and the borehole instrument housing material, it is likely that the vast majority of PBO GTSM instruments will require a location-specific cross-coupling model in order to reconcile the, sometimes large, differences between the measured formation strain and the "true" formation strain.

CHAPTER 4

Viewing the Seismic Wavefield through Calibrated GTSM Instrument Data

Abstract

We discuss three techniques that use calibrated borehole Gladwin Tensor Strainmeter (GTSM) instrument data in order to analyze various aspects of the seismic wavefield. The first two techniques take advantage of the unique measurement tool created by a co-located borehole GTSM instrument and a broadband seismometer. The first technique, based on spatial gradient analysis in one-dimension (1D), was developed in *Langston and Liang* [2008] for seismic waves originating from an isotropic source and polarized in one direction. With the propagation direction known, this technique enables the information related to the change in geometrical spreading and horizontal phase velocity to be derived from the calibrated areal strain and radial ground velocity measurements at a single location. The second technique, developed here, enables information related to the propagation direction and horizontal phase velocity to be derived from the calibrated areal strain, calibrated normal differential strain, and horizontal ground velocity measurements at a single location. This second technique assumes plane-wave propagation from an isotropic source, so the geometrical spreading and radiation pattern terms are considered constant. The third technique takes advantage of dense borehole GTSM arrays that may exist within the PBO deployment. With all the GTSM instruments within an array calibrated, it will be possible to apply various array processing techniques to recover different aspects of the seismic wavefield, including the propagation direction and horizontal phase velocity. In this study, we chose to apply a frequency/wavenumber beam-forming technique, although other array processing techniques based on correlation, stacking, or other smoothing operations are just as easy to implement.

Combining co-located borehole GTSM instrument data with broadband seismometer data is only the beginning. The combination of a co-located borehole GTSM instrument data with a horizontal rotation-meter and a broadband seismometer would enable the entire seismic wavefield, available through gradiometry analysis, to be decomposed at a single point on the earth. Such a "point seismic array" would yield important properties of the seismic wavefield that could not have been identified in the past without a dense array of seismometers.

Introduction

The usual practice for analyzing the seismic wavefield with the spatial gradient analysis technique of *Langston* [2007a, b, c] involves using data exclusively from a dense seismic array. In the one-dimensional (1D) case, the spatial displacement gradients derived from a seismic array, in addition to the radial ground displacement and velocity, are used to derive properties about the seismic wavefield associated with the change in the geometrical spreading factor and phase velocity. In the two-dimensional (2D) case, the spatial displacement gradients derived from a seismic array, in addition to both components of the horizontal ground displacement and velocity, are used to derive properties about the seismic wavefield that not only include the parameters in the 1D case, but also the propagation azimuth and azimuthal radiation pattern.

The problem with using seismic data exclusively is that the aperture of the array limits the high frequency resolution of the spatial displacement gradients through an inverse-proportional relationship. Therefore, the motivation behind this study is to be able to derive most of the above properties without having to rely on techniques for estimating the spatial displacement gradients that may not be well suited above a specific high frequency threshold. For example, during the strainmeter calibration process in the previous chapter (Chapter 3), the ~40km aperture of the 10-element array subset of the Anza Seismic Network in southern California (see Figure 4) limited our high frequency resolution to approximately 0.03 Hz waves. However, with a borehole GTSM instrument

co-located with a broadband seismometer, we show here that it is possible to increase the high frequency resolution to a point that is only limited by the quality of data and/or sample rate(s) of the co-located instruments.

In this study, we develop and describe two techniques for deriving useful information about the wavefield using data collected by a borehole GTSM instrument co-located with a broadband seismometer. We also discuss an additional technique for deriving information about the wavefield using data collected by a dense array of borehole GTSM instruments. The first technique was presented in *Langston and Liang* [2008] and, under the assumption that the propagation direction of a wave from an isotropic source is known, enables information about the change in geometrical spreading and horizontal phase velocity to be derived from data collected by a borehole GTSM instrument and a co-located broadband seismometer. The second technique is developed here and, under the assumption that a propagating plane-wave originates from an isotropic source, enables information about the propagation direction and horizontal phase velocity to be derived from data collected by a borehole GTSM instrument and a co-located broadband seismometer. The third technique, discussed here, is an array processing technique for decomposing a plane-wave field using a frequency/wavenumber beam-forming approach. Other array processing techniques associated with correlation, stacking, or other smoothing operations are just as applicable in processing data collected by a dense array of borehole GTSM instruments, but are not discussed here.

In order to demonstrate the effectiveness of each technique for different types of seismic waves, one set of data from a regional earthquake and one from a teleseismic earthquake are considered for examples in this study. We again employ the same set of 7 borehole GTSM instruments inside the Anza Seismic Network, but we can only employ seismic stations FRD, KNW, and PFO because they are the only ones effectively co-located with B087, B081, and B084, respectively (see Figure 4). We chose the M5.5 Chino Hills earthquake (2008/07/29) as the regional earthquake and the M7.0 Haitian earthquake (2010/01/12) as the teleseismic earthquake. For each earthquake, the idea is to process the data using each technique for different frequency bands in order to better describe seismic phases that might travel with different center or dominant frequencies.

We find that important information can be derived using each of the three techniques, which may be able to address topics related to wave scattering, regional velocity variation, seismic phase identification/interpretation, etc. However, if it were possible to incorporate a horizontal rotation-meter into the setup described above, for a borehole GTSM instrument co-located with a broadband seismometer, then the entire wavefield could be characterized using spatial gradient analysis in 2D.

Methods

In this section, we will describe the formulation necessary to characterize the seismic wavefield using various combinations of borehole GTSM instruments and broadband seismometers. The first two methods use data from a calibrated borehole GTSM instrument co-located with a broadband seismometer in order to characterize properties about the seismic wavefield associated with changes in geometrical spreading, horizontal phase velocity, and propagation direction. The third method uses data from a dense array of borehole GTSM instruments to infer properties about the seismic wavefield associated with horizontal phase velocity and propagation direction.

Method One: Polarized Plane-Wave from Isotropic Source

As described in *Langston and Liang* [2008], the assumption that the propagation direction of an incoming wave originating from an isotropic source is known leads to an equality between the areal strain (e_a) and the radial displacement gradient ($\partial/\partial r$) of the radial ground displacement (u_r). Under these conditions, Equation (23) becomes:

$$\begin{aligned} e_a &= \frac{\partial u_r(t,r,\theta)}{\partial r} = A_R u_r(t,r,\theta) - B_R \dot{u}_r(t,r,\theta) \\ 0 &= \frac{\partial u_r(t,r,\theta)}{\partial \theta} = \frac{R'(\theta)}{R(\theta)} u_r(t,r,\theta) \end{aligned} , \tag{43}$$

where

$$\begin{aligned} A_R &= \frac{G_r'(r)}{G_r(r)} \\ B_R &= \left[s_r(r) + s_r'(r)(r - r_0) \right] \end{aligned} . \tag{44}$$

The object is then to find the coefficients A_R and B_R at each time step from the combination of the areal strain data derived from a single, calibrated borehole GTSM instrument and the radial ground displacement and velocity data from a co-located broadband seismometer. If the geometrical spreading and the horizontal phase velocity are reasonably constant, then A_R should approach zero and B_R should approach the negative of the radial slowness.

Method Two: Plane-Wave from Isotropic Source

As described in *Gomberg et al.* [1999], the assumption that a plane-wave propagating from an isotropic source at constant horizontal phase velocity leads to the following relationship for the diagonal elements of the 2D strain tensor (see Equation 28) when the spatial displacement gradients are small:

$$\begin{aligned} \varepsilon_{11} &= u_{1,1} = -s_r \dot{u}_1 \sin(\theta) \\ \varepsilon_{22} &= u_{2,2} = -s_r \dot{u}_2 \cos(\theta) \end{aligned} , \tag{45}$$

where s_r is the radial slowness, θ is the propagation direction, $\dot{u}_1$ is the east-west component of ground velocity, $\dot{u}_2$ is the north-south component of ground velocity. In the above equation, the radial slowness term may be described in terms of the horizontal slowness in the east-west and north-south directions through:

$$\begin{aligned} s_1 &= s_r \sin(\theta) \\ s_2 &= s_r \cos(\theta) \end{aligned} \quad , \tag{46}$$

respectively. From here, it is straightforward to relate the horizontal slowness in the east-west and north-south directions to the apparent propagation direction through:

$$\frac{s_1}{s_2} = \tan(\theta) \quad . \tag{47}$$

The object is then to find the horizontal slowness in the east-west and north-south directions at each time step from the combination of the areal strain and differential normal strain data derived from a single, calibrated borehole GTSM instrument and the two horizontal components of ground velocity data from a co-located broadband seismometer. When the diagonal elements of the 2D strain tensor are derived from:

$$\begin{bmatrix} \varepsilon_{11} \\ \\ \varepsilon_{22} \end{bmatrix} = \frac{1}{2} \begin{bmatrix} 1 & 1 \\ \\ 1 & -1 \end{bmatrix} \begin{bmatrix} e_a \\ \\ \gamma_1 \end{bmatrix} \quad , \tag{48}$$

the horizontal slowness in the east-west and north-south directions may be determined at a time step i by selecting a window of ground velocity data $\pm$ m (m>0) time steps about time step i and relating it to the calibrated strain data corresponding to the same time window. This inverse problem may be cast in the form of **Gm**=**d**, where

$$\mathbf{G} = \begin{bmatrix} -\dot{u}_1(i+m) & -\dot{u}_2(i+m) \\ \vdots & \vdots \\ -\dot{u}_1(i) & -\dot{u}_2(i) \\ \vdots & \vdots \\ -\dot{u}_1(i-m) & -\dot{u}_2(i-m) \end{bmatrix} \quad ,$$

$$\mathbf{m} = \begin{bmatrix} s_1(i) \\ \\ s_2(i) \end{bmatrix}, \quad \text{and}$$

$$\mathbf{d} = \begin{bmatrix} \varepsilon_{11}(i+m) & \varepsilon_{22}(i+m) \\ \vdots & \vdots \\ \varepsilon_{11}(i) & \varepsilon_{22}(i) \\ \vdots & \vdots \\ \varepsilon_{11}(i-m) & \varepsilon_{22}(i-m) \end{bmatrix} .$$

The best fit estimates of the horizontal slowness in the east-west and north-south directions at a time step *i* may be found, in a least squares sense, through:

$$\mathbf{m} = \left(\mathbf{G}^T\mathbf{G}\right)\mathbf{G}^T\mathbf{d} \quad . \tag{49}$$

Using the result in Equation (49), the apparent propagation direction may be determined through the relationship in Equation (47) and the radial slowness may be determined by finding the magnitude of vector **m**.

Method Three: Plane-Wave from Isotropic Source

Unlike spatial gradient analysis, which is founded on a formulation that obeys the fundamental physics associated with wave propagation, array processing techniques often rely on forming beams, stacking, correlation, etc. in order to decompose the basic characteristics of propagation from a plane-wave field [*Langston*, 2007b]. As an example, we choose to employ a frequency/wavenumber beam-forming approach to process calibrated strain data collected by a dense array of borehole GTSM instruments. The processing associated with this approach is very straightforward when carried out in the

frequency domain. The first step is to select a window of time domain data and to choose an appropriate 1D frequency range and 2D wavenumber range to form beams. The second step is to Fourier transform the time domain data, from a specific component of motion recorded by each station in the array for the same window in time, into the frequency domain where the bulk of processing will be done. Next, the phase of the data at each frequency increment are adjusted according to a specific horizontal slowness in the east-west (or *x*-) and north-south (or *y*-) direction. The fourth step is to sum the phase-delayed data at each frequency, square the sum, and then sum the squared-summed-phase-delayed data over the frequency band of interest. This scalar is stored in a matrix at the row and column that correspond to the specific horizontal slowness vector in question. When this matrix is fully populated, the values may be normalized to a range between 0 and 1. The final step is to identify the direction and slowness of different waves propagating across the array, within the specified time window, from the peaks that correspond to the horizontal slowness values that result in the most coherent beams.

The formation strain information derived from calibrated borehole GTSM instrument data should yield waveforms that are similar enough in nature that the standard array processing techniques, such as the one described above, can be applied. Each component of the formation strain describes the relationship between that strain measurement and a type of seismic wave (i.e., P-wave, S-wave, or Surface wave). Therefore, an informative exercise is to form beams using different components of the formation strain in order to better characterize these different wave types.

Results

Examples of the three applications discussed in this study are presented here using data collected from a regional seismic event, the M5.5 Chino Hills earthquake (2008/07/29), and a teleseismic event, the M7.0 Haitian earthquake (2010/01/12). In this study, we can apply the three techniques to data collected by the same set of 7 borehole GTSM instruments inside the Anza Seismic Network, as the previous chapters, and Anza

broadband seismometers FRD, KNW, and PFO (see Figure 4). The choice of these three seismometers is based on the fact that they are nearly co-located with borehole GTSM stations, namely B087, B081, and B084, respectively. A nominal distance of 99m, 387m, and 281m separates the three sets of stations, respectively.

We analyze various seismic phases throughout the seismic and strain records by band-pass filtering the data over different frequency intervals in order to highlight phases that may have different center or dominant frequencies. The maximum frequency interval used in these analyses depend upon several factors: 1) the quality of data (i.e., the signal-to-noise ratio), 2) the minimum sample rate between the borehole GTSM instruments and the broadband seismic instruments (i.e., 20 vs. 40 samples-per-second), 3) the actual distance between the borehole GTSM instrument and "co-located" broadband seismometer, and 4) timing issues between the two types of instruments. With respect to the third consideration, we expect to see the two techniques that utilize data from co-located instruments begin to breakdown at higher frequency intervals for station pair KNW and B081 first.

Regional Event: M5.5 Chino Hills earthquake (2008/07/29)

We first examine an example of applying Method (1) to the combination of calibrated areal strain, radial ground displacement, and radial ground velocity associated with the M5.5 Chino Hills earthquake (2008/07/29). In order to reduce redundancy, we only look at data collected by the station pair created from borehole GTSM station B087 and co-located Anza seismometer FRD (see Figure 31). Method (1) was applied to this set of data for 5 different frequency intervals ranging from 0.05 to 2.0 Hz. Figures (32) and (4.03) illustrate only the 2 lower frequency intervals, namely 0.33 to 0.66 Hz and 0.05 to 0.33 Hz, because the other results are difficult to interpret (see supplemental Figures A50 – A55 in Appendix 3). There is very little consistency in the slowness estimates associated with the P-wave (~0.1 s/km), S-wave (~0.15 s/km), and the Rayleigh wave (~0.15 s/km) in Figure (32). However, for lower frequency bands the method

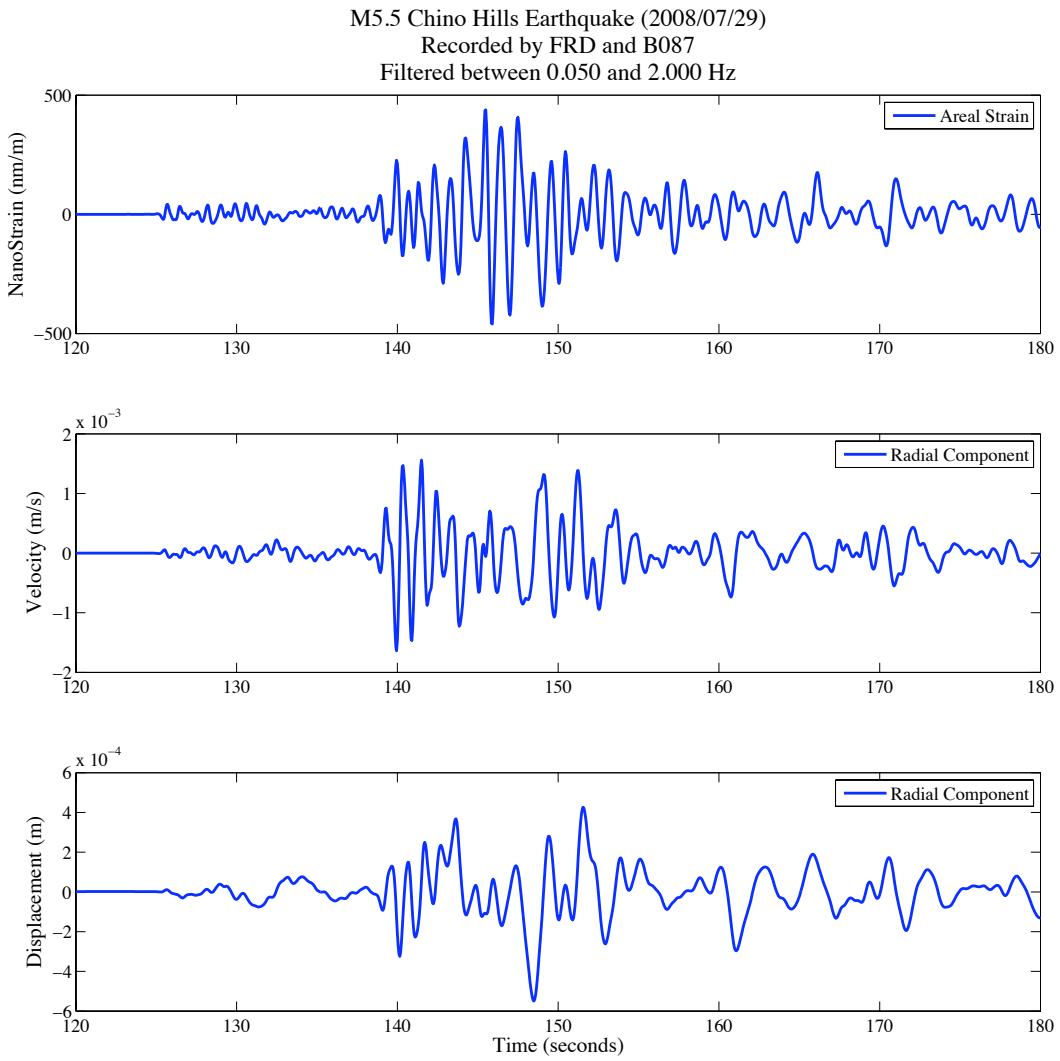

Figure 31. Data used for Method (1) include the areal strain (TOP), the radial ground velocity (MIDDLE), and the radial ground displacement (BOTTOM). Calibrated strain data correspond to borehole GTSM station B087 and the seismic data correspond to Anza broadband seismometer FRD. The original seismograms correspond to the 29 July 2008 M5.5 Chino Hills earthquake band-pass filtered between 0.05 Hz and 2.0 Hz with a 4-pole Butterworth acausal filter.

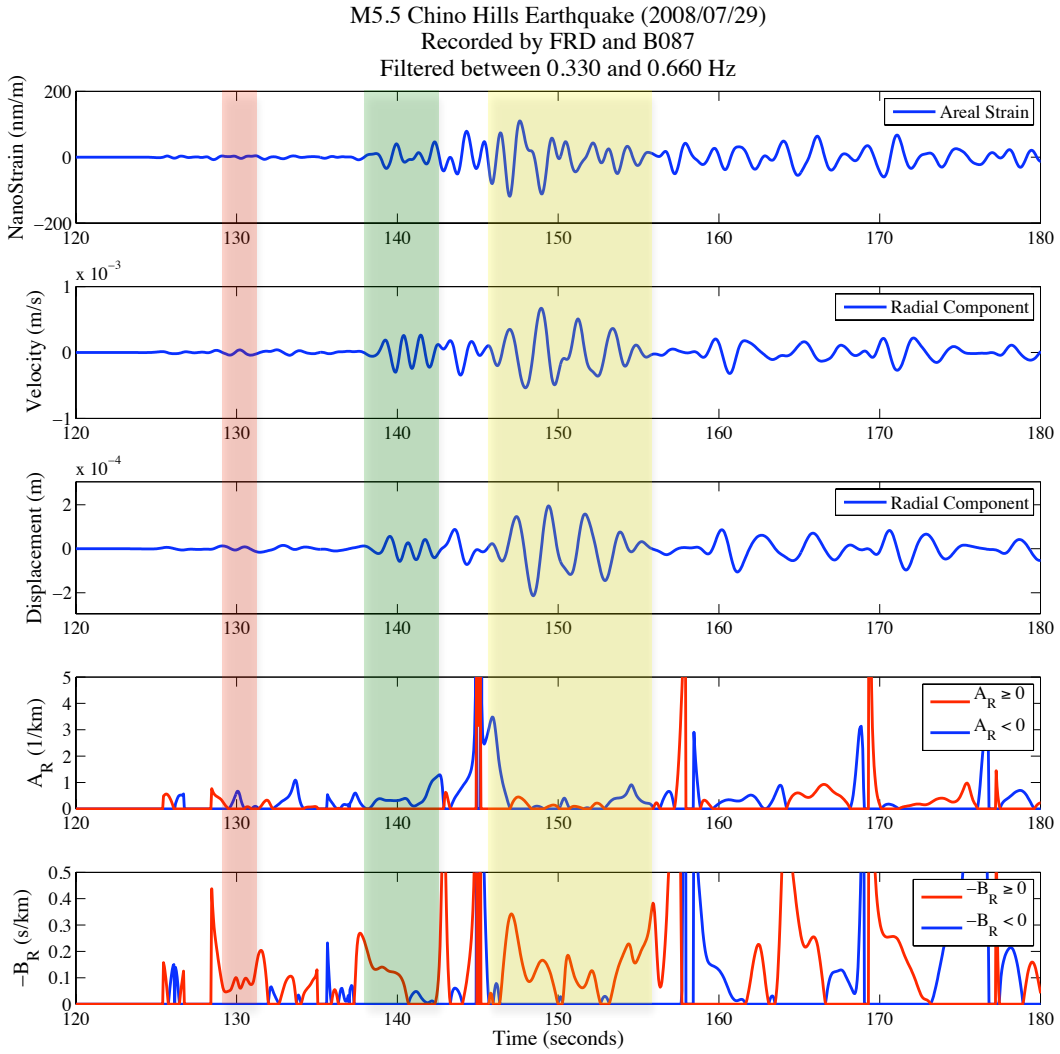

Figure 32. The result of applying Method (1) to the data corresponding to Figure (31) band-pass filtered between 0.33 Hz and 0.66 Hz with a 4-pole Butterworth acausal filter. Instability (or "glitches") in 1D spatial gradient result is likely due to interfering waves at a particular point in time or due to an inappropriate assumption of propagation model. The RED, GREEN, and YELLOW translucent bars illustrate P-wave (0.1 s/km), S-wave (0.15 s/km), and Rayleigh wave phases (0.15 s/km), respectively. The inconsistent nature of the slowness estimates does not make this method a good candidate for other regional seismic events.

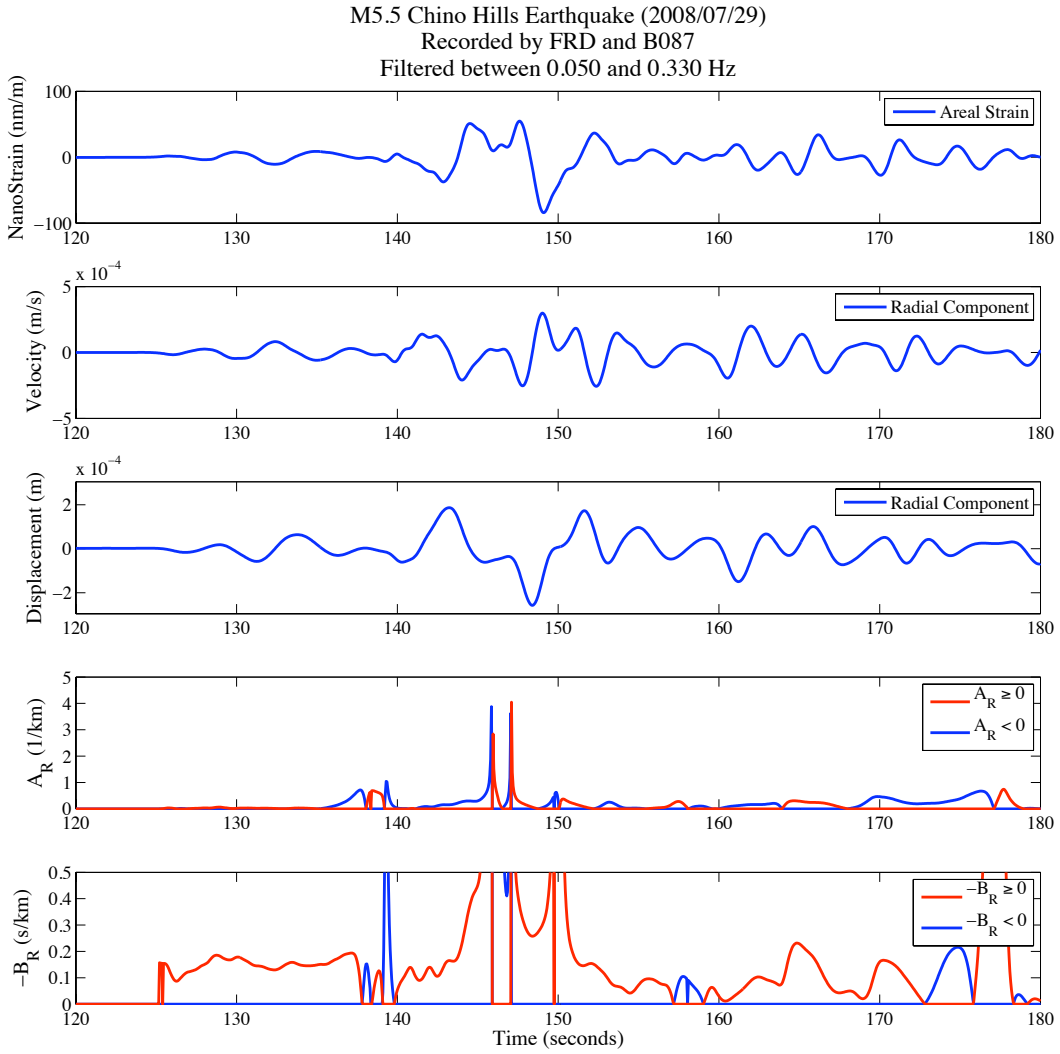

Figure 33. The result of applying Method (1) to the data corresponding to Figure (31) band-pass filtered between 0.05 Hz and 0.33 Hz with a 4-pole Butterworth acausal filter. Instability (or "glitches") in 1D spatial gradient result is likely due to interfering waves at a particular point in time or due to an inappropriate assumption of propagation model. The most consistent section of the record is between 125 and 137 seconds, where stable estimates of the slowness ~0.15 s/km appear to be given.

appears to produce stable slowness estimates of 0.15 s/km between the P- and S-wave in Figure (33). The negative slowness estimates indicate that this method may not be suitable at high frequencies for analyzing regional earthquakes because of the underlying assumption of a plane wave field propagating in a single direction from an isotropic source.

We next examine an example of applying Method (2) to the combination of calibrated formation strain and horizontal ground velocity associated with the same regional earthquake described above. Again, to reduce redundancy, we only look at data collected by the station pair created from borehole GTSM station B087 and co-located Anza seismometer FRD (see Figure 34). Method (2) was applied to this set of data for the same 5 different frequency intervals described above. Figures (35) and (36) illustrate only the 2 lower frequency intervals, namely 0.33 to 0.66 Hz and 0.05 to 0.33 Hz, in order to compare the results between this method and method above (see supplemental Figures A56 – A61 in Appendix 3). The results illustrated in Figures (35) and (36) indicate that this method is able to produce stable results associated with both the propagation direction and radial propagation slowness for regional seismic events. Figure (35) illustrates consistent P-wave slowness values of ~0.13 s/km, S-wave slowness values of ~0.2 s/km, and Rayleigh wave slowness values of ~0.17 s/km. However, at one point the propagation direction jumps down suddenly. By applying Method (2) over a suite of frequency intervals, it may be possible to characterize a variety of seismic phases that may be associated with different center or dominate frequencies. When we decreased the filter range in Figure (36), the sudden propagation drop around 158 seconds in Figure (35) is nearly gone. It's possible that scattered waves interacted with that part of the record and caused the inconsistent direction measurements.

Finally, we examine an example of applying Method (3) to areal strain data, associated with the same earthquake described above, collected by the dense array of calibrated borehole GTSM instruments. Since B082 and B089 are effectively co-located, we only consider the data from one of these instruments. Method (3) was only applied to this set of data for one frequency interval, namely between 0.05 an 0.1 Hz, because the aperture of the 7-element borehole GTSM array is ~40km. A beam was created using

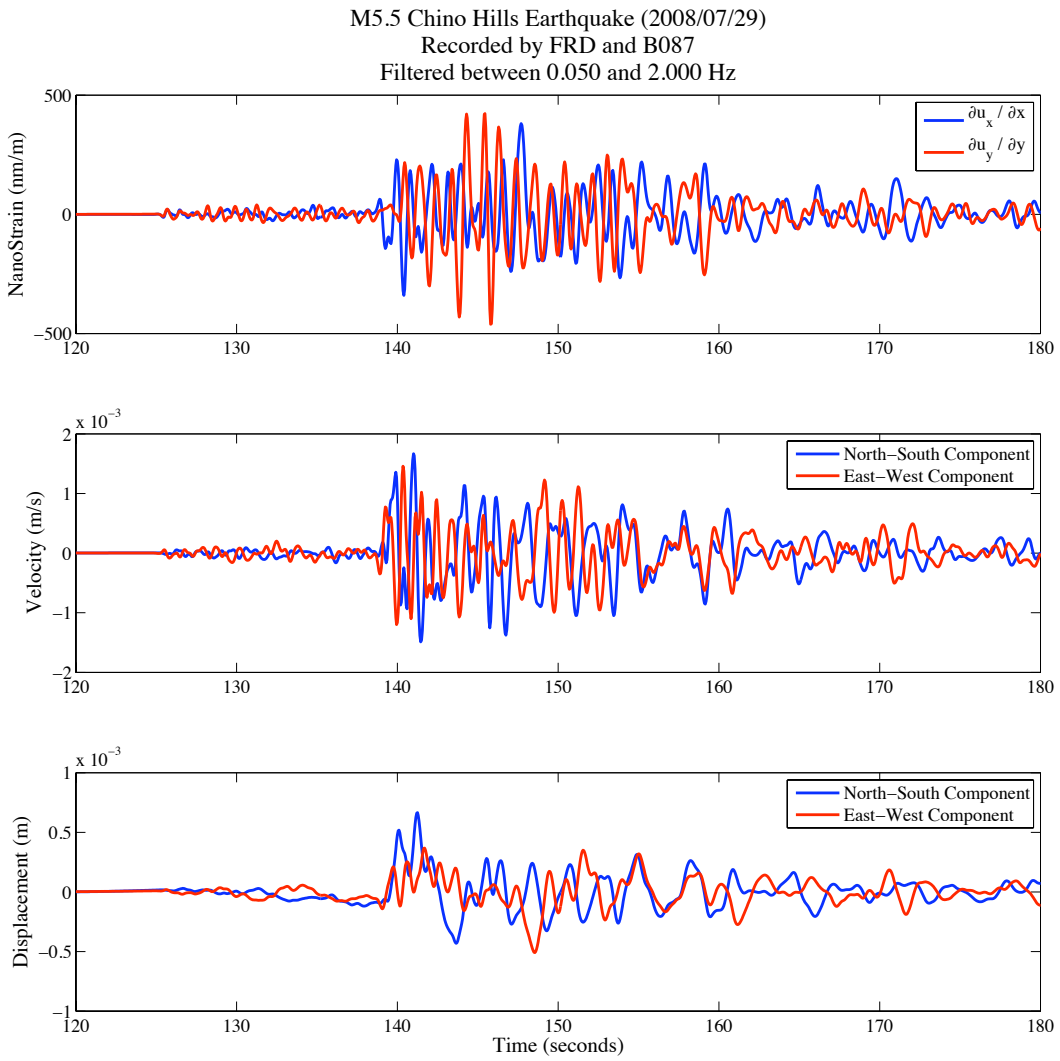

Figure 34. Data used for Method (2) include the diagonal elements of the 2D strain tensor (TOP – BLUE and RED) and the two horizontal components of the ground velocity (MIDDLE – BLUE and RED). Calibrated strain data correspond to borehole GTSM station B087 and the seismic data correspond to Anza broadband seismometer FRD. The original seismograms correspond to the 29 July 2008 M5.5 Chino Hills earthquake band-pass filtered between 0.05 Hz and 2.0 Hz with a 4-pole Butterworth acausal filter.

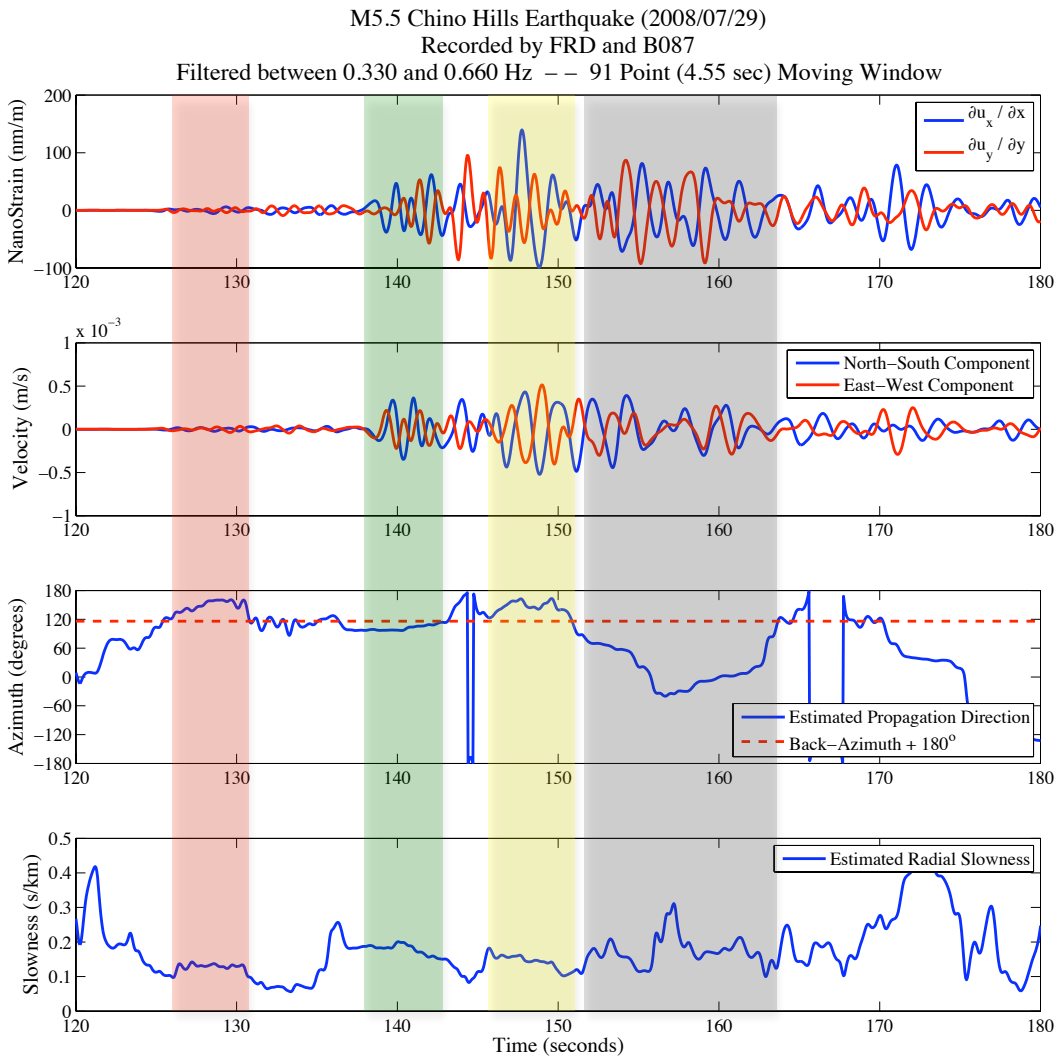

Figure 35. The result of applying Method (2) to the data corresponding to Figure (34) band-pass filtered between 0.33 Hz and 0.66 Hz with a 4-pole Butterworth acausal filter. The dashed line in the "Azimuth" plot indicates the predicted propagation direction across the array had the waves originated from an isotropic source and traveled through an isotropic medium. Instability (or "glitches") in inversion for the horizontal slowness parameters are likely due to interfering waves within the specific time window. at a particular point in time or due to an inappropriate assumption of propagation model. The RED, GREEN, and YELLOW translucent bars illustrate P-wave (0.13 s/km), S-wave (0.2 s/km), and Rayleigh wave phases (0.17 s/km), respectively, while the GRAY translucent bar may be associated with either back-scattered or interfering waves.

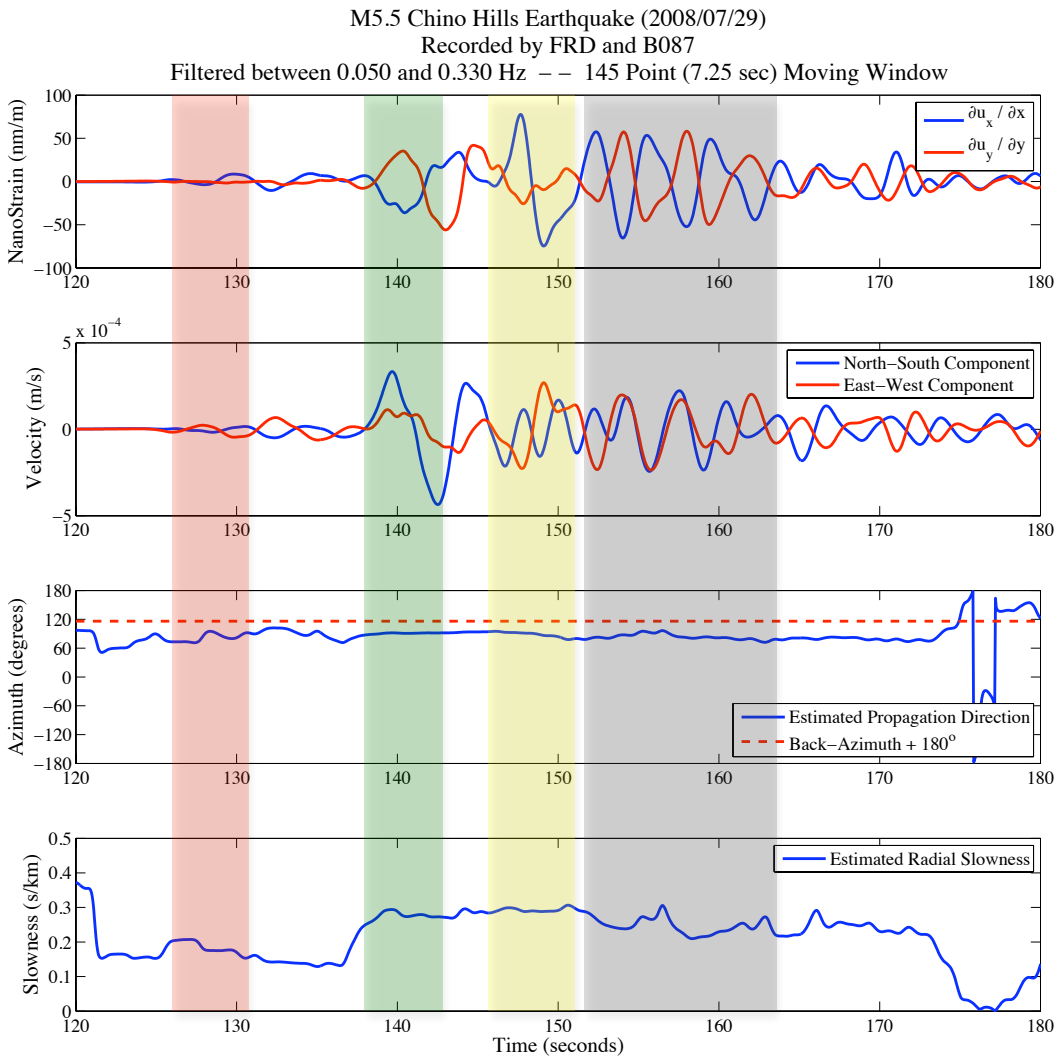

Figure 36. The result of applying Method (2) to the data corresponding to Figure (34) band-pass filtered between 0.05 Hz and 0.33 Hz with a 4-pole Butterworth acausal filter. The dashed line in the "Azimuth" plot indicates the predicted propagation direction across the array had the waves originated from an isotropic source and traveled through an isotropic medium. Instability (or "glitches") in inversion for the horizontal slowness parameters are likely due to interfering waves within the specific time window. The RED, GREEN, and YELLOW translucent bars illustrate P-wave (0.18 s/km), S-wave (0.28 s/km), and Rayleigh wave phases (0.3 s/km), respectively. The GRAY translucent bar in this figure does not seem to contain the same jump in propagation direction associated with the previous frequency increment. The derived azimuth of the waves inside this GRAY bar also appears to be more consisted with the expected propagation direction. Therefore, it may not be likely that the jump in the propagation direction in Figure (35) is related to back-scattering.

the single most dominant waveform in the areal strain record, and the back-azimuth result indicated in Figure (37) was approximately 6 degrees from the back-azimuth estimated from the relative location between the source and center of array (i.e., B086). The radial slowness estimate appears to be 20% smaller than the result indicated for the same time window in Figure (36) using Method (2). However, this could be explained by the fact that higher frequency waves, which do not sample the crust as deep, dominate the signal in that same figure. Another interesting concept, illustrated in Figure (38), is to use the waves in the coda to map out potential sources of scattering in the region surrounding the paired borehole GTSM instrument and broadband seismometer. In a similar manner, it may also be possible map anisotropy by analyzing a large number of coda waves that propagate across the point array to determine whether a statistically significant relationship may be found related to the direction of wave propagation and the horizontal slowness.

Teleseismic Event: M7.0 Haitian earthquake (2010/02/12)

We first examine an example of applying Method (1) to the combination of calibrated areal strain and radial ground velocity associated with the M7.0 Haitian earthquake (2010/01/12). In order to reduce redundancy, we only look at data collected by the station pair created from borehole GTSM station B087 and co-located Anza seismometer FRD (see Figure 39). Method (1) was applied to this set of data for 3 different frequency intervals ranging from 0.008 to 0.05 Hz. Figures (40) and (41) illustrate only the 2 upper frequency intervals, namely 0.03 to 0.05 Hz and 0.01 to 0.03 Hz (see supplemental Figures A62 – A66 in Appendix 3). The results indicate that this method is relatively well suited for analyzing teleseismic earthquakes because, at these source/station distances, we observe very little change in the propagation direction. The S/Ps/Ss phases are consistently around slowness values of ~0.12 s/km for both Figure (40) and (41). The Love wave is not well resolved in either figure because only the radial components of velocity and displacement are used in this analysis. The

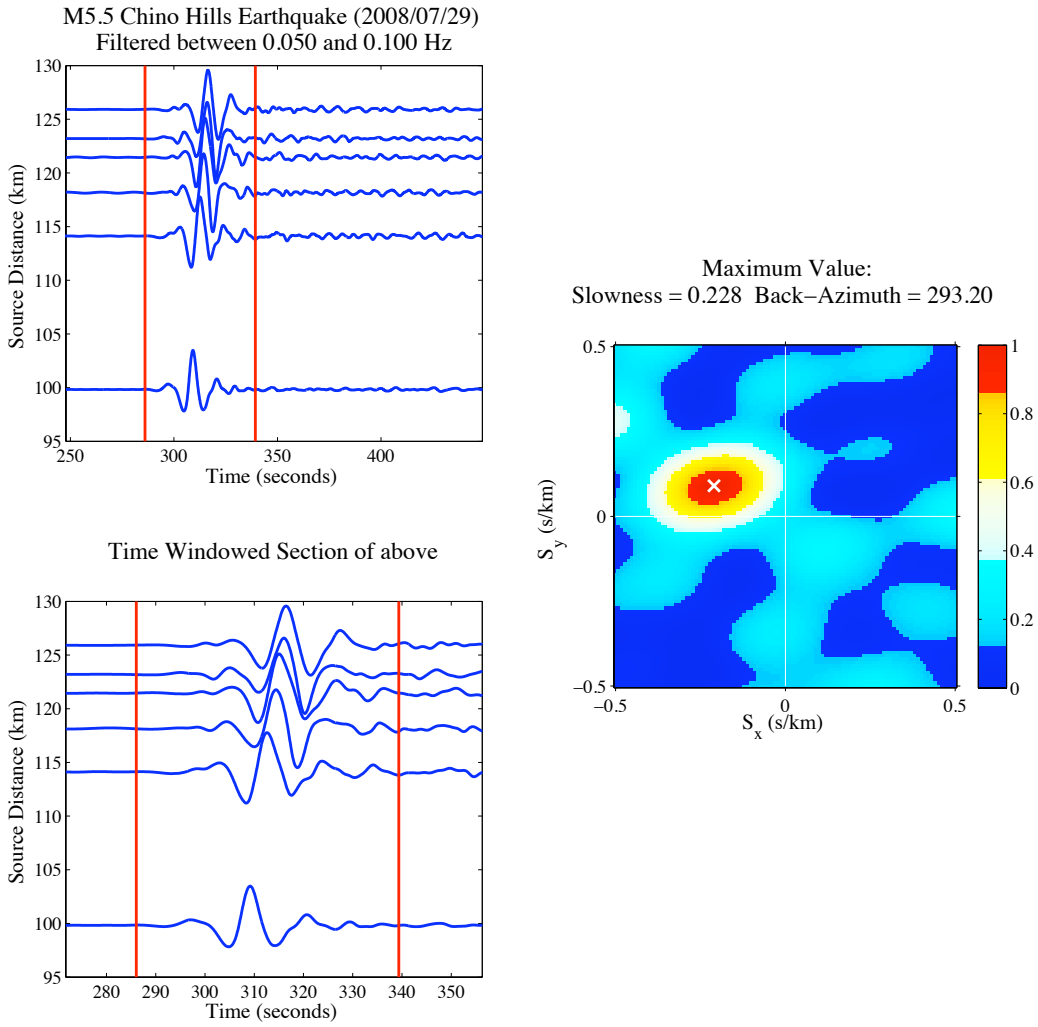

Figure 37. The result of applying Method (3) to the data corresponding to the 29 July 2008 M5.5 Chino Hills earthquake band-pass filtered between 0.05 Hz and 0.1 Hz with a 4-pole Butterworth acausal filter. The vertical red lines in the LEFT panels indicated the time window used to form beams in the frequency/wavenumber domain. The frequency interval considered, in this case, ranged from 0.05 to 0.1 Hz and the 2D wavenumber interval ranged from -0.5 to 0.5 s/km in both the east-west (or *x*) and north-south (or *y*) direction. The "true" back-azimuth estimated from the relative location between the source and B086, which is approximately the center of this 7-elment borehole GTSM array, was found to be ~287 degrees (compare to ~293 degrees above).

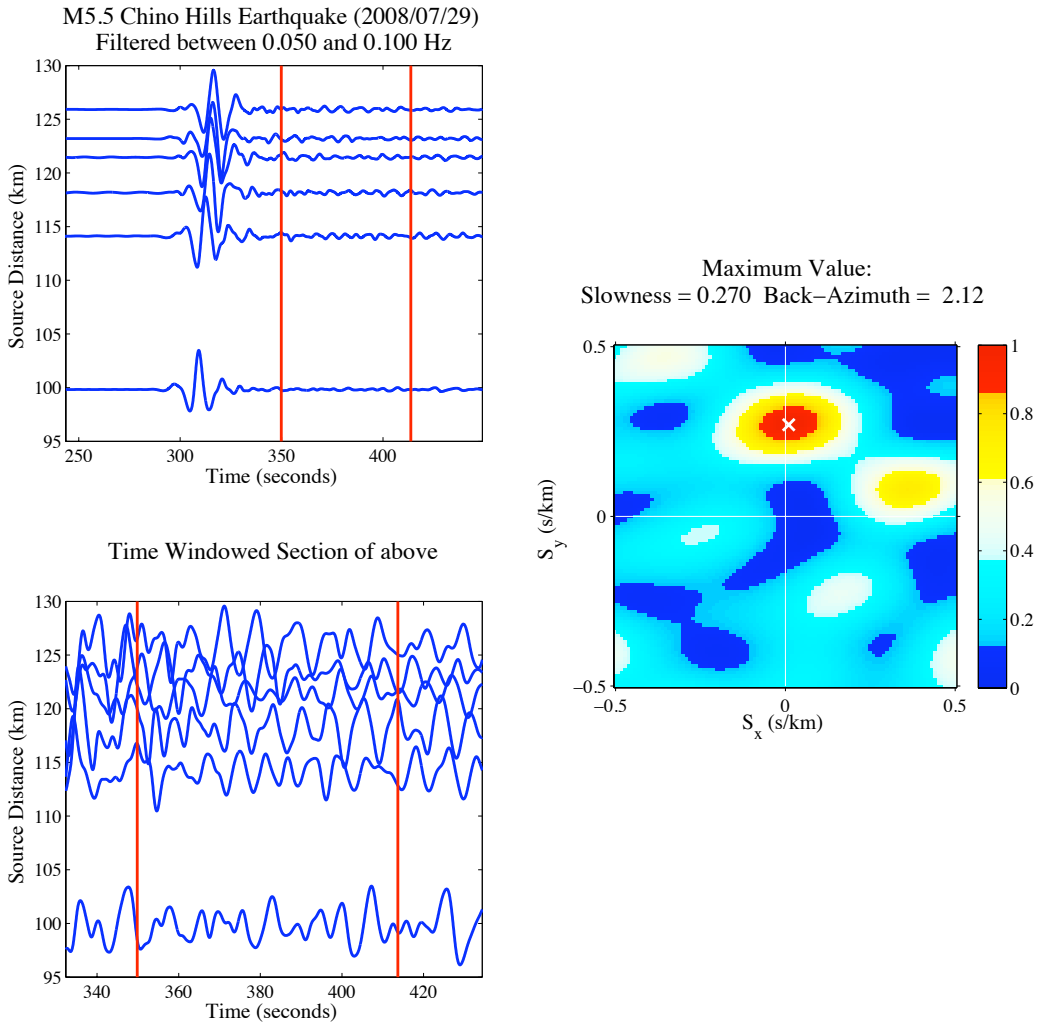

Figure 38. The result of applying Method (3) to the data corresponding to the 29 July 2008 M5.5 Chino Hills earthquake band-pass filtered between 0.05 Hz and 0.1 Hz with a 4-pole Butterworth acausal filter. Nearly identical setup as Figure (37), where instead a window is selected around apparent incoherent noise. However, beam-forming analysis indicates that some of the noise may be coherent after all. In fact, the back-azimuth indicated above may be related to waves back-scattered from sections of the San Andreas Fault, which runs approximately from the south-east to the north-west, located to the north of the study location.

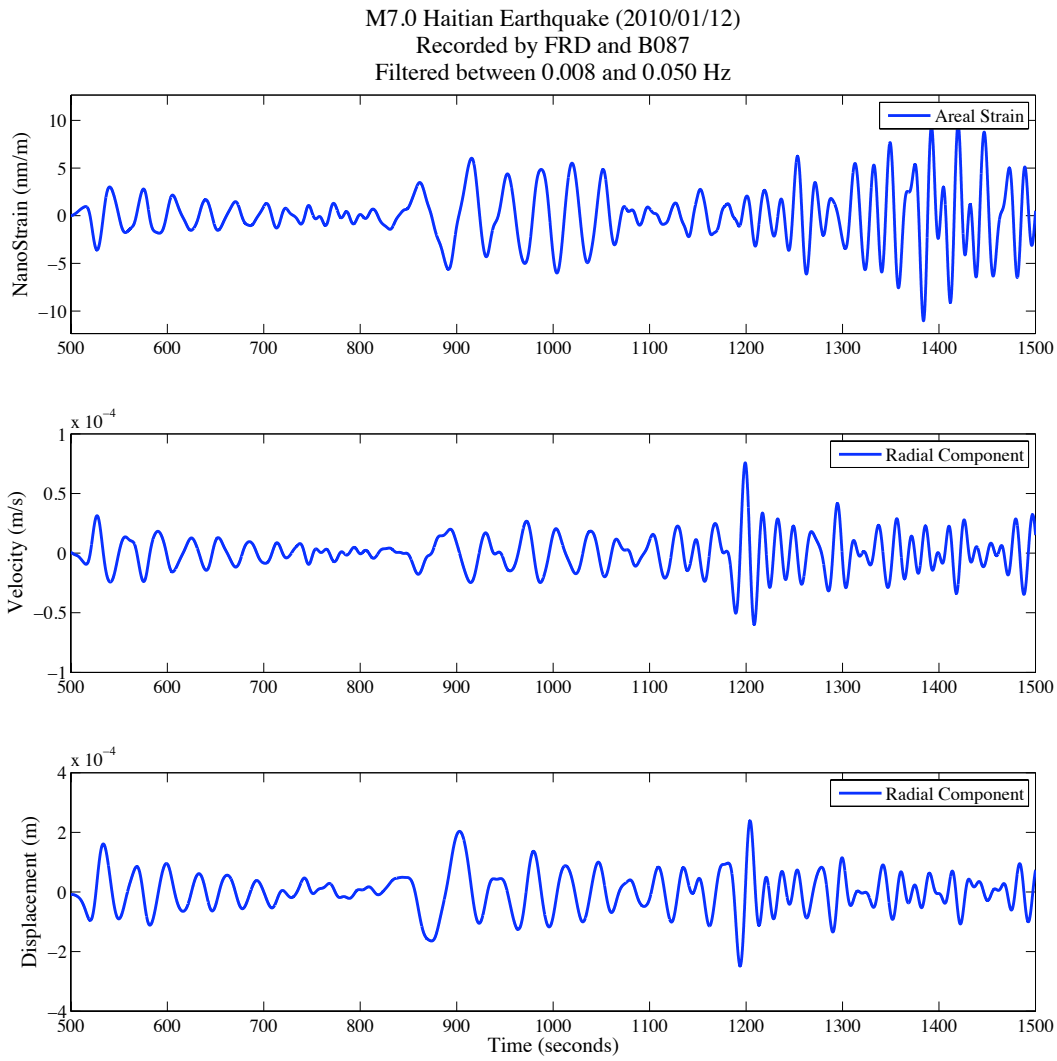

Figure 39. Data used for Method (1) include the areal strain (TOP – BLUE), the radial ground velocity (MIDDLE – BLUE), and the radial ground displacement (BOTTOM – BLUE). Calibrated strain data correspond to borehole GTSM station B087 and the seismic data correspond to Anza broadband seismometer FRD. The original seismograms correspond to the 12 January 2010 M7.0 Haitian earthquake band-pass filtered between 0.008 Hz and 0.05 Hz with a 4-pole Butterworth acausal filter.

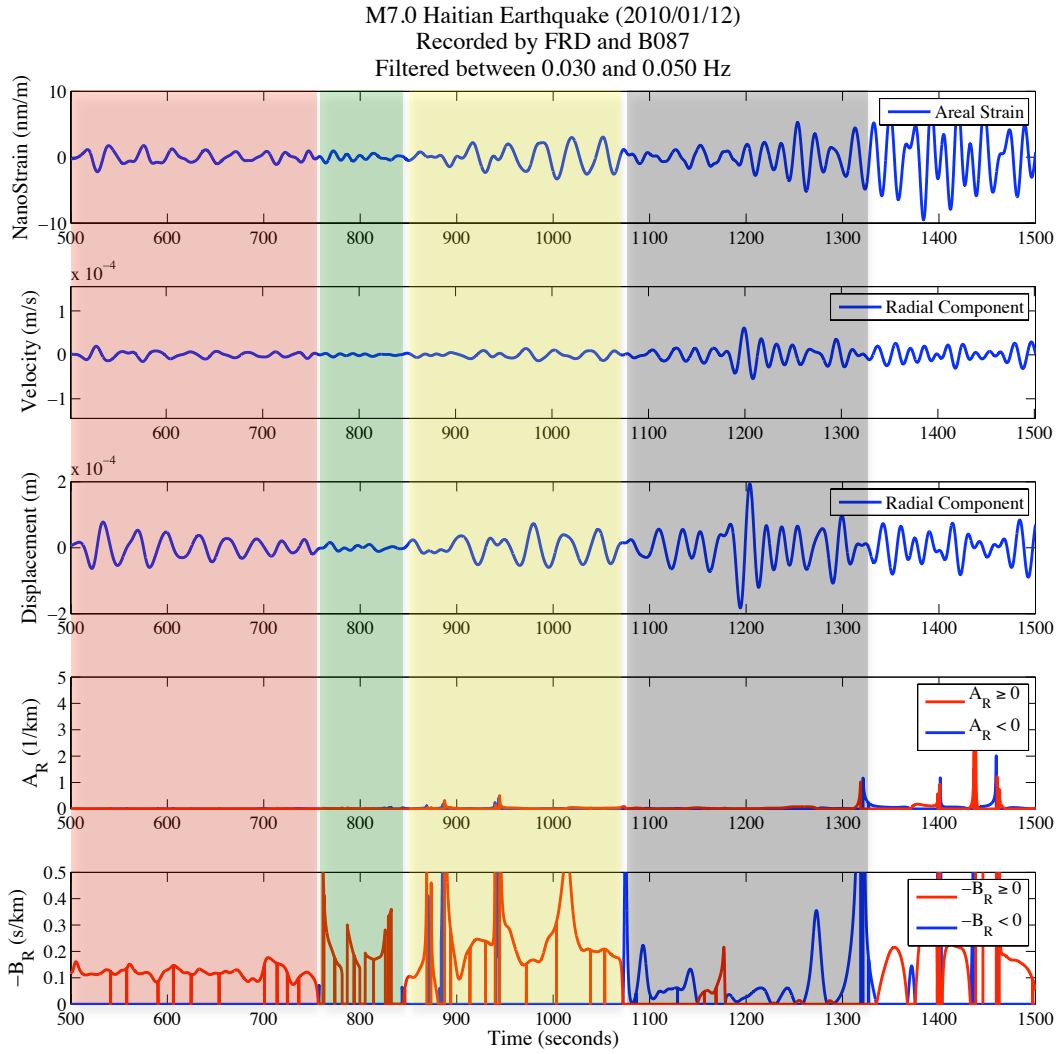

Figure 40. The result of applying Method (1) to the data corresponding to Figure (39) band-pass filtered between 0.03 Hz and 0.05 Hz with a 4-pole Butterworth acausal filter. Instability (or "glitches") in the 1D spatial gradient result is likely due to interfering waves at a particular point in time or due to an inappropriate assumption of propagation direction. The RED, GREEN, and YELLOW translucent bars illustrate S/Ps/Ss waves (0.12 s/km), Love wave (nearly non-existent on radial component), and Rayleigh waves (0.2 s/km). The waves inside the GRAY translucent bar appear to propagate with near 0 slowness, however, we speculate that wave scattering may be causing this result.

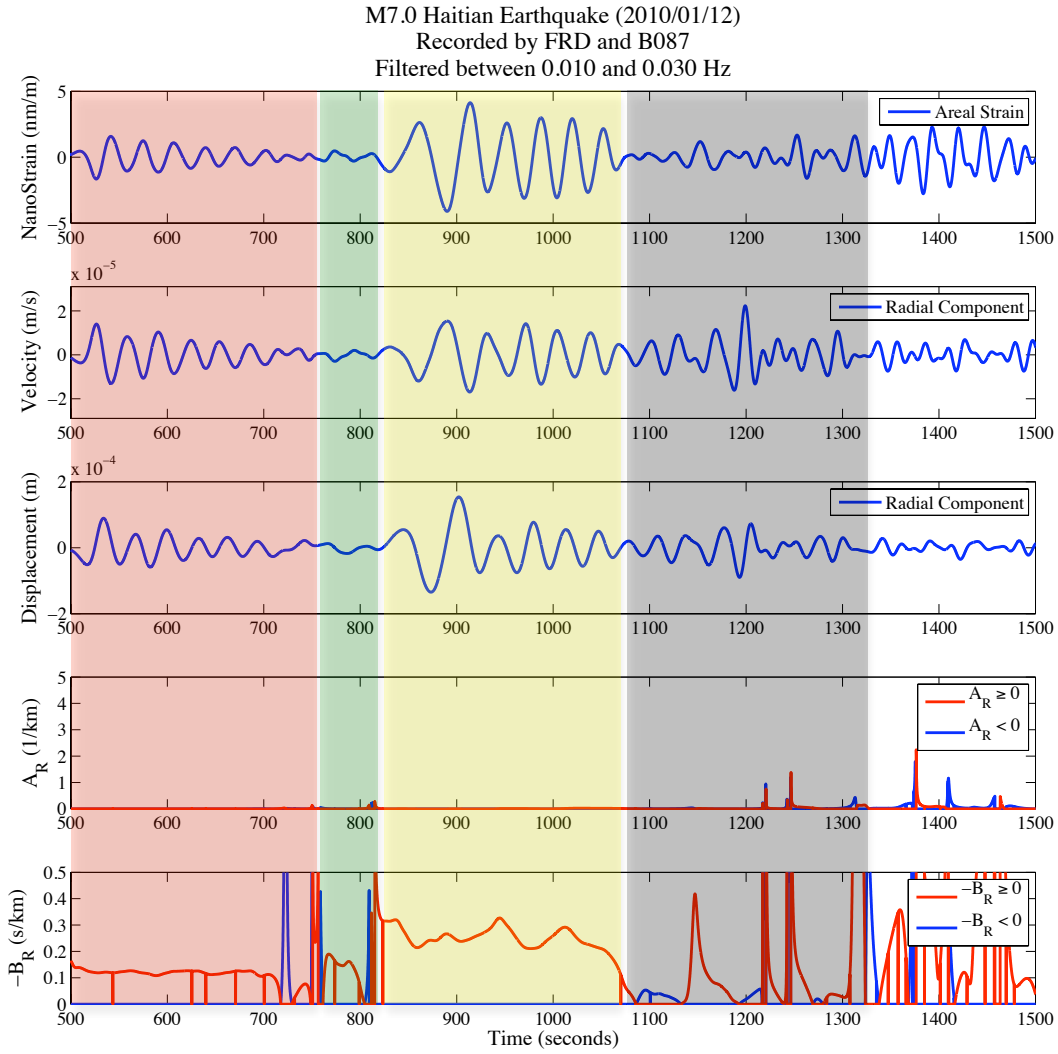

Figure 41. The result of applying Method (1) to the data corresponding to Figure (39) band-pass filtered between 0.01 Hz and 0.03 Hz with a 4-pole Butterworth acausal filter. Instability (or "glitches") in 1D spatial gradient result is likely due to interfering waves at a particular point in time or due to an inappropriate assumption of propagation direction. The RED, GREEN, and YELLOW translucent bars illustrate S/Ps/Ss waves (0.13 s/km), Love wave (nearly non-existent on radial component), and Rayleigh waves (0.23 s/km). Again, the waves inside the GRAY translucent bar appear to propagate with near 0 slowness, however, without additional information we speculate that wave scattering may be causing this result.

inconsistencies observed with the Rayleigh wave in Figure (40) are cleared up by moving to a lower frequency band in Figure (41). Here the Rayleigh wave slowness values are consistently between 0.2 and 0.3 s/km.

We next examine an example of applying Method (2) to the combination of calibrated formation strain and horizontal ground velocity associated with the same teleseismic earthquake described above. Again, to reduce redundancy, we only look at data collected by the station pair created from borehole GTSM station B087 and co-located Anza seismometer FRD (see Figure 42). Method (2) was applied to this set of data for the same 3 different frequency intervals described above. Figures (43) and (44) illustrate only the 2 upper frequency intervals, namely 0.03 to 0.05 Hz and 0.01 to 0.03 Hz, in order to compare the results between this method and method above (see supplemental Figures A67 – A71 in Appendix 3). The results illustrated in Figures (43) and (44) indicate that this method is able to produce stable results associated with both the propagation direction and radial propagation slowness for teleseismic events. We observe very consistent estimates of the propagation direction across the "point seismic array" in both Figure (43) and (44). Slowness values for S/Ps/Ss phases are consistently ~0.13 s/km between both figures. Slowness values for the Rayleigh wave become more consistent at lower frequency bands, reaching ~0.3 s/km. After the Rayleigh wave, we do not see the bizarre propagation characteristics observed for the same waves using Method (1). It would be possible to explain the near-zero slowness values derived from the previous method had the waves propagated across the "point seismic array" perpendicular to the assumed propagation direction. However, we do not observe such a shift in the propagation direction during the same time period using Method (2). Another explanation for the inconsistent nature of the slowness results between Method (1) and Method (2) may be related to the techniques themselves. The slowness information derived using Method (2), at each point in time, is an average over a time window while the same slowness information derived using Method (1) is essentially done on a point-by-point basis. It appears, in these two example data sets, that averaging the strain and seismic information over a small time window yields much more stable estimates of the propagation information.

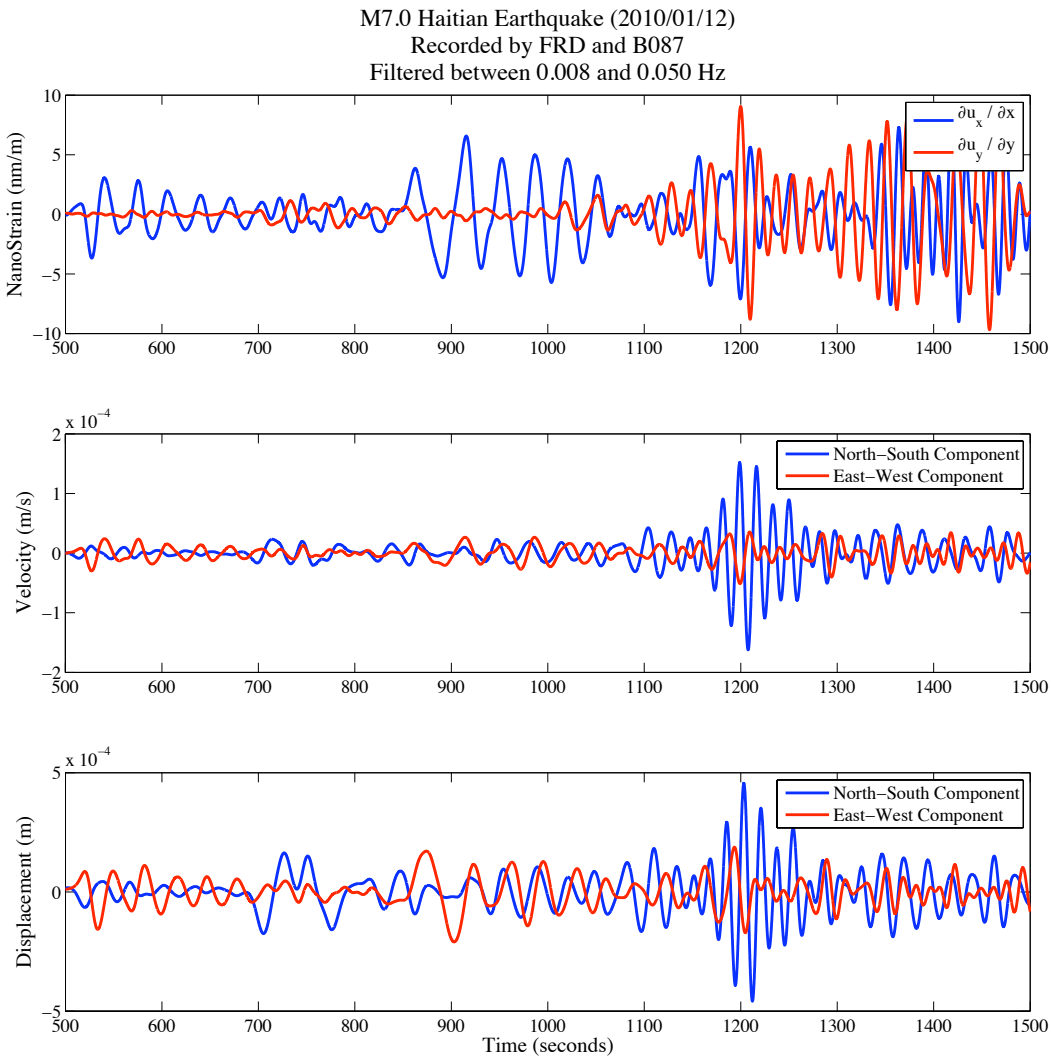

Figure 42. Data used for Method (2) include the diagonal elements of the 2D strain tensor (TOP – BLUE and RED) and the two horizontal components of the ground velocity (MIDDLE – BLUE and RED). Calibrated strain data correspond to borehole GTSM station B087 and the seismic data correspond to Anza broadband seismometer FRD. The original seismograms correspond to the 12 January 2010 M7.0 Haitian earthquake band-pass filtered between 0.008 Hz and 0.05 Hz with a 4-pole Butterworth acausal filter.

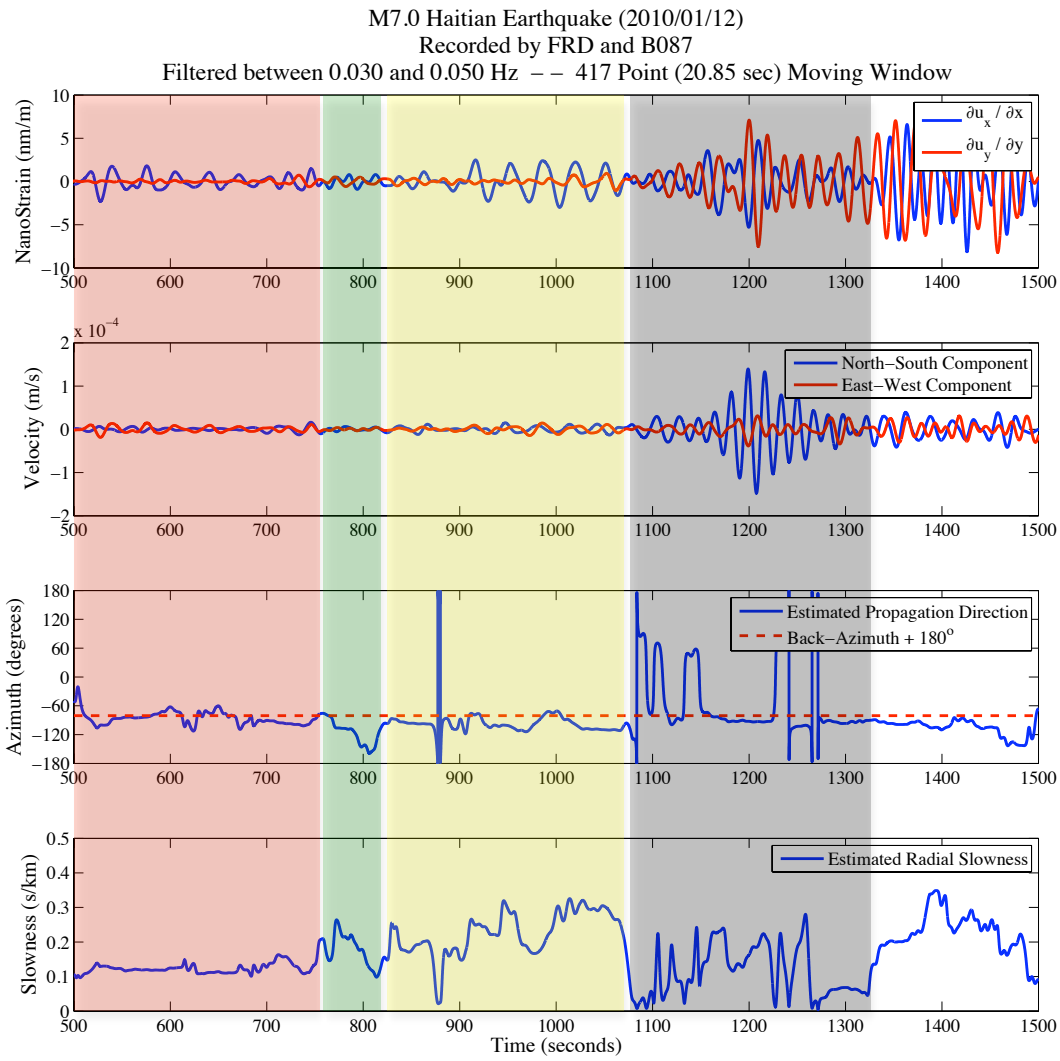

Figure 43. The result of applying Method (2) to the data corresponding to Figure (42) band-pass filtered between 0.03 Hz and 0.05 Hz with a 4-pole Butterworth acausal filter. The dashed line in the "Azimuth" plot indicates the predicted propagation direction across the array had the waves originated from an isotropic source and traveled through an isotropic medium. Instability (or "glitches") in inversion for the horizontal slowness parameters are likely due to interfering waves within the specific time window. The RED, GREEN, and YELLOW translucent bars illustrate S/Ps/Ss waves (0.13 s/km), Love wave (nearly non-existent on the above components), and Rayleigh waves (0.3 s/km). The waves inside the GRAY translucent bar appear to propagate between 0.1 s/km and 0.25 s/km using this method. It is unclear what causes near 0 estimates of the slowness in Figure (40) and (41).

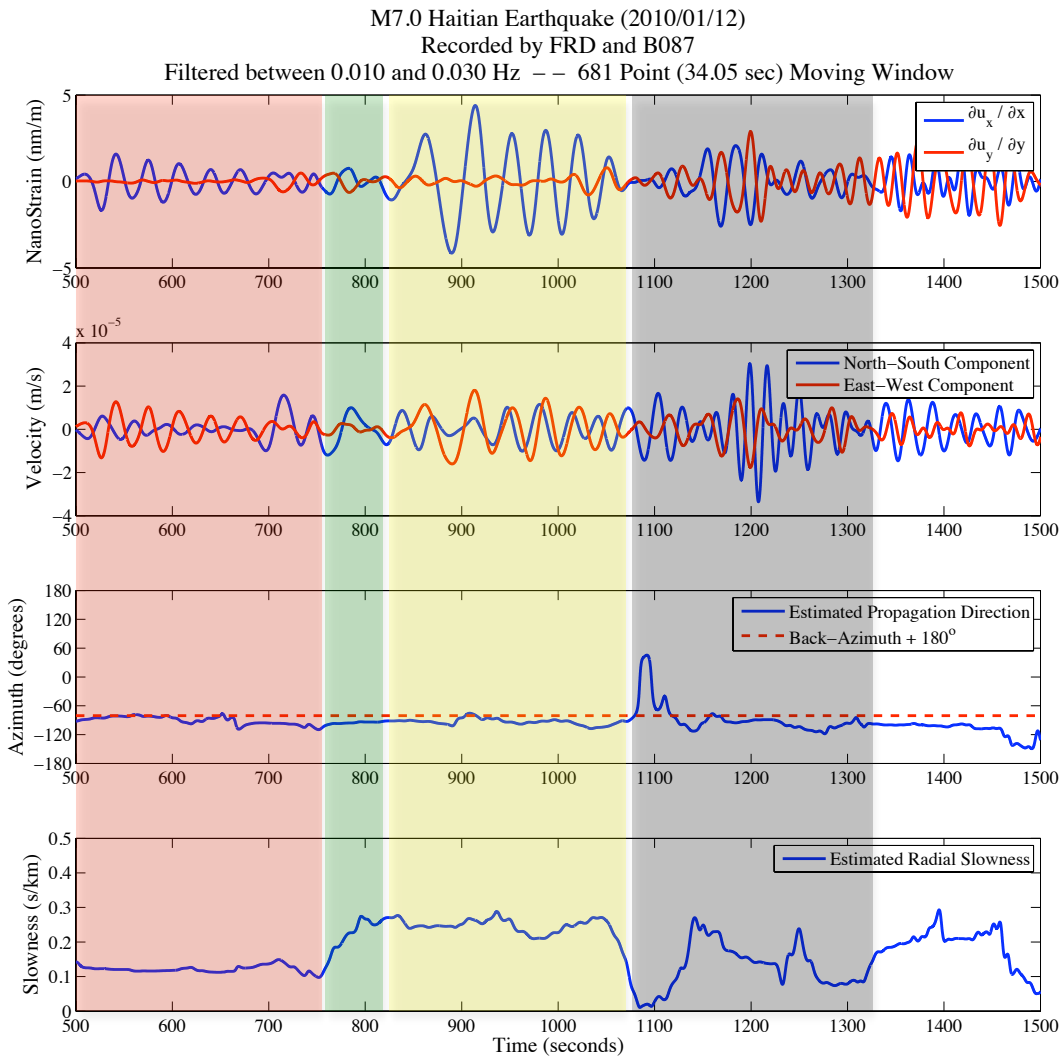

Figure 44. The result of applying Method (2) to the data corresponding to Figure (42) band-pass filtered between 0.01 Hz and 0.03 Hz with a 4-pole Butterworth acausal filter. The dashed line in the "Azimuth" plot indicates the predicted propagation direction across the array had the waves originated from an isotropic source and traveled through an isotropic medium. Instability (or "glitches") in inversion for the horizontal slowness parameters are likely due to interfering waves within the specific time window. The RED, GREEN, and YELLOW translucent bars illustrate S/Ps/Ss waves (0.12 s/km), Love wave (nearly non-existent on the above components), and Rayleigh waves (0.27 s/km). The waves inside the GRAY translucent bar appear to propagate between 0.1 s/km and 0.3 s/km using this method.

Discussion

In this study we examine three potentially useful applications for data collected by a borehole GTSM instrument co-located with a broadband seismometer. These applications are based on either array processing techniques or spatial gradient analysis (also called "wave gradiometry"). However, before applying either method, special care must be taken in order to ensure that all the underlying assumptions associated with that method are maintained during the course of analysis. In addition, the most important assumption to initially verify is that the borehole GTSM instruments are properly calibrated. The results of this study indicate that depending on the specific array configuration, whether a "point array" or a dense array of borehole GTSM instruments, very useful information related to the seismic wavefield can be derived by making simple assumptions about the characteristics associated with propagation. Specifically, these techniques enable estimates of the change in geometrical spreading, horizontal phase velocity, and propagation direction. From this information, it may be possible to characterize potential sources of wave scattering and local anisotropy. Creating maps of this information across a specific region, which contain the types of array configurations described here, would certainly be enlightening. Finally, the applications described in this study are merely a stepping-stone to the ultimate goal of forming a co-located 3-element array consisting of a borehole GTSM instrument, a horizontal rotation-meter, and broadband seismometer. Such a "point array" would enable all the properties associated with wave gradiometry to be fully characterized at a single location on the surface of the earth without having to make the same simplifications/ assumptions found in this study.

CHAPTER 5

Conclusions

We discussed and offered solutions to the problems associated with measurements currently made by borehole Gladwin Tensor Strainmeter (GTSM) instruments associated with the Plate Boundary Observatory (PBO). In addition, we demonstrated that the coefficients derived from seismic data in this study were successful in calibrating and aligning seven borehole GTSM instruments located in southern California. Finally, we discussed techniques that can take advantage of calibrated GTSM instrument data in order to derive useful propagation information associated with seismic wave fields.

Estimating Spatial Displacement Gradients using Seismic Data

Four methods for estimating the spatial displacement gradient using seismic data were presented and tested in this study. The first was the seismo-geodetic method of *Spudich et al.* [1995], the second was the bi-harmonic spline interpolation method of *Sandwell* [1987], the third was the plane-wave polynomial interpolation method (developed here), and the fourth was the method based on the spatial gradient analysis in *Langston* [2007b]. Both synthetic and real sets of data were used in a variety of tests in order to quantify the consistency of each method under different conditions. We found that the third and fourth methods in Chapter (2) were able to calculate accurate spatial displacement gradients more consistently than the first two methods, especially in cases where estimates of the spatial displacement gradient were needed at arbitrary locations toward the perimeter of the array. We found that this was because; 1) the seismo-geodetic method tends to introduce bias into the spatial displacement gradient result when the displacements are not uniform across the seismic array and especially when the gradient

result is derived at a location with an un-even geometrical distribution of stations in the surrounding area, and 2) the biharmonic spline method is not an effective tool for extrapolation in virtually all circumstances. The results of this study were used to decide the choice of spatial displacement gradient estimation to use in the calibration study (i.e., Chapter 3).

Calibrating GTSM Instruments using Seismic Data

We presented a method based on the calibration technique of *Hart et al.* [1996] for successfully deriving the linear relationship between the instrument strain recorded by a borehole GTSM and the reference strain derived from a dense array of seismometers. We also presented a method for quantifying the uncertainty in the estimated calibration coefficients by observing how the coefficient estimates vary with different subsets of the amplitude information across the entire 20-event catalog. We found that, in general, the calibration coefficients for each station do not exhibit significant variation across the ~2 year time period between January 2007 and February 2009. When we compared our calibration result for B081 against the calibration result from *Roeloffs* [2010], we found reasonably good agreement. We also discovered that the default isotropic coupling model for each of the seven borehole GTSM instruments, considered in this study, is not valid. All seven stations required additional cross-coupling parameters in order to reconcile the differences between the measured instrument strains and the reference strains derived from broadband seismometers. We also observed, in some cases, significant errors associated with misalignment up to 50 degrees off the specified instrument orientation (see Table 3.09 for specific values).

Viewing the Seismic Wavefield through Calibrated GTSM Data

We discussed three techniques that utilize calibrated borehole GTSM data. The first two techniques required data collected by a "point seismic array," which consists of a borehole GTSM instrument collocated with either a broadband seismometer, a horizontal rotation-meter, or both. In this study, we discussed and demonstrated that important characteristics of seismic wave fields can be decomposed at a single location on the earth's surface using data collected by co-located strain and seismic instruments. We also demonstrated that simple array processing techniques can be applied to strain data collected by a dense network of calibrated borehole GTSM instruments to determine the horizontal phase velocity and propagation direction of a wave that traverses an array.

Future Work

The results of this study demonstrate that borehole GTSM instruments can be calibrated using strain information derived from seismic data. Unfortunately, not all borehole GTSM instruments are surrounded by a dense, high-quality seismic network like the Anza array in southern California. Instead it may be necessary to setup PASCAL experiments for individual borehole GTSM stations or small groups of borehole GTSM stations that need calibration. After leaving a small group of broadband seismometers in the field for at least one year, enough data corresponding to large (M>7) teleseismic events should be available to be applied to the borehole strainmeter calibration process described in this study. Alternatively, a single broadband seismometer may be installed at the same location as a borehole GTSM in order to perform the necessary calibration. As described in Chapter (2), the spatial displacement gradients needed to estimate the reference formation strains can be determined at a single location when the ground velocity, propagation direction, and horizontal wave slowness is known. The broadband seismometer would provide the ground velocity measurements, the source location

relative to the station location would provide the propagation direction, and simple models of earth structure may be assumed in order to derive the apparent slowness associated with each major phase within the seismogram.

We hope the popularity of "point arrays" grows over time to the point where broadband seismic instruments are routinely installed at the same location as a borehole strainmeter, a horizontal rotation-meter, or both. This is because all the properties of the seismic wave field that can be described by spatial gradient analysis in 2D may characterized at a single "point" location on the surface of the earth. The measurement capabilities of a tool such as this would be unprecedented.

Since some borehole GTSM instruments in this study exhibited large alignment errors (not to mention the unknown alignment errors associated with the co-installed, short-period borehole seismometers), it might be beneficial to include the type of analysis performed here as an additional form of control in tidal calibration software [e.g., *Agnew*, 1996] currently available today. Other considerations for the future include an easy-to-use Matlab® software program capable of performing all the necessary calibration related analyses described in this study.

BIBLIOGRAPHY

Agnew, D. C. (1996), SPOTL: Some programs for ocean-tide loading, SIO Ref. Ser. 96-8, Scripps Institution of Oceanography, La Jolla, CA.

Bodin, P., et al. (1997), Dynamic Deformations of Shallow Sediments in the Valley of Mexico, Part I: Three-Dimensional Strains and Rotations Recorded on a Seismic Array, *Bulletin of the Seismological Society of America*, Vol. 87, p. 528 – 539.

EarthScope Website (2009), [http://www.earthscope.org].

Frank, F. C. (1966), Deduction of Earth strains from survey data, *Bulletin of the Seismological Society of America*, Vol. 56, p. 35 – 42.

Gladwin, M. T. and Hart, R. H. G. (1985), Design parameters for borehole strain instrumentation, *Pure and Applied Geophysics*, Vol. 123, p. 59 – 80.

Gladwin, M. T., et al. (1985), Tidal calibration of borehole vector strain instruments (abstract), *Eos: Transactions of the American Geophysical Union*, Vol. 66, p. 1057.

Gladwin Tensor Strainmeter (GTSM) Technologies Website (2010), [http://www.gtsmtechnologies.com].

Gomberg, J., et al. (1999), The strain in the array is mainly in the plane (waves below 1 Hz), *Bulletin of the Seismological Society of America*, Vol. 89, p. 1428 – 1438.

Hart, R. H. G., et al. (1996), Tidal calibration of borehole strain meters: Removing the effects of small-scale inhomogeneity, Journal of Geophysical Research, Vol. 101, No. B11, p. 25553 – 25571.

Incorporated Research Institutions for Seismology (IRIS) Website (2010), [http://www.iris.edu].

Jackson, M. E. and K. R. Bohnenstiehl (2005), EarthScope Plate Boundary Observatory GPS and Strainmeter Site Permitting: A Perspective Two Years into the Construction Phase, Seismological Research Letters, Vol. 76, No. 6, p. 671 – 672.

Johnston, M. J. S. et al. (2006), Continuous borehole strain and pore pressure in the near field of the 2004 M 6.0 Parkfield, California, Earthquake: Implications for nucleation, fault response, earthquake prediction, and tremor, *Bulletin of the Seismological Society of America*, Vol. 96, p. S56 – S72.

Langston, C. A. (2007a), Spatial gradient analysis for linear seismic arrays, *Bulletin of the Seismological Society of America*, Vol. 97, p. 265 – 280.

Langston, C. A. (2007b), Wave gradiometry in two dimensions, *Bulletin of the Seismological Society of America*, Vol. 97, p. 401 – 416.

Langston, C. A. (2007c), Wave gradiometry in the time domain, *Bulletin of the Seismological Society of America*, Vol. 97, p. 926 – 933.

Langston, C. A. and Liang, C. (2008), Gradiometry for polarized seismic waves, *Journal of Geophysical Research*, Vol. 113, B08305.

Linde, A. T. et al. (1996), A slow earthquake sequence on the San Andreas fault, *Nature*, Vol. 283, p. 65 – 68.

McCausland, W. A. et al. (2008), New insights into Cascadia slow slip events using Plate Boundary Observatory borehole strainmeters, *Eos, Transactions, American Geophysical Union*, Vol. 89, No. 53, Fall Meeting Supplement, Abstract G21B-0691.

Paolucci, R. and Smerzini, C. (2008), Earthquake-induced Transient Ground Strains from Dense Seismic Networks, *Earthquake Spectra,* Vol. 24, No. 2, p. 453 – 470.

Roeloffs, E. (2010), Tidal calibration of PBO borehole strainmeters: The role of vertical and shear coupling, Journal of Geophysical Research, Vol. 115, B06405.

Roeloffs, E., et al. (2004). Review of borehole strainmeter data collected by the U.S. Geological Survey, 1985-2004, PBO Standing committee, EarthScope, 55 pp.

Sandwell, D. T. (1987), Biharmonic spline interpolation of GEOS-3 and SEASAT altimeter data, *Geophysical Research Letters*, Vol. 2, p. 139 – 142.

Shimada, S. et al. (1987), Coseismic strain steps observed by three-component borehole strainmeters, *Tectonophysics*, Vol. 144, p. 207 – 214.

Smerzini, C., et al. (2006), Surface ground strains evaluated from weak motion records of dense seismograph arrays: the case of Parkway Valley, New Zealand, *Proceedings of the 1st European Conference on Earthquake Engineering and Seismology*, Geneva, Paper No. 879.

Spudich, P., et al. (1995), Transient stresses at Parkfield, California, produced by the M7.4 Landers earthquake of June 28, 1992: Observations from the UP-SAR dense seismograph array, *Journal of Geophysical Research*, Vol. 100, No. B1, p. 675 – 690.

Spudich, P. and Fletcher, J. B. (2008), Observation and Prediction of Dynamic Ground Strains, Tilts, and Torsions Caused by the Mw 6.0 2004 Parkfield, California, Earthquake and Aftershocks, Derived from UPSAR Array Observations, *Bulletin of the Seismological Society of America*, Vol. 98, p. 1898 – 1914.

Sturkell, E. et al. (2006), Volcano geodesy and magma dynamics in Iceland, *Journal of Volcanology and Geothermal Research*, Vol. 150, p. 14 – 34.

University NAVSTAR Consortium (UNAVCO) (2004), Critical design of PBO borehole strainmeter network, Plate Boundary Observatory, Boulder, Colorado, 72 pp.

University NAVSTAR Consortium (UNAVCO) Website (2010), [http://pboweb.unavco.org].

Vernon, F. L. (1989), Analysis of data recorded on the ANZA seismic network, Ph.D. Thesis. University of California San Diego.

Wessel, P., and W. H. F. Smith (1998), New, improved version of generic mapping tools released, *Eos, Transactions, American Geophysical Union*, Vol. 79, No. 579.

APPENDIX 1

Supplemental Information for Chapter Two

Summary

A supplemental script written in Matlab® is included in this appendix in order to illustrate a particularly useful set of optimization tools. In this example, the minimization problem consists of a very simple objective function associated with the correlation between two windows of seismic data. The timelag that results in the smallest misfit between the two windows of seismic data is returned. See the next section for the example.

Supplemental figures are included in this appendix in order to provide the reader with additional visual verification/insight to the words and figures available in Chapter (2). The synthetic data in Figures (A1) – (A16) were generated based on an array configuration similar to the Anza Seismic Network, in Southern California, and a 7-element subset of the Plate Boundary Observatory (PBO) GTSM instruments inside the Anza network (see Figure 4). The main purpose of Figures (A1) – (A16) is to identify the largest resolvable wavenumber associated with each method of spatial displacement gradient estimation for an array configured similar to a 10-element subset of the Anza Seismic Network. Figures (A1) – (A8) illustrate the result from performing a Leave Out Station Scenario (LOSS) for Anza seismic stations FRD and LVA2, where the synthetic seismic displacement data at the remaining 9 stations are used to predict the displacements at the "left out" station (see pages 33 – 40 for more details). Figures (A9) – (A16) illustrate the result from predicating the spatial displacement gradients at PBO GTSM stations B087 and B088, where the synthetic seismic displacement data at all 10 stations are used to estimate the spatial displacement gradient at each PBO GTSM station (see pages 33 – 40 for more details).

The main purpose of Figures (A17) – (A24) is to illustrate the performance of each method of spatial displacement gradient estimation, for the same 10-element subset of the Anza Seismic Network, for the 2009/09/29 M8.1 Samoa Island earthquake. Figures (A17) – (A21) illustrate the result from performing a Leave Out Station Scenario (LOSS) for Anza seismic stations FRD and LVA2, where the real seismic displacement data at the remaining 9 stations are used to predict the displacements at the "left out" station (see pages 40 – 50 for more details). Figures (A22) – (A24) are similar to Figures (14) – (16), except the LOSS is performed on Anza station LVA2.

Sample Program

```
function timelag = tlag_search(Trace01, Trace02, dt)

%%%%%%%%%%%%%%%%%%%%%%%%%%%%%%%%%%%%%%%%%%%%%%%%%%%%%%%%%%%%%%%%%%%%%%%%%%%%
%   "tlag_search" searches for the "timelag" that results in the best
%   correlation between "Trace01" and "Trace02". Let "N01" and "N02"
%   be equal to the number of time samples in "Trace01" and "Trace02",
%   respectively. "N01" and "N02" must not be equal, "N02" must be
%   greater than "N01" and both must be ODD. The center of both
%   "Trace01" and "Trace02" must correspond to the same instant in
%   time or else the time-lag result is meaningless.
%
%   - INPUT PARAMTERS -
%   "Trace01" = window from reference seismogram (col/row vector)
%   "Trace02" = window from seismogram to compare (col/row vector)
%   "dt" = time increment of "Trace01" and "Trace02" (scalar)
%
%   - OUTPUT PARAMTERS –
%   "timelag" = time-lag resulting from best correlation (scalar)
%
%%%%%%%%%%%%%%%%%%%%%%%%%%%%%%%%%%%%%%%%%%%%%%%%%%%%%%%%%%%%%%%%%%%%%%%%%%%%

    N01 = numel(Trace01);
    N02 = numel(Trace02);

    if  mod(N01,2) == 0 || mod(N02,2) == 0
        error('N01 and N02 must be ODD!');
    end
    if N01 >= N02
        error('N02 must be greater than N01!');
    end

    N01mid = (N01-1)/2 + 1;
    N02mid = (N02-1)/2 + 1;
    Ndiff = (N02-N01)/2;

    t02 = 0:dt:(N02-1)*dt;
    t01 = t02(Ndiff+1:N02-Ndiff);

    timelag = fminbnd(@fun01, -Ndiff*dt, Ndiff*dt);

    % "fun01" accepts "trylag" as input, and outputs "sse",
    % the sum of squares error, between "Trace01" and interpolated
    % time-lag data from "Trace02".
    function sse = fun01(trylag)

        temp02 = spline(t02,Trace02,t01+trylag);
        sse = sum(abs(Trace01-temp02).^2);

    return
    end
return
end
```

Figures

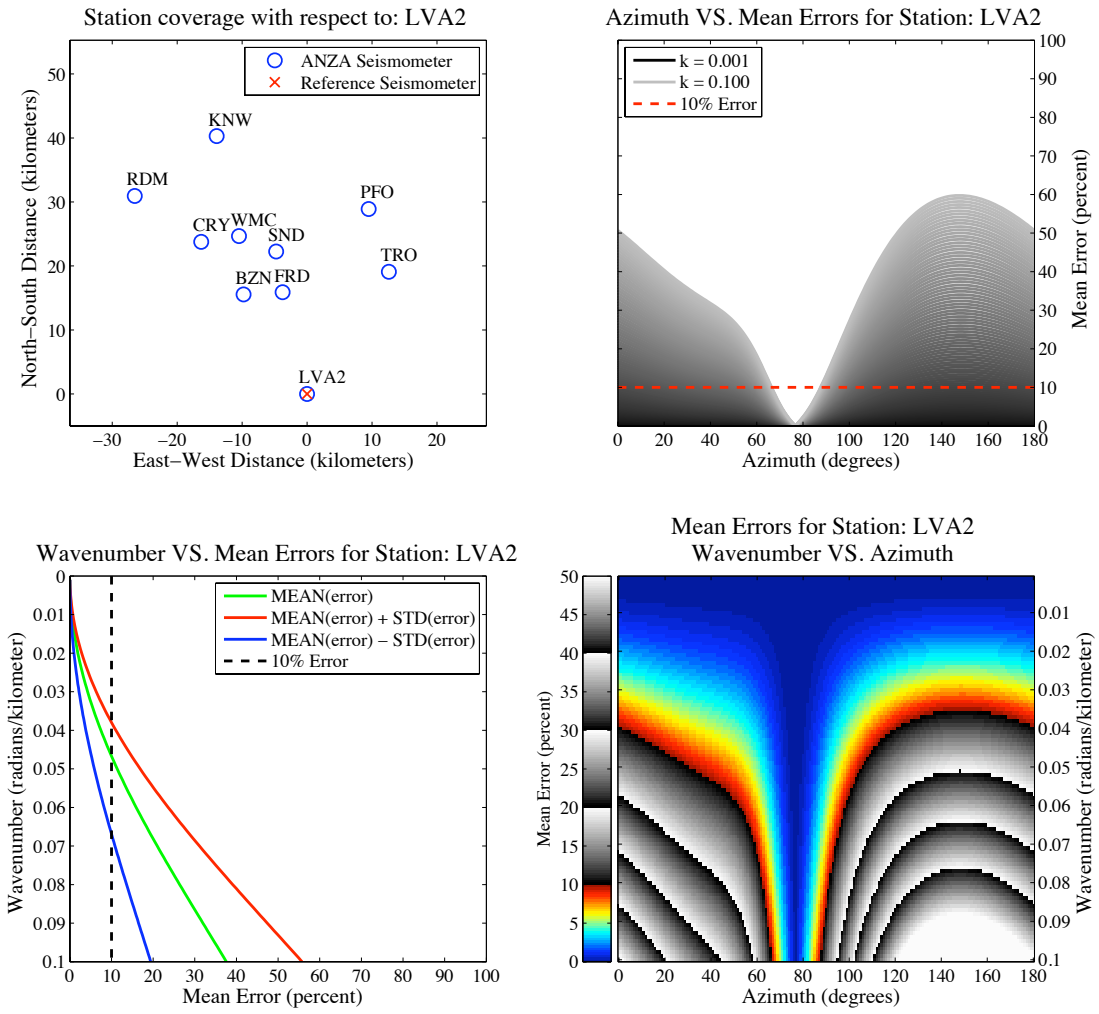

Figure A1. Illustrates the errors resulting from performing a Leave Out Station Scenario (LOSS) using Method (1) to predict the displacements at Anza station LVA2.

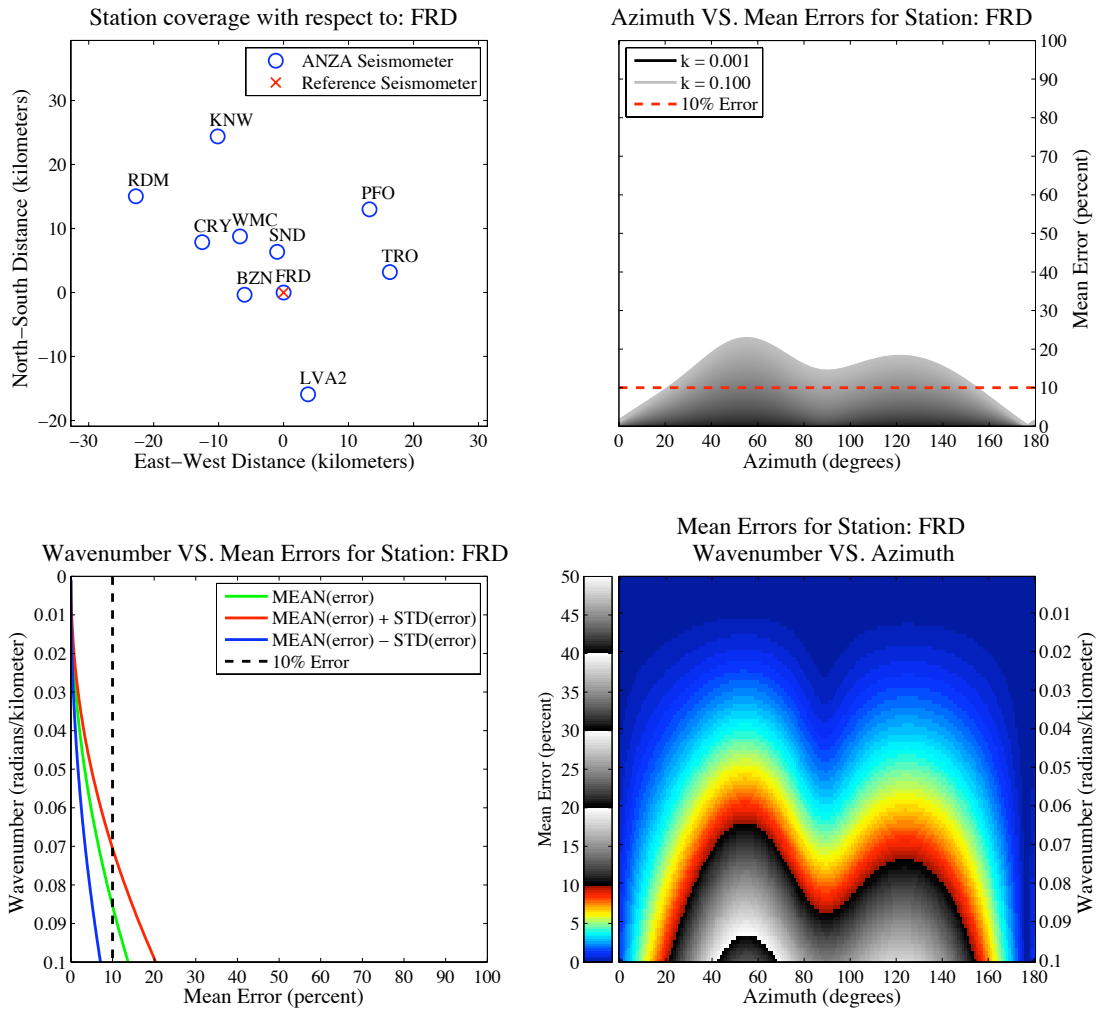

Figure A2. Illustrates the errors resulting from performing a Leave-Out Station Scenario (LOSS) using Method (1) to predict the displacements at Anza station FRD.

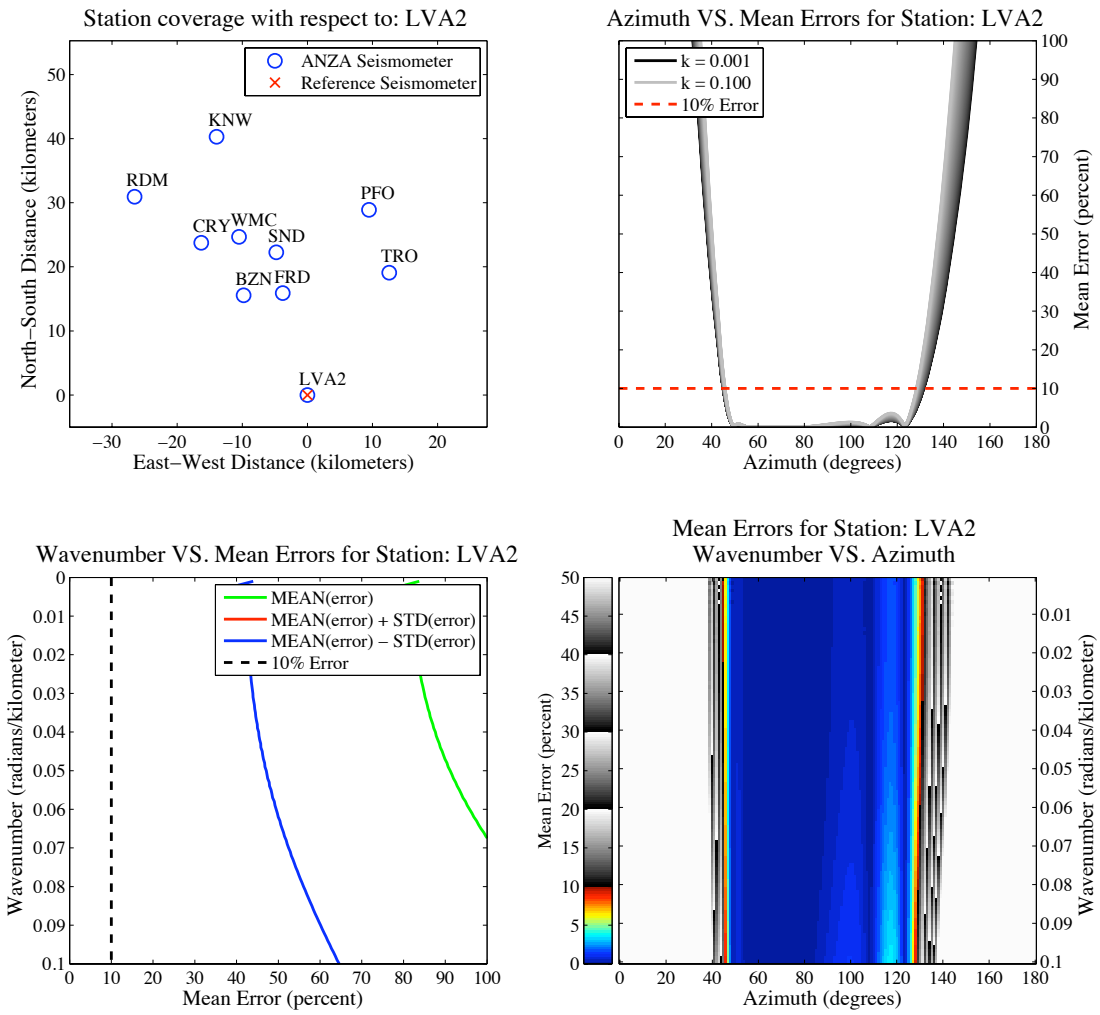

Figure A3. Illustrates the errors resulting from performing a Leave Out Station Scenario (LOSS) using Method (2) to predict the displacements at Anza station LVA2.

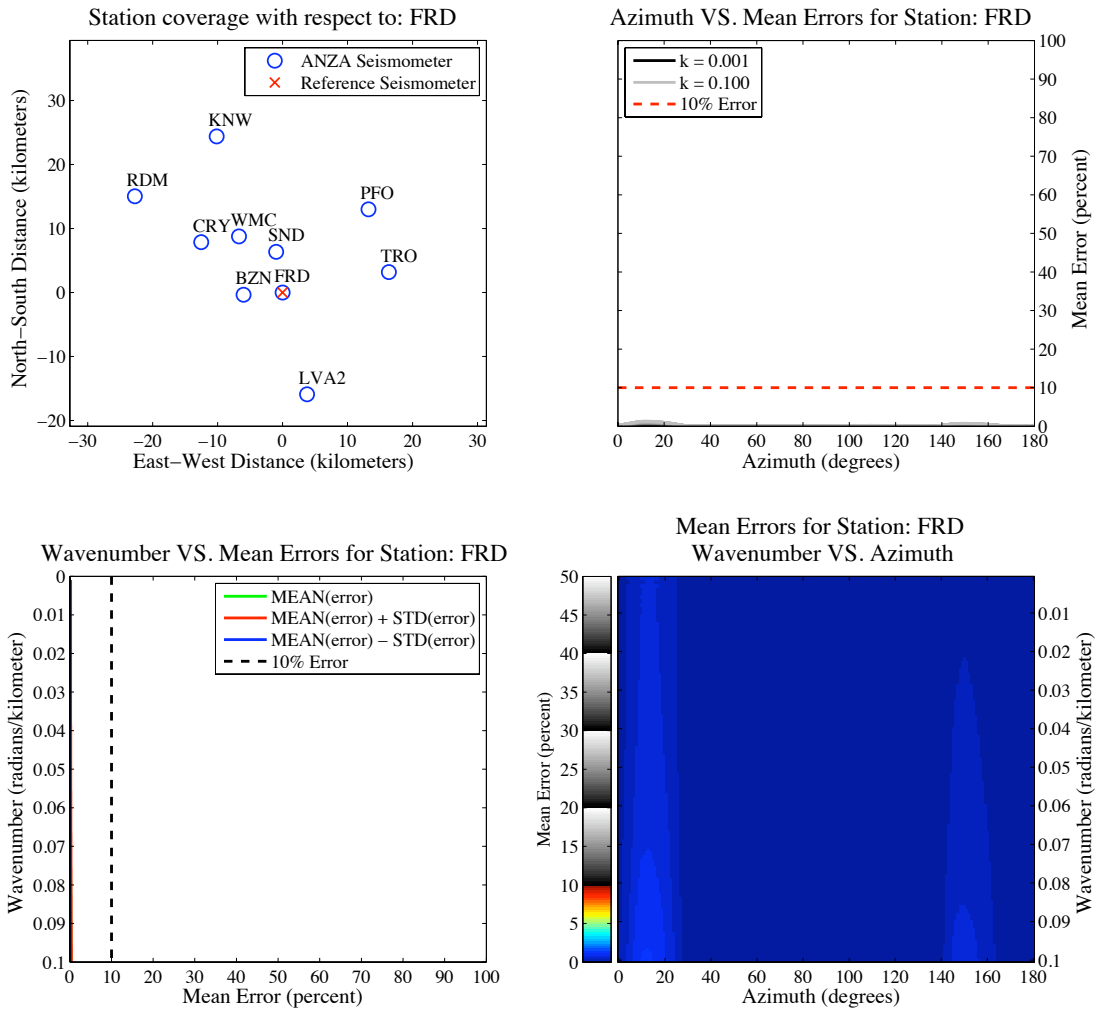

Figure A4. Illustrates the errors resulting from performing a Leave Out Station Scenario (LOSS) using Method (2) to predict the displacements at Anza station FRD.

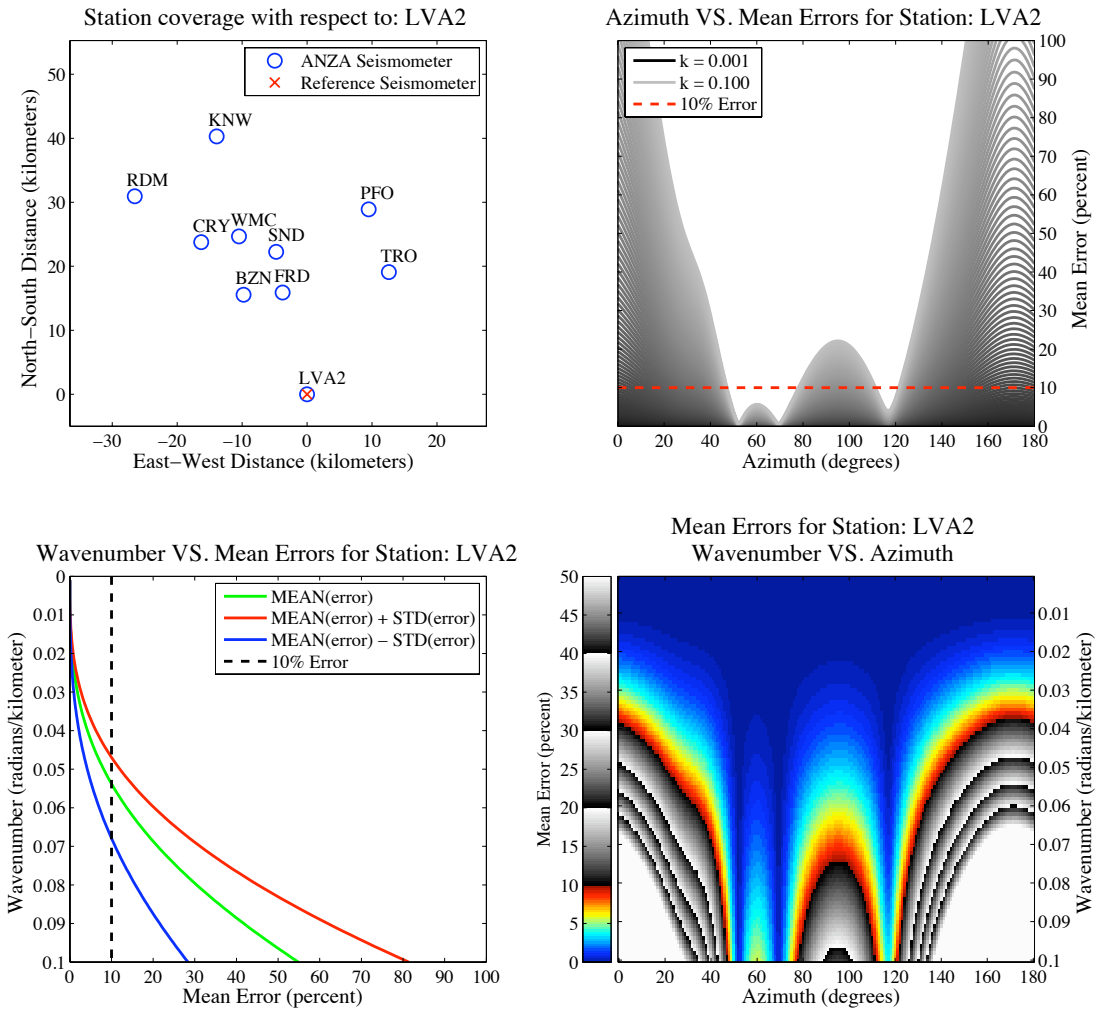

Figure A5. Illustrates the errors resulting from performing a Leave Out Station Scenario (LOSS) using Method (3a) to predict the displacements at Anza station LVA2.

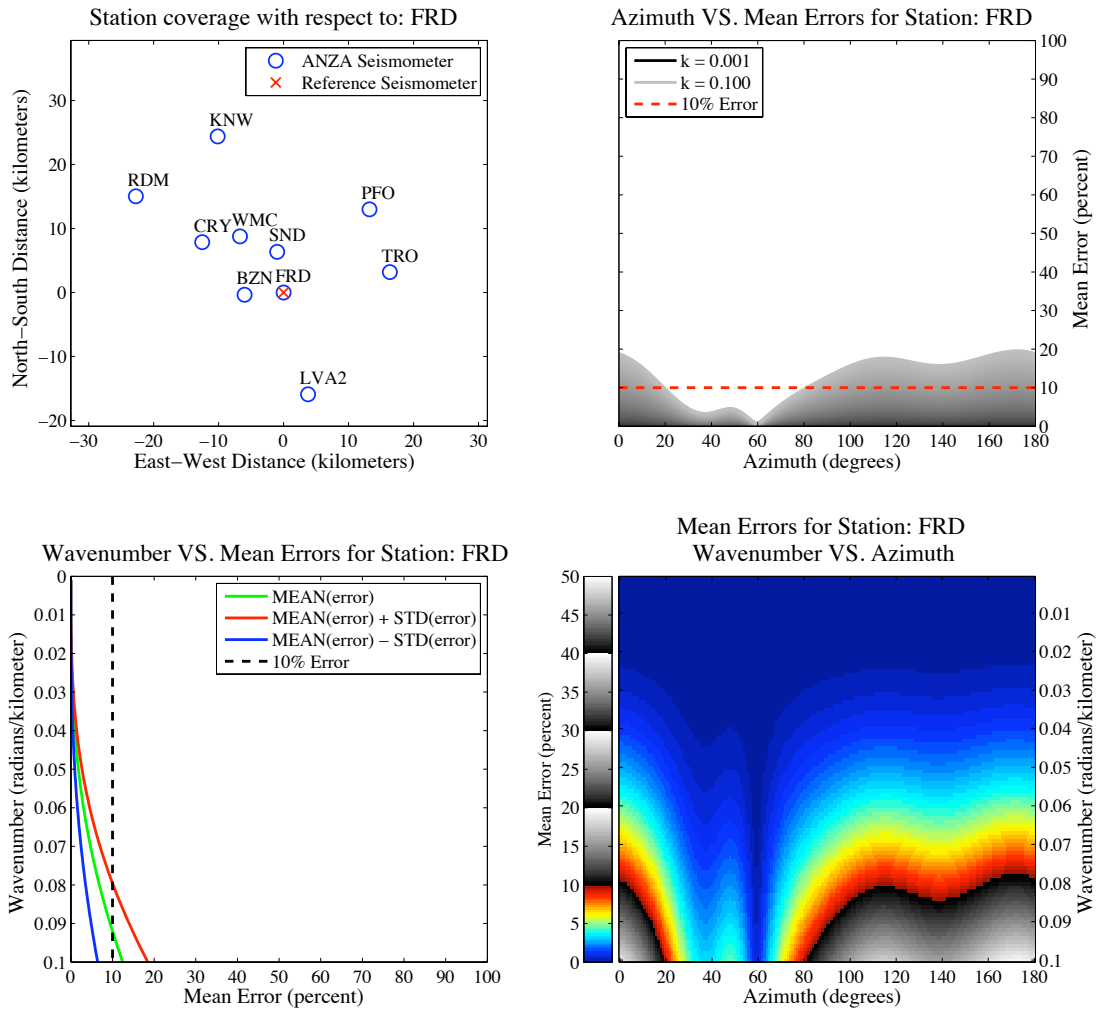

Figure A6. Illustrates the errors resulting from performing a Leave Out Station Scenario (LOSS) using Method (3a) to predict the displacements at Anza station FRD.

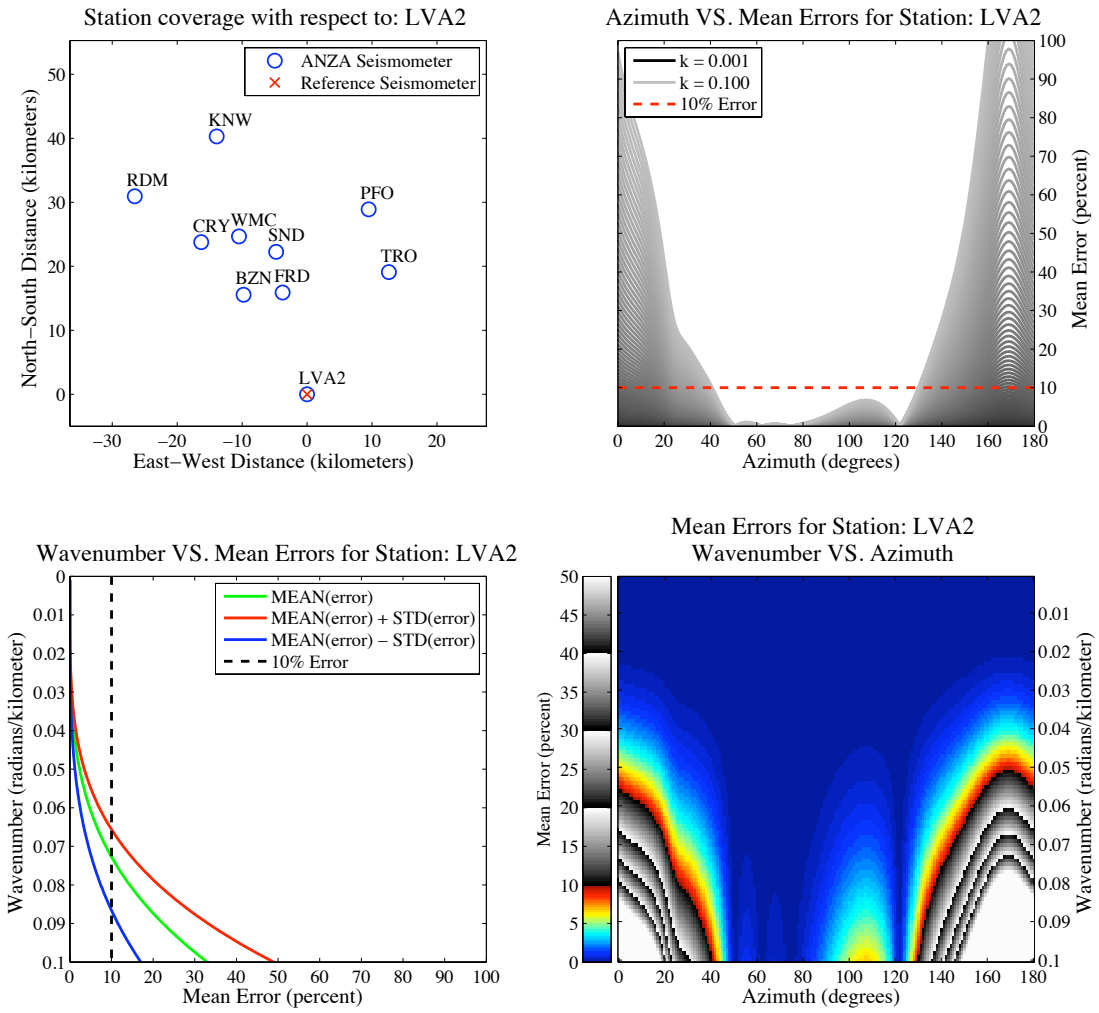

Figure A7. Illustrates the errors resulting from performing a Leave Out Station Scenario (LOSS) using Method (3b) to predict the displacements at Anza station LVA2.

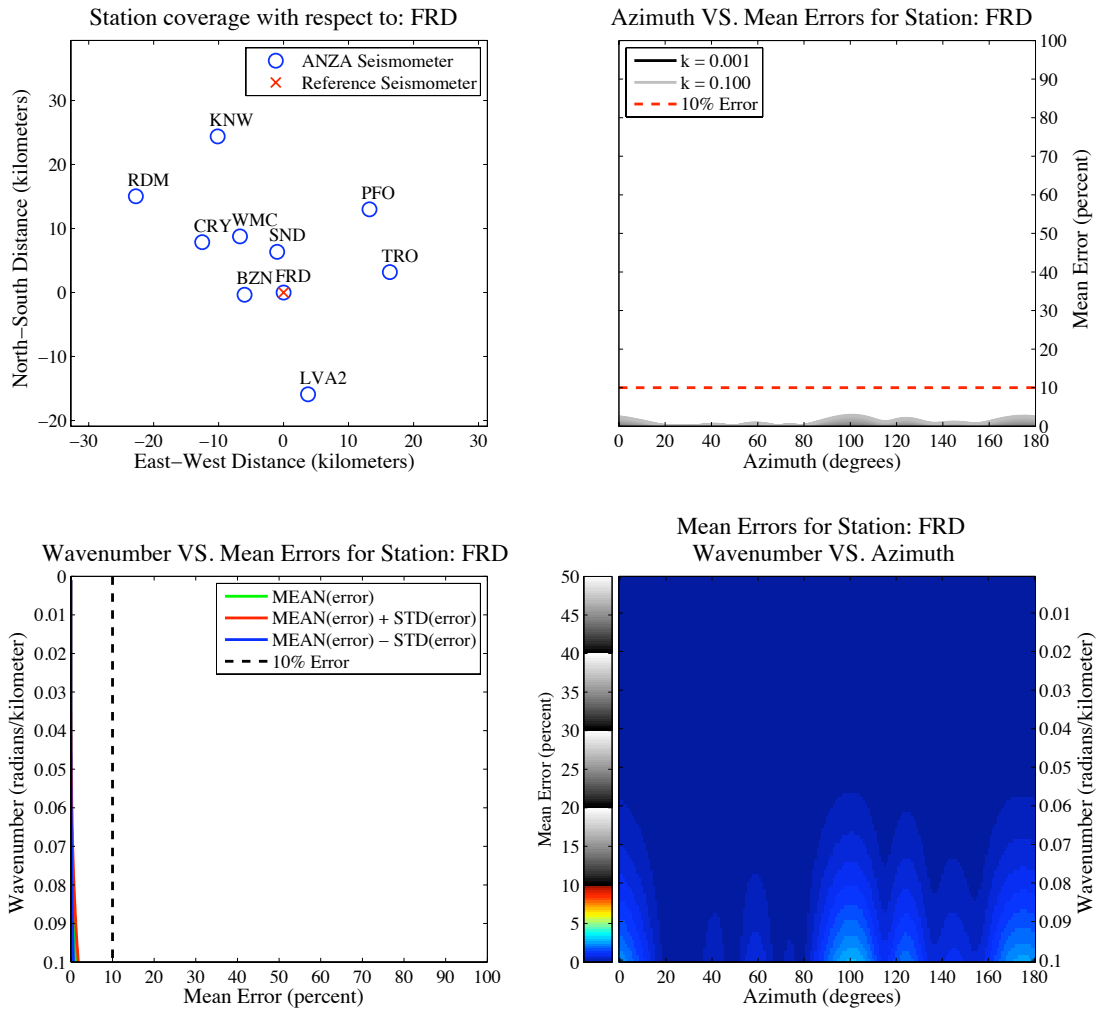

Figure A8. Illustrates the errors resulting from performing a Leave Out Station Scenario (LOSS) using Method (3b) to predict the displacements at Anza station FRD.

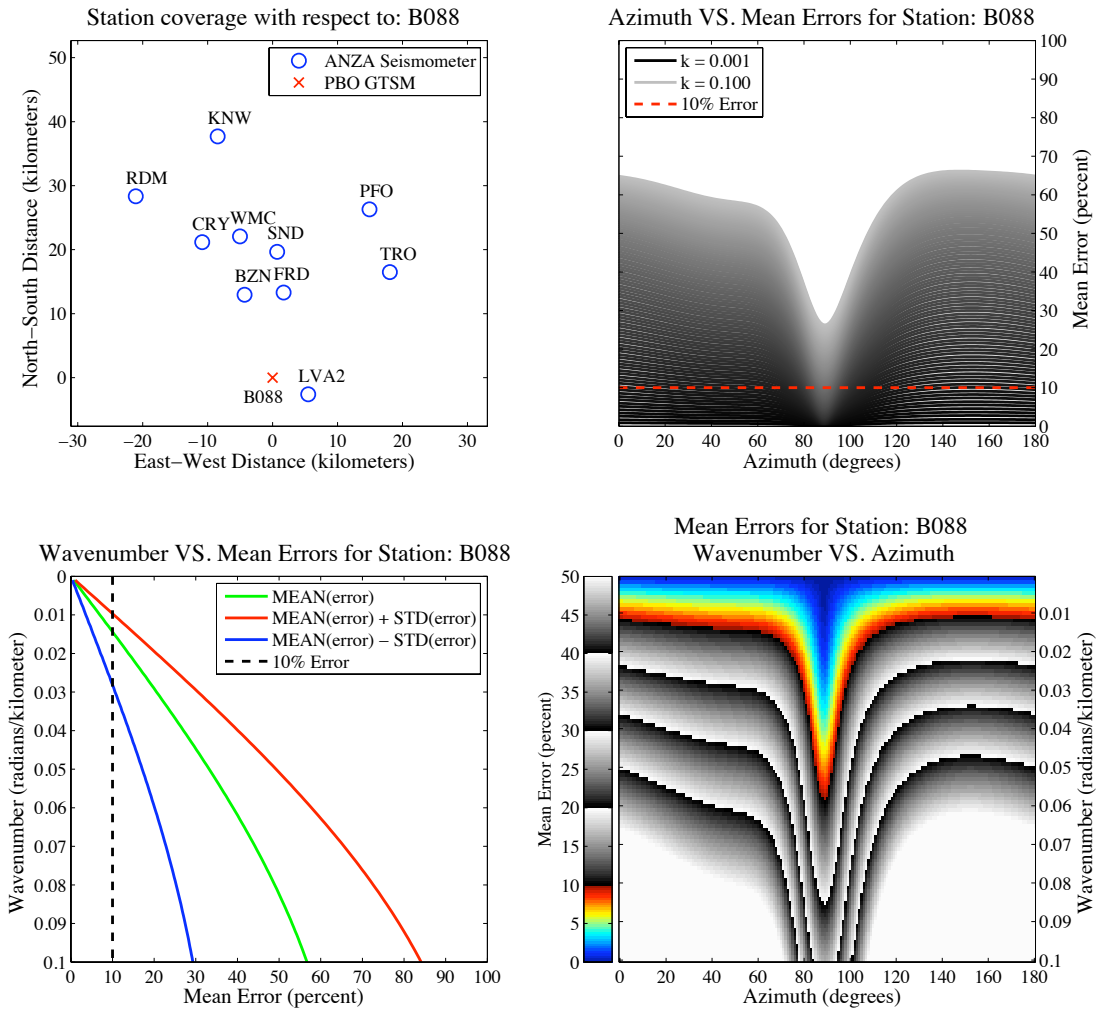

Figure A9. Illustrates the errors resulting from estimating the displacement gradients using Method (1) at PBO GTSM instrument B088.

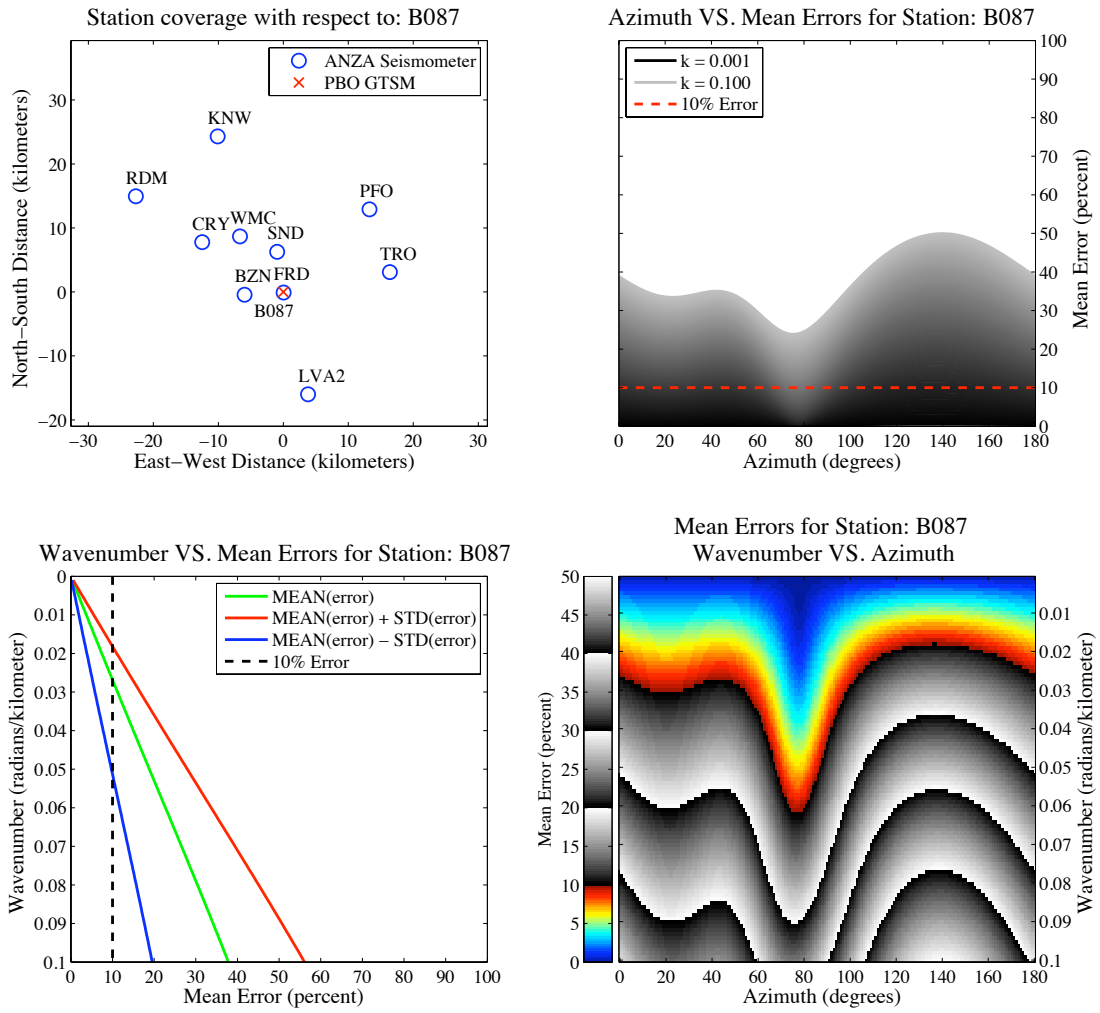

Figure A10. Illustrates the errors resulting from estimating the displacement gradients using Method (1) at PBO GTSM instrument B087.

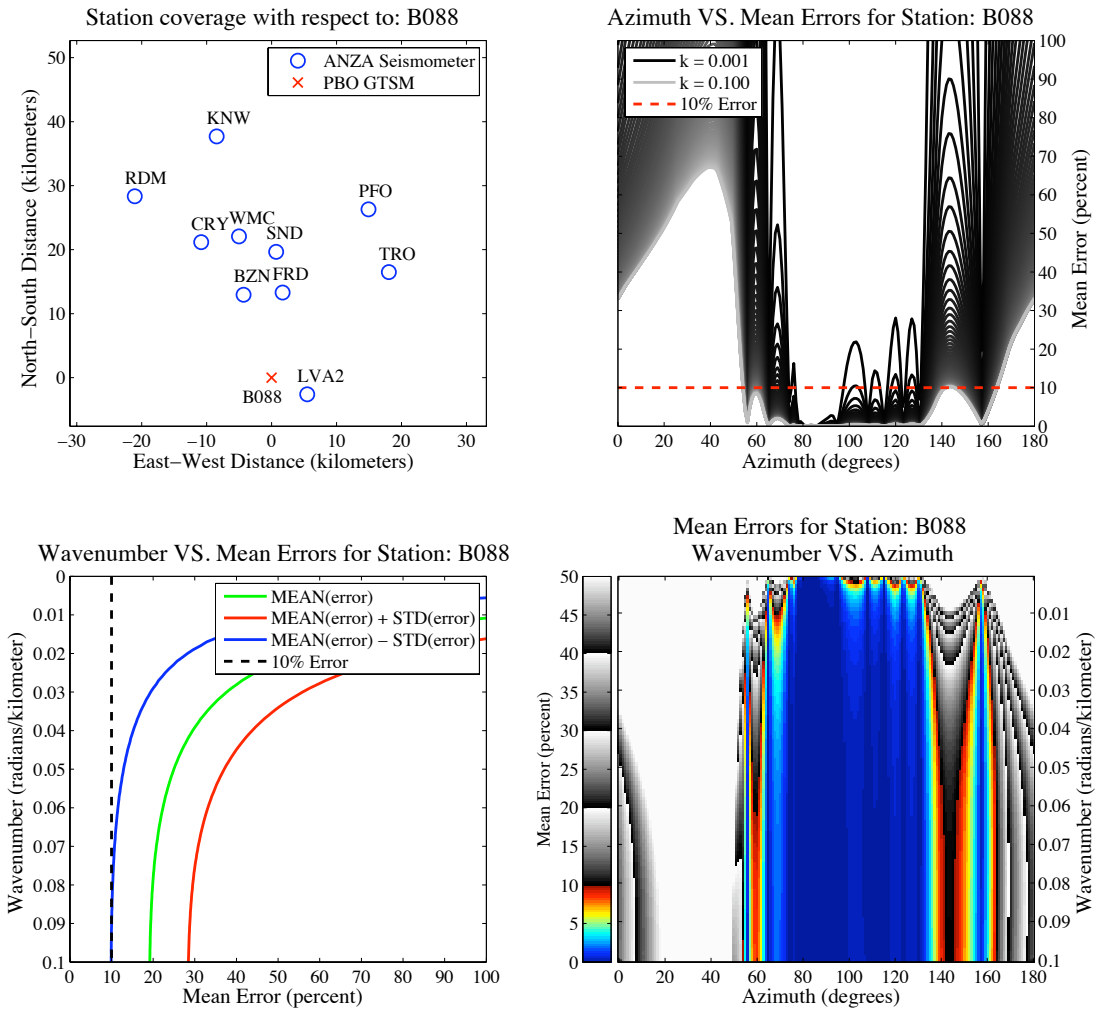

Figure A11. Illustrates the errors resulting from estimating the displacement gradients using Method (2) at PBO GTSM instrument B088.

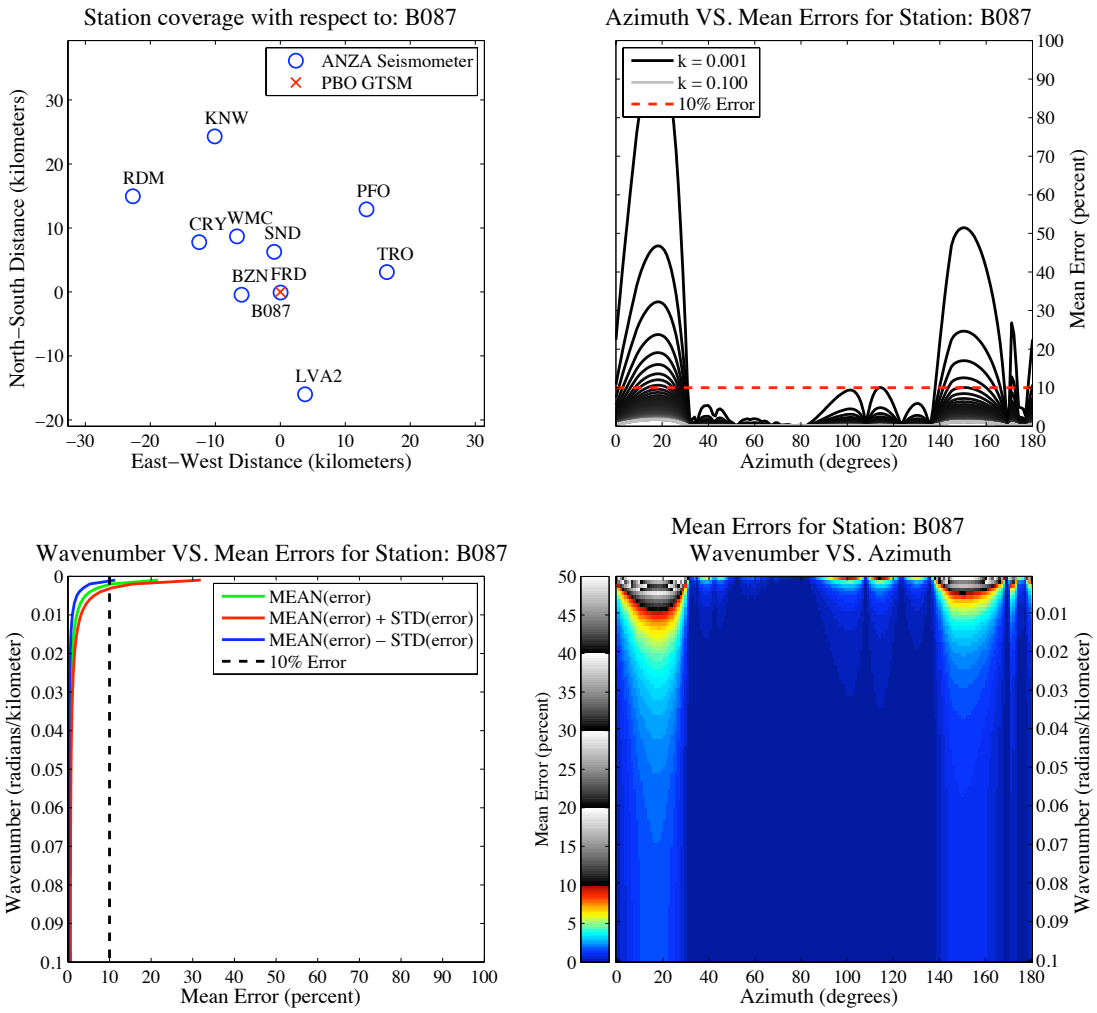

Figure A12. Illustrates the errors resulting from estimating the displacement gradients using Method (2) at PBO GTSM instrument B087.

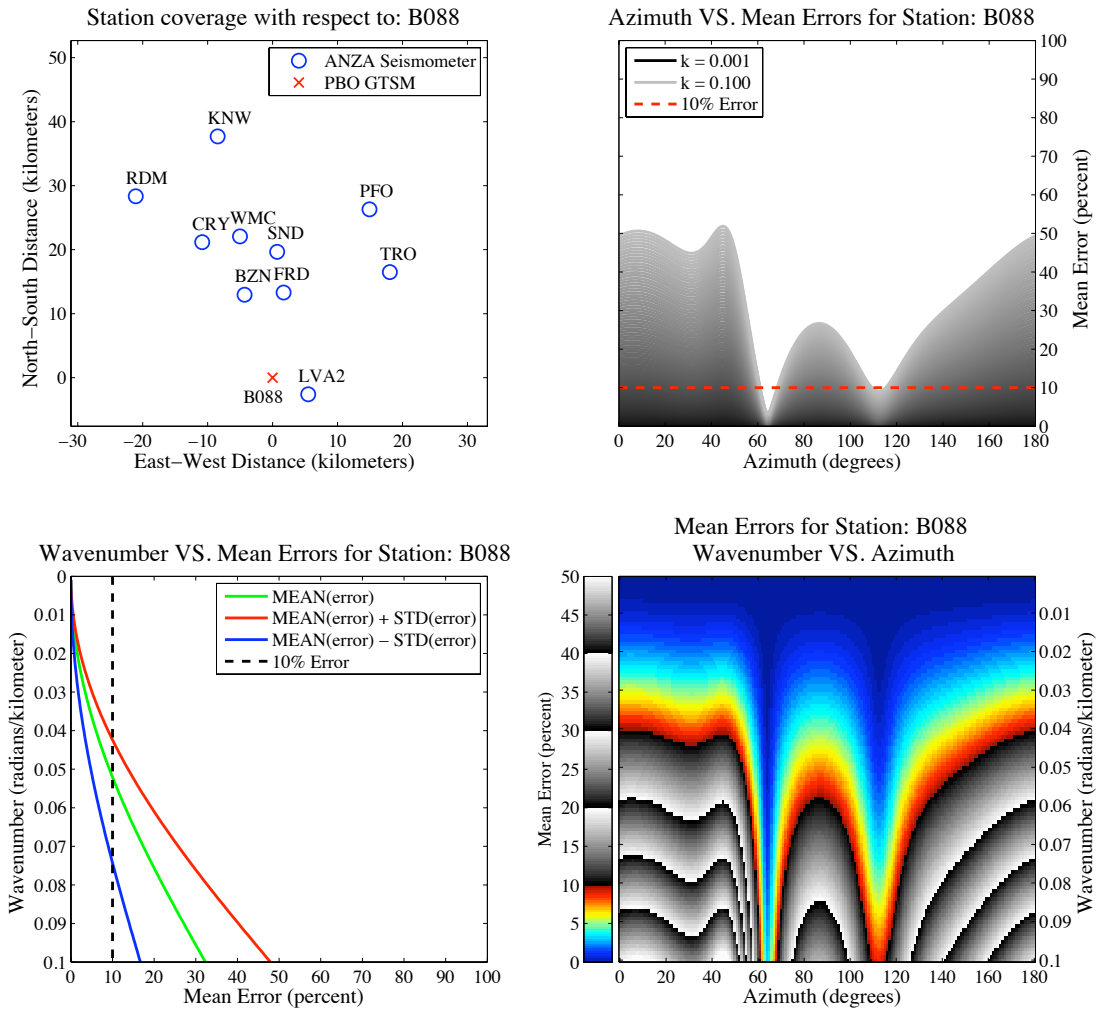

Figure A13. Illustrates the errors resulting from estimating the displacement gradients using Method (3a) at PBO GTSM instrument B088.

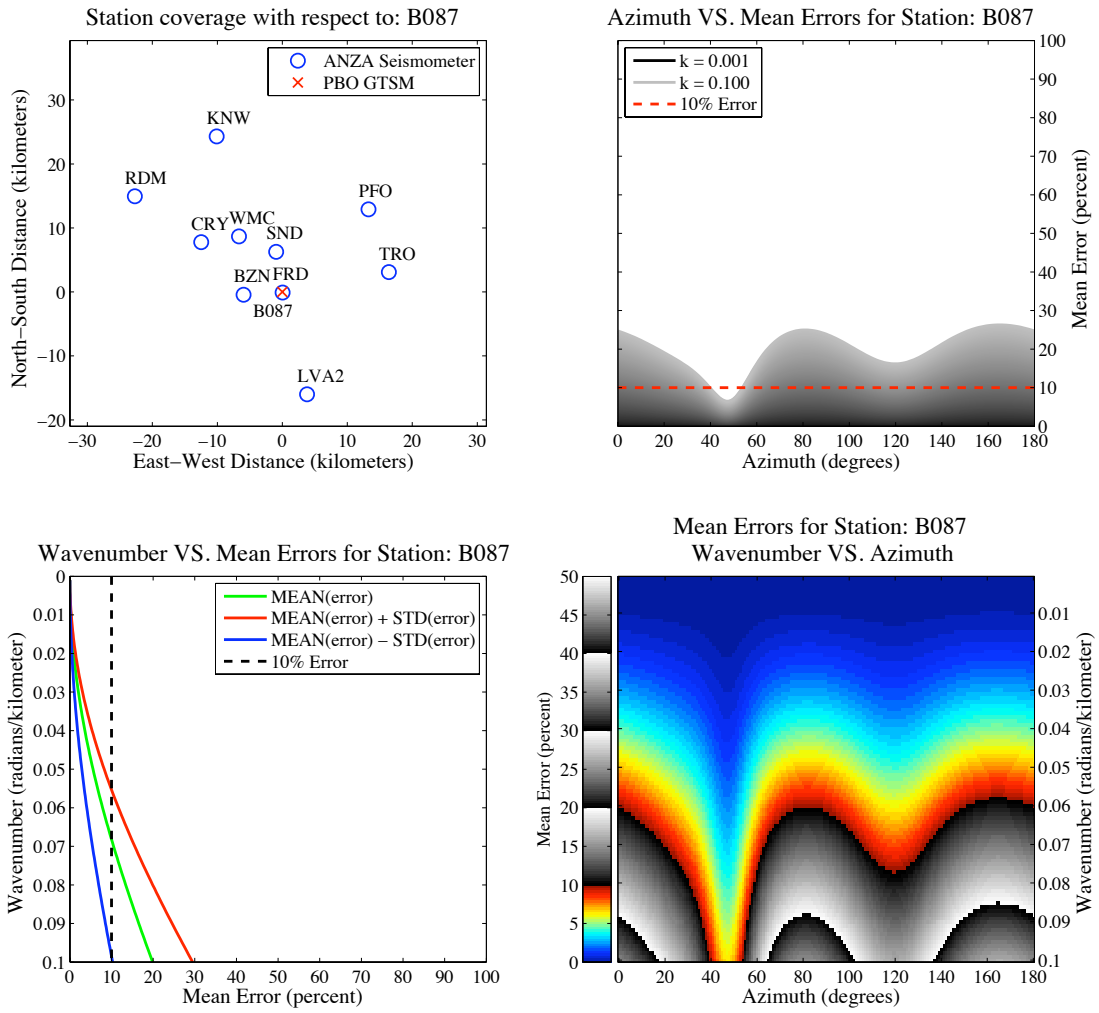

Figure A14. Illustrates the errors resulting from estimating the displacement gradients using Method (3a) at PBO GTSM instrument B087.

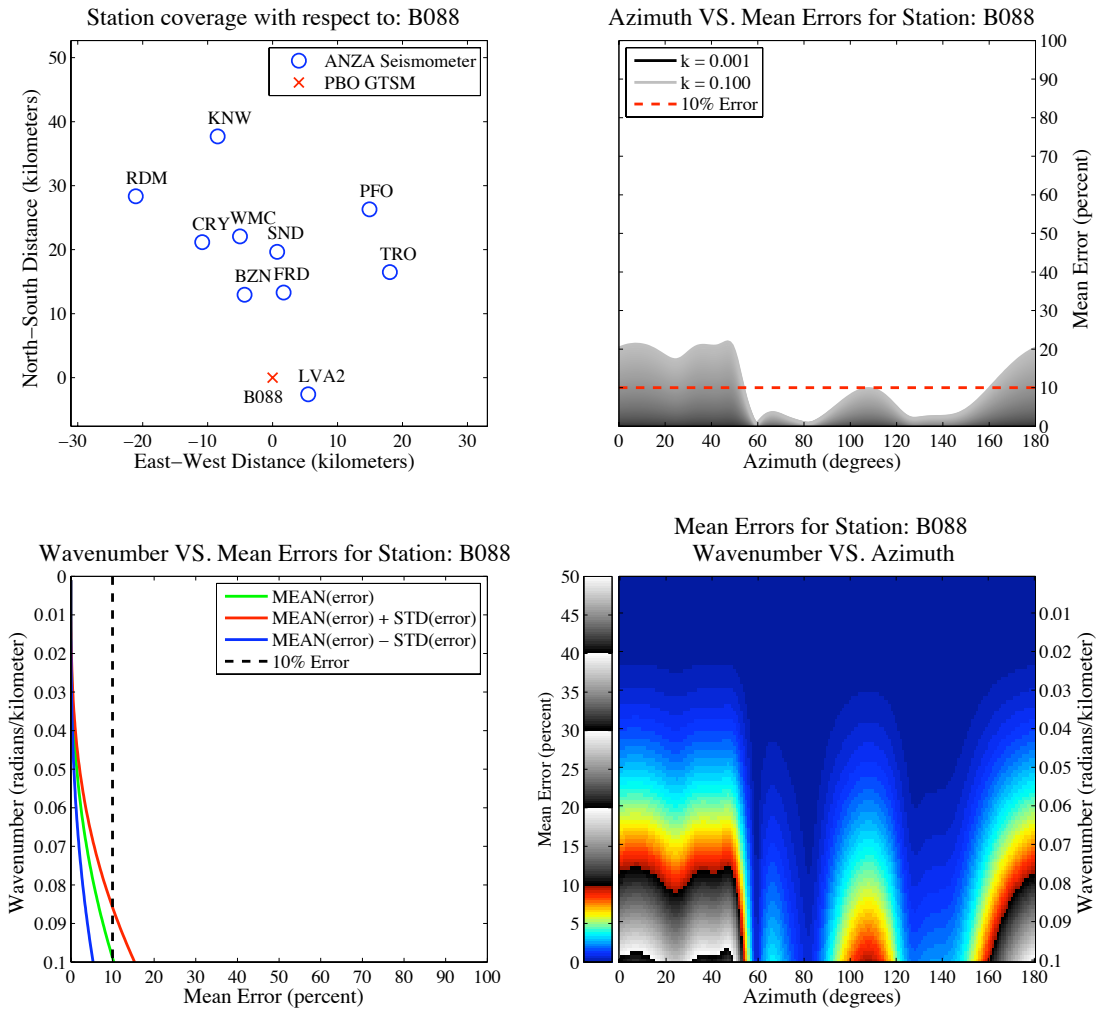

Figure A15. Illustrates the errors resulting from estimating the displacement gradients using Method (3b) at PBO GTSM instrument B088.

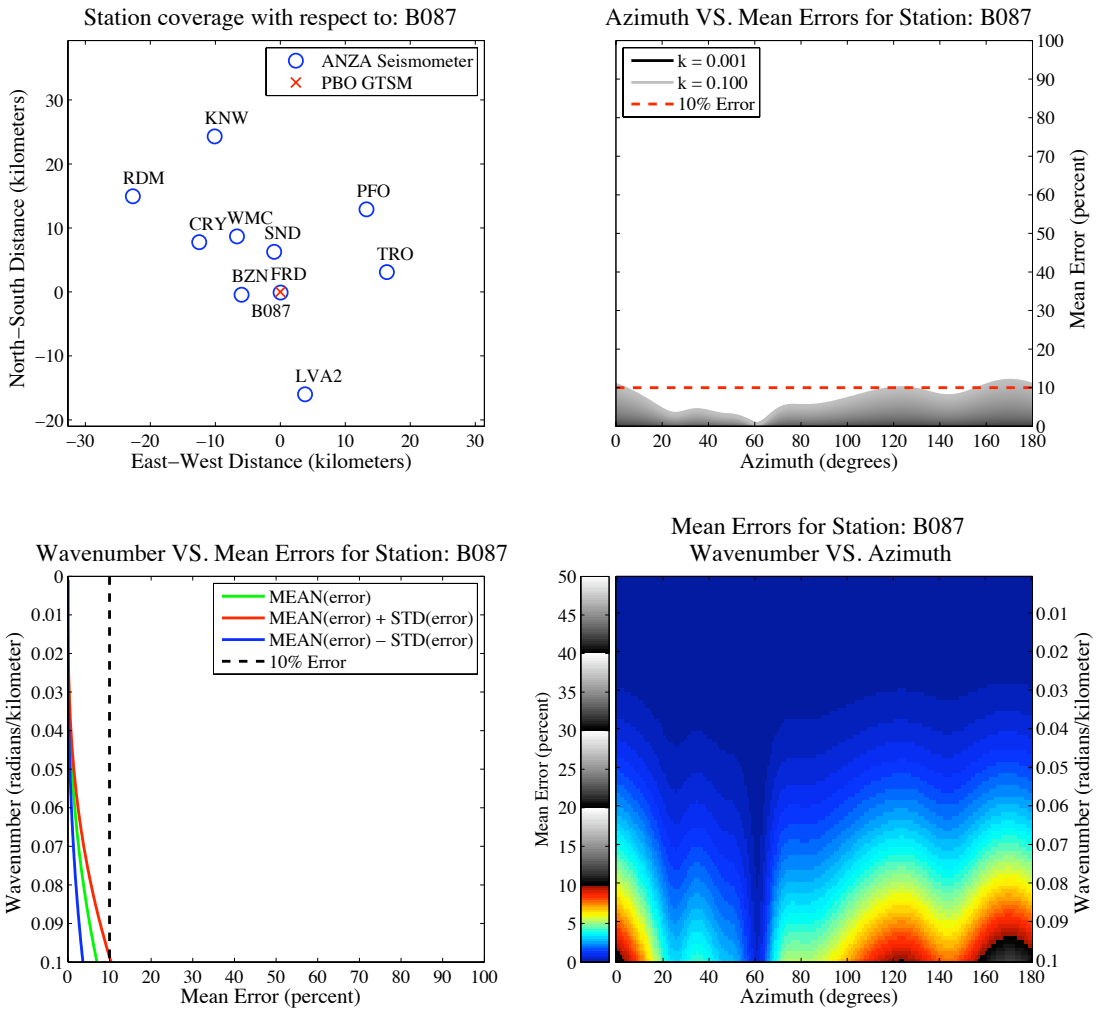

Figure A16. Illustrates the errors resulting from estimating the displacement gradients using Method (3b) at PBO GTSM instrument B087.

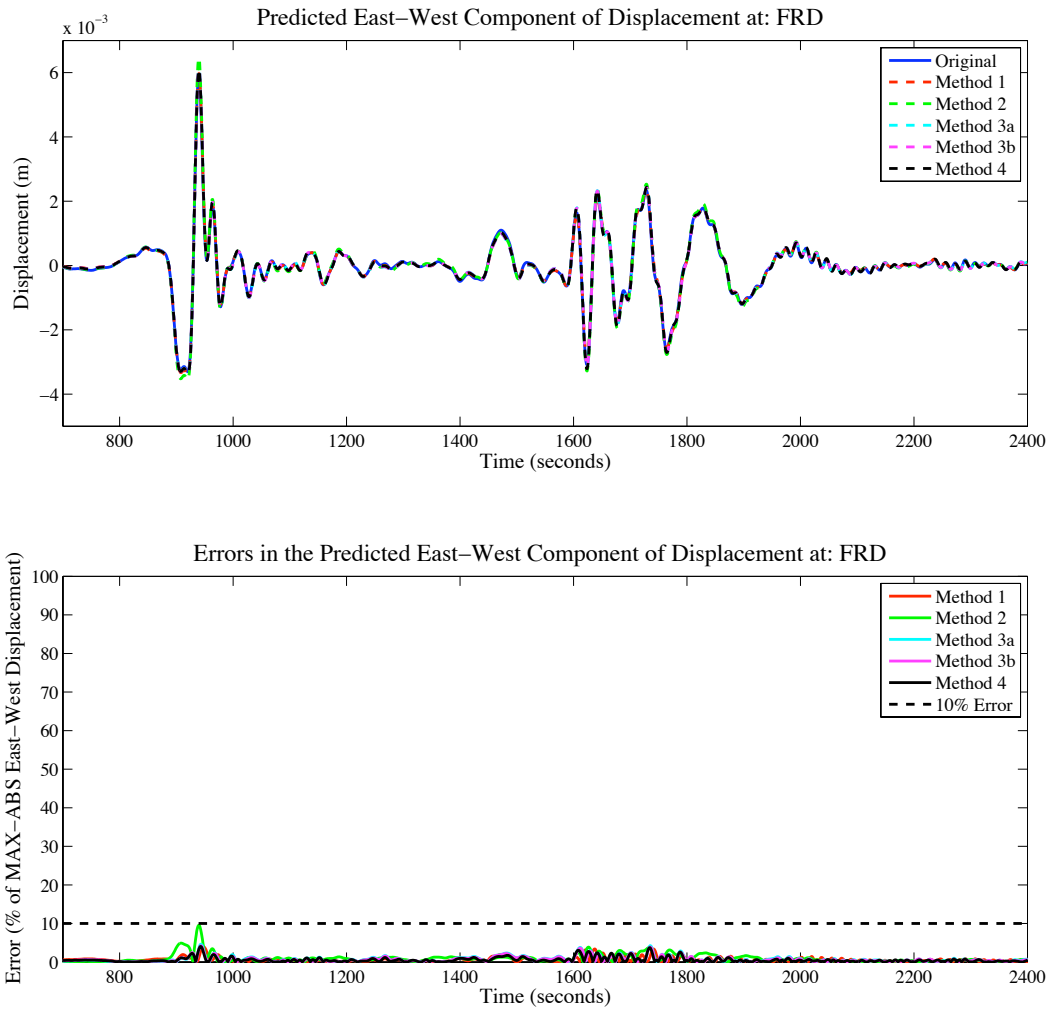

Figure A17. Illustrates the errors in the predicted east-west component of displacement at FRD using Methods (1), (2), (3a), (3b), and (4). Original seismogram corresponds to the 29 September 2009 M8.1 Samoa Island earthquake band-pass filtered between 0.005 Hz and 0.05 Hz with a 4-pole Butterworth acausal filter.

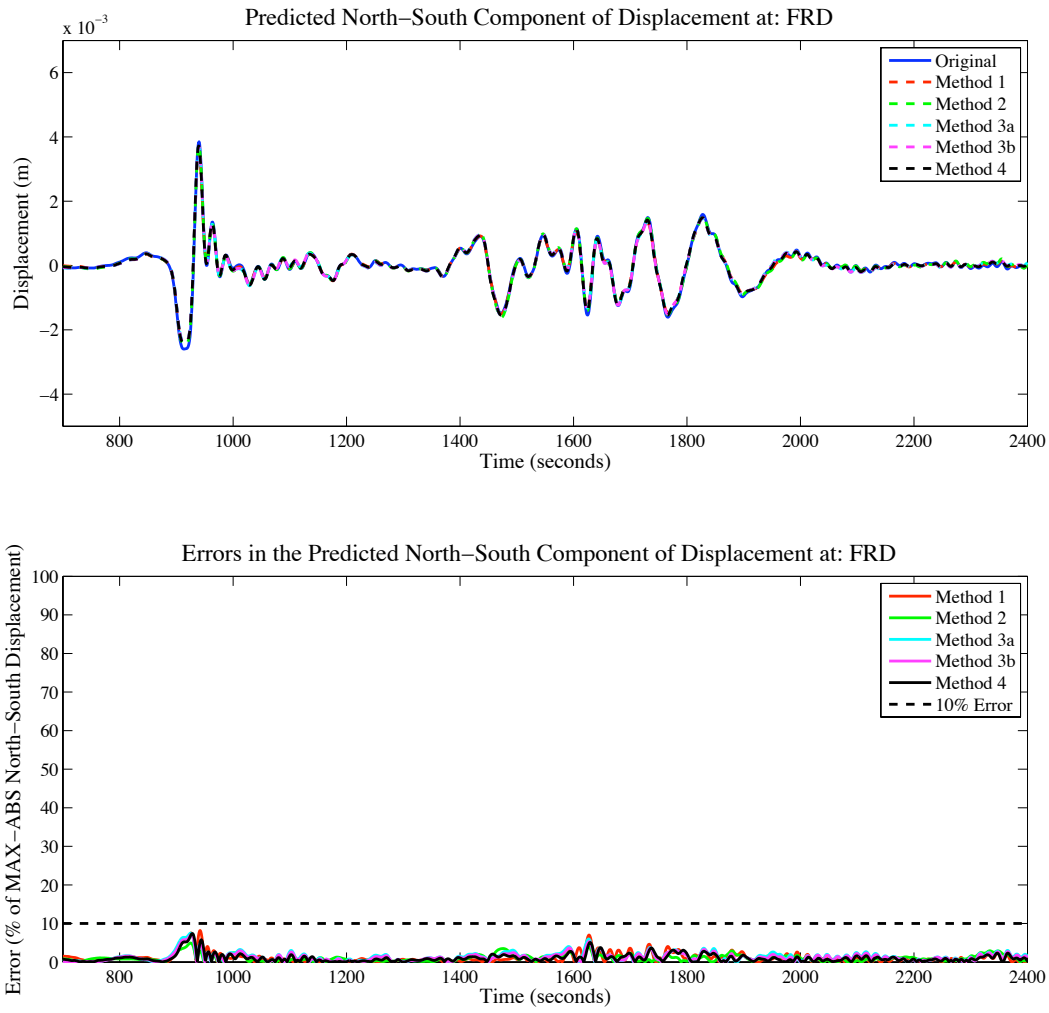

Figure A18. Illustrates the errors in the predicted north-south component of displacement at FRD using Methods (1), (2), (3a), (3b), and (4). Original seismogram corresponds to the 29 September 2009 M8.1 Samoa Island earthquake band-pass filtered between 0.005 Hz and 0.05 Hz with a 4-pole Butterworth acausal filter.

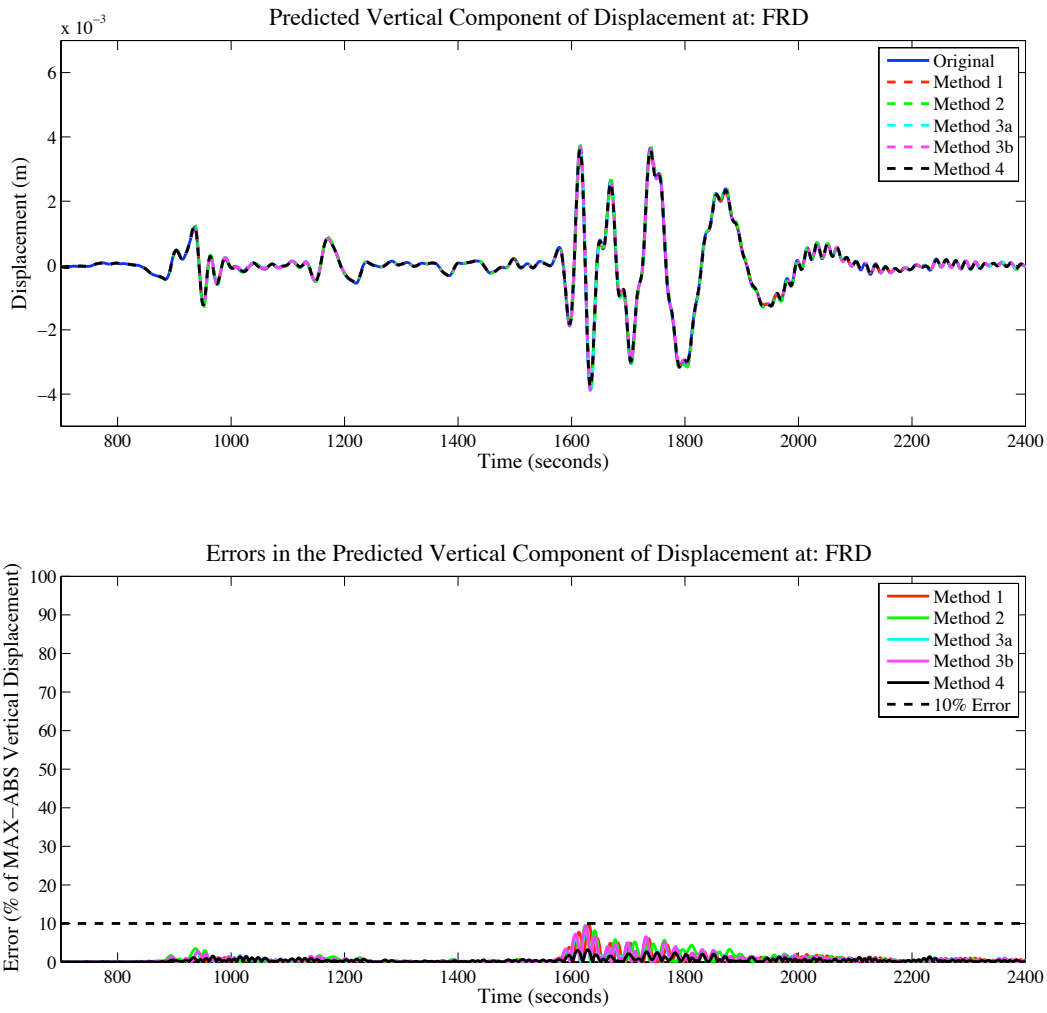

Figure A19. Illustrates the errors in the predicted vertical component of displacement at FRD using Methods (1), (2), (3a), (3b), and (4). Original seismogram corresponds to the 29 September 2009 M8.1 Samoa Island earthquake band-pass filtered between 0.005 Hz and 0.05 Hz with a 4-pole Butterworth acausal filter.

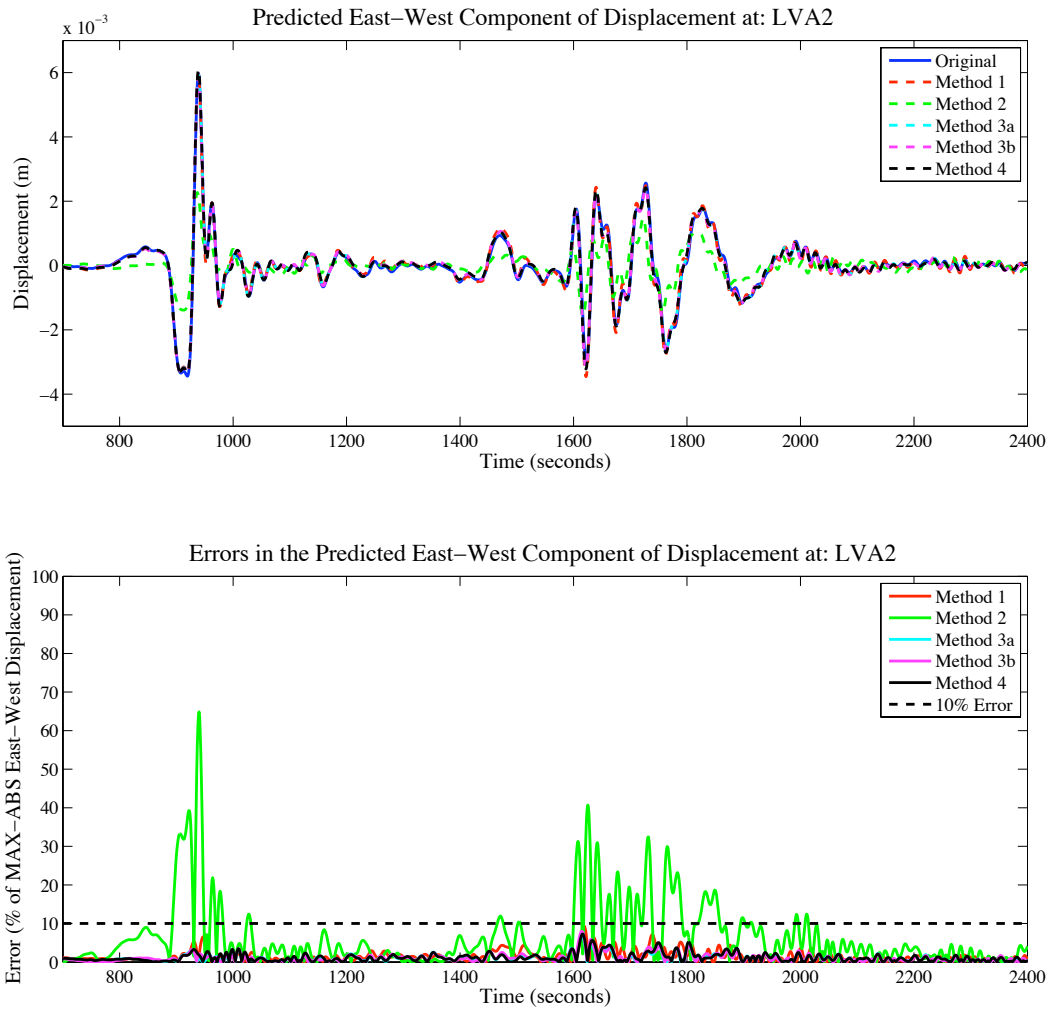

Figure A20. Illustrates the errors in the predicted east-west component of displacement at LVA2 using Methods (1), (2), (3a), (3b), and (4). Original seismogram corresponds to the 29 September 2009 M8.1 Samoa Island earthquake band-pass filtered between 0.005 Hz and 0.05 Hz with a 4-pole Butterworth acausal filter.

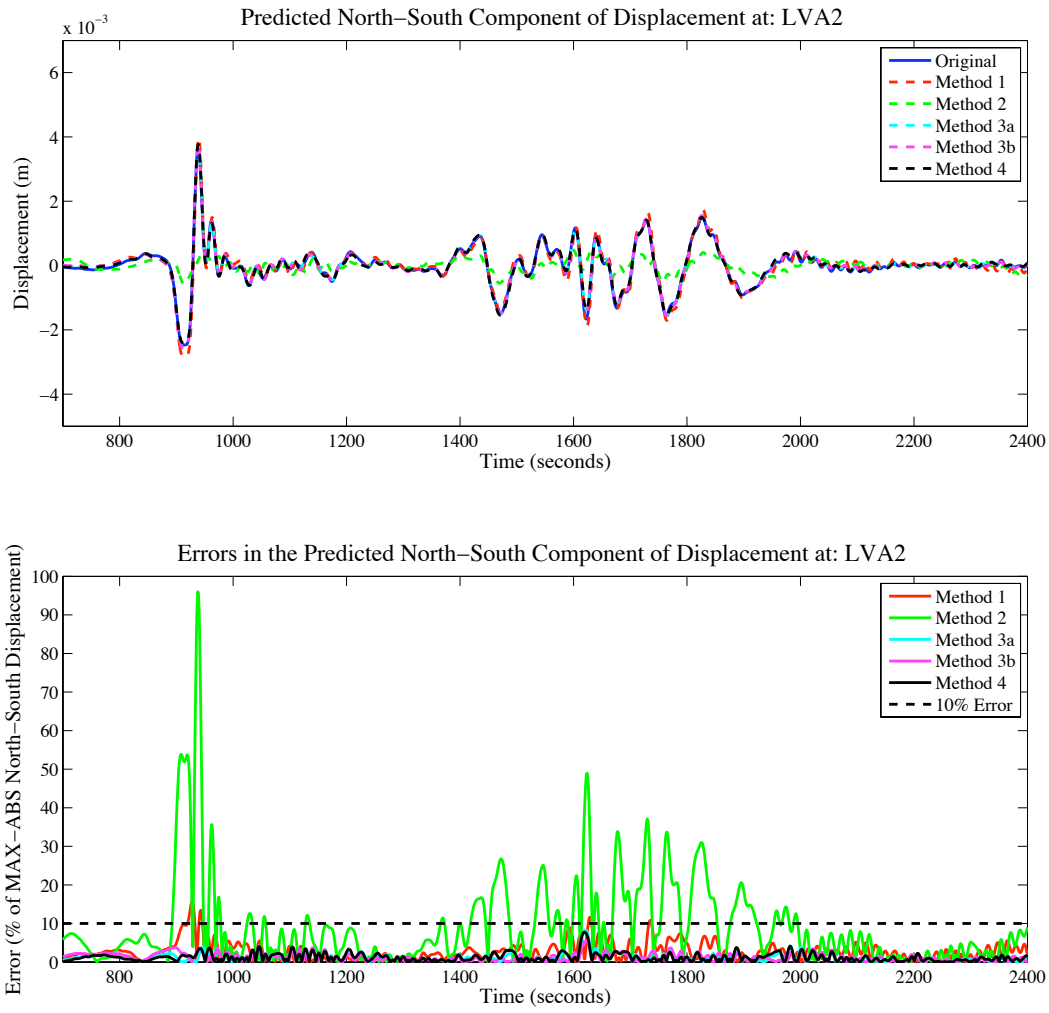

Figure A21. Illustrates the errors in the predicted north-south component of displacement at LVA2 using Methods (1), (2), (3a), (3b), and (4). Original seismogram corresponds to the 29 September 2009 M8.1 Samoa Island earthquake band-pass filtered between 0.005 Hz and 0.05 Hz with a 4-pole Butterworth acausal filter.

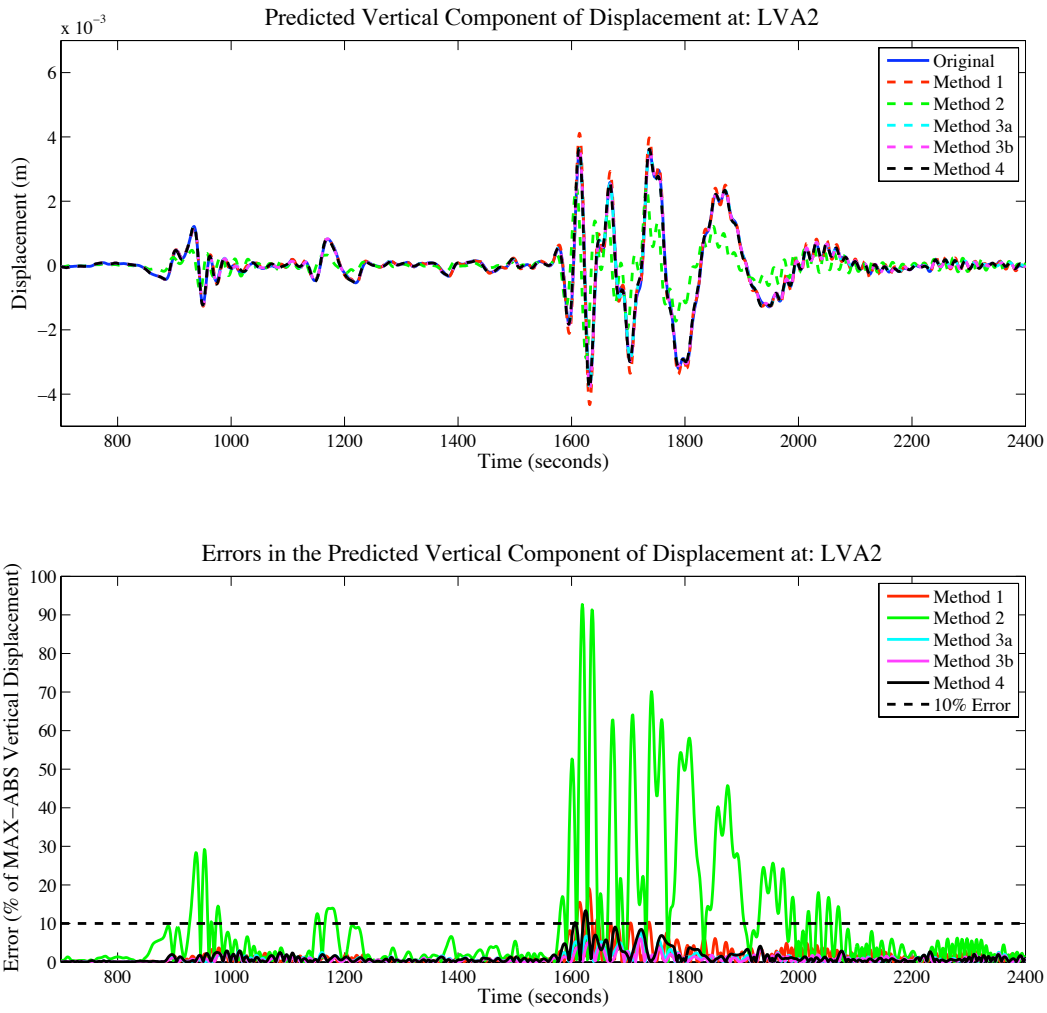

Figure A22. Illustrates the errors in the predicted vertical component of displacement at LVA2 using Methods (1), (2), (3a), (3b), and (4). Original seismogram corresponds to the 29 September 2009 M8.1 Samoa Island earthquake band-pass filtered between 0.005 Hz and 0.05 Hz with a 4-pole Butterworth acausal filter.

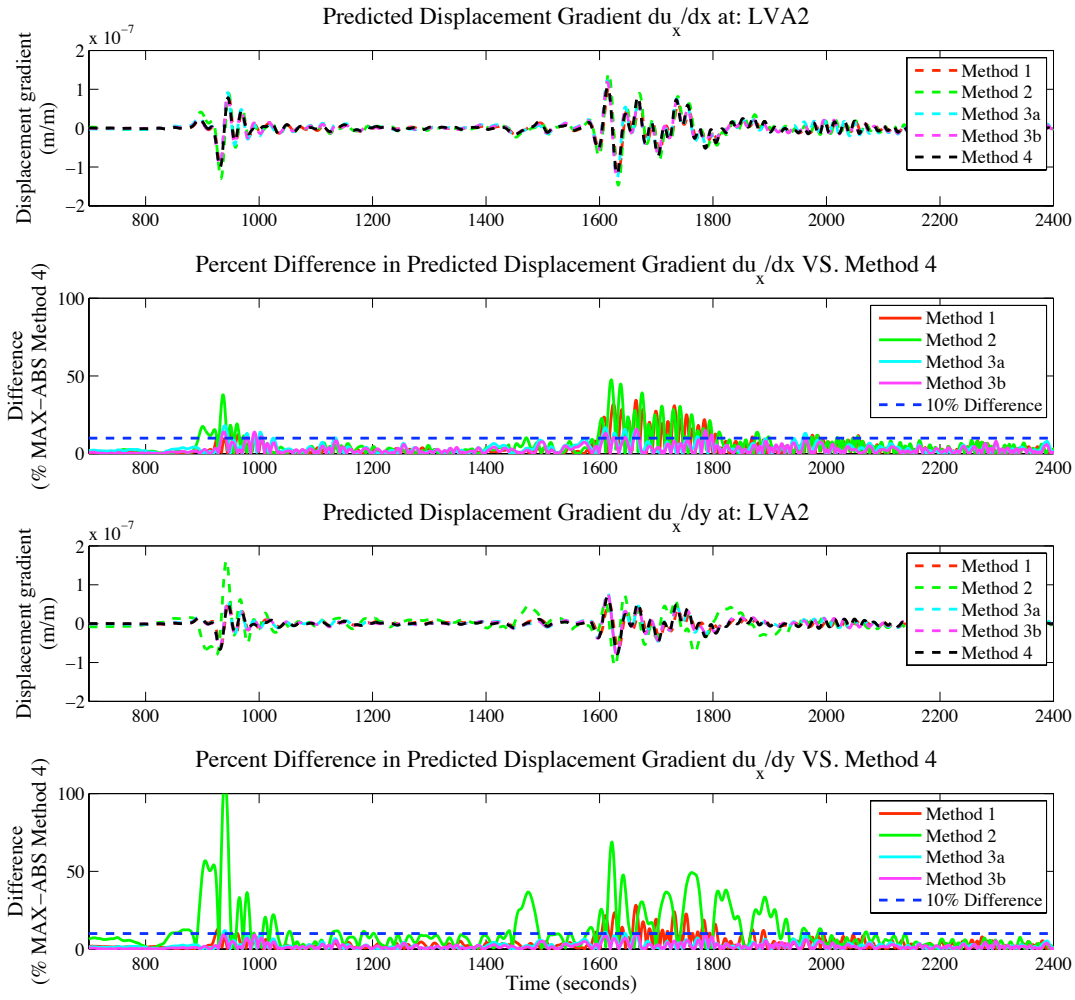

Figure A23. Illustrates the horizontal displacement gradients (i.e., $\partial/\partial x$ and $\partial/\partial y$) associated with the east-west component of ground displacement (i.e., u_x) at LVA2 using Methods (1), (2), (3a), (3b), and (4). The error plots indicate the difference between each of the results from the first three methods and the result from Method (4). The original seismograms correspond to the 29 September 2009 M8.1 Samoa Island earthquake band-pass filtered between 0.005 Hz and 0.05 Hz with a 4-pole Butterworth acausal filter.

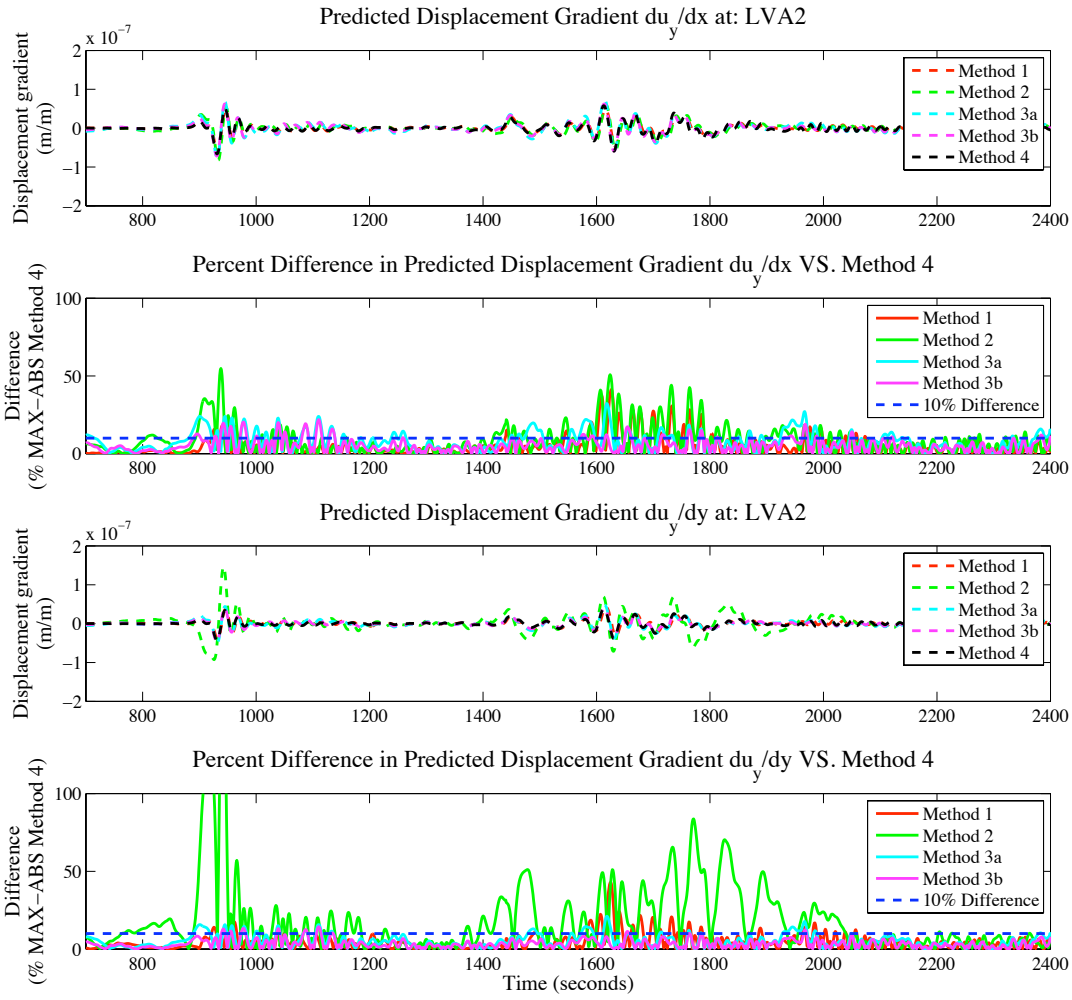

Figure A24. Illustrates the horizontal displacement gradients (i.e., $\partial/\partial x$ and $\partial/\partial y$) associated with the north-south component of ground displacement (i.e., u_y) at LVA2 using Methods (1), (2), (3a), (3b), and (4). The error plots indicate the difference between each of the results from the first three methods and the result from Method (4). The original seismograms correspond to the 29 September 2009 M8.1 Samoa Island earthquake band-pass filtered between 0.005 Hz and 0.05 Hz with a 4-pole Butterworth acausal filter.

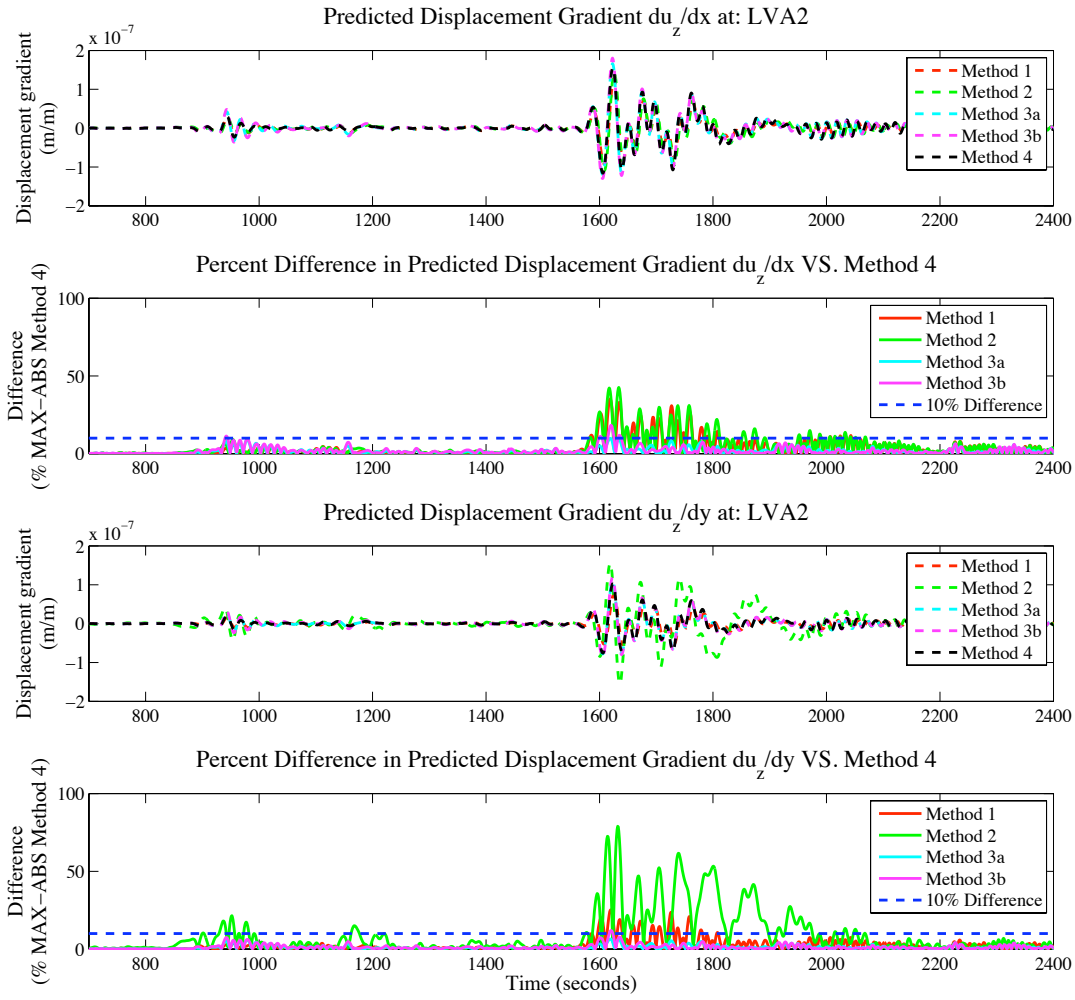

Figure A25. Illustrates the horizontal displacement gradients (i.e., $\partial/\partial x$ and $\partial/\partial y$) associated with the vertical component of ground displacement (i.e., u_z) at LVA2 using Methods (1), (2), (3a), (3b), and (4). The error plots indicate the difference between each of the results from the first three methods and the result from Method (4). The original seismograms correspond to the 29 September 2009 M8.1 Samoa Island earthquake band-pass filtered between 0.005 Hz and 0.05 Hz with a 4-pole Butterworth acausal filter.

APPENDIX 2

Supplemental Information for Chapter Three

Summary

Supplemental details explaining the reasoning behind the formulation associated with Equation (37) are located in the next section.

Supplemental figures are included in this appendix in order to provide the reader with additional visual verification/insight to the words and figures available in Chapter (3). This collection of figures illustrates the result of calibrating borehole GTSM instruments B082, B084, B086, B087, B088, and B089. For each borehole GTSM station, there are figures that illustrate: 1) the probability density functions (PDFs) associated with each complex calibration coefficient estimate derived from frequency domain information, 2) the consistency of the best fit calibration coefficients, in a least squares sense, across a period of more than 2 years, and 3) an example of the formation strain information derived from each calibrated borehole GTSM instrument.

Linear Dependence of the Formation Strain derived using Seismic Data

The reason formation strain amplitude data is required from multiple strain-inducing events is due to our assumption of plane-wave propagation across a seismic array. Under the assumption of plane-propagation across a 2D seismic array at the surface, the elements of the 2D strain tensor ($\boldsymbol{\varepsilon}$) are:

$$\begin{bmatrix} \varepsilon_{11} & \varepsilon_{12} \\ \varepsilon_{21} & \varepsilon_{22} \end{bmatrix} = \begin{bmatrix} \dfrac{\partial u_x}{\partial x} & \dfrac{1}{2}\left(\dfrac{\partial u_y}{\partial x} + \dfrac{\partial u_x}{\partial y}\right) \\ \dfrac{1}{2}\left(\dfrac{\partial u_y}{\partial x} + \dfrac{\partial u_x}{\partial y}\right) & \dfrac{\partial u_y}{\partial y} \end{bmatrix} = \begin{bmatrix} -s_x \dot{u}_x \sin(\theta) & -\dfrac{1}{2}\left(s_x \dot{u}_x \cos(\theta) + s_y \dot{u}_y \sin(\theta)\right) \\ -\dfrac{1}{2}\left(s_x \dot{u}_x \cos(\theta) + s_y \dot{u}_y \sin(\theta)\right) & -s_y \dot{u}_y \cos(\theta) \end{bmatrix}, \quad \text{(A1)}$$

where s_x and s_y are the propagation slowness in the x- and y-direction according to a Cartesian coordinate system (positive x points east and positive y points north), $\dot{u}_x$ and $\dot{u}_y$ are the x- and y-components of the seismic velocity, and θ is the propagation azimuth (measured clockwise from north) across the array [*Gomberg et al.,* 1999]. The above may be simplified to:

$$\begin{bmatrix} \varepsilon_{11} \\ \varepsilon_{22} \\ \varepsilon_{12} \end{bmatrix} = \begin{bmatrix} \sin(\theta) & 0 \\ 0 & \cos(\theta) \\ \dfrac{1}{2}\cos(\theta) & \dfrac{1}{2}\sin(\theta) \end{bmatrix} \begin{bmatrix} -s_x \dot{u}_x \\ -s_y \dot{u}_y \end{bmatrix} . \quad \text{(A2)}$$

In terms of the formation strain,

$$\begin{bmatrix} e_a \\ \gamma_1 \\ \gamma_2 \end{bmatrix} = \begin{bmatrix} \varepsilon_{11} + \varepsilon_{22} \\ \varepsilon_{11} - \varepsilon_{22} \\ \varepsilon_{12} + \varepsilon_{21} \end{bmatrix} = \begin{bmatrix} \sin(\theta) & \cos(\theta) \\ \sin(\theta) & -\cos(\theta) \\ \cos(\theta) & \sin(\theta) \end{bmatrix} \begin{bmatrix} -s_x \dot{u}_x \\ \\ -s_y \dot{u}_y \end{bmatrix} \quad . \tag{A3}$$

The question becomes, when the formation strain derived from seismic data are assumed to have resulted from plane-wave propagation across the array in a single direction, are the estimates of the formation strain actually linearly independent from one another? This can be determined by finding the rank of **A**, for example:

$$\mathbf{A} = \begin{bmatrix} e_a(t_i) & e_a(t_j) & e_a(t_k) \\ \gamma_1(t_i) & \gamma_1(t_j) & \gamma_1(t_k) \\ \gamma_2(t_i) & \gamma_2(t_j) & \gamma_2(t_k) \end{bmatrix} = \begin{bmatrix} \sin(\theta) & \cos(\theta) \\ \sin(\theta) & -\cos(\theta) \\ \cos(\theta) & \sin(\theta) \end{bmatrix} \begin{bmatrix} -s_x^i \dot{u}_x(t_i) & -s_x^j \dot{u}_x(t_j) & -s_x^k \dot{u}_x(t_k) \\ \\ -s_y^i \dot{u}_y(t_i) & -s_y^j \dot{u}_y(t_j) & -s_y^k \dot{u}_y(t_k) \end{bmatrix}, \tag{A4}$$

where the indices i, j, and k ($i \neq j$, $i \neq k$, $j \neq k$) are used to denote the formation strain at a specific instant in time, the slowness in the x- and y-direction at a specific instant in time, and the x- and y-components of the seismic velocity at a specific instant in time. It can be shown that, regardless of whether or not the slowness in Equation (A4) is constant through time, the rank of **A** is less than 3. However, it can also be shown that if the formation strain amplitudes at different instances in time are the result of plane-wave propagation from more than one direction, then the formation strain amplitudes contain enough linear independence such that the rank of **A** is 3. The example in Equation (A4) represents the horizontal concatenation of 3 column vectors of the formation strain. However, concatenating more than 3 formation strain vectors are likely to help produce more robust estimates of the calibration coefficients during the inversion process explained in the above sections.

Figures

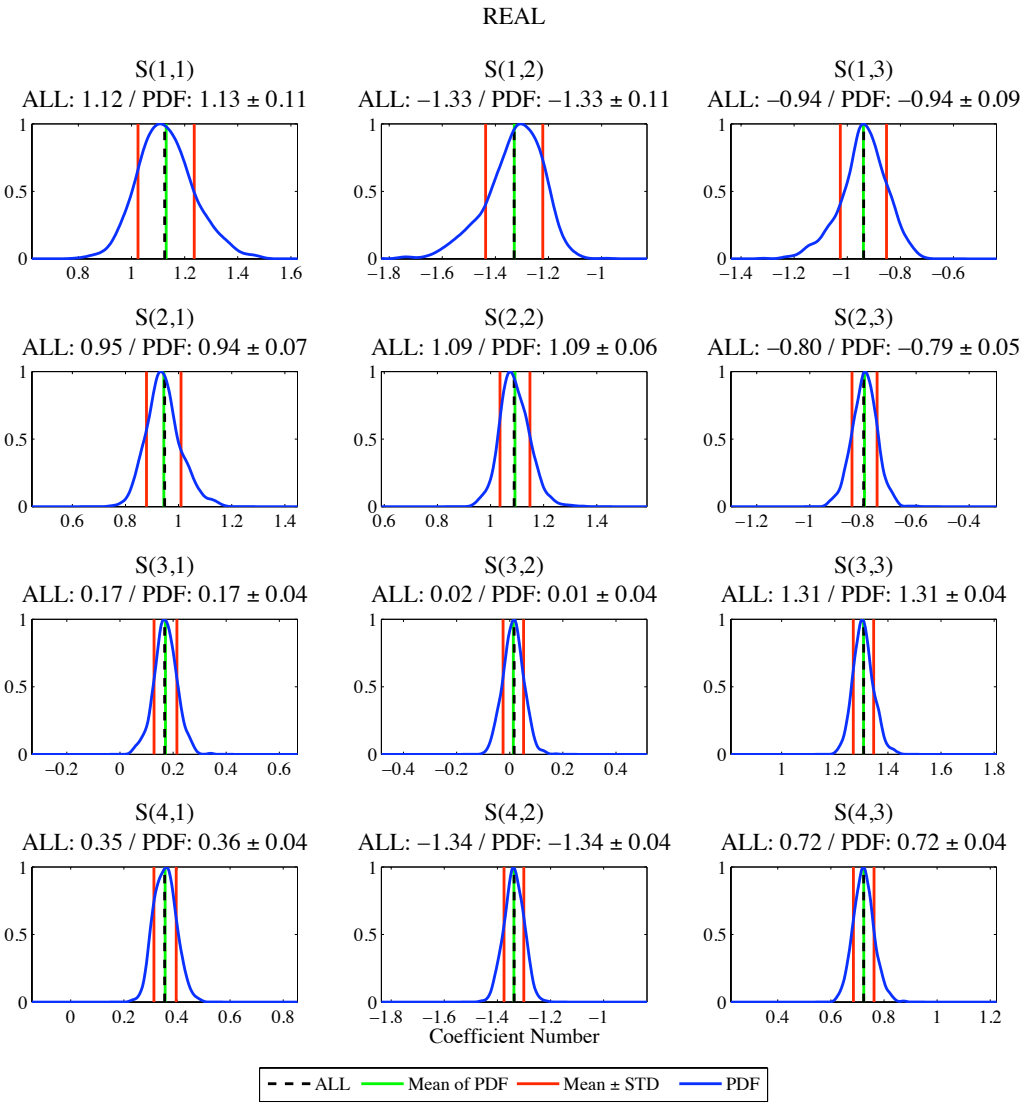

Figure A26. Illustration of the normalized probability density functions (PDF) associated with the REAL calibration coefficients derived for B082 using seismic data. The normalized PDF (BLUE line) about each coefficient value is the result from randomly selecting 71 (~5%) of the available 1411 sets of instrument and reference strain amplitudes, performing an inversion (similar to Equation 41) using these data, and repeating (1000 iterations total). The mean of the normalized PDF is indicated by the GREEN solid line, while the standard deviation about the mean is indicated by RED solid lines. The result from inverting all 1411 sets of strain information is indicated by the BLACK dashed line.

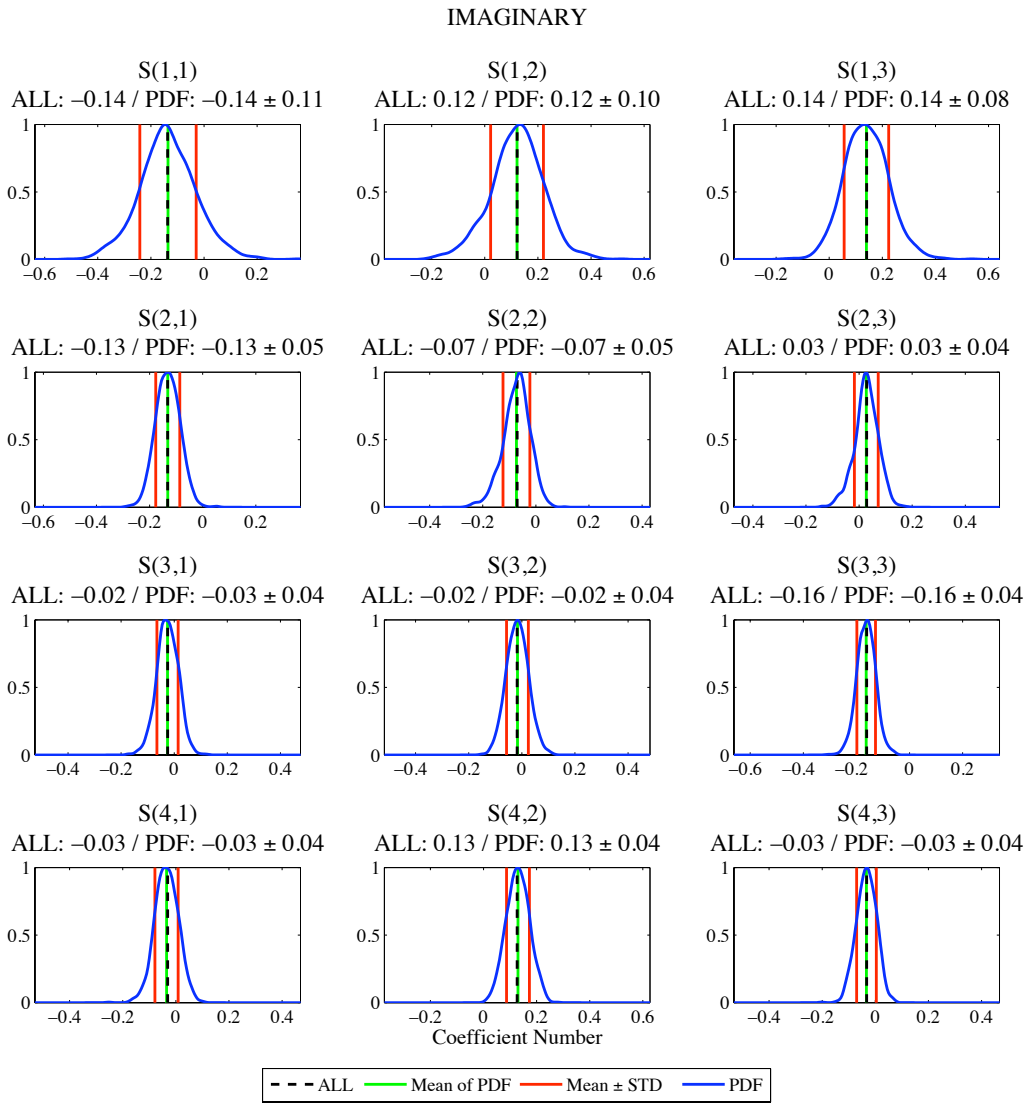

Figure A27. Illustration of the normalized probability density functions (PDF) associated with the IMAGINARY calibration coefficients derived for B082 using seismic data. The normalized PDF (BLUE line) about each coefficient value is the result from randomly selecting 71 (~5%) of the available 1411 sets of instrument and reference strain amplitudes, performing an inversion (similar to Equation 41) using these data, and repeating (1000 iterations total). The mean of the normalized PDF is indicated by the GREEN solid line, while the standard deviation about the mean is indicated by RED solid lines. The result from inverting all 1411 sets of strain information is indicated by the BLACK dashed line.

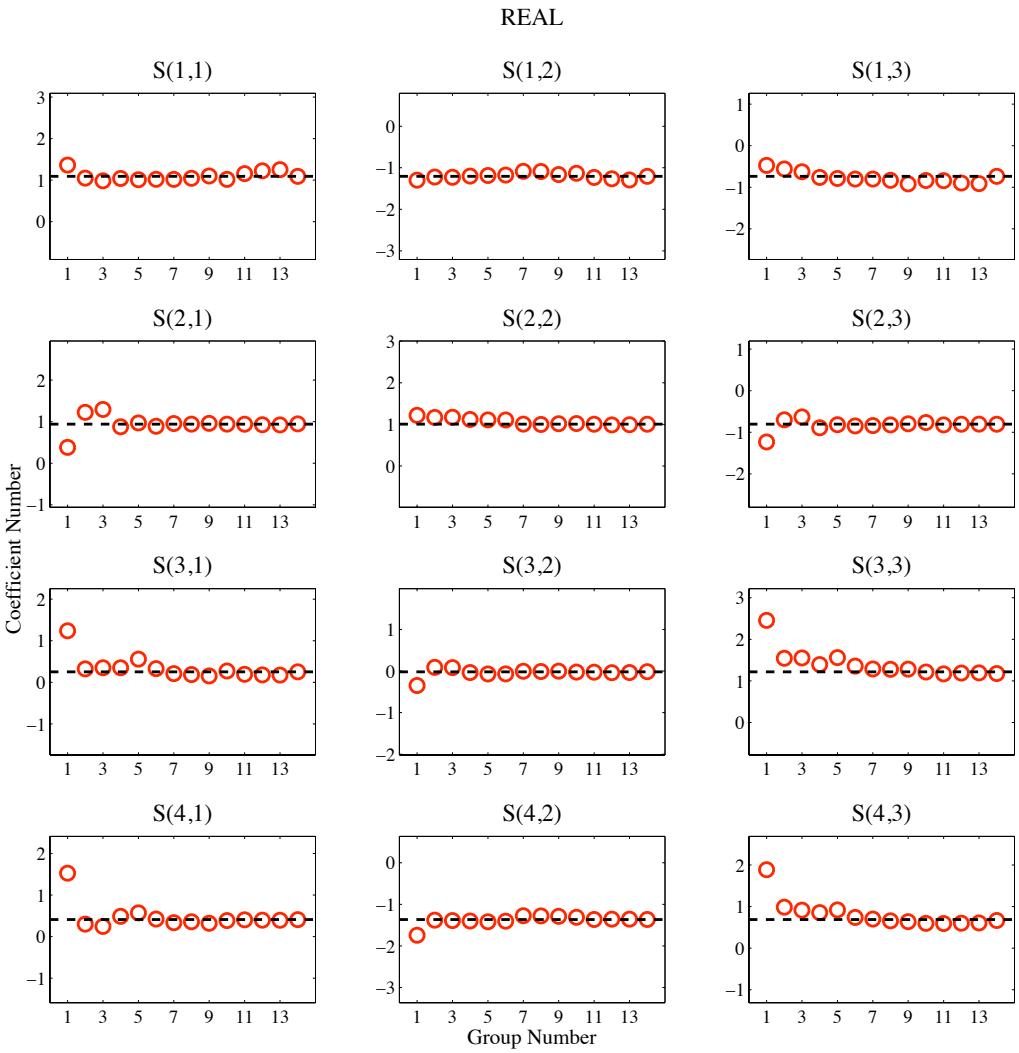

Figure A28. Illustration of the consistency between the calibration coefficients derived for B082 at different periods of time over a 2-year period. The calibration coefficient result from each group (RED circle) represents 332 strain amplitude sets associated with 4 teleseismic events. The groups are organized such that group number 1 represents events 1, 2, 3, and 4; group number 2 represents events 2, 3, 4, and 5; etc. according to data coverage listed in Table (10). The result from inverting all 1411 sets of strain information is indicated by the BLACK dashed line.

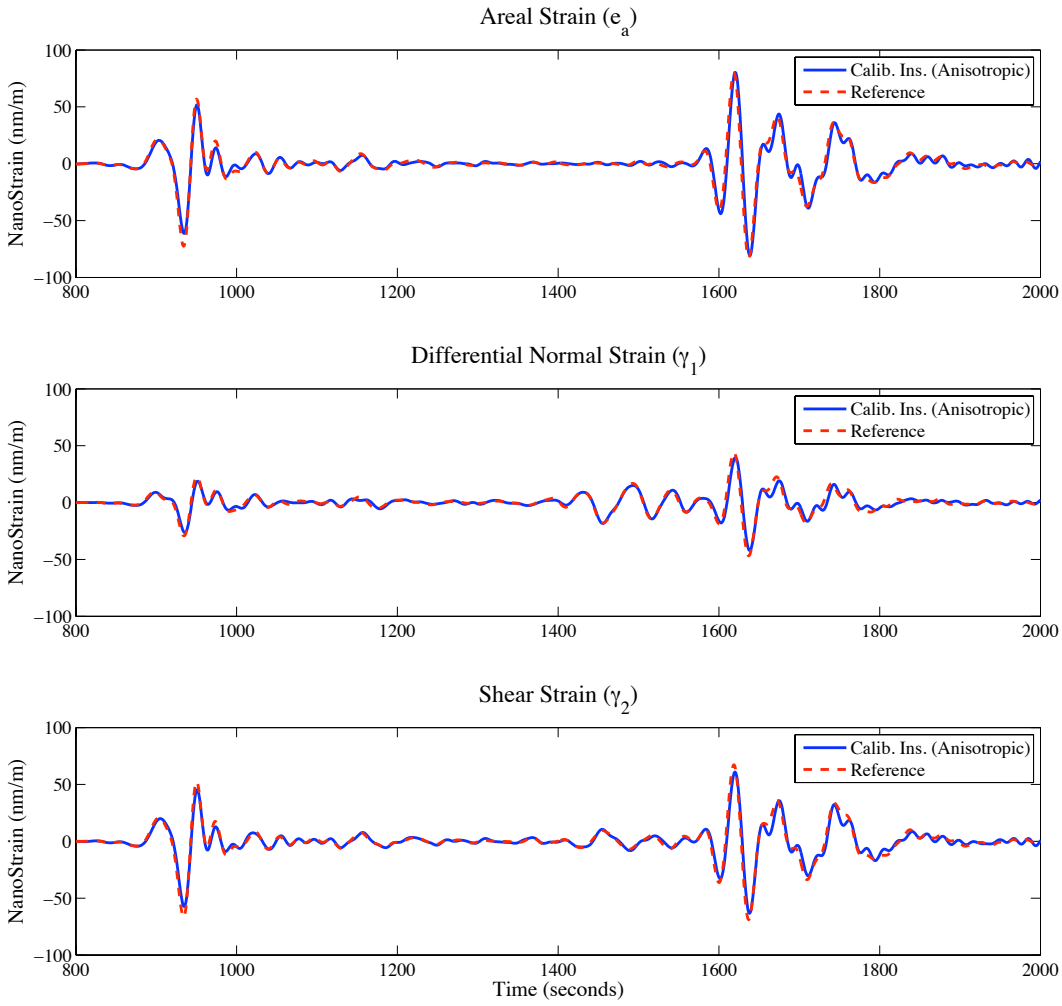

Figure A29. Illustration of the result from calibrating the instrument data associated with event 16 (2009/09/29) recorded by B082 using the calibration coefficients listed in Table (12).

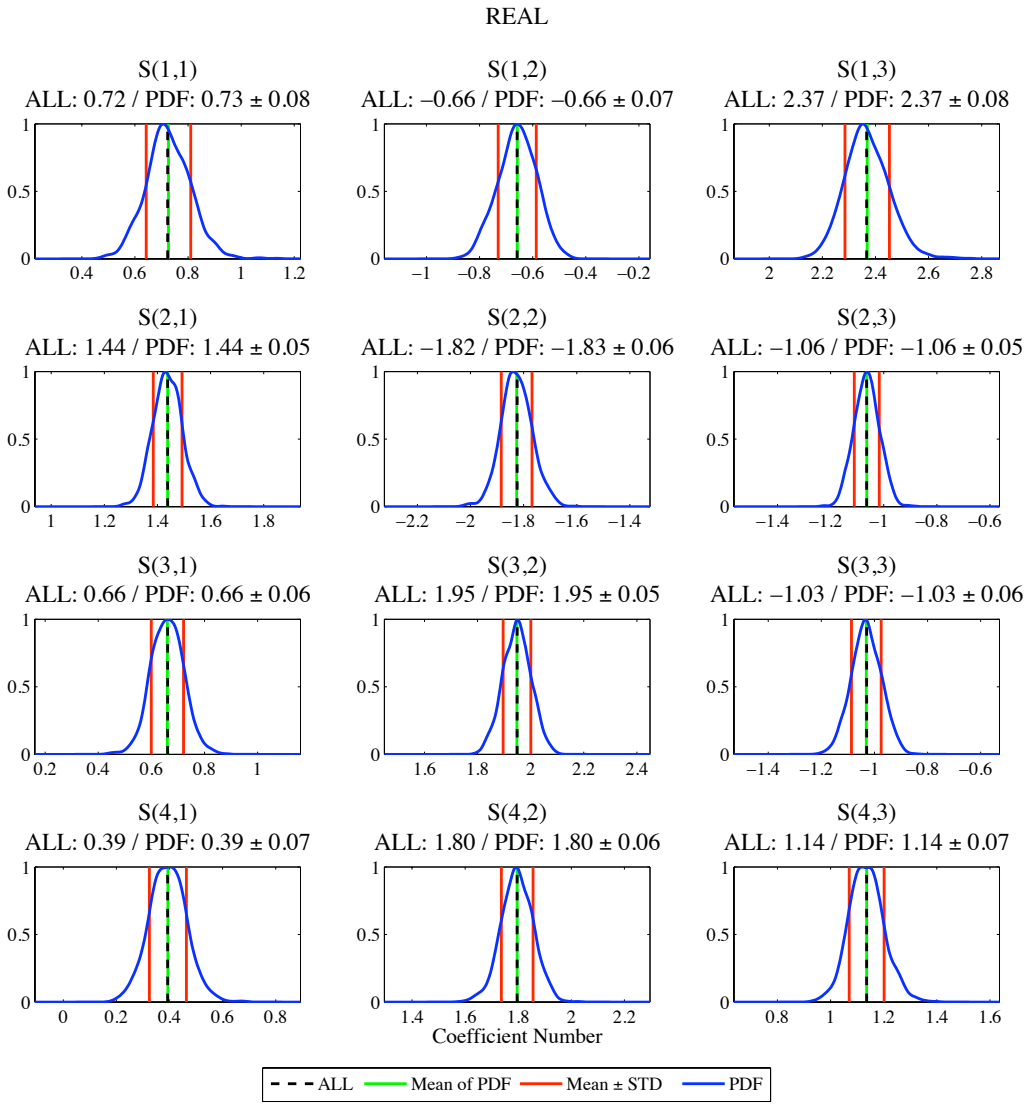

Figure A30. Illustration of the normalized probability density functions (PDF) associated with the REAL calibration coefficients derived for B084 using seismic data. The normalized PDF (BLUE line) about each coefficient value is the result from randomly selecting 71 (~5%) of the available 1411 sets of instrument and reference strain amplitudes, performing an inversion (similar to Equation 41) using these data, and repeating (1000 iterations total). The mean of the normalized PDF is indicated by the GREEN solid line, while the standard deviation about the mean is indicated by RED solid lines. The result from inverting all 1411 sets of strain information is indicated by the BLACK dashed line.

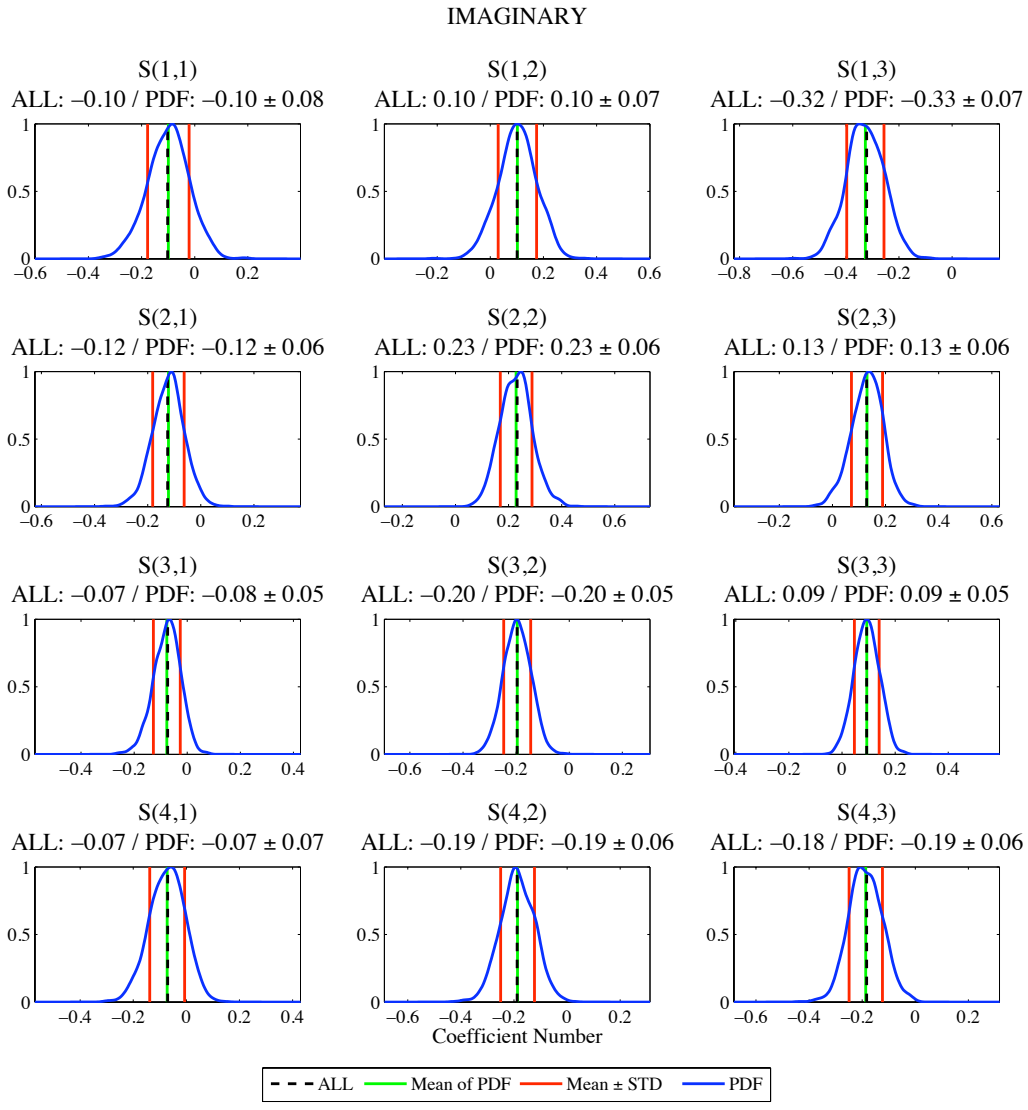

Figure A31. Illustration of the normalized probability density functions (PDF) associated with the IMAGINARY calibration coefficients derived for B084 using seismic data. The normalized PDF (BLUE line) about each coefficient value is the result from randomly selecting 71 (~5%) of the available 1411 sets of instrument and reference strain amplitudes, performing an inversion (similar to Equation 41) using these data, and repeating (1000 iterations total). The mean of the normalized PDF is indicated by the GREEN solid line, while the standard deviation about the mean is indicated by RED solid lines. The result from inverting all 1411 sets of strain information is indicated by the BLACK dashed line.

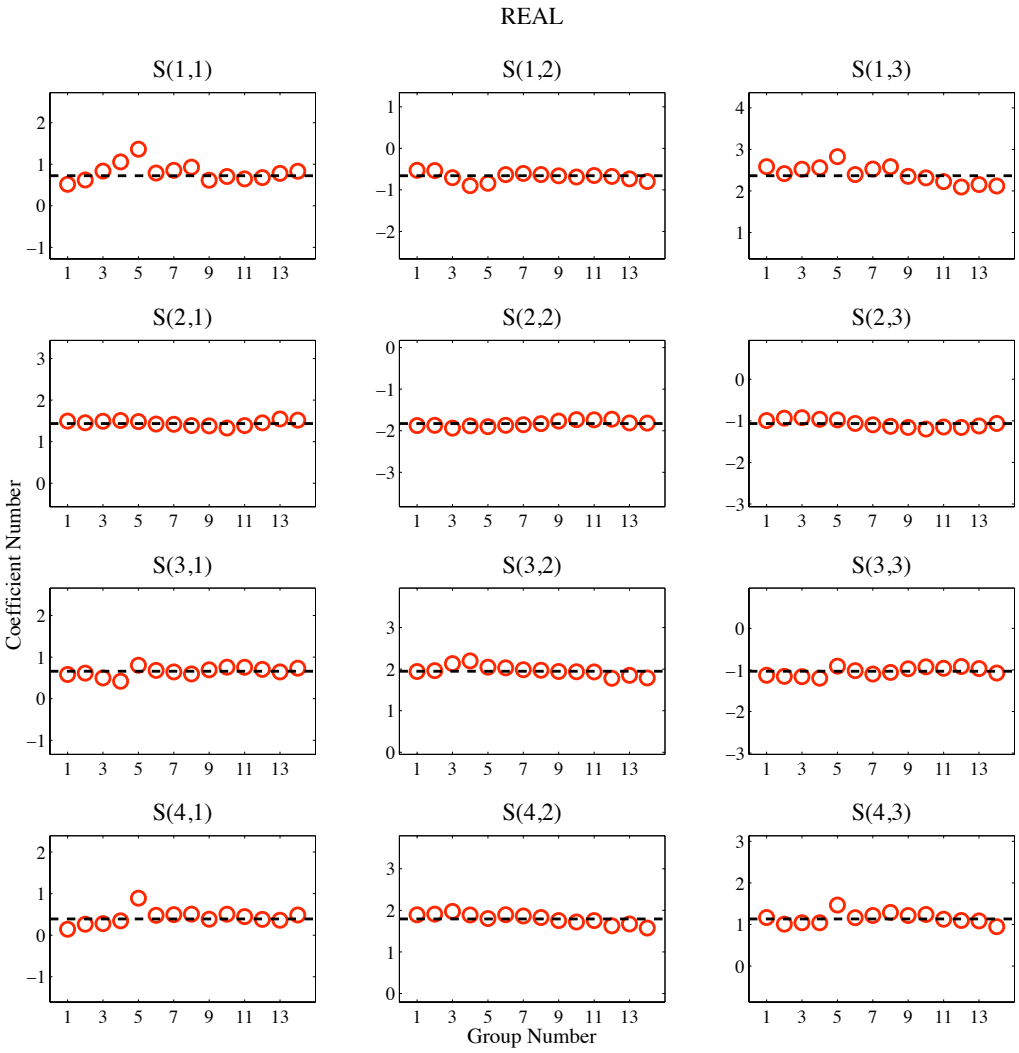

Figure A32. Illustration of the consistency between the calibration coefficients derived for B084 at different periods of time over a 2-year period. The calibration coefficient result from each group (RED circle) represents 332 strain amplitude sets associated with 4 teleseismic events. The groups are organized such that group number 1 represents events 1, 2, 3, and 4; group number 2 represents events 2, 3, 4, and 5; etc. according to data coverage listed in Table (10). The result from inverting all 1411 sets of strain information is indicated by the BLACK dashed line.

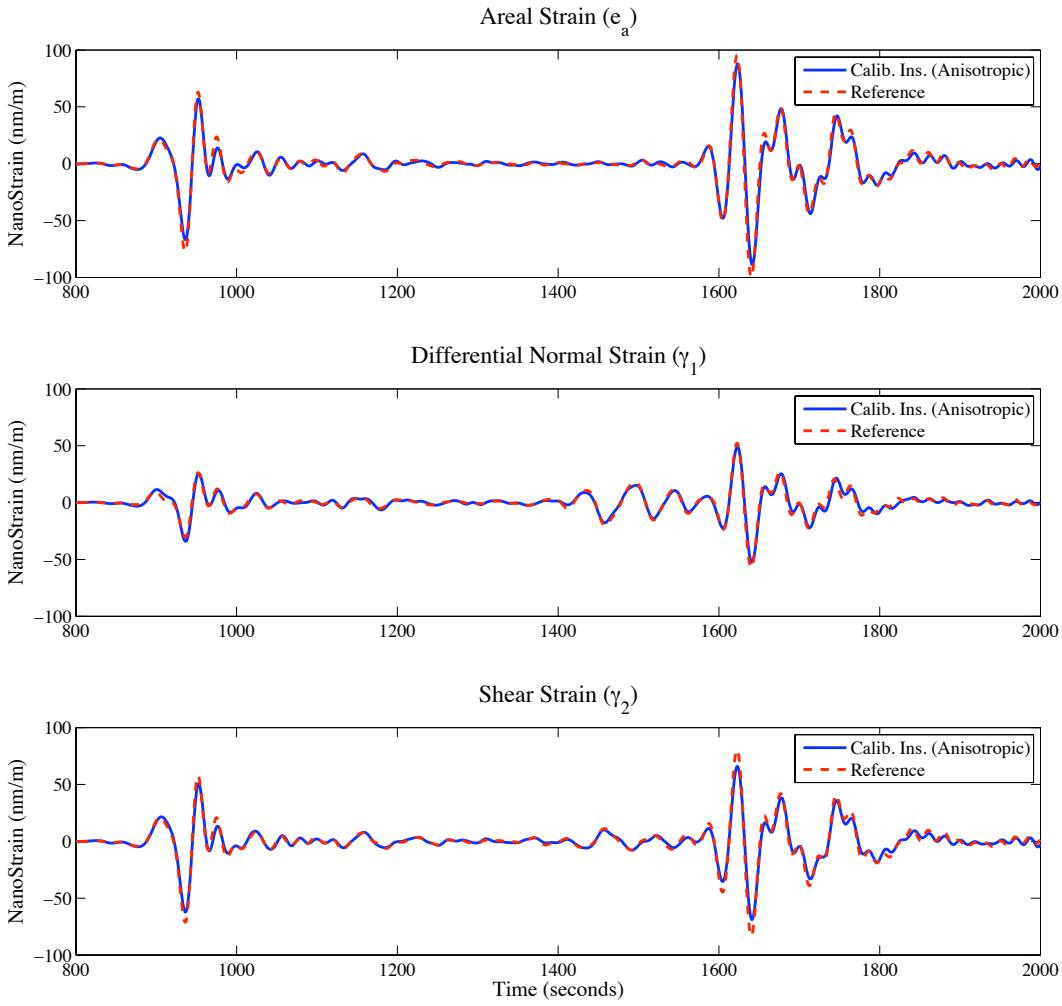

Figure A33. Illustration of the result from calibrating the instrument data associated with event 16 (2009/09/29) recorded by B084 using the calibration coefficients listed in Table (17).

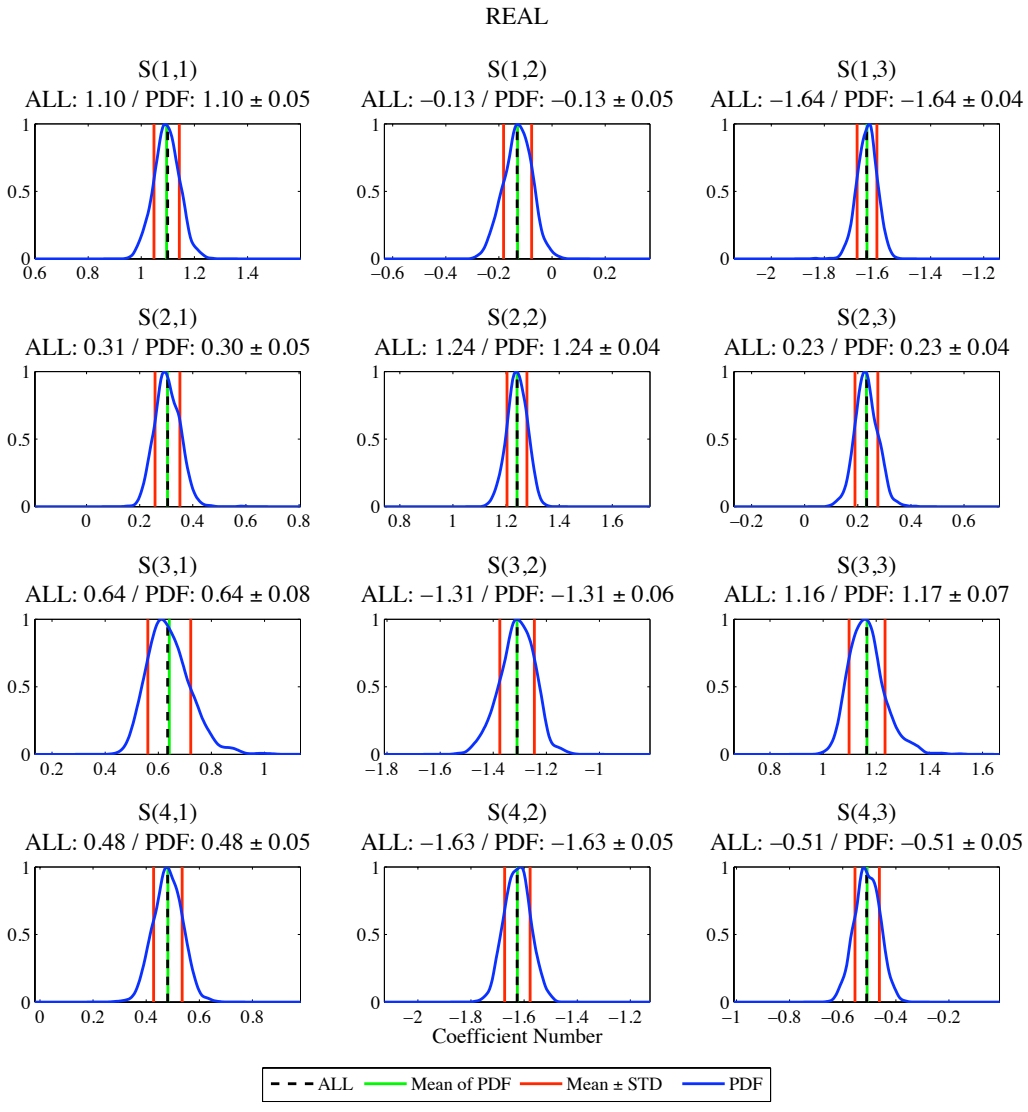

Figure A34. Illustration of the normalized probability density functions (PDF) associated with the REAL calibration coefficients derived for B086 using seismic data. The normalized PDF (BLUE line) about each coefficient value is the result from randomly selecting 58 (~5%) of the available 1162 sets of instrument and reference strain amplitudes, performing an inversion (similar to Equation 41) using these data, and repeating (1000 iterations total). The mean of the normalized PDF is indicated by the GREEN solid line, while the standard deviation about the mean is indicated by RED solid lines. The result from inverting all 1162 sets of strain information is indicated by the BLACK dashed line.

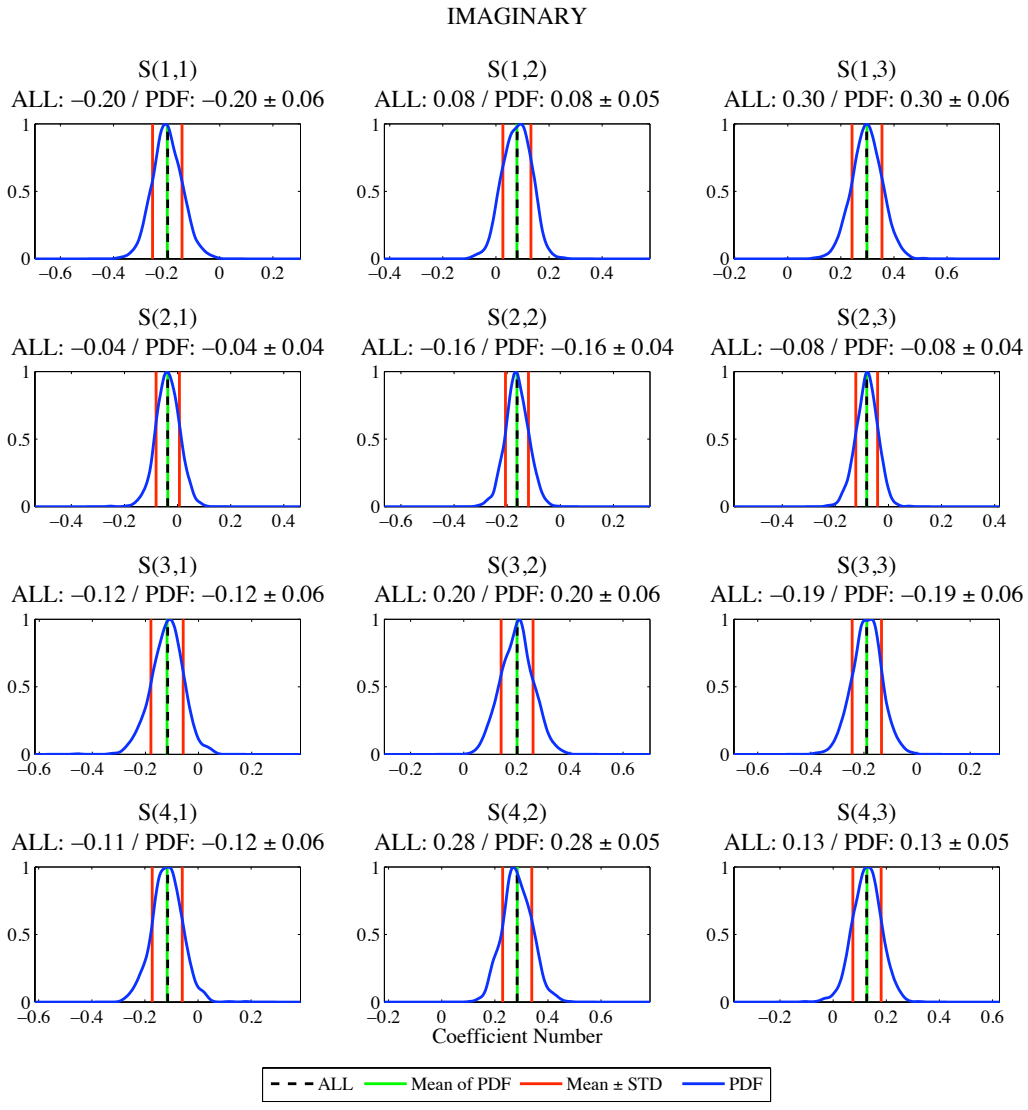

Figure A35. Illustration of the normalized probability density functions (PDF) associated with the IMAGINARY calibration coefficients derived for B086 using seismic data. The distribution of the coefficient values (BLUE line) are the result from inverting for the calibration coefficients over 1000 iterations of randomly selecting 5% (or ~58) of the 1162 sets of instrument strain and reference strain amplitudes. The peak of the normalized PDF is indicated by the BLACK dashed line, while the result from inverting all 1162 sets of strain information is indicated by the GREEN solid line.

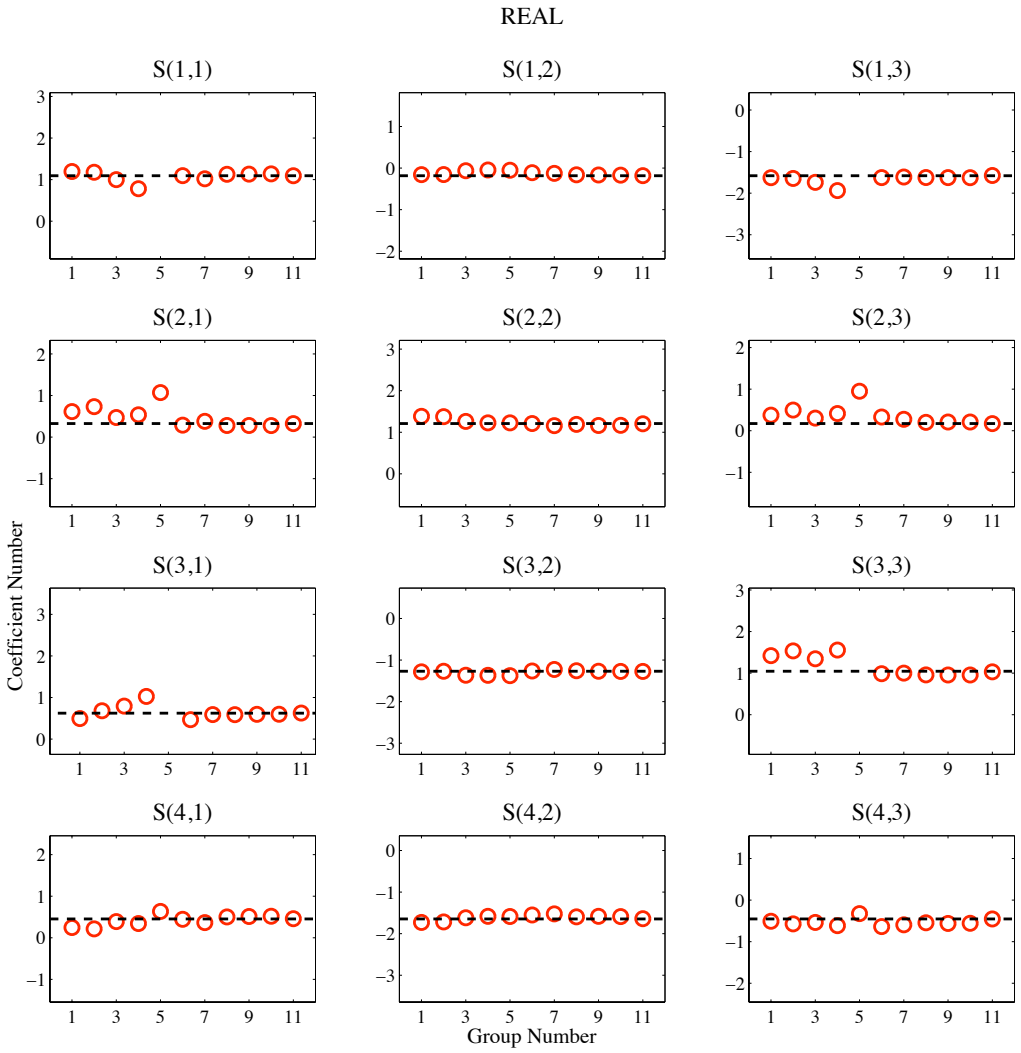

Figure A36. Illustration of the consistency between the calibration coefficients derived for B086 at different periods of time over a 2-year period. The calibration coefficient result from each group (RED circle) represents 332 strain amplitude sets associated with 4 teleseismic events. The groups are organized such that group number 1 represents events 2, 3, 5, and 6; group number 2 represents events 3, 5, 6, and 7; etc. according to data coverage listed in Table (10). The result from inverting all 1162 sets of strain information is indicated by the BLACK dashed line.

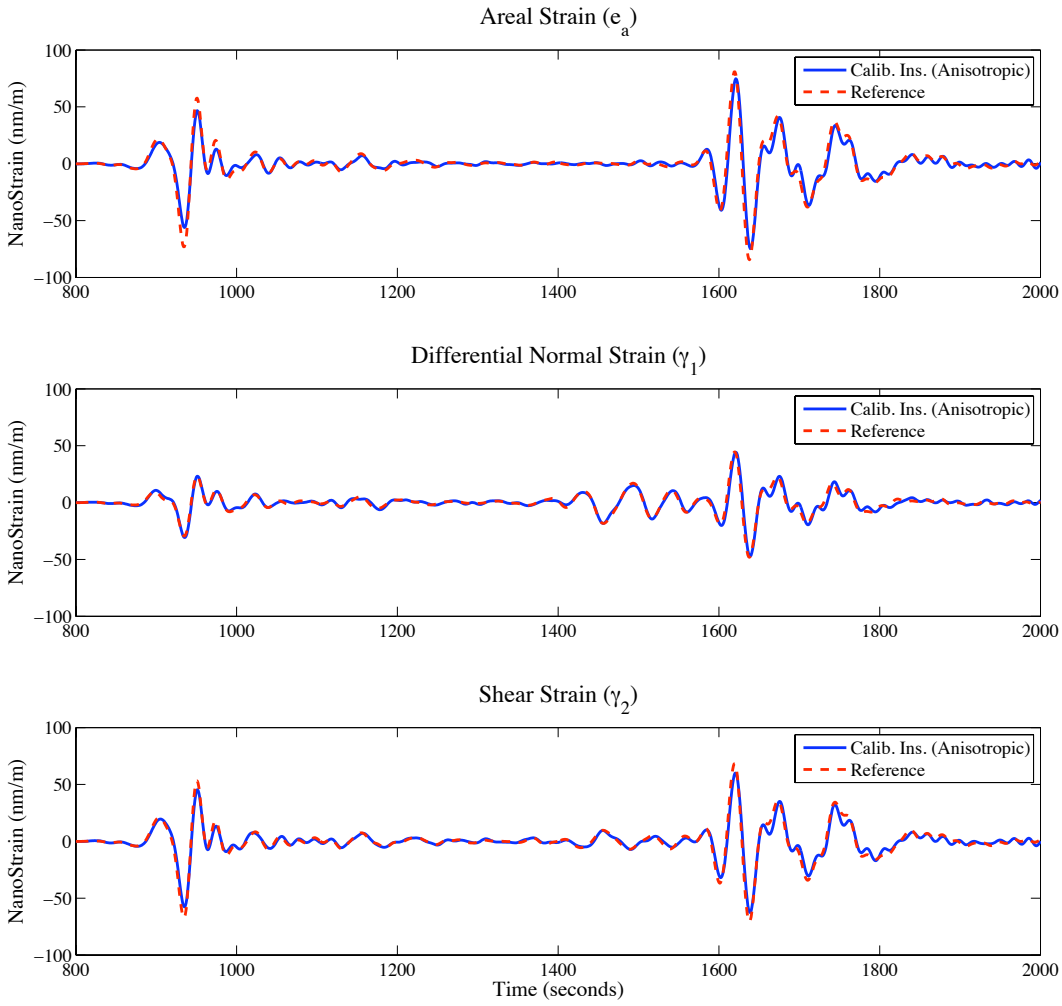

Figure A37. Illustration of the result from calibrating the instrument data associated with event 16 (2009/09/29) recorded by B086 using the calibration coefficients listed in Table (19).

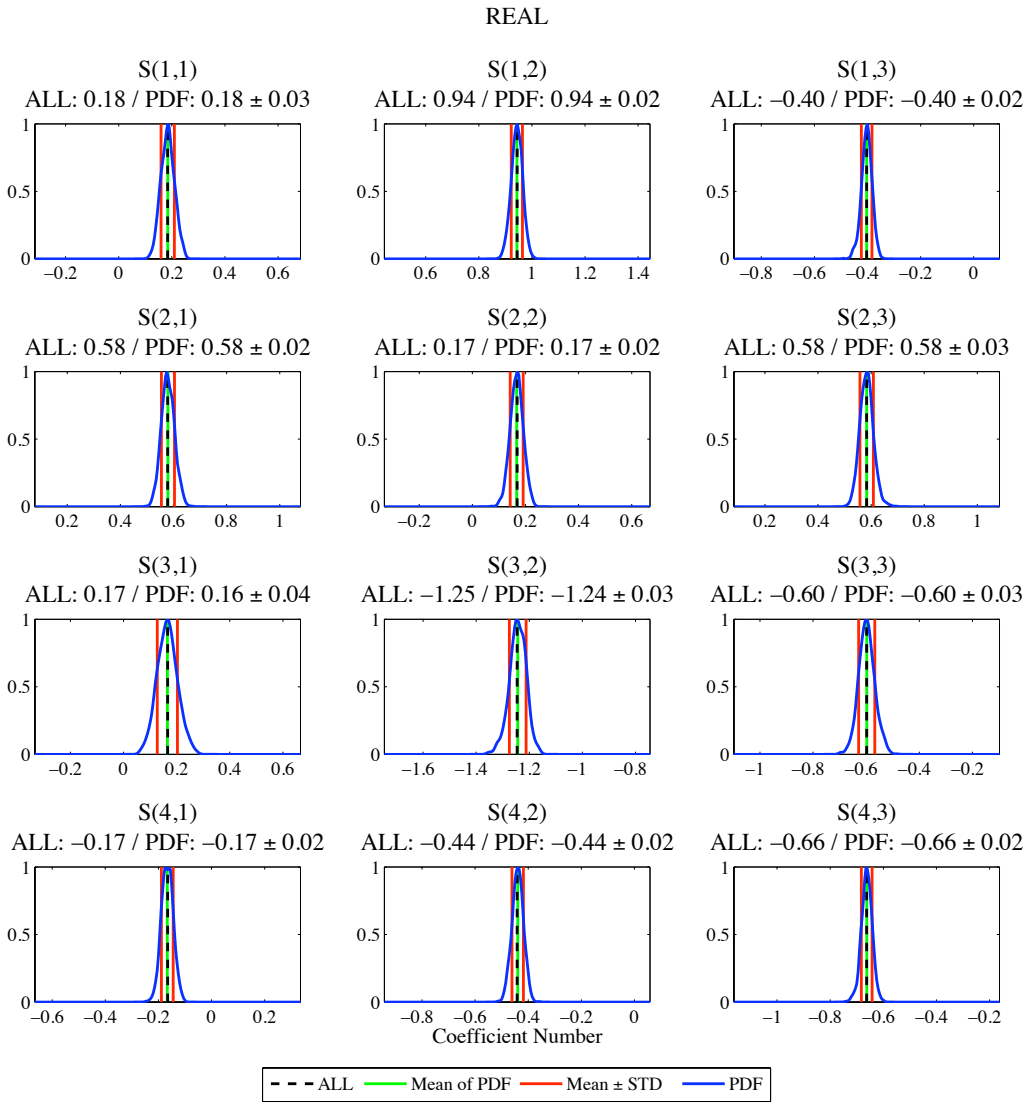

Figure A38. Illustration of the normalized probability density functions (PDF) associated with the REAL calibration coefficients derived for B087 using seismic data. The normalized PDF (BLUE line) about each coefficient value is the result from randomly selecting 71 (~5%) of the available 1411 sets of instrument and reference strain amplitudes, performing an inversion (similar to Equation 41) using these data, and repeating (1000 iterations total). The mean of the normalized PDF is indicated by the GREEN solid line, while the standard deviation about the mean is indicated by RED solid lines. The result from inverting all 1411 sets of strain information is indicated by the BLACK dashed line.

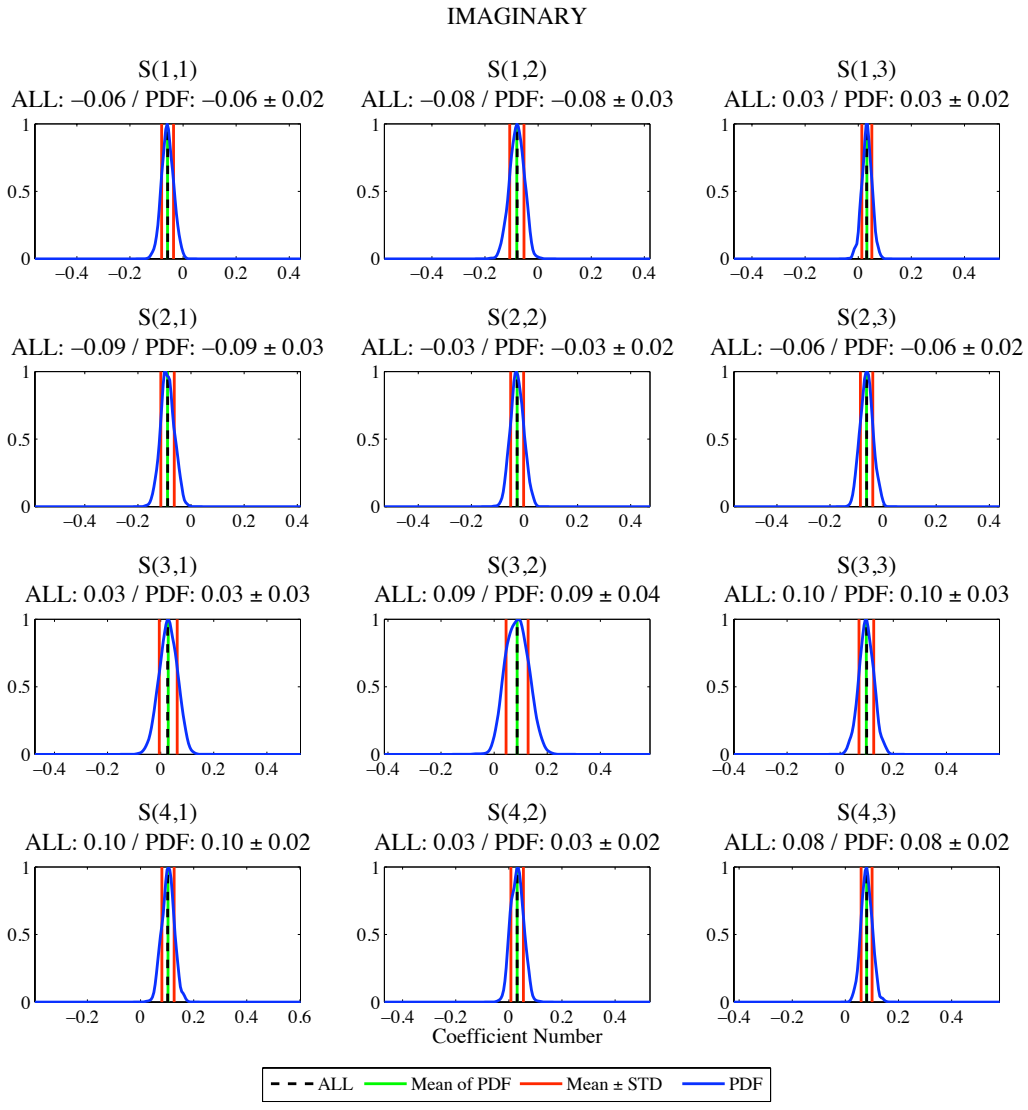

Figure A39. Illustration of the normalized probability density functions (PDF) associated with the IMAGINARY calibration coefficients derived for B0847 using seismic data. The normalized PDF (BLUE line) about each coefficient value is the result from randomly selecting 71 (~5%) of the available 1411 sets of instrument and reference strain amplitudes, performing an inversion (similar to Equation 41) using these data, and repeating (1000 iterations total). The mean of the normalized PDF is indicated by the GREEN solid line, while the standard deviation about the mean is indicated by RED solid lines. The result from inverting all 1411 sets of strain information is indicated by the BLACK dashed line.

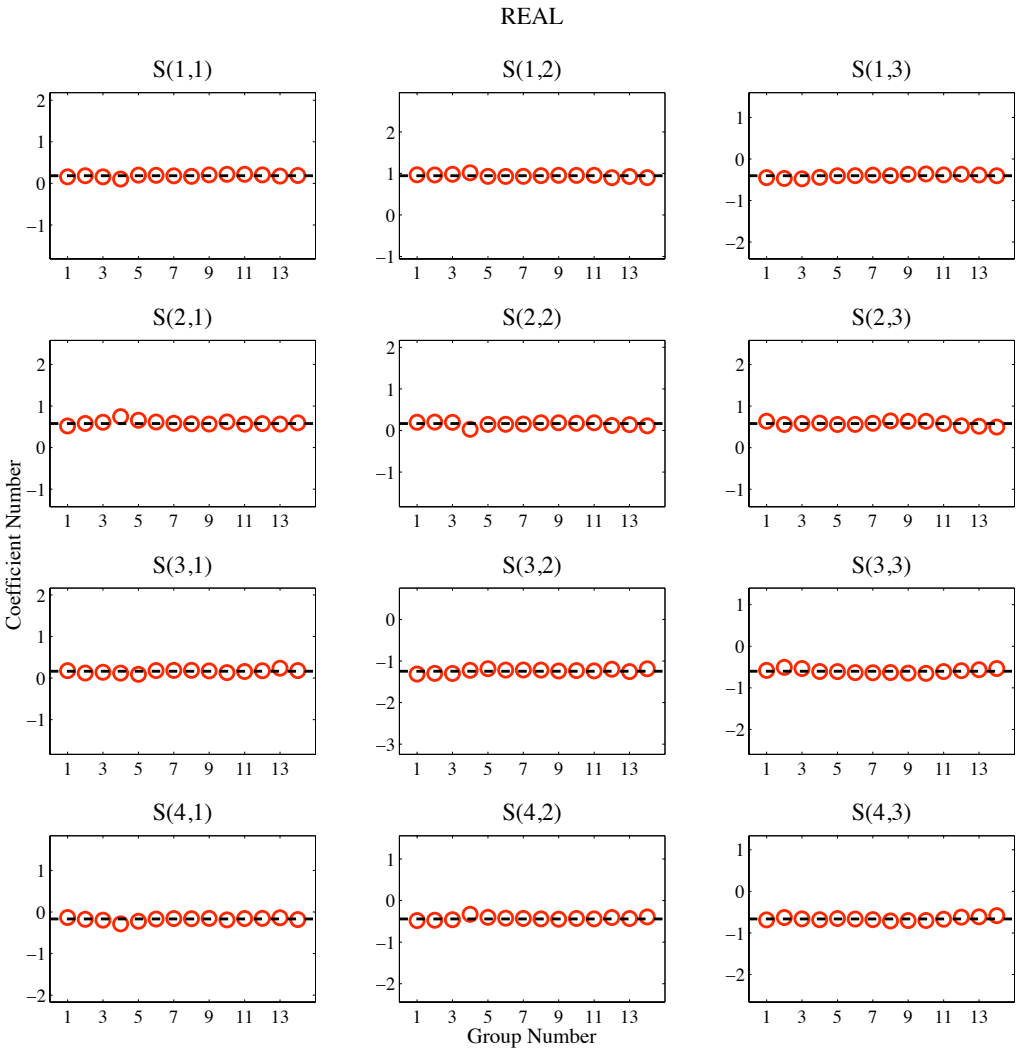

Figure A40. Illustration of the consistency between the calibration coefficients derived for B087 at different periods of time over a 2-year period. The calibration coefficient result from each group (RED circle) represents 332 strain amplitude sets associated with 4 teleseismic events. The groups are organized such that group number 1 represents events 1, 2, 3, and 4; group number 2 represents events 2, 3, 4, and 5; etc. according to data coverage listed in Table (10). The result from inverting all 1411 sets of strain information is indicated by the BLACK dashed line.

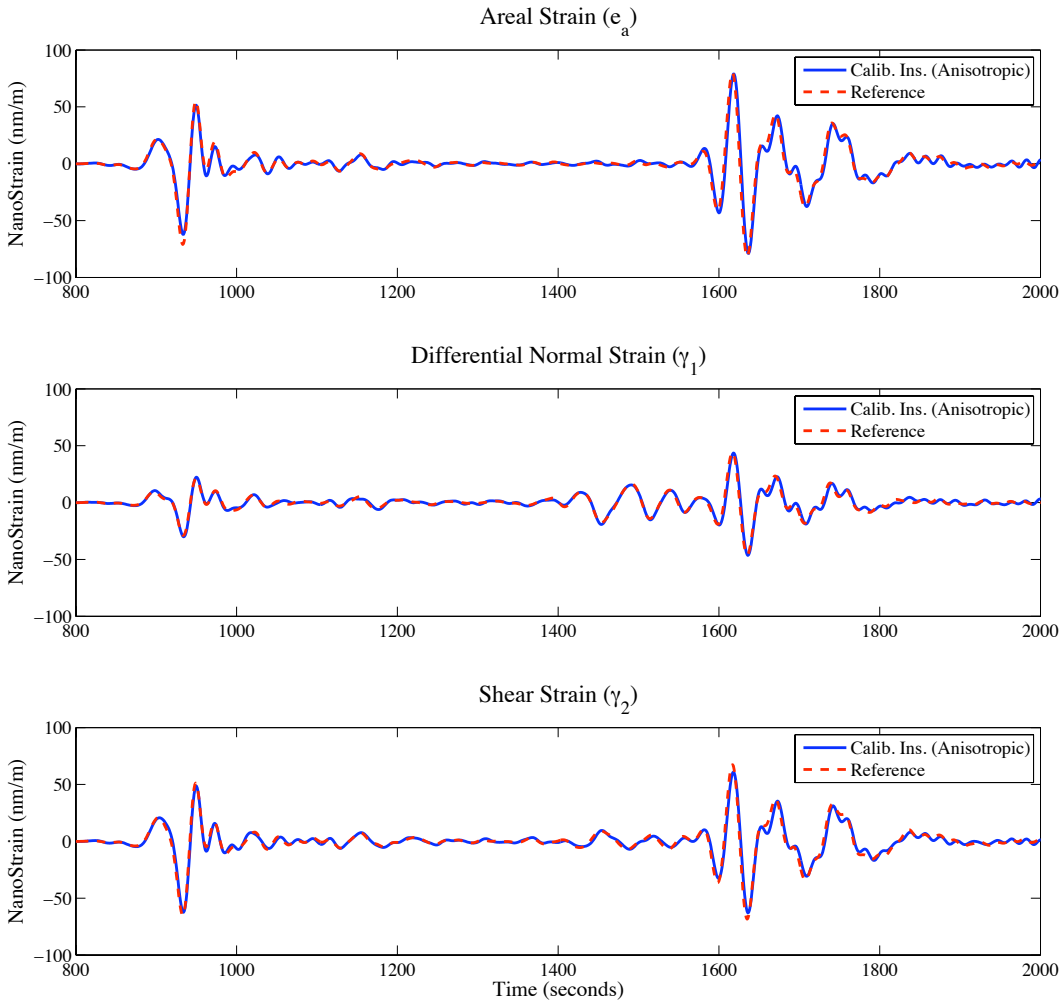

Figure A41. Illustration of the result from calibrating the instrument data associated with event 16 (2009/09/29) recorded by B087 using the calibration coefficients listed in Table (21).

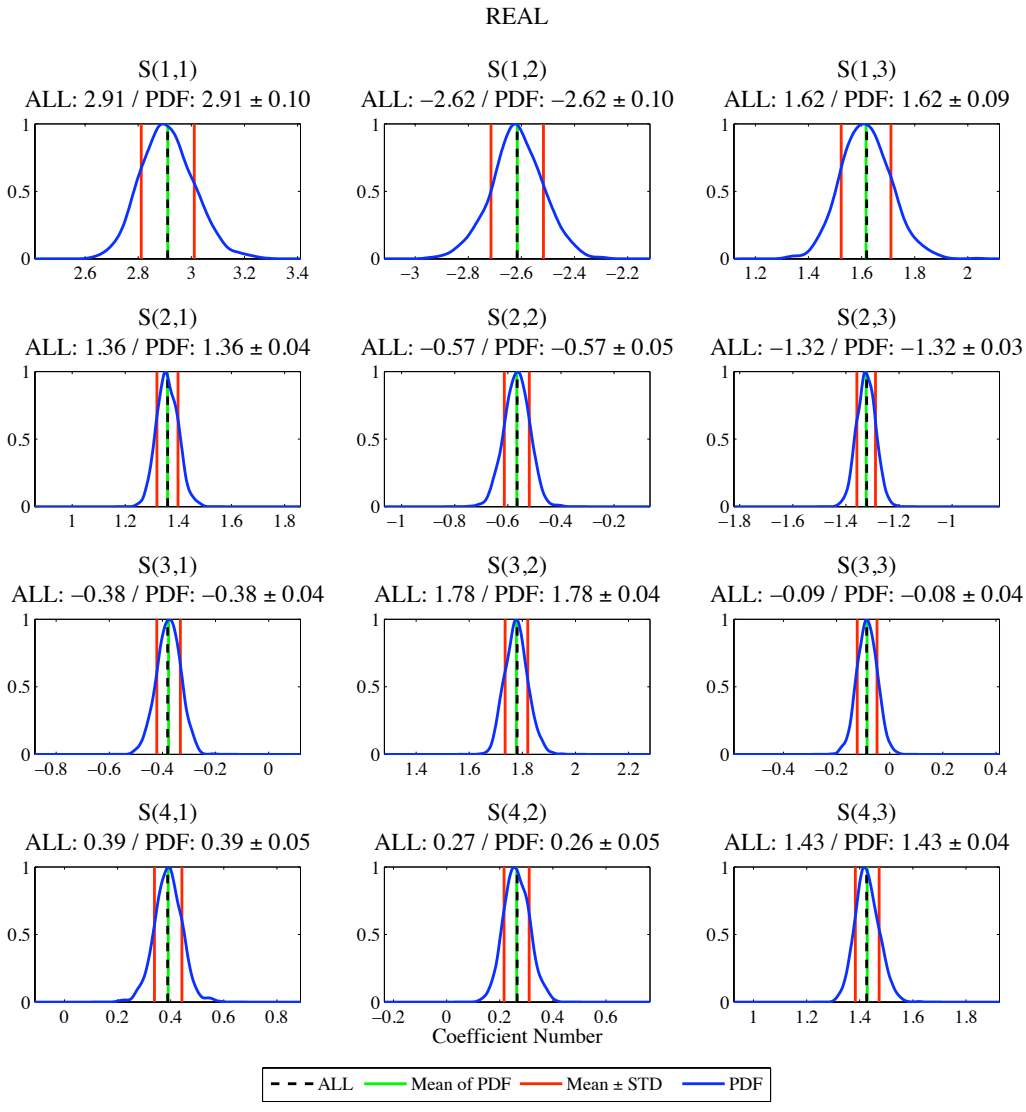

Figure A42. Illustration of the normalized probability density functions (PDF) associated with the REAL calibration coefficients derived for B088 using seismic data. The normalized PDF (BLUE line) about each coefficient value is the result from randomly selecting 71 (~5%) of the available 1411 sets of instrument and reference strain amplitudes, performing an inversion (similar to Equation 41) using these data, and repeating (1000 iterations total). The mean of the normalized PDF is indicated by the GREEN solid line, while the standard deviation about the mean is indicated by RED solid lines. The result from inverting all 1411 sets of strain information is indicated by the BLACK dashed line.

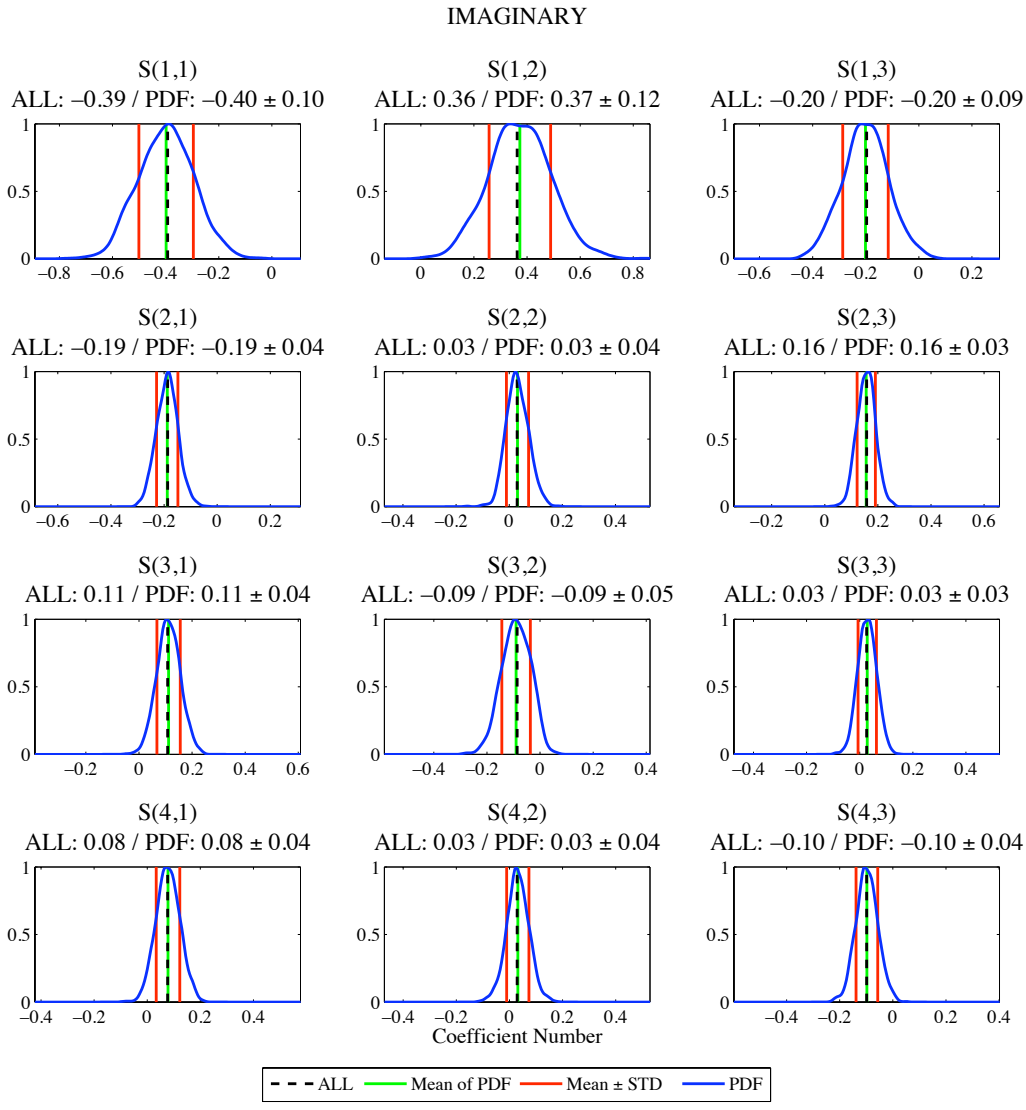

Figure A43. Illustration of the normalized probability density functions (PDF) associated with the REAL calibration coefficients derived for B088 using seismic data. The normalized PDF (BLUE line) about each coefficient value is the result from randomly selecting 71 (~5%) of the available 1411 sets of instrument and reference strain amplitudes, performing an inversion (similar to Equation 41) using these data, and repeating (1000 iterations total). The mean of the normalized PDF is indicated by the GREEN solid line, while the standard deviation about the mean is indicated by RED solid lines. The result from inverting all 1411 sets of strain information is indicated by the BLACK dashed line.

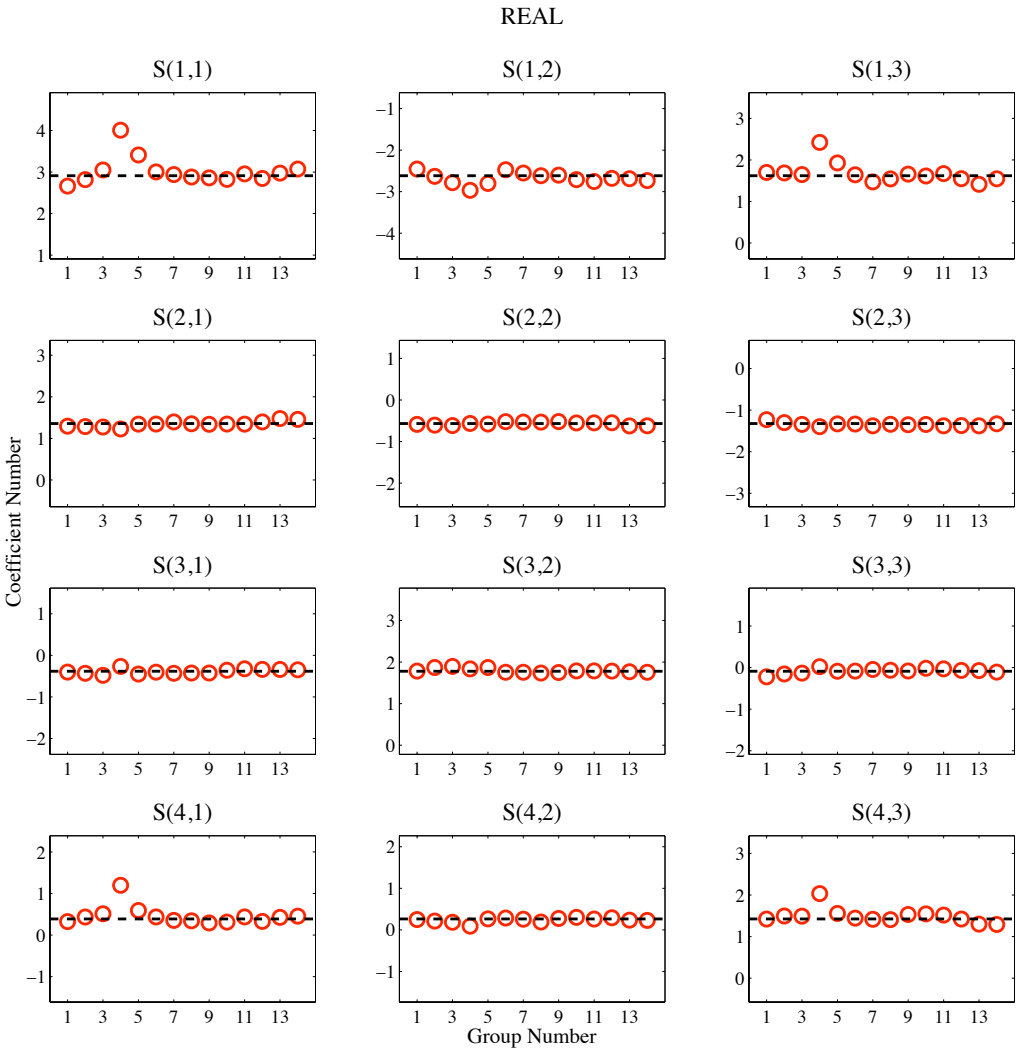

Figure A44. Illustration of the consistency between the calibration coefficients derived for B088 at different periods of time over a 2-year period. The calibration coefficient result from each group (RED circle) represents 332 strain amplitude sets associated with 4 teleseismic events. The groups are organized such that group number 1 represents events 2, 3, 4, and 5; group number 2 represents events 3, 4, 5, and 6; etc. according to data coverage listed in Table (10). The result from inverting all 1411 sets of strain information is indicated by the BLACK dashed line.

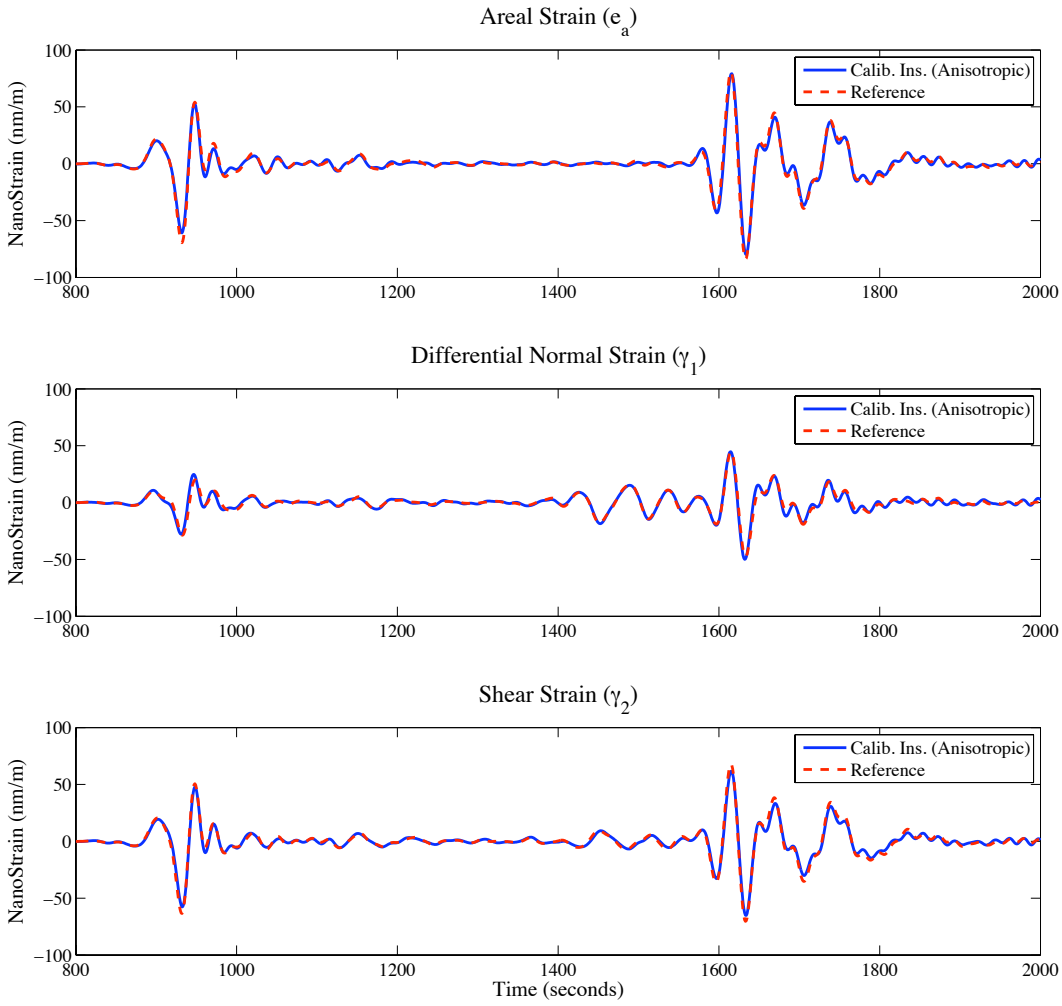

Figure A45. Illustration of the result from calibrating the instrument data associated with event 16 (2009/09/29) recorded by B088 using the calibration coefficients listed in Table (23).

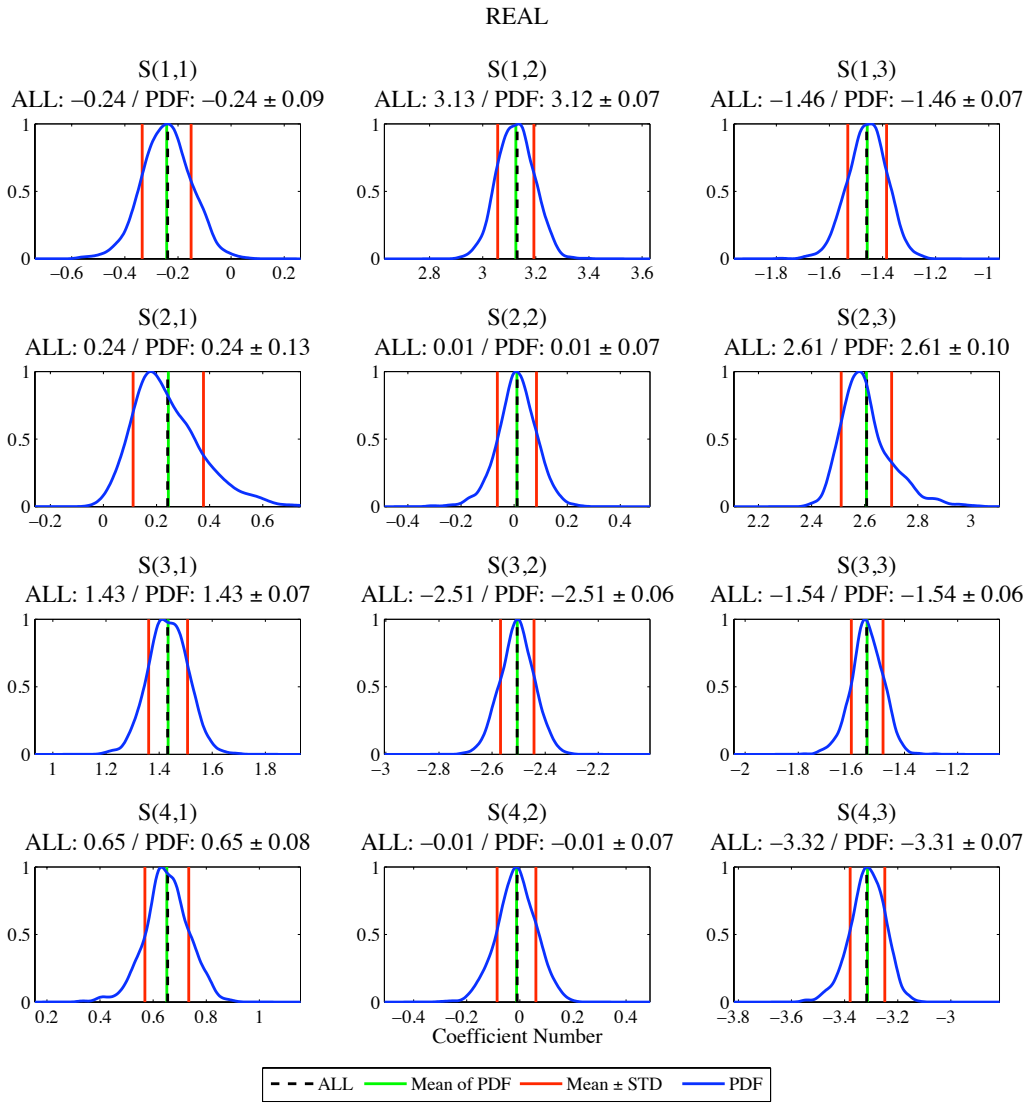

Figure A46. Illustration of the normalized probability density functions (PDF) associated with the REAL calibration coefficients derived for B089 using seismic data. The normalized PDF (BLUE line) about each coefficient value is the result from randomly selecting 74 (~5%) of the available 1494 sets of instrument and reference strain amplitudes, performing an inversion (similar to Equation 41) using these data, and repeating (1000 iterations total). The mean of the normalized PDF is indicated by the GREEN solid line, while the standard deviation about the mean is indicated by RED solid lines. The result from inverting all 1494 sets of strain information is indicated by the BLACK dashed line.

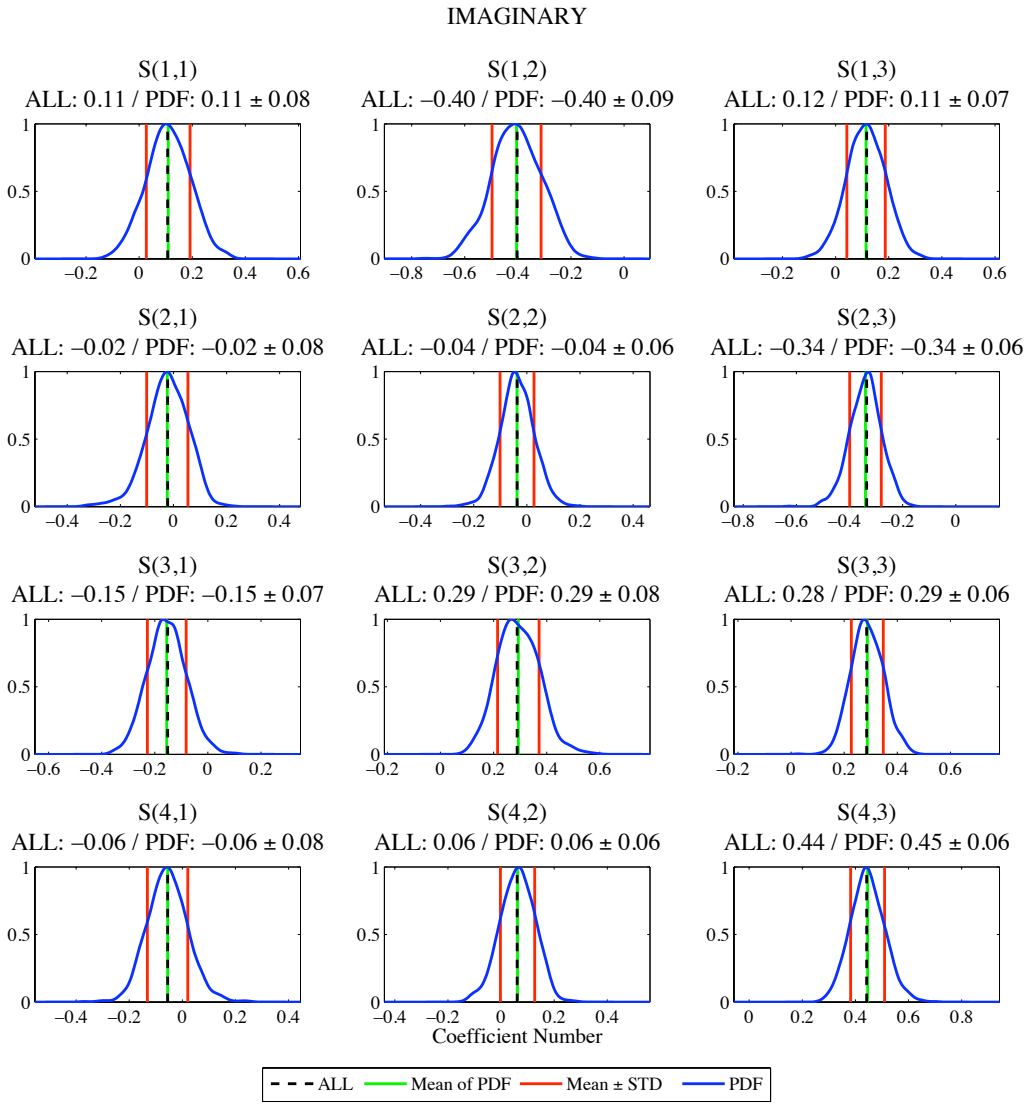

Figure A47. Illustration of the normalized probability density functions (PDF) associated with the IMAGINARY calibration coefficients derived for B089 using seismic data. The normalized PDF (BLUE line) about each coefficient value is the result from randomly selecting 74 (~5%) of the available 1494 sets of instrument and reference strain amplitudes, performing an inversion (similar to Equation 41) using these data, and repeating (1000 iterations total). The mean of the normalized PDF is indicated by the GREEN solid line, while the standard deviation about the mean is indicated by RED solid lines. The result from inverting all 1494 sets of strain information is indicated by the BLACK dashed line.

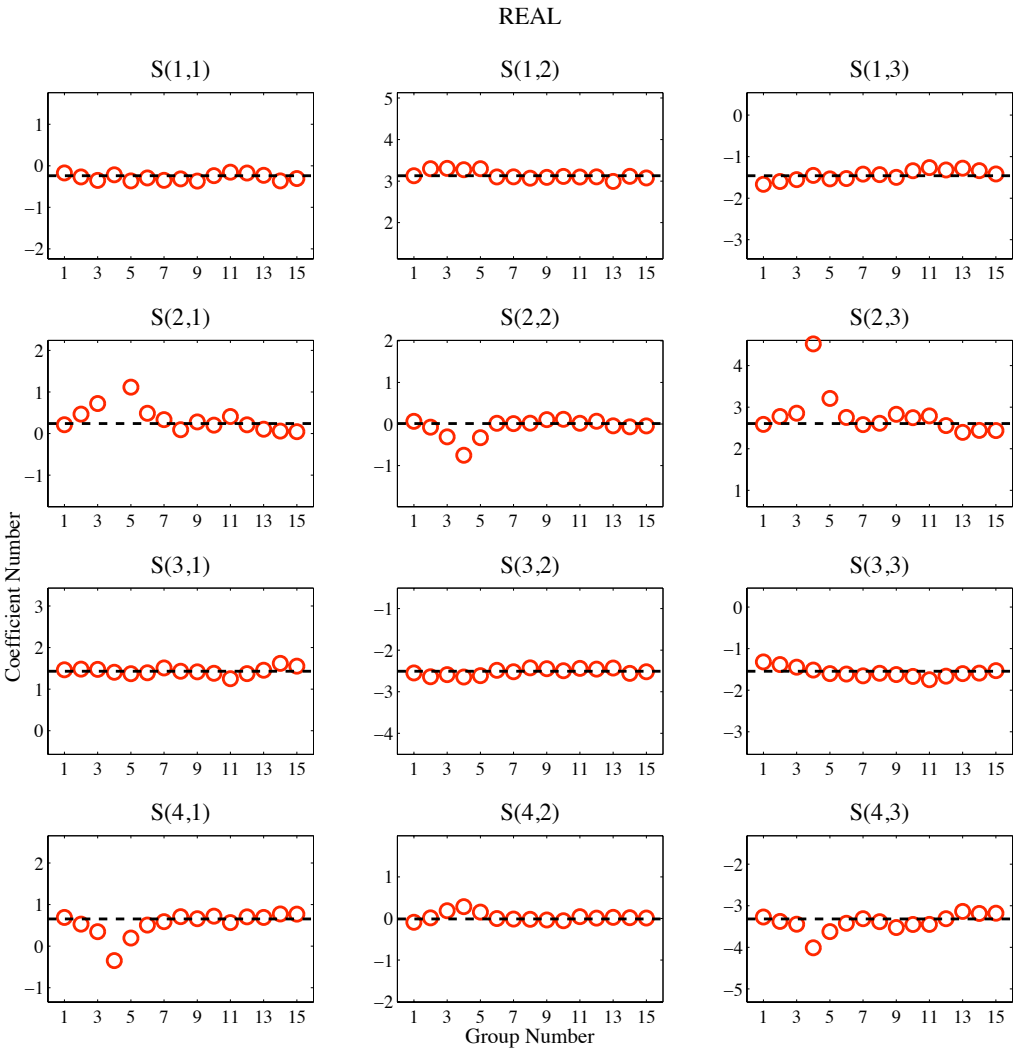

Figure A48. Illustration of the consistency between the calibration coefficients derived for B089 at different periods of time over a 2-year period. The calibration coefficient result from each group (RED circle) represents 332 strain amplitude sets associated with 4 teleseismic events. The groups are organized such that group number 1 represents events 2, 3, 4, and 5; group number 2 represents events 3, 4, 5, and 6; etc. according to data coverage listed in Table (10). The result from inverting all 1494 sets of strain information is indicated by the BLACK dashed line.

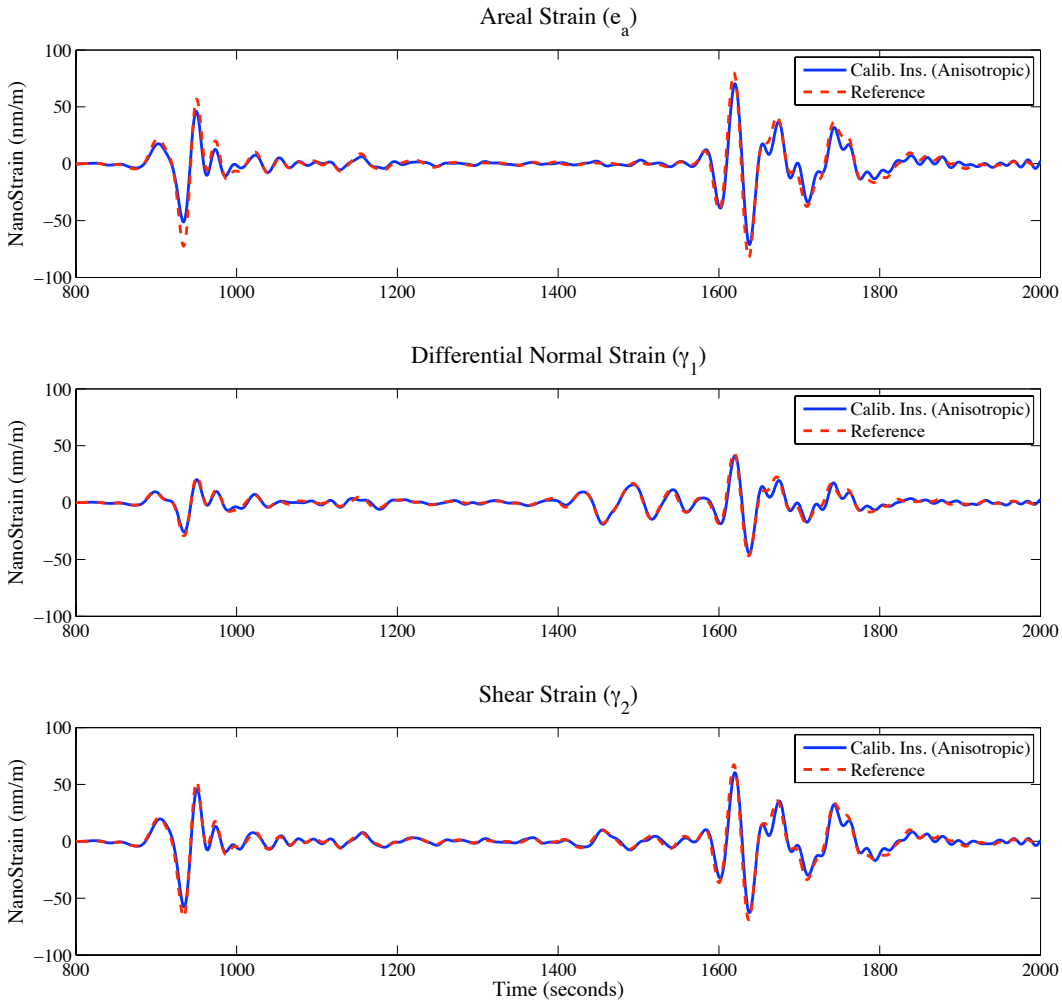

Figure A49. Illustration of the result from calibrating the instrument data associated with event 16 (2009/09/29) recorded by B089 using the calibration coefficients listed in Table (25).

APPENDIX 3

Supplemental Information for Chapter Four

Summary

Supplemental figures are included in this appendix in order to provide the reader with additional visual verification/insight to the words and figures available in Chapter (4). The strain and seismic records illustrated in this section correspond to the M5.5 Chino Hills earthquake (2009/07/29), in southern California, and the M7.0 Haitian earthquake (2010/01/12). All the figures in Chapter (4) associated with Methods (1) and (2) are essentially a subset of the figures found in this section. The purpose for duplicating these figures is to illustrate the performance of each method for different frequency intervals for the same example events described above.

Figures

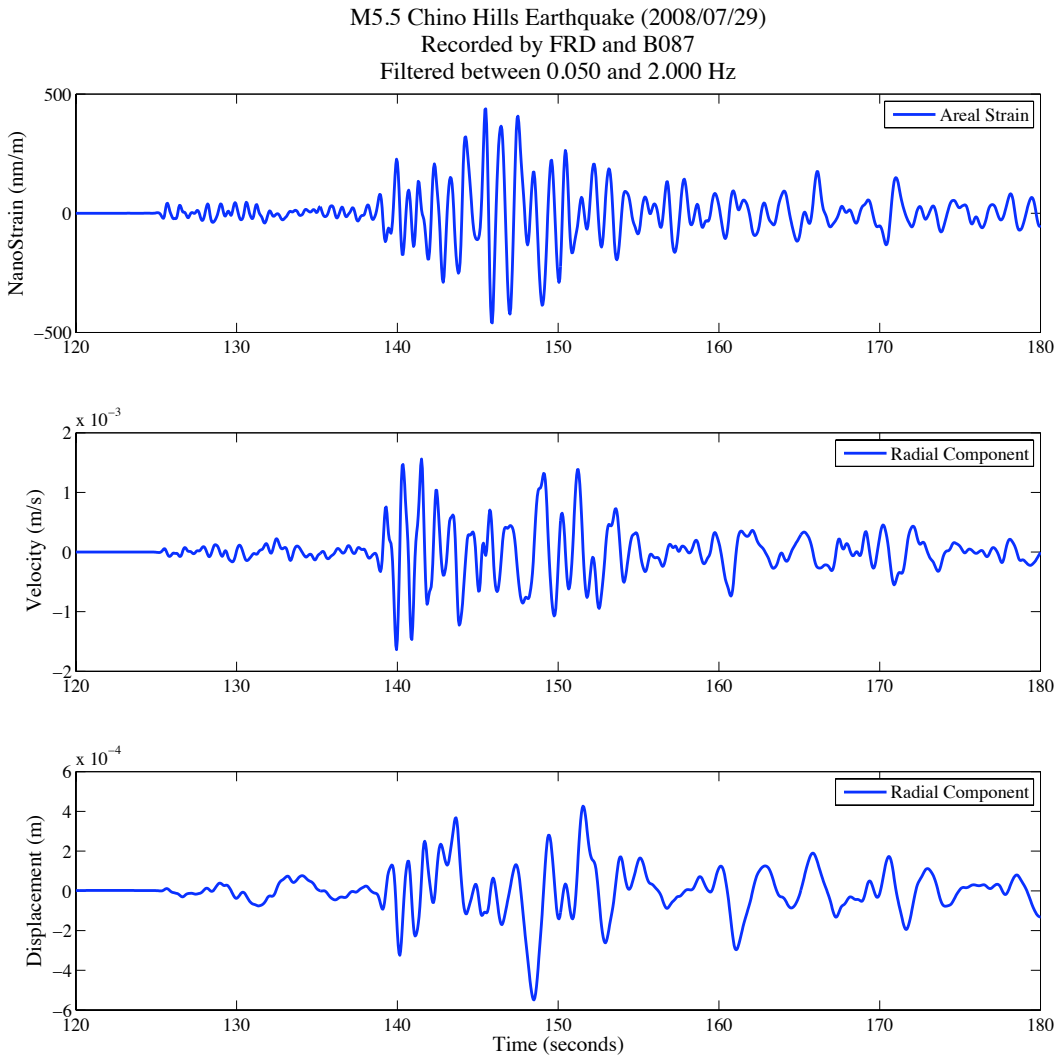

Figure A50. Data used for Method (1) include the areal strain (TOP – BLUE), the radial ground velocity (MIDDLE – BLUE), and the radial ground displacement (BOTTOM – BLUE). Calibrated strain data correspond to borehole GTSM station B087 and the seismic data correspond to Anza broadband seismometer FRD. The original seismograms correspond to the 29 July 2008 M5.5 Chino Hills earthquake band-pass filtered between 0.05 Hz and 2.0 Hz with a 4-pole Butterworth acausal filter.

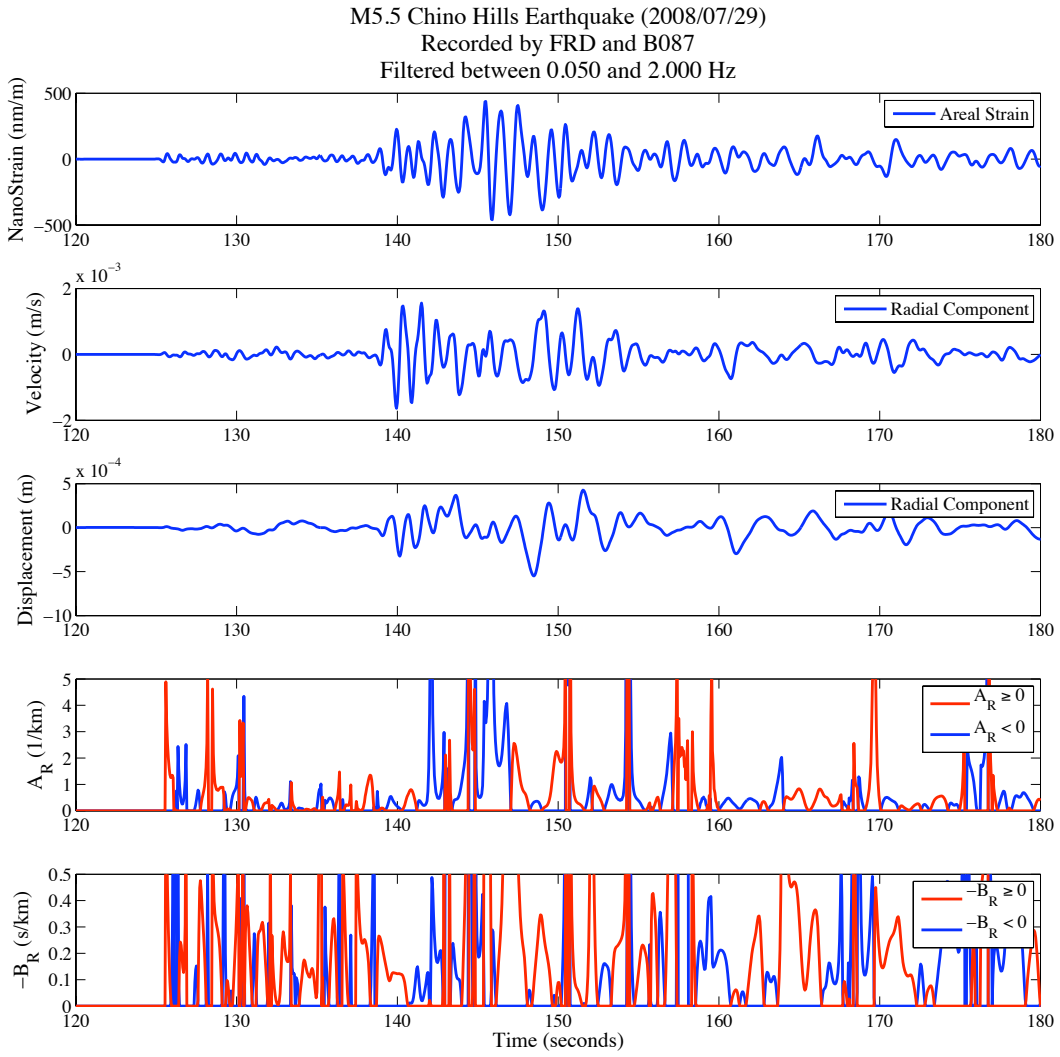

Figure A51. The result of applying Method (1) to the data corresponding to Figure (A50) band-pass filtered between 0.05 Hz and 2.0 Hz with a 4-pole Butterworth acausal filter. Instability (or "glitches") in 1D spatial gradient result is likely due to interfering waves at a particular point in time or due to an inappropriate assumption of propagation direction.

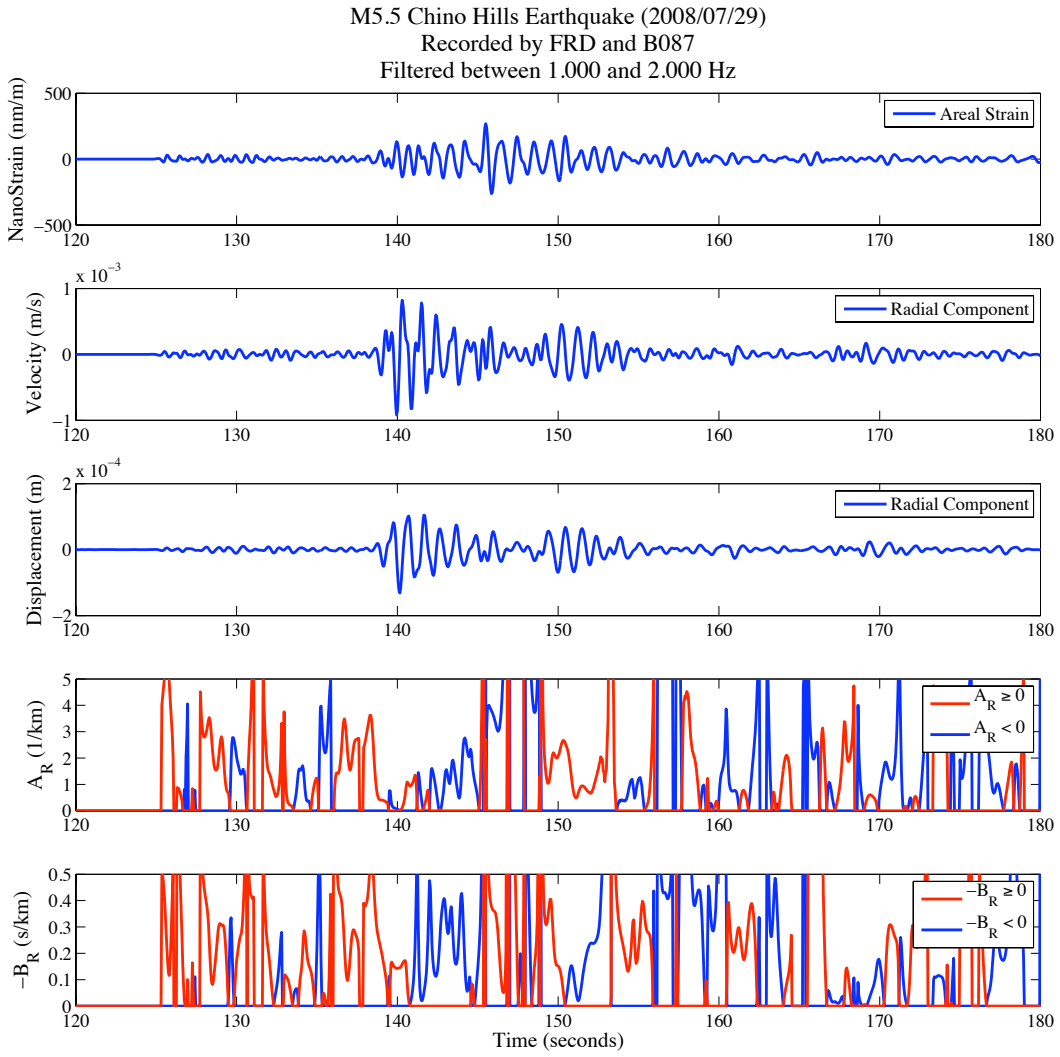

Figure A52. The result of applying Method (1) to the data corresponding to Figure (A50) band-pass filtered between 1.0 Hz and 2.0 Hz with a 4-pole Butterworth acausal filter. Instability (or "glitches") in 1D spatial gradient result is likely due to interfering waves at a particular point in time or due to an inappropriate assumption of propagation direction.

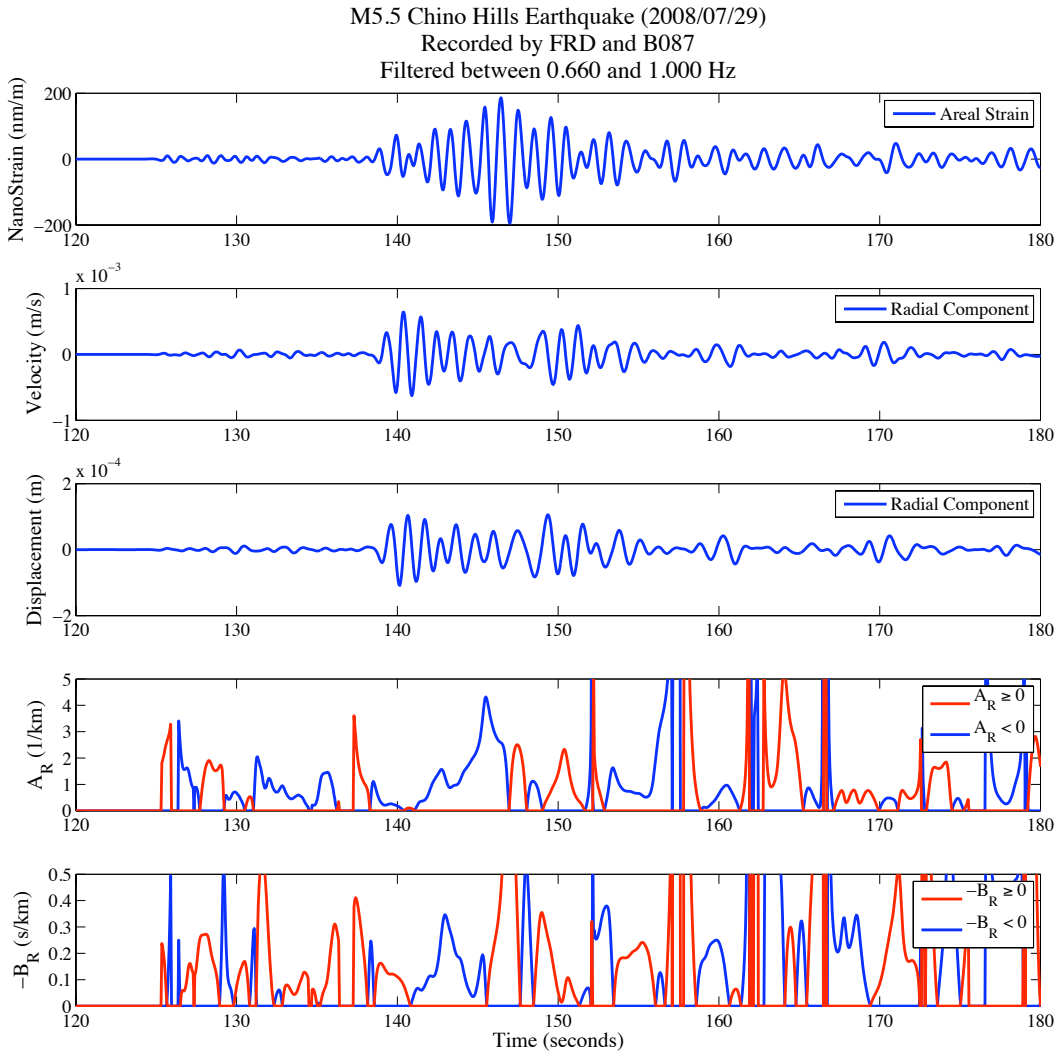

Figure A53. The result of applying Method (1) to the data corresponding to Figure (A50) band-pass filtered between 0.66 Hz and 1.0 Hz with a 4-pole Butterworth acausal filter. Instability (or "glitches") in 1D spatial gradient result is likely due to interfering waves at a particular point in time or due to an inappropriate assumption of propagation direction.

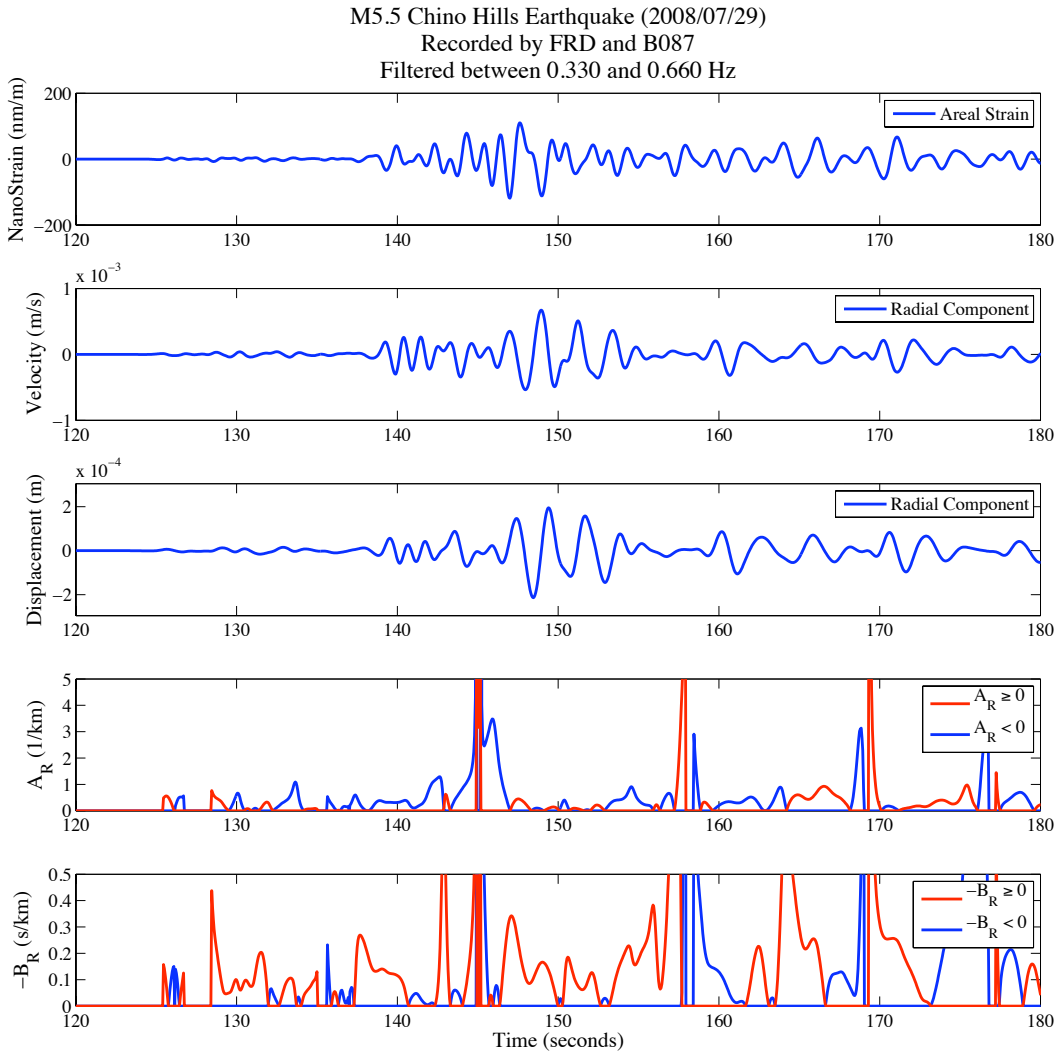

Figure A54. The result of applying Method (1) to the data corresponding to Figure (A50) band-pass filtered between 0.33 Hz and 0.66 Hz with a 4-pole Butterworth acausal filter. Instability (or "glitches") in 1D spatial gradient result is likely due to interfering waves at a particular point in time or due to an inappropriate assumption of propagation direction.

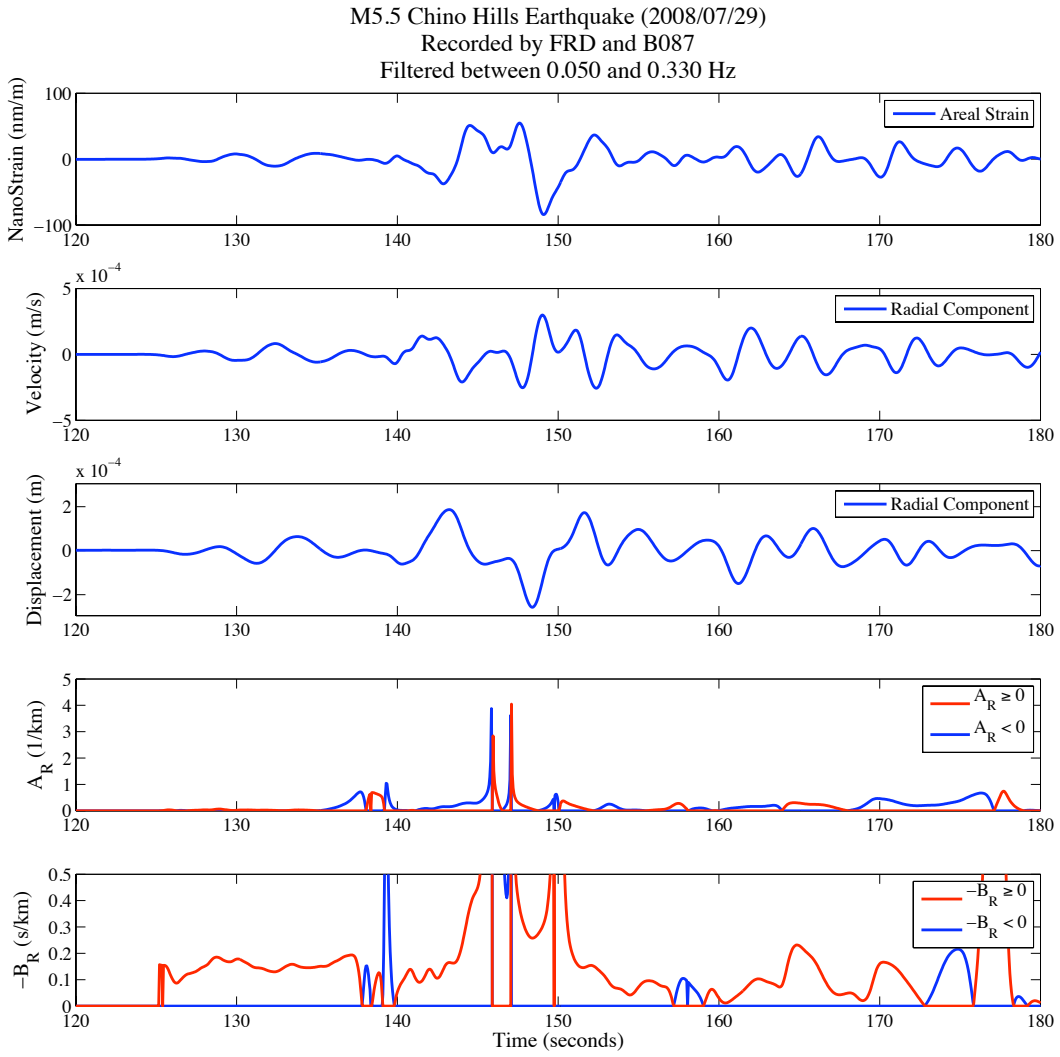

Figure A55. The result of applying Method (1) to the data corresponding to Figure (A50) band-pass filtered between 0.05 Hz and 0.33 Hz with a 4-pole Butterworth acausal filter. Instability (or "glitches") in 1D spatial gradient result is likely due to interfering waves at a particular point in time or due to an inappropriate assumption of propagation direction.

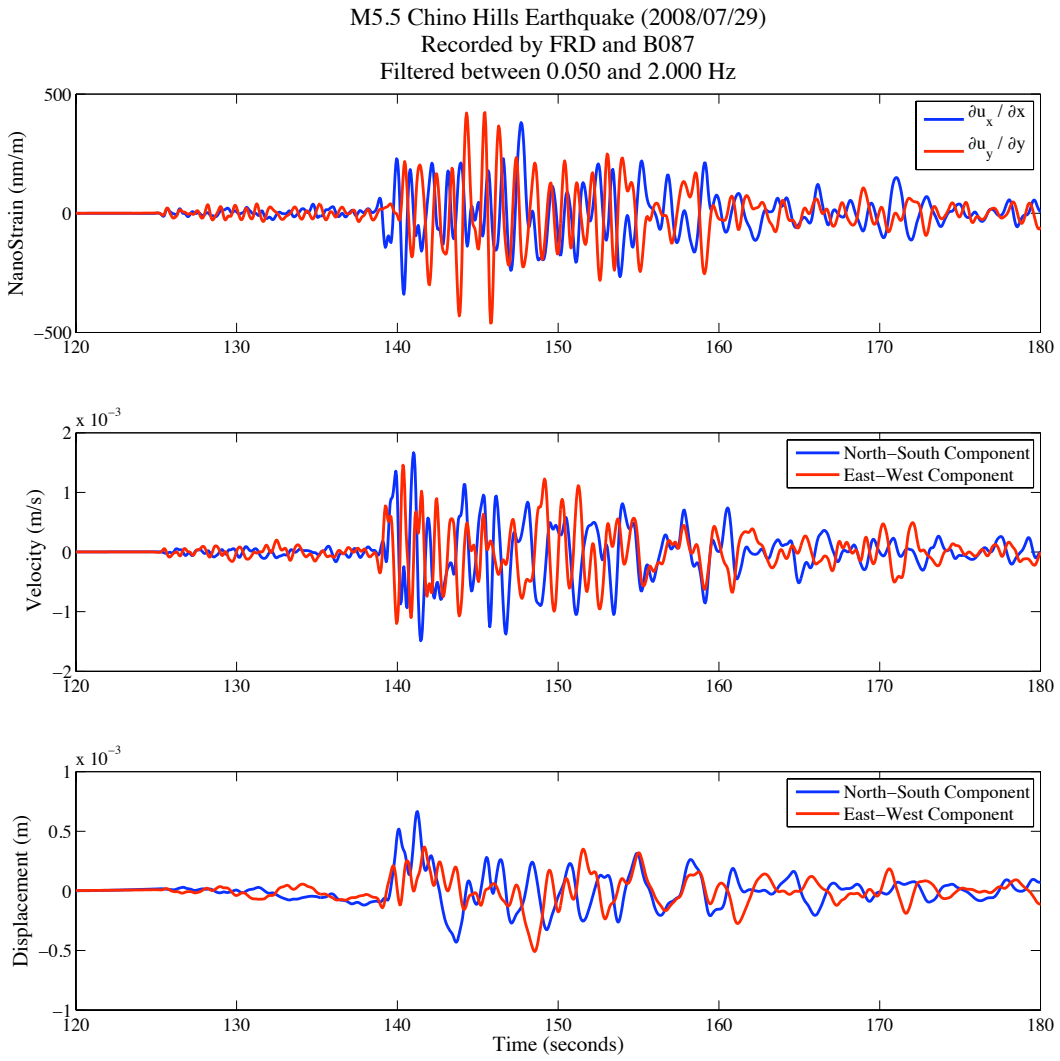

Figure A56. Data used for Method (2) include the diagonal elements of the 2D strain tensor (TOP – BLUE and RED) and the two horizontal components of the ground velocity (MIDDLE – BLUE and RED). Calibrated strain data correspond to borehole GTSM station B087 and the seismic data correspond to Anza broadband seismometer FRD. The original seismograms correspond to the 29 July 2008 M5.5 Chino Hills earthquake band-pass filtered between 0.05 Hz and 2.0 Hz with a 4-pole Butterworth acausal filter.

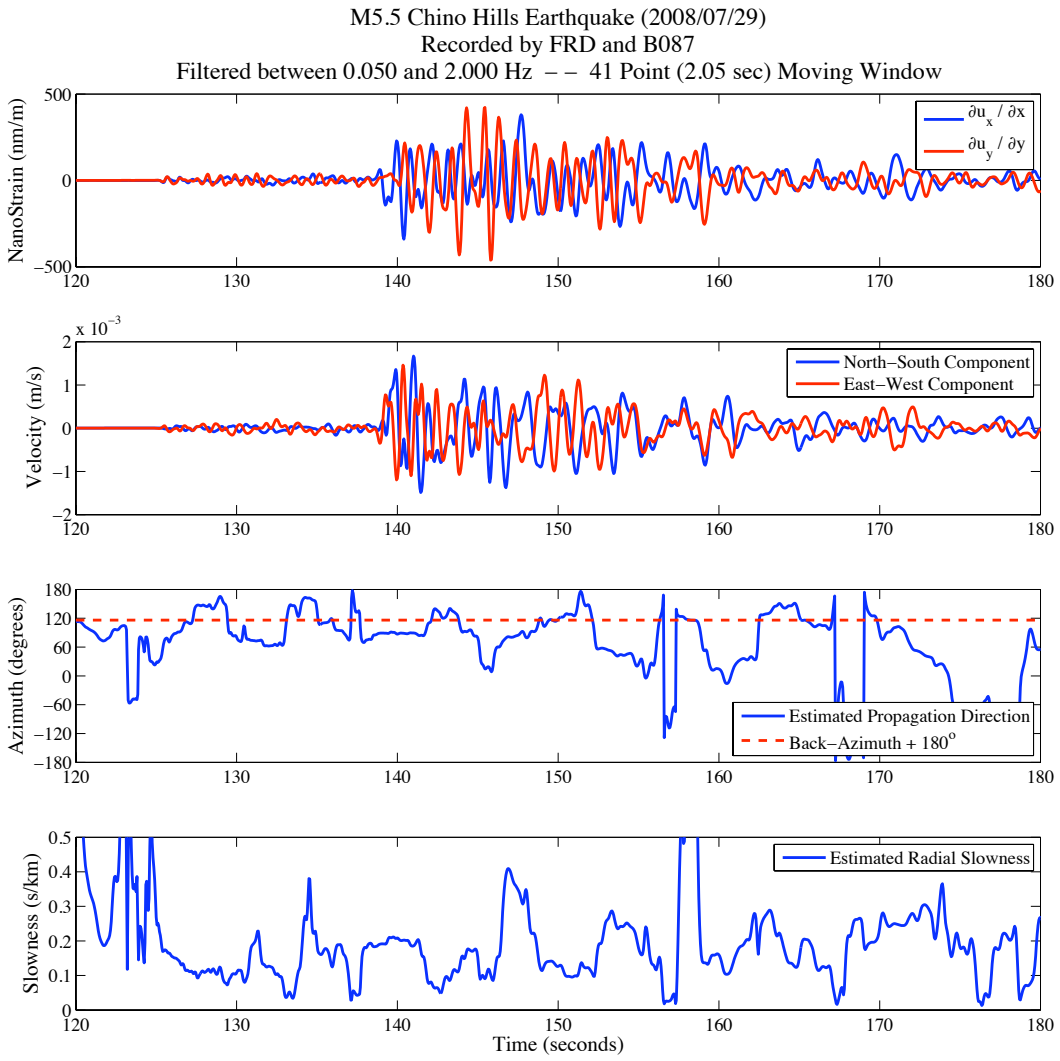

Figure A57. The result of applying Method (2) to the data corresponding to Figure (A56) band-pass filtered between 0.05 Hz and 2.0 Hz with a 4-pole Butterworth acausal filter. The dashed line in the "Azimuth" plot indicates the predicted propagation direction across the array had the waves originated from an isotropic source and traveled through an isotropic medium. Instability (or "glitches") in inversion for the horizontal slowness parameters are likely due to interfering waves within the specific time window.

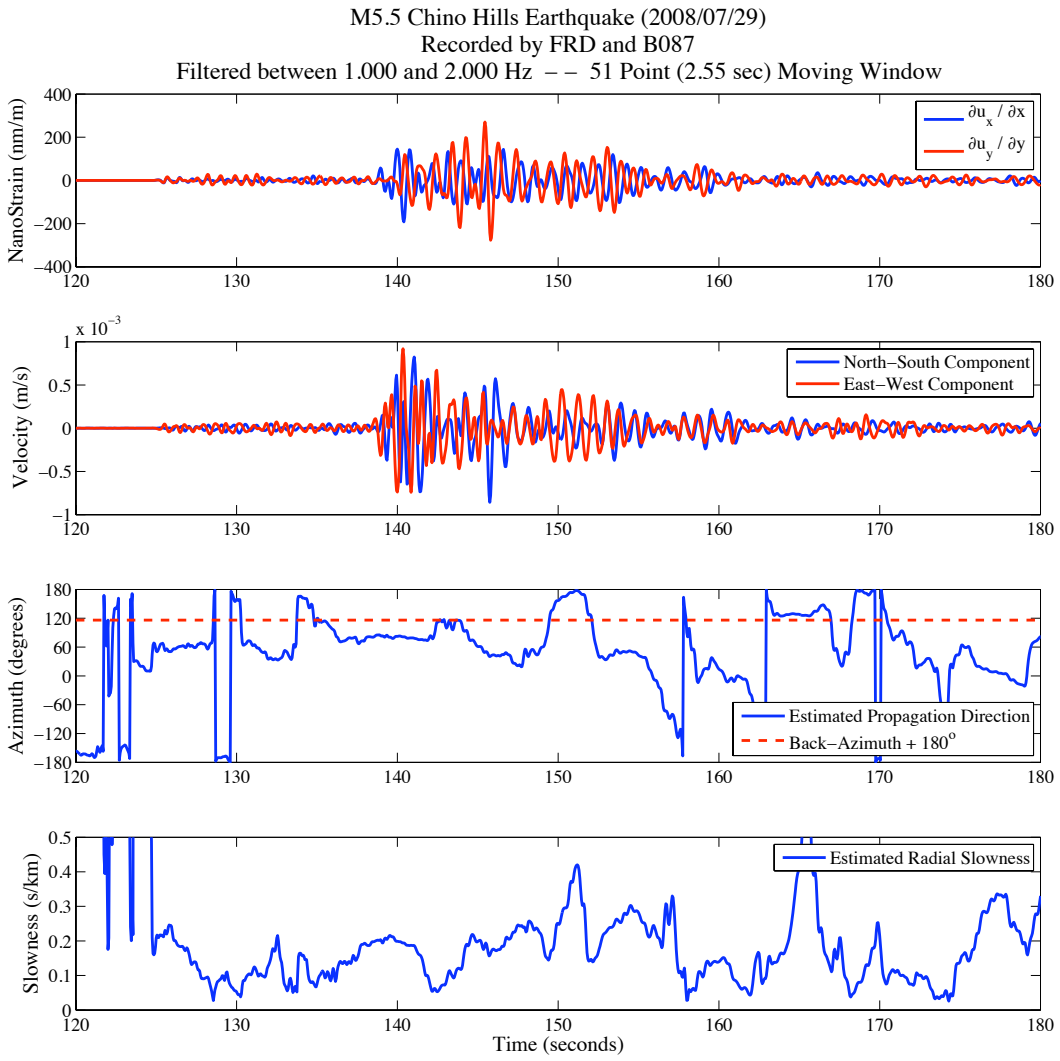

Figure A58. The result of applying Method (2) to the data corresponding to Figure (A56) band-pass filtered between 1.0 Hz and 2.0 Hz with a 4-pole Butterworth acausal filter. The dashed line in the "Azimuth" plot indicates the predicted propagation direction across the array had the waves originated from an isotropic source and traveled through an isotropic medium. Instability (or "glitches") in inversion for the horizontal slowness parameters are likely due to interfering waves within the specific time window.

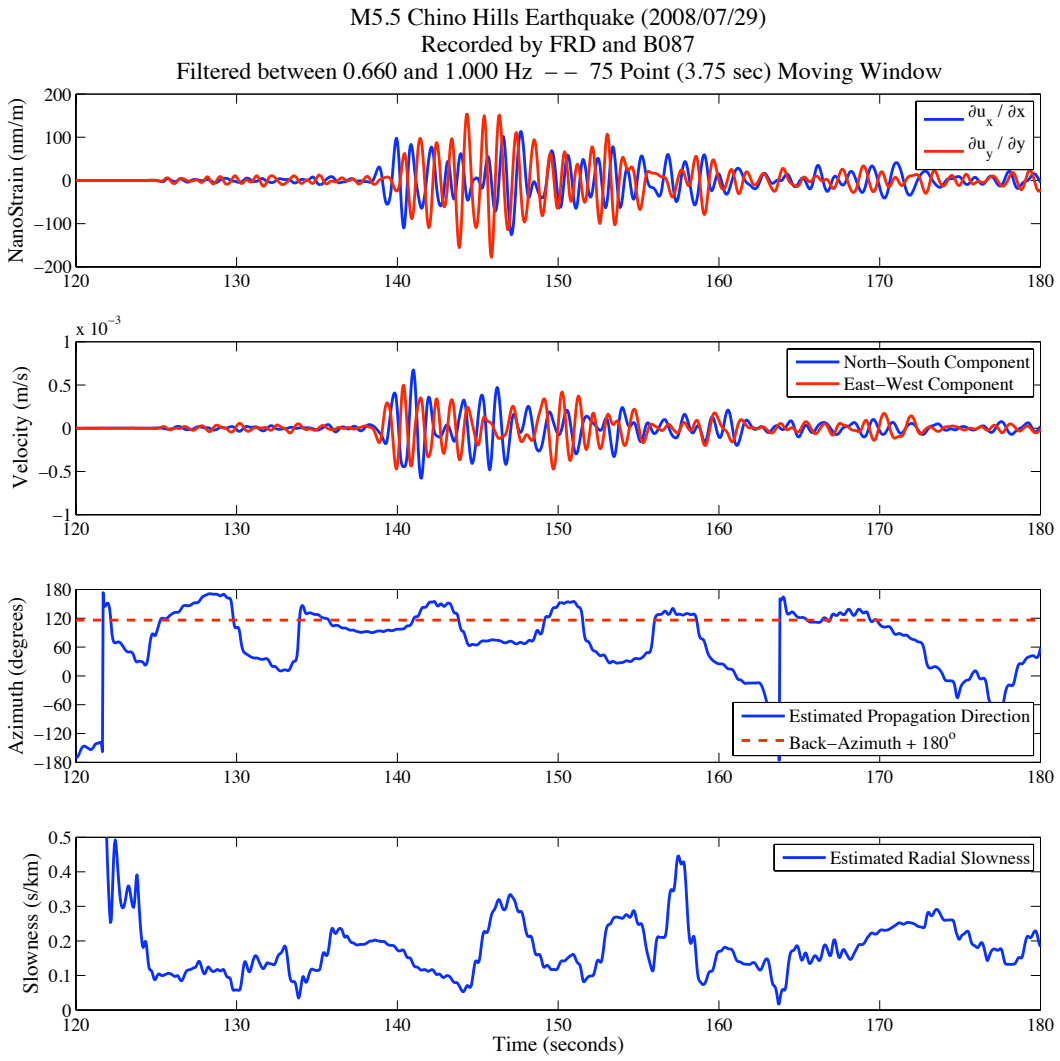

Figure A59. The result of applying Method (2) to the data corresponding to Figure (A56) band-pass filtered between 0.66 Hz and 1.0 Hz with a 4-pole Butterworth acausal filter. The dashed line in the "Azimuth" plot indicates the predicted propagation direction across the array had the waves originated from an isotropic source and traveled through an isotropic medium. Instability (or "glitches") in inversion for the horizontal slowness parameters are likely due to interfering waves within the specific time window.

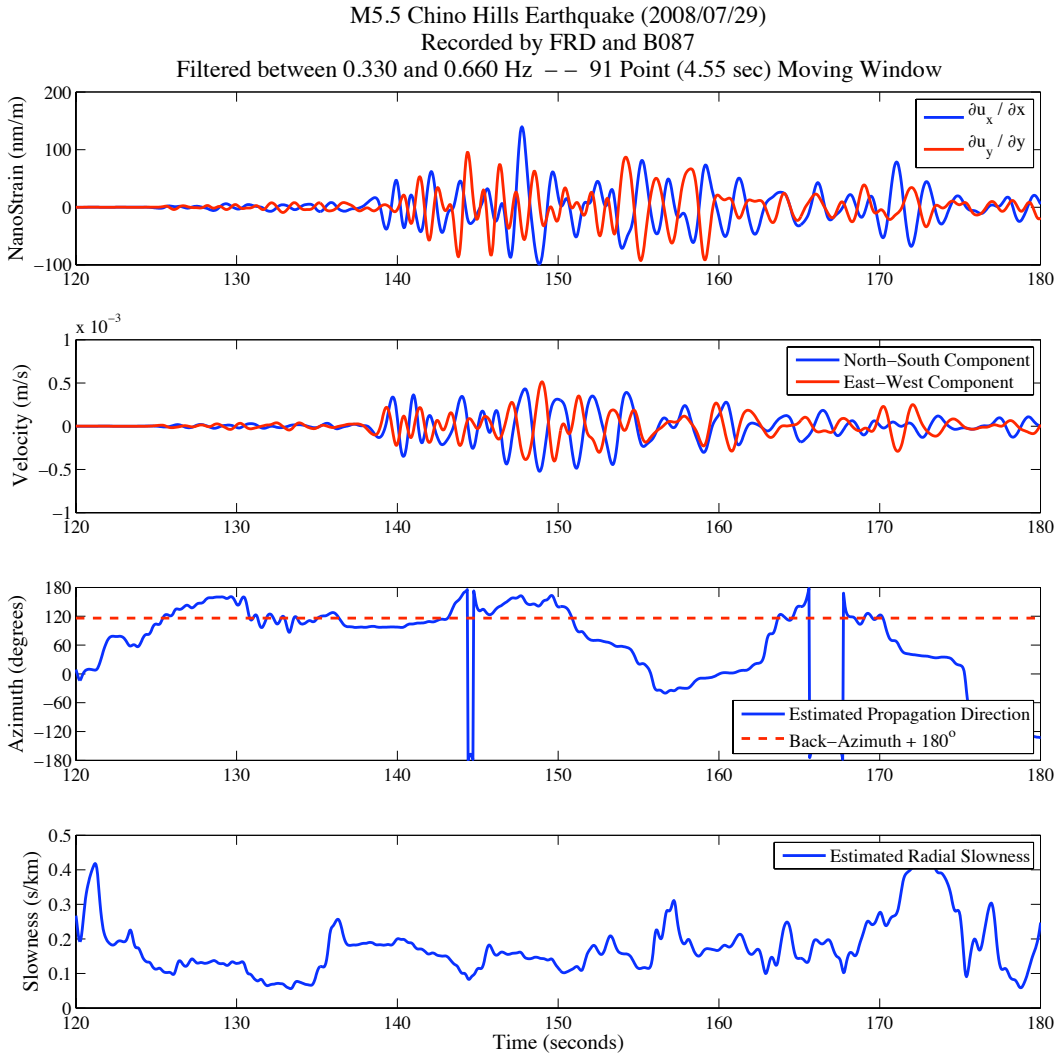

Figure A60. The result of applying Method (2) to the data corresponding to Figure (A56) band-pass filtered between 0.33 Hz and 0.66 Hz with a 4-pole Butterworth acausal filter. The dashed line in the "Azimuth" plot indicates the predicted propagation direction across the array had the waves originated from an isotropic source and traveled through an isotropic medium. Instability (or "glitches") in inversion for the horizontal slowness parameters are likely due to interfering waves within the specific time window.

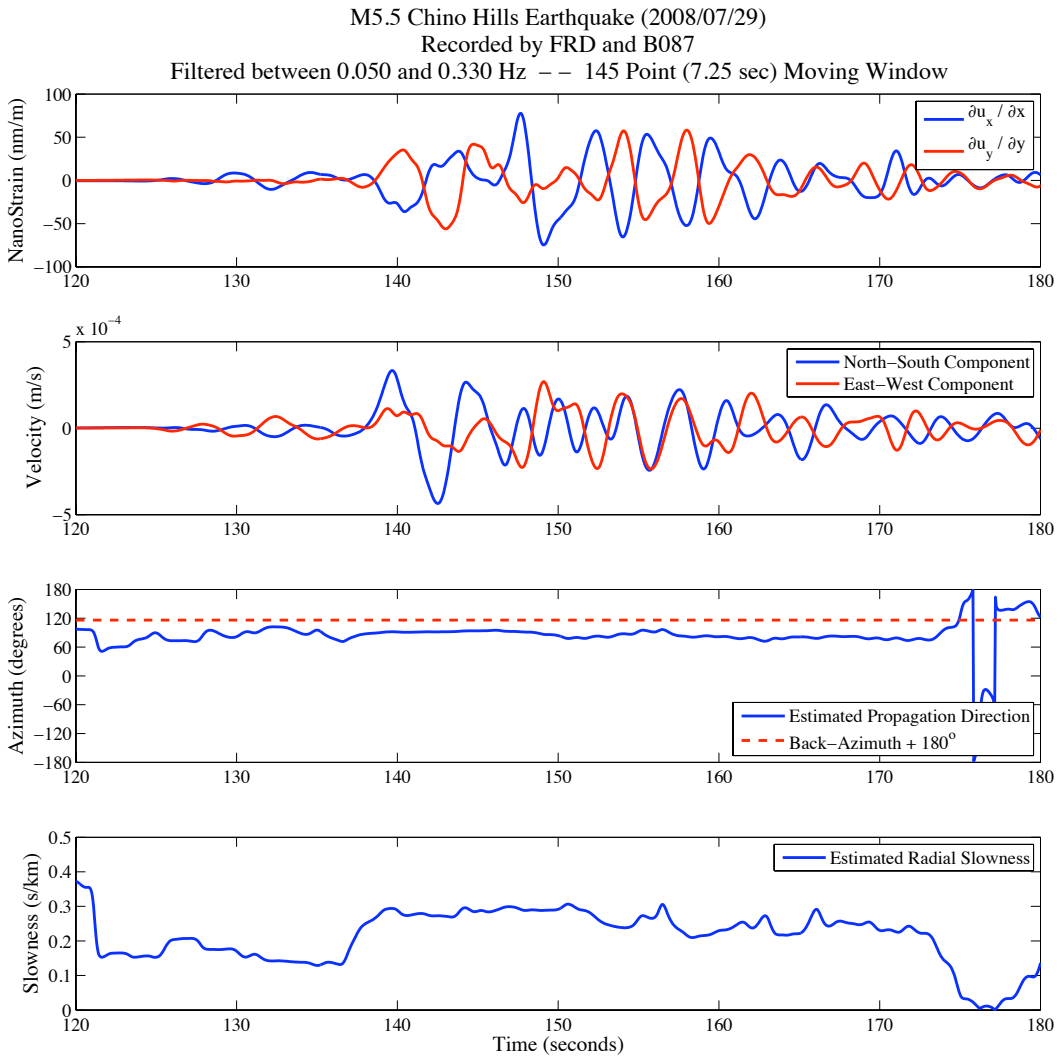

Figure A61. The result of applying Method (2) to the data corresponding to Figure (A56) band-pass filtered between 0.05 Hz and 0.33 Hz with a 4-pole Butterworth acausal filter. The dashed line in the "Azimuth" plot indicates the predicted propagation direction across the array had the waves originated from an isotropic source and traveled through an isotropic medium. Instability (or "glitches") in inversion for the horizontal slowness parameters are likely due to interfering waves within the specific time window.

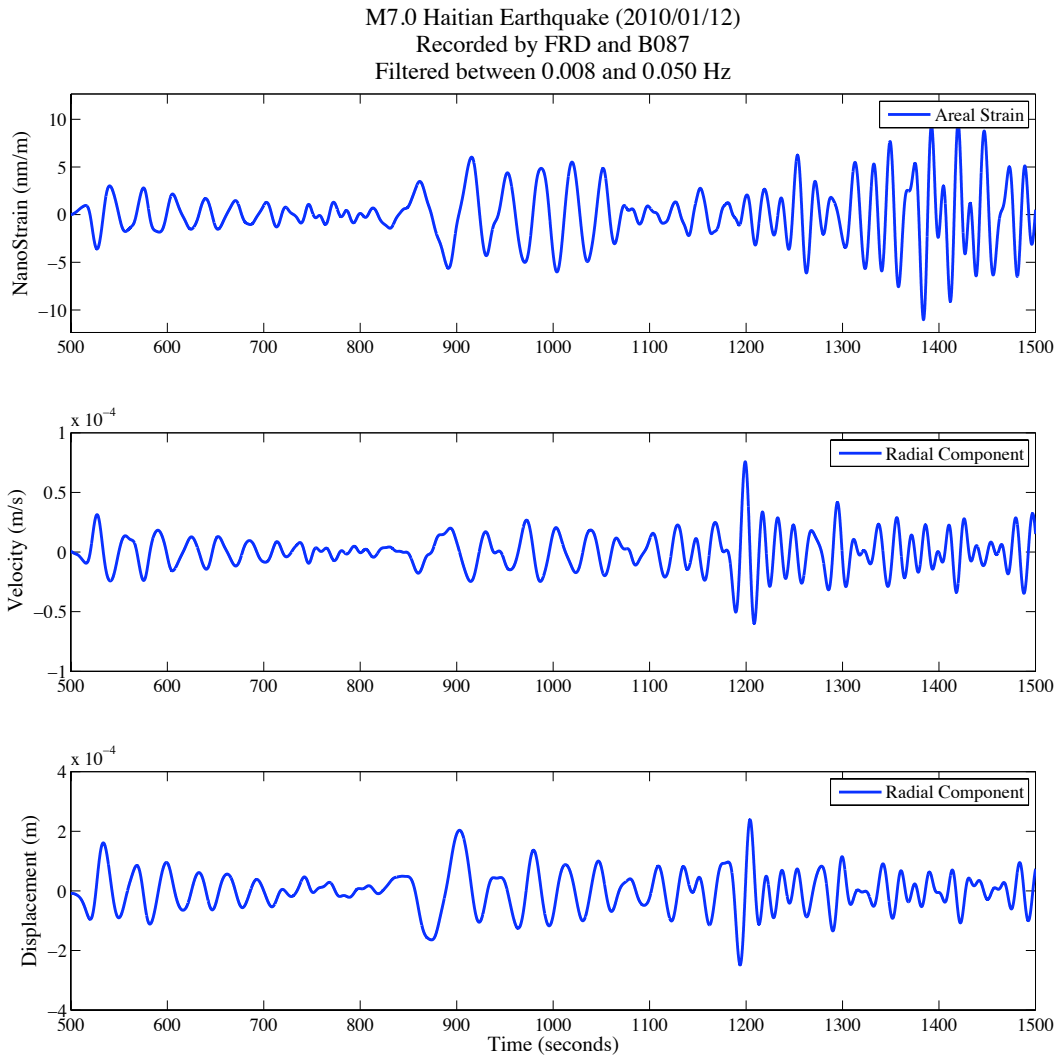

Figure A62. Data used for Method (1) include the areal strain (TOP – BLUE), the radial ground velocity (MIDDLE – BLUE), and the radial ground displacement (BOTTOM – BLUE). Calibrated strain data correspond to borehole GTSM station B087 and the seismic data correspond to Anza broadband seismometer FRD. The original seismograms correspond to the 12 January 2010 M7.0 Haitian earthquake band-pass filtered between 0.008 Hz and 0.05 Hz with a 4-pole Butterworth acausal filter.

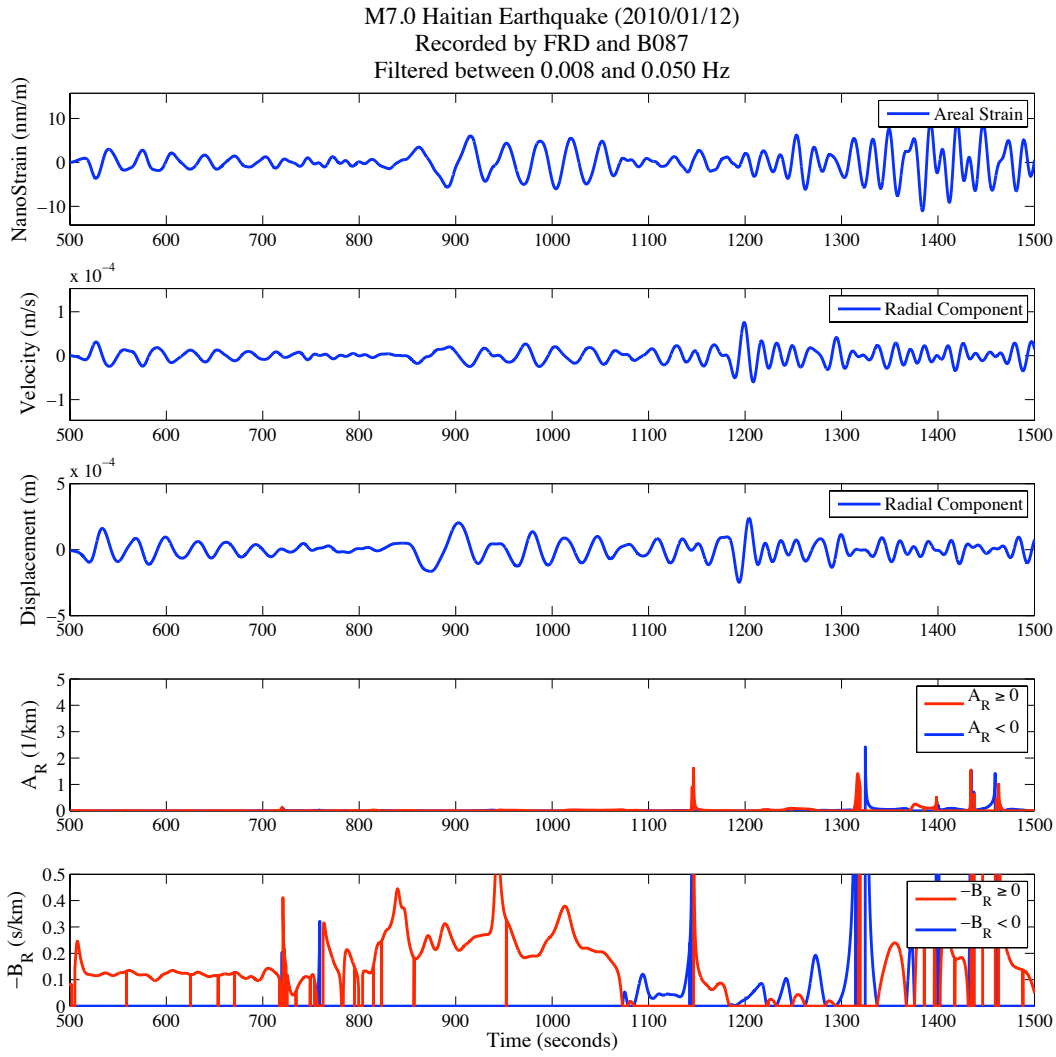

Figure A63. The result of applying Method (1) to the data corresponding to Figure (A62) band-pass filtered between 0.008 Hz and 0.05 Hz with a 4-pole Butterworth acausal filter. Instability (or "glitches") in 1D spatial gradient result is likely due to interfering waves at a particular point in time or due to an inappropriate assumption of propagation direction.

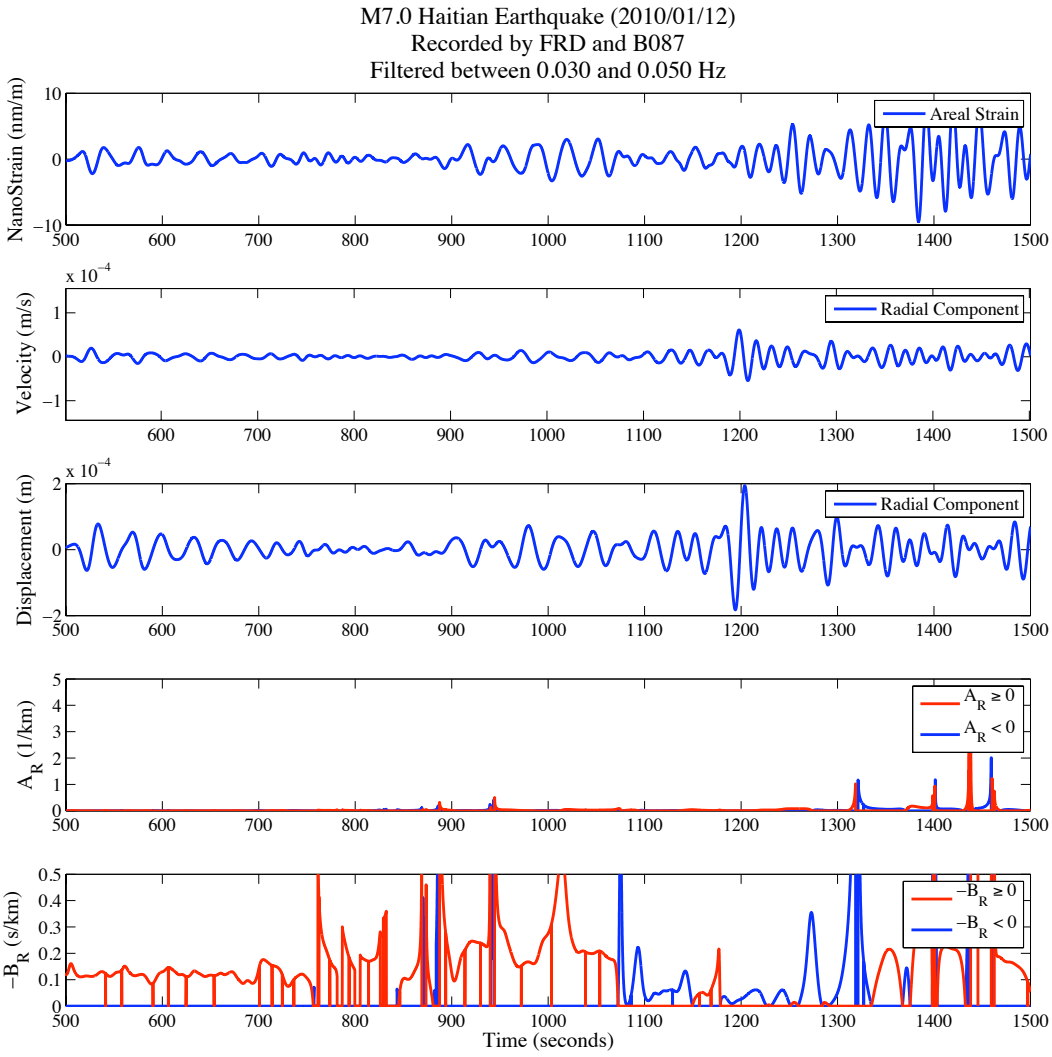

Figure A64. The result of applying Method (1) to the data corresponding to Figure (A62) band-pass filtered between 0.03 Hz and 0.05 Hz with a 4-pole Butterworth acausal filter. Instability (or "glitches") in 1D spatial gradient result is likely due to interfering waves at a particular point in time or due to an inappropriate assumption of propagation direction.

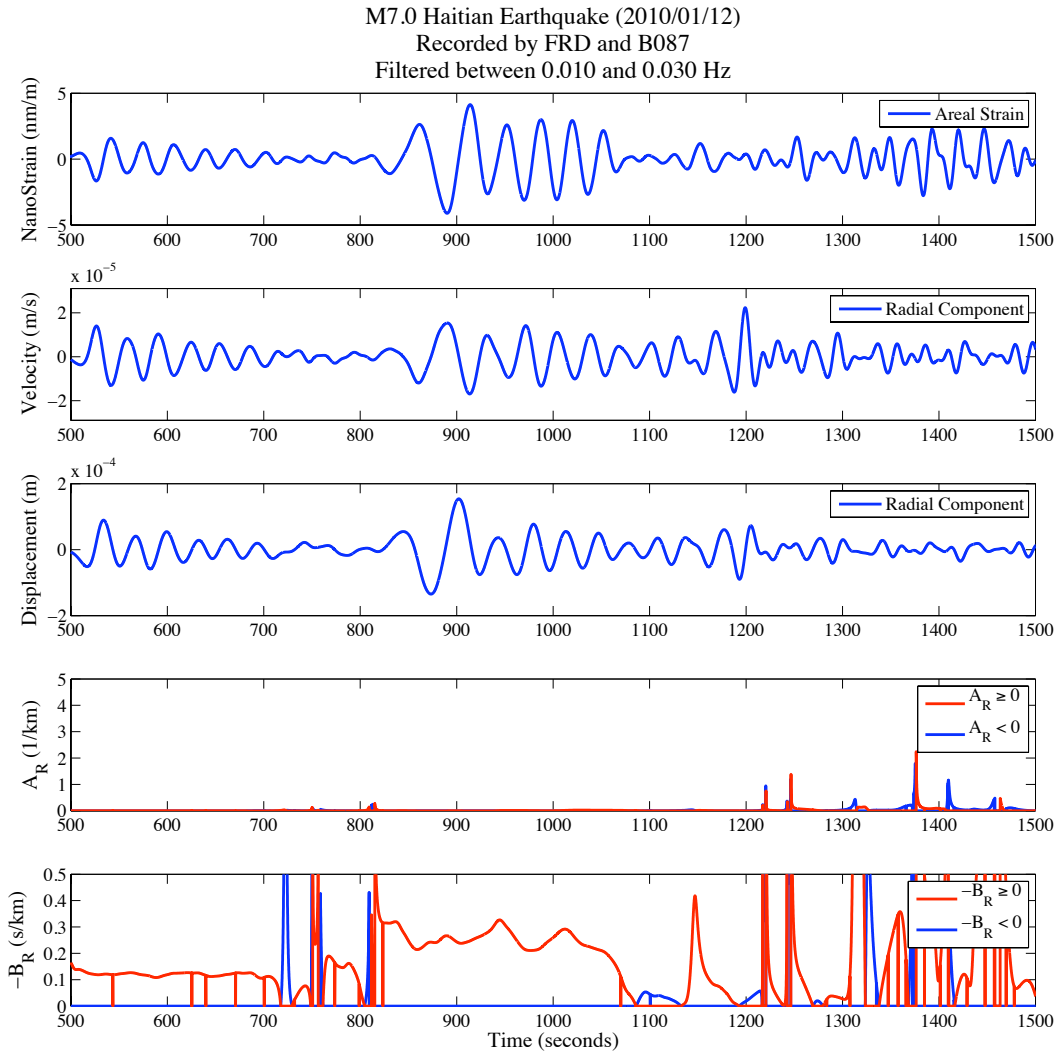

Figure A65. The result of applying Method (1) to the data corresponding to Figure (A62) band-pass filtered between 0.01 Hz and 0.03 Hz with a 4-pole Butterworth acausal filter. Instability (or "glitches") in 1D spatial gradient result is likely due to interfering waves at a particular point in time or due to an inappropriate assumption of propagation direction.

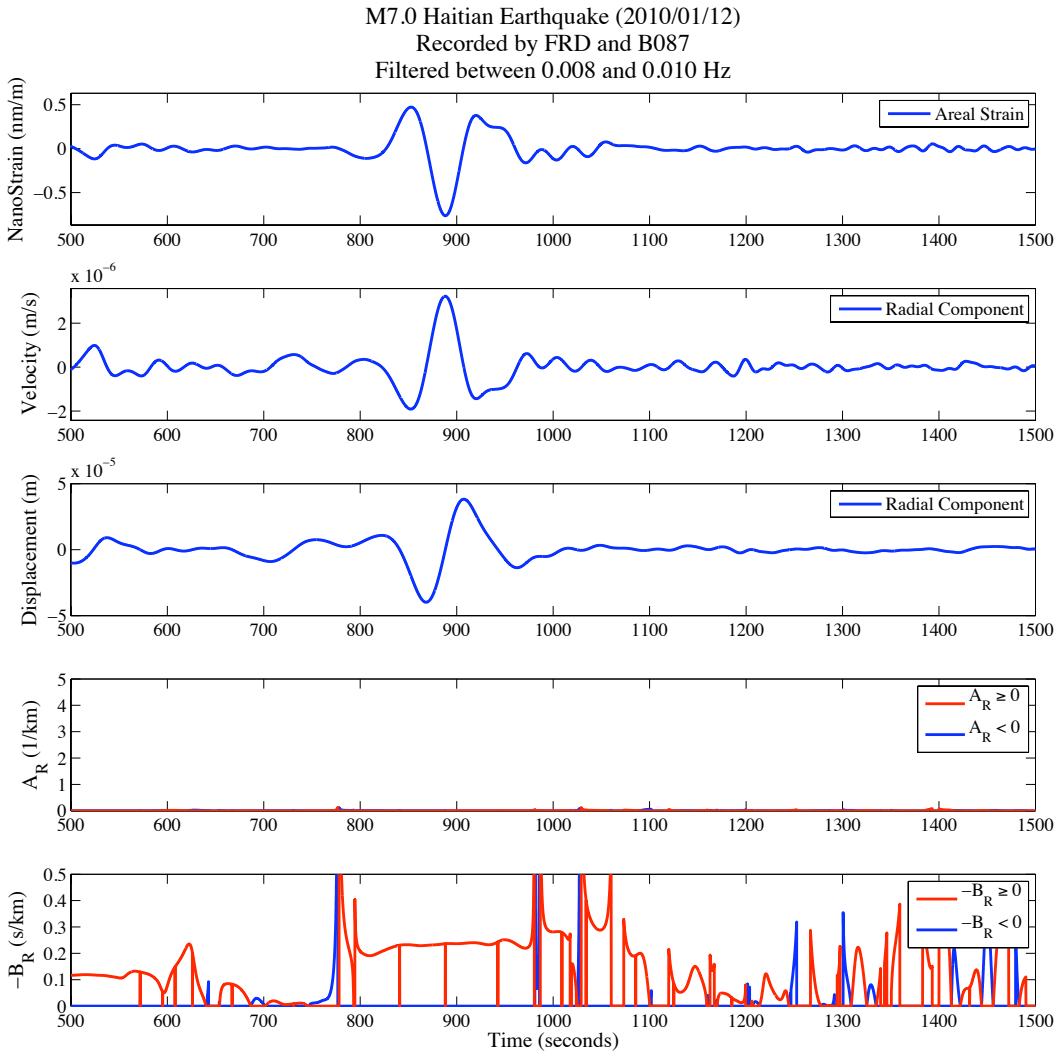

Figure A66. The result of applying Method (1) to the data corresponding to Figure (A62) band-pass filtered between 0.008 Hz and 0.01 Hz with a 4-pole Butterworth acausal filter. Instability (or "glitches") in 1D spatial gradient result is likely due to interfering waves at a particular point in time or due to an inappropriate assumption of propagation direction.

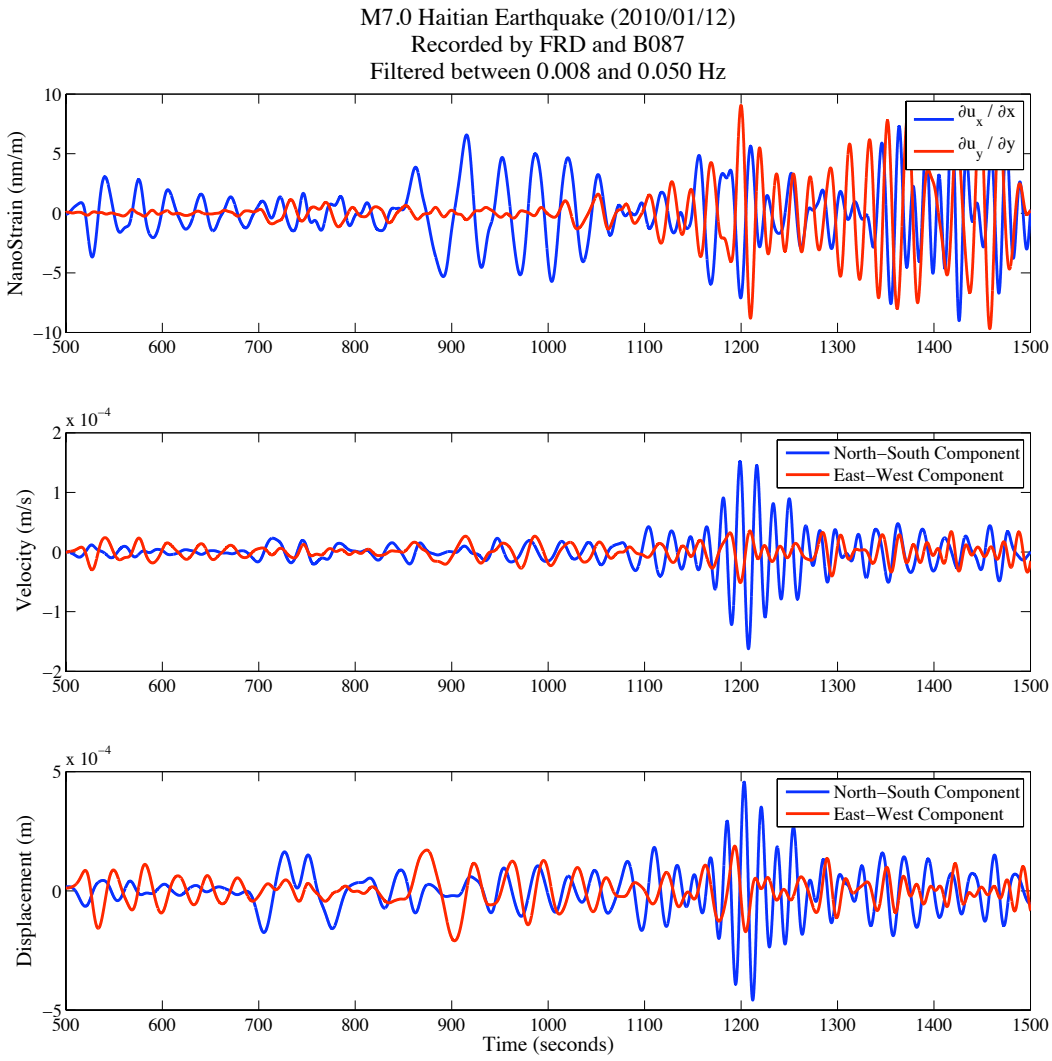

Figure A67. Data used for Method (2) include the diagonal elements of the 2D strain tensor (TOP – BLUE and RED) and the two horizontal components of the ground velocity (MIDDLE – BLUE and RED). Calibrated strain data correspond to borehole GTSM station B087 and the seismic data correspond to Anza broadband seismometer FRD. The original seismograms correspond to the 12 January 2010 M7.0 Haitian earthquake band-pass filtered between 0.008 Hz and 0.05 Hz with a 4-pole Butterworth acausal filter.

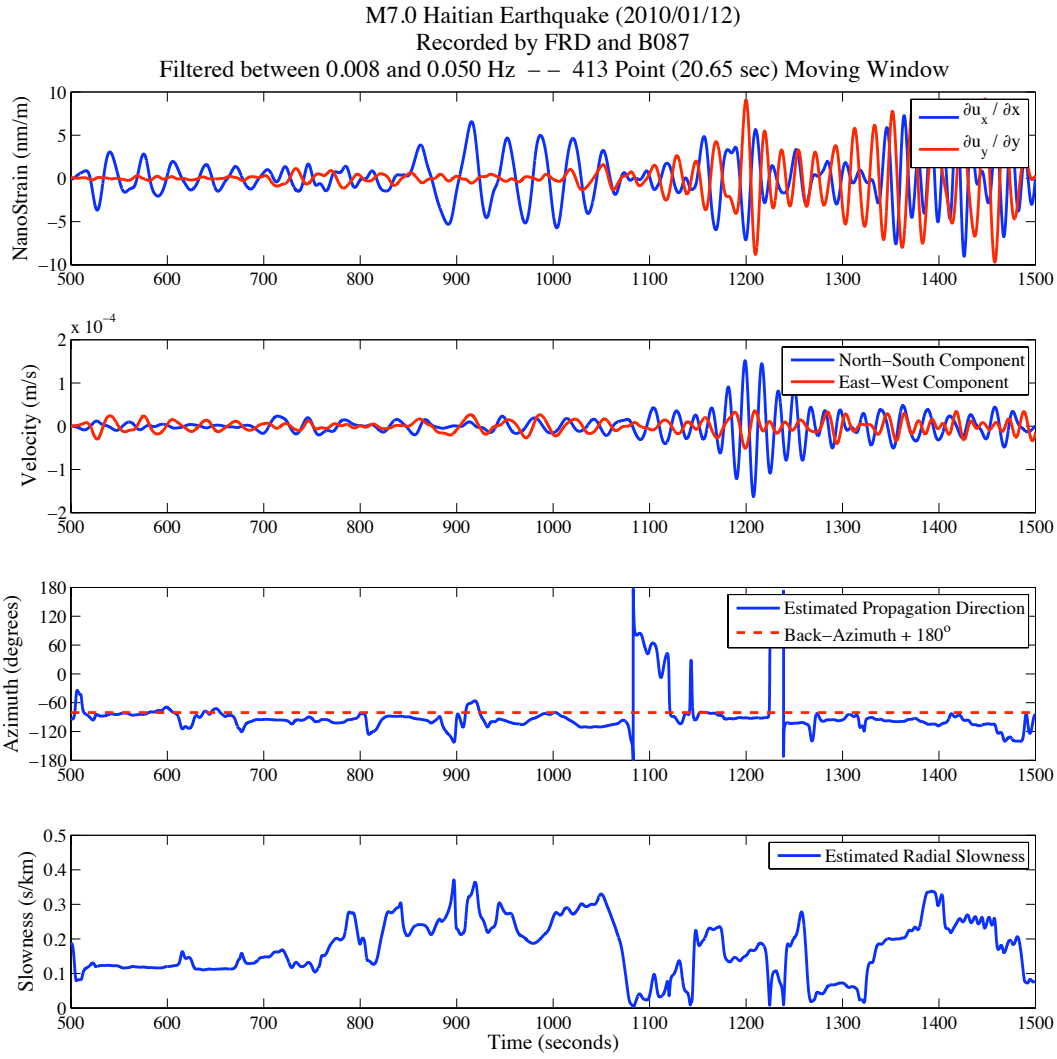

Figure A68. The result of applying Method (2) to the data corresponding to Figure (A67) band-pass filtered between 0.008 Hz and 0.05 Hz with a 4-pole Butterworth acausal filter. The dashed line in the "Azimuth" plot indicates the predicted propagation direction across the array had the waves originated from an isotropic source and traveled through an isotropic medium. Instability (or "glitches") in inversion for the horizontal slowness parameters are likely due to interfering waves within the specific time window.

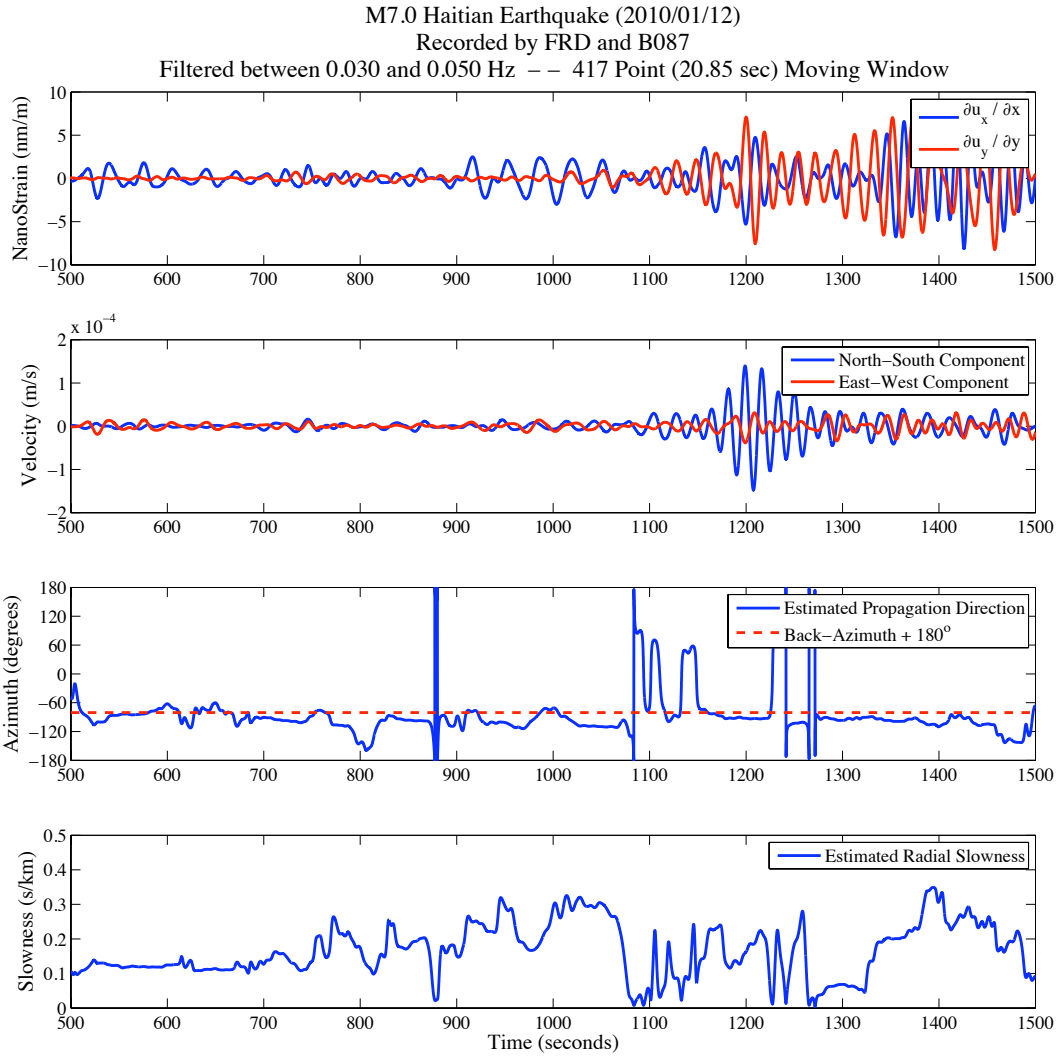

Figure A69. The result of applying Method (2) to the data corresponding to Figure (A67) band-pass filtered between 0.03 Hz and 0.05 Hz with a 4-pole Butterworth acausal filter. The dashed line in the "Azimuth" plot indicates the predicted propagation direction across the array had the waves originated from an isotropic source and traveled through an isotropic medium. Instability (or "glitches") in inversion for the horizontal slowness parameters are likely due to interfering waves within the specific time window.

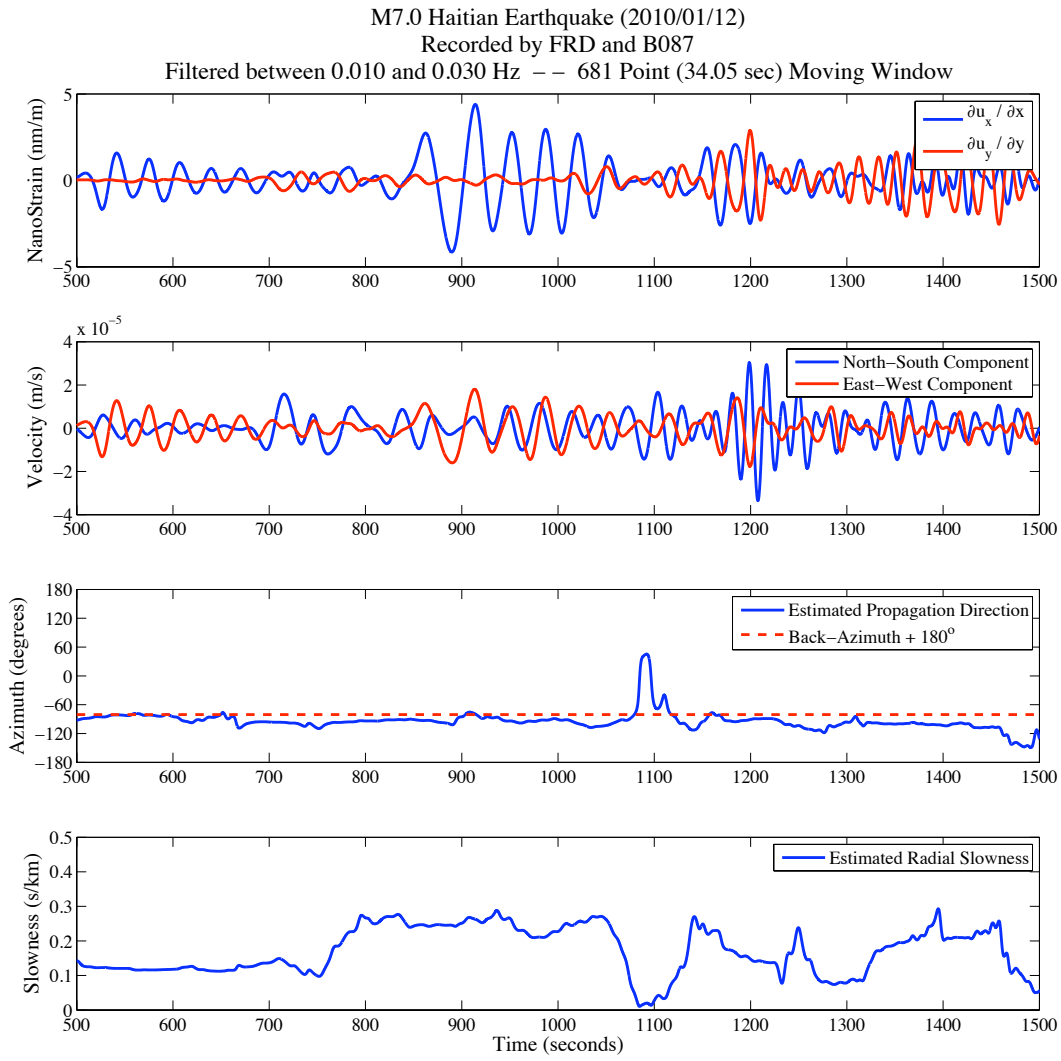

Figure A70. The result of applying Method (2) to the data corresponding to Figure (A67) band-pass filtered between 0.01 Hz and 0.03 Hz with a 4-pole Butterworth acausal filter. The dashed line in the "Azimuth" plot indicates the predicted propagation direction across the array had the waves originated from an isotropic source and traveled through an isotropic medium. Instability (or "glitches") in inversion for the horizontal slowness parameters are likely due to interfering waves within the specific time window.

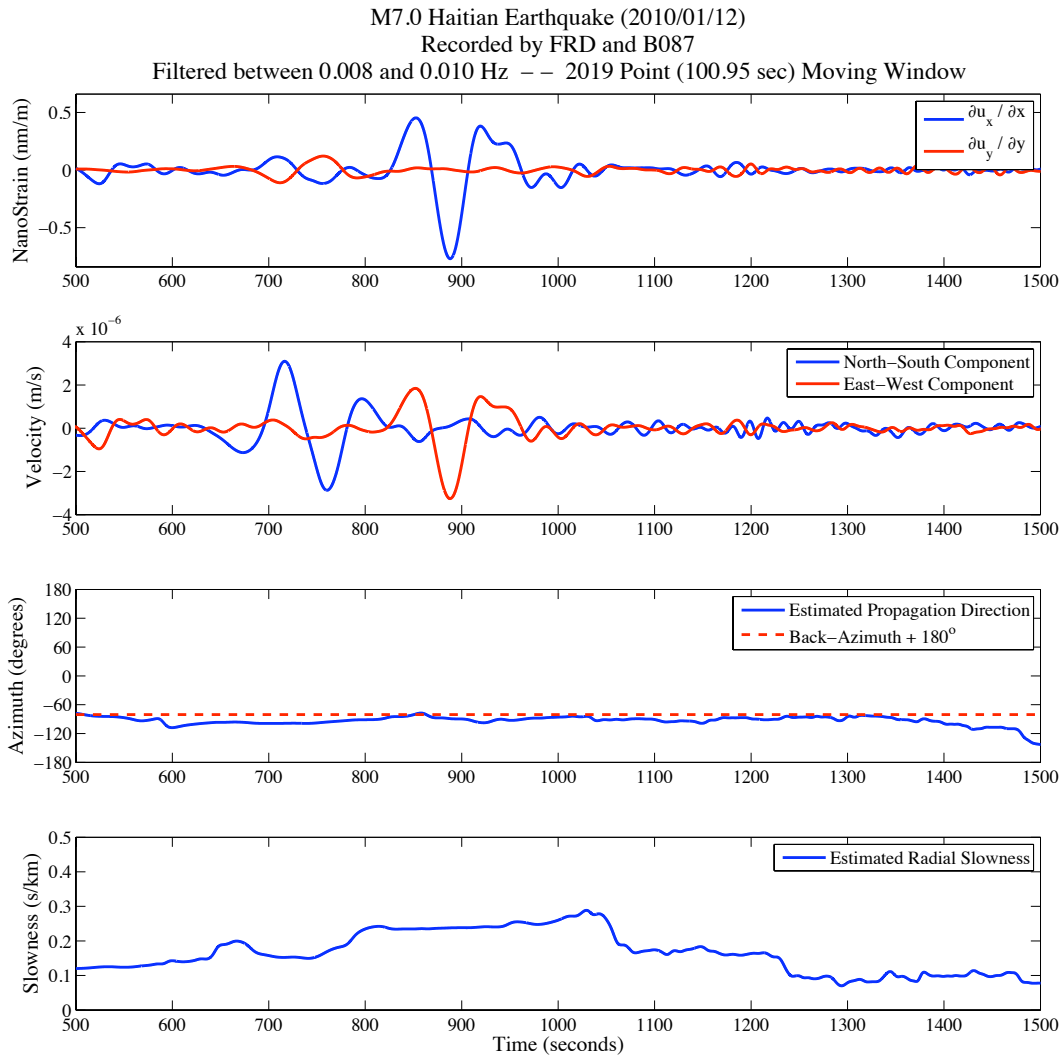

Figure A71. The result of applying Method (2) to the data corresponding to Figure (A67) band-pass filtered between 0.008 Hz and 0.01 Hz with a 4-pole Butterworth acausal filter. The dashed line in the "Azimuth" plot indicates the predicted propagation direction across the array had the waves originated from an isotropic source and traveled through an isotropic medium. Instability (or "glitches") in inversion for the horizontal slowness parameters are likely due to interfering waves within the specific time window.